# Investigation of the martensitic transformation and the deformation mechanisms occurring in the superelastic Ti-24Nb-4Zr-8Sn alloy

Yang Yang

## To cite this version:

Yang Yang. Investigation of the martensitic transformation and the deformation mechanisms occurring in the superelastic Ti-24Nb-4Zr-8Sn alloy. Material chemistry. INSA de Rennes, 2015. English. <NNT : 2015ISAR0002>. <tel-01136204>

**HAL Id: tel-01136204**

**https://tel.archives-ouvertes.fr/tel-01136204**

Submitted on 26 Mar 2015

**HAL** is a multi-disciplinary open access archive for the deposit and dissemination of scientific research documents, whether they are published or not. The documents may come from teaching and research institutions in France or abroad, or from public or private research centers.

L'archive ouverte pluridisciplinaire **HAL**, est destinée au dépôt et à la diffusion de documents scientifiques de niveau recherche, publiés ou non, émanant des établissements d'enseignement et de recherche français ou étrangers, des laboratoires publics ou privés.

Thèse

SPECIMEN NON IMPRIMABLE

**THESE INSA Rennes**
sous le sceau de l'Université européenne de Bretagne
pour obtenir le titre de
**DOCTEUR DE L'INSA DE RENNES**
Spécialité : Sciences des Matériaux

présentée par

Yang YANG

**ECOLE DOCTORALE : *SDLM***
**LABORATOIRE : *ISCR/CM***

# Etude de la transformation martensitique et des mécanismes de déformation se produisant dans l'alliage superélastique Ti-24Nb-4Zr-8Sn

**Thèse soutenue le 24.02.2015**
devant le jury composé de :

**Joël DOUIN**
Directeur de Recherche CNRS - CEMES Toulouse / Président et Rapporteur

**Denis FAVIER**
Professeur des Universités - Université de Grenoble / Rapporteur

**Yulin HAO**
Professeur - Institute of Metal Research - CAS – Shenyang / Examinateur

**Frédéric PRIMA**
Maître de Conférences - ENSCP Paris / Examinateur

**Philippe CASTANY**
Maître de Conférences - INSA Rennes / Co-Encadrant de Thèse

**Thierry GLORIANT**
Professeur des Universités - INSA Rennes / Directeur de Thèse

# Investigation of the martensitic transformation and the deformation mechanisms occurring in the superelastic Ti-24Nb-4Zr-8Sn alloy

## *Etude de la transformation martensitique et des mécanismes de déformation se produisant dans l'alliage superélastique Ti-24Nb-4Zr-8Sn*

Yang YANG

ueb

Institut des Sciences Chimiques de Rennes
UMR CNRS 6226

INSA
INSTITUT NATIONAL
DES SCIENCES
APPLIQUÉES
RENNES

# Acknowledgements

This work has been realized in the laboratory of Chemical-Metallurgy in INSA de Rennes. Now I would like to express all my thanks to members of jury for my thesis defense. I am pleasure to invite Prof. Joël DOUIN from CEMES Toulouse and Prof. Denis FAVIER from university of Grenoble to be the reviewer of my thesis. Also thanks should be given to Prof. Yulin HAO from IMR-CAS, Dr. Frédéric PRIMA from ENSCP Paris to be examiner.

I would like to give my sincere thanks to my dear supervisor Prof. Thierry GLORIANT. I am really pound and appreciate to be his student. Under his supervision, I was improved comprehensively. He gave a lot of patience when I met difficulties. Also he taught me the way of logic thinking, how to plan an experiment, how to give a good speech, how to write my first publication and so on.

Then, I would like to give thanks to my vice-supervisor Philippe CASTANY who taught me so much knowledge on the crystallography and materials without showing any impatience. His passionate attitude towards work merits me to learn in all my life. I also want to give thanks to my other supervisor Marilyne CORNEN, I am really grateful for her as I would not come to our lab without your endeavor four years before. The pleasant time we passed together will never be forgotten.

Now, I must give my thanks and appreciation to our secretary Nadine BRIE. She helped me a lot to prepare the documents for travelling business. I think I always bring her some troubles. A lot of thanks must be given to our technician Denis LAILLE for helping me to do experiments. I always feel amazing that he can resolve all the technical problems, from the repairing the furnace, the computers, to operate all the numerous devices and machines in the lab. A lot of thanks also must be given to Sandrine GEFFROY, she always be warm and nice to me with big smiles when I need her help. I should not forget to express my thanks to Isabelle THIBON who helped to answer the questions on texture and EBSD. Also, my thanks need to be given to Doina GORDIN, Henri FRANCILLETTE, Annie GUILLOU, Denis ANSEL and Amelie FILLON. Although we didn't talk too much, there is always an agreeable relationship between us and I will never forget all of you. A lot of thanks must be given to all my colleagues with whom I worked together in the last four years; they are Cécile FIZANNE, Emmanuel BERTRAND, Andry RAMAROLAHY, Jennifer DUPUIS, Lorene HERAUD, Yvan BEDOUIN, Mariana Cristina TABIRCA and Erlla Shara Silva de OLIVEIRA. I really cherish these valuable memories and moments!

Furthermore, special thanks must be given to Prof. Yulin HAO and Shujun Li. Without their Ti-24Nb-4Zr-8Sn alloy, I will not have the chance to continue my work on it. I also want to thank especially Dr. Fan SUN for his initial help when I arrived in France. Special thanks also need to be given to Mr. Patrick WEBER for the preparation of my specimens. That is the first step and really important for the successful proceeding of my thesis. The special thanks need to be given to Ms. Isabelle PERON who offered me selfish help for my EBSD experiments. The special thanks also give to Ms. Aurore GOUIN for her help and some administrative problems. Of course, I want to thank all my Chinese friends around me for bringing happiness in the foreign country. They are Han YUAN, Yi LIU, Duo WANG, Wei LIU, Jiali XU, Cheng WANG, Hua FU, Yanping WANG, Qingyuan GU, Gang HUANG, Xiao FAN, Dandan YAO, Tian XIA, Jia FU, Hua LU, Jianhua FAN, Xiao SONG, Yong HUANG, Shijian WANG.

In the end, I want to thank my dear mam, dad, elder sister Ying YANG, younger brother Liang YANG and my boyfriend Zheng MA for being my strongest supports in my life!

Yang YANG
2015.03.10

# Table of Contents

**Table of Contents ........................................................ iii**

**General introduction ........................................................ 1**

**Chapter I: Literature review ........................................................ 3**

1. Introduction ........................................................ 5
2. Orthopaedic implants for biomedical applications ........................................................ 6
    - 2.1 Orthopaedic implants and stress shielding effect ........................................................ 6
    - 2.2 Low modulus metastable β Ti alloys ........................................................ 8
3. Physical metallurgy of titanium ........................................................ 10
    - 3.1 Pure titanium ........................................................ 10
        - 3.1.1 Basic properties of pure titanium ........................................................ 10
        - 3.1.2 Equilibrium phases in pure titanium ........................................................ 11
    - 3.2 Titanium alloys ........................................................ 13
        - 3.2.1 Elements addition in titanium alloys ........................................................ 13
        - 3.2.2 Classification of titanium alloys ........................................................ 14
        - 3.2.3 Non-equilibrium phases in metastable β titanium alloys ........................................................ 18
4. Martensitic transformation and shape memory alloys ........................................................ 28
    - 4.1 Characteristic temperatures of martensitic transformations ........................................................ 29
    - 4.2 Shape memory effect and superelasticity ........................................................ 29
        - 4.2.1 Twinned and detwinned martensite ........................................................ 30
        - 4.2.2 Shape memory effect ........................................................ 31
        - 4.2.3 Superelasticity ........................................................ 32
    - 4.3 The development of Ti-Nb-based shape memory alloys ........................................................ 33
        - 4.3.1 Binary Ti-Nb alloys ........................................................ 34
        - 4.3.2 Ternary Ti-Nb-X (X=O, N, Al) alloys ........................................................ 35
        - 4.3.3 Quaternary Ti-Nb-Ta-Zr alloy ........................................................ 37
5. Ti-24Nb-4Zr-8Sn alloy ........................................................ 38
    - 5.1 Alloy designation ........................................................ 38
        - 5.1.1 Primary consideration ........................................................ 38
        - 5.1.2 Alloy design ........................................................ 40
    - 5.2 Elastic properties of single crystal ........................................................ 41
    - 5.3 Superelasticity depending on processing route ........................................................ 42
    - 5.4 Effect of heat treatment on microstructure and mechanical properties ........................................................ 43
    - 5.5 Corrosion resistance ........................................................ 46
    - 5.6 Fatigue properties ........................................................ 46
        - 5.6.1 High-cycle fatigue ........................................................ 47
        - 5.6.2 Low-cycle fatigue ........................................................ 48
    - 5.7 Biocompability ........................................................ 49
    - 5.8 Unresolved problems ........................................................ 49

References ........................................................ 50

**Chapter II: Material and methods ........................................................................................61**

1. Material and preparation of samples ....................................................................63
2. Mechanical tests ..................................................................................................65
   - 2.1 Conventional tensile tests ...........................................................................65
   - 2.2 Cyclic tensile tests ......................................................................................66
3. Microstructural characterizations ........................................................................67
   - 3.1 Optical microscopy .....................................................................................67
   - 3.2 X-ray diffraction .........................................................................................67
   - 3.3 Crystallographic texture .............................................................................68
     - 3.3.1 Definition of crystallographic texture ...................................................68
     - 3.3.2 Principle of texture measurement .........................................................69
   - 3.4 Electron backscattered diffraction ..............................................................70
   - 3.5 Transmission electron microscopy ..............................................................71
4. *In situ* synchrotron X-ray diffraction .................................................................72
5. Dynamic mechanical analysis ..............................................................................73
   - 5.1 Principle of dynamic mechanical analysis ..................................................73
   - 5.2 DMA tests ..................................................................................................74

References ..............................................................................................................75

**Chapter III: Primary investigations on the superelasticity of the Ti2448 alloy ........................77**

1. Introduction .........................................................................................................79
2. Mechanical properties ..........................................................................................80
3. Superelasticity depending on thermal treatment ..................................................81
4. Microstructural characterization ..........................................................................83
   - 4.1 X-ray diffraction .........................................................................................83
   - 4.2 Optical microstructure ................................................................................84
5. Texture analysis ...................................................................................................86
   - 5.1 Texture evolution depending on thermo-mechanical treatment ...................86
   - 5.2 Superelasticity dependence on texture ........................................................91
6. Conclusion ..........................................................................................................92

References ..............................................................................................................93

**Chapter IV: Characterization of the martensitic transformation by *in situ* synchrotron X-ray diffraction and dynamic mechanical analysis ..............................................................95**

1. Introduction .........................................................................................................97
2. Microstructure and mechanical properties ...........................................................98
3. *In situ* synchrotron X-ray diffraction .................................................................99
   - 3.1 Indexation of whole spectrum .....................................................................99
   - 3.2 Evolution of partial spectra with applied strains .......................................100
   - 3.3 Measurement of cell parameters ...............................................................103
     - 3.3.1 Cell parameters under loading condition ............................................103
     - 3.3.2 Cell parameters under unloading condition ........................................105
4. Dynamic mechanical analysis ............................................................................106
   - 4.1 Determination of characteristic temperatures ...........................................106

4.2 Evolution of storage modulus curves and damping factor curves depending on applied stresses ........ 107
4.3 Characteristic temperatures depending on applied stresses ........ 110
5. Comparison between SXRD, DMA and tensile curves ........ 112
6. Conclusions ........ 113
References ........ 114

**Chapter V: Plastic deformation mechanisms in the Ti2448 alloy ........ 117**

1. Introduction ........ 119
1.1 Stress-induced martensitic α″ phase ........ 119
1.2 Lattice correspondence between β and α″ phases ........ 119
1.3 Crystallographic theory of twinning ........ 120
2. Experimental results ........ 123
2.1 Tensile behavior and optical microstructure of ST alloy ........ 123
2.2 EBSD analysis of ST alloy ........ 125
2.3 TEM observations on the deformation twining of ST alloy ........ 126
2.4 TEM observations of dislocations in ST and FT alloys ........ 129
3. Discussion ........ 130
3.1 Determination of twinning systems in ST alloy ........ 130
3.2 Sequence of plastic deformation in ST alloy ........ 135
4. Conclusions ........ 137
References ........ 138

**General conclusion ........ 141**

**Document de synthèse en français ........ 145**

References ........ 153

# General introduction

Development of biomaterials for application in orthopedic implants is challenging due to problems like toxicity, stress shielding effect and biocompatibility existing in the currently used Ti-6Al-4V alloy, 316L stainless steel and Co-based alloys in medicine. The toxicity and biocompability can be resolved by using non-toxic alloying elements, while the stress shielding effect can be resolved by the design of new alloys exhibiting low elastic modulus. Among all the candidate materials, β-metastable titanium alloys are currently under development to replace the Ti-6Al-4V for orthopedic applications such as hip prosthesis for example.

The design of biocompatible β-metastable titanium alloys are mainly focused on the use of transition metal alloying elements which contain rich d-electrons. Such kind of binary alloys including Ti-Nb, Ti-Mo, Ti-Ta and Ti-Zr systems are known to exhibit a potentially low modulus if the electron per atom ratio (e/a) value is lower enough. Based on it, Hao et al. employed the Ti-24Nb system (wt.% ) in order to develop a new β titanium alloy, in which the value of e/a nearly approaches the minimum limit situated at 4.15. Further addition of Zr and Sn are also used in order to effectively suppress the $\omega_{ath}$ phase and $\alpha''$ martensitic transformation in the β-metastable microstructure obtained by quenching but maintaining the value of e/a unchanged. The present investigated superelastic Ti-24Nb-4Zr-8Sn (wt. %) alloy composition (Ti2448 for short) was finally developed.

This β-metastable Ti2448 alloy presents high strength (>800MPa), low modulus (42GPa), as well as superelasticity characterized by a maximum recoverable strain of 3.3 %. Comprehensive evaluations on biocompability and fatigue tests have proved its possibility to be used in medicine. However, the deformation behavior of this alloy, especially elastic and plastic mechanisms, remains unclear due to a complex associated metallurgy. In the frame of this thesis, the work was focused on the investigation of the different deformation mechanisms in relationship with the superelastic behavior and the martensitic transformation occurring in such alloy. In the present manuscript, five chapters are included as follows:

In the first chapter, a bibliographic study was carried out. The investigation context was detailed concerning on basic requirements for the biomedical materials used for orthopedic implant. Physical metallurgy of titanium emphasizing on metastable $\alpha''$ and ω phases was then introduced. Next, the superelasticity and shape memory effect related to martensitic $\alpha''$ transformation were explained in view of its response to mechanical load and temperature. After that, the recently investigated β-metastable Ti-Nb-based titanium alloys were presented, followed by an introduction of the present Ti2448 alloy.

In the second chapter, all the procedures for preparing the material and experimental techniques were presented. The as-received hot forged ingot was subjected to different thermo-mechanical treatments. Conventional and cyclic tensile tests were used to evaluate the mechanical properties and the superelastic properties. X-ray diffraction was employed to investigate the texture of the material. On the other hand, *in situ* synchrotron X-ray diffraction (SXRD) and dynamic mechanical analysis (DMA) were used to characterize the martensitic transformation. Finally, optical microscopy, EBSD and TEM techniques were used to observe the deformed microstructures.

In the third chapter, preliminary investigations of the microstructures, the mechanical properties and the superelasticity were conducted. Also, the influence of texture change due to different cold rolling reduction rate was analyzed in this chapter.

In the fourth chapter, the stress-induced martensitic (SIM) transformation was characterized by *in situ* SXRD under both loading and unloading conditions. Phase transformations and cell parameter evolutions were then evaluated from the different SXRD profiles obtained. A three step deformation sequence can be thus proposed. In this chapter, the characteristic temperatures of martensitic transformation were also measured from DMA experiments, in which the critical stress for inducing the martensitic transformation can be compared with the conventional tensile tests.

In the final chapter, the deformation microstructures of solution-treated and flash thermal-treated alloys were observed mainly by EBSD and TEM. The lattice correspondence between $\beta$ and $\alpha''$ phases was used to deduce the crystallographic orientation of SIM $\alpha''$ phase under loading conditions. Therefore, the plastic deformation mechanisms including twin formation are reported.

# Chapter I: Literature review

# 1. Introduction

Biomaterials can be derived either from nature or synthesized in laboratories using metallic components, polymers, ceramics or composite materials through chemical approaches (*Williams 1986*), which can be used to replace or repair the lost or diseased biological structure in order to restore its form and function. Since 1969, the field of biomaterials began to gain its due recognition after the first meeting held on biomaterials at Clemson University (*Geetha 2009*).

The application of biomaterials varies from joint replacement, trauma and spinal fixation devices, cardiovascular stents and replacement of spinal discs. Amongst all these, the number of implants used for spinal, hip and knee replacements are extremely high. Because human joints suffering from degenerative diseases such as arthritis can lead to pain or bone loss. It has already been estimated that 90% of population over the age of 40 suffers from these kinds of degenerative diseases and the aged people population has increased tremendously in recent past (*Geetha 2009*). By 2030, the demand for primary total hip arthroplasty is estimated to grow by 174% to get 572 000 cases per year in the world. In the same time, the demand for primary total knee arthroplasty is projected to grow by 673% to 3.48 million procedures (*Kurtz 2007*).

**Table 1-1.** Implants division and type of metallic materials used (*Hermawan 2011*).

| Division | Example of implants | Type of metal |
|---|---|---|
| Cardiovascular | Stent | 316L SS; CoCrMo; Ti |
| | Artificial valve | Ti6Al4V |
| Orthopaedic | Bone fixation (plate, screw, pin) | 316L SS; Ti; Ti6Al4V |
| | Artificial joints | CoCrMo; Ti6Al4V; Ti6Al7Nb |
| Dentistry | Orthodontic wire | 316L SS; CoCrMo; TiNi; TiMo |
| | Filling | AgSn(Cu) amalgam; Au |
| Craniofacial | Plate and screw | 316L SS; CoCrMo; Ti; Ti6Al4V |

Table 1-1 lists typical examples of metallic biomaterials and their application in clinic. Specific requirements for biomaterials depend on the specific implant applications. Fig. 1-1 gives some pictures of implants used as dental implants, artificial joints and spin screw.

**Fig. 1-1** Examples of an artificial joints and spin screw.

Based on this background, a general situation of orthopaedic implants will be elaborated firstly in this chapter, including basic requirement and stress shielding effect which is an important problem affecting the success of implant surgery. Meanwhile, due to the requirements for orthopaedic implants, β metastable titanium alloys stand out from competition. After a brief introduction of the physical metallurgy of titanium and titanium alloys, the martensitic transformation involving the superelasticity and shape memory effect will be presented in detail. Finally, the previous studies on the presently investigated superelastic β Ti-24Nb-4Zr-8Sn alloy will be summarized.

# 2. Orthopaedic implants for biomedical applications

## 2.1 Orthopaedic implants and stress shielding effect

Presently, metallic materials used for orthopedic implants include stainless steels, Co-based alloys and Ti-based alloys. However, the stainless steels have low cost but cause toxicity due to ions releasing into body fluid and eventually lead to failure of implants. The Co-based alloys exhibit an excellent wear resistance but high hardness. In terms of Ti-based alloys, the mainly used one is the Ti-6Al-4V alloy which was not purpose-designed and originally developed for the aerospace industry. Recent studies show that the release of both Al and V ions from the Ti-6Al-4V alloy might cause long-term health problems, such as peripheral neuropathy, osteomalacia, and Alzheimer diseases (*Nag 2005*).

One common disadvantage for these existing metallic orthopaedic materials is their elastic modulus significantly higher (>100GPa) than that of bone tissue (10-40GPa), leading to stress shielding effect (*Long 1998*) that can potentially causes bone resorption and failure of the implant.

The stress shielding is the name given to *in vivo* reduction in bone density following the introduction of the implant (*Huiskes 1992*). As an example, in a natural state, a femur carries the external load all by itself, and the load is transmitted from the femoral head through the femoral neck to the cortical bone of the proximal femur as shown in Fig. 1-2. Once an artificial stiffer stem was provided to the canal, it will share the load and the carrying capacity with bone. As a result, the bone is subjected to reduced stresses and hence stress shielded. The change in stress distribution in the affected bone originates from the mismatch of stiffness between bone and implants (*Yang 2011, Wan 1999*). The main route to improve the match of stiffness between the implant and the bone is then to reduce the elastic modulus of the implanted material which is 3 or 4 times higher than the bone one (4-30GPa) with the materials actually used.

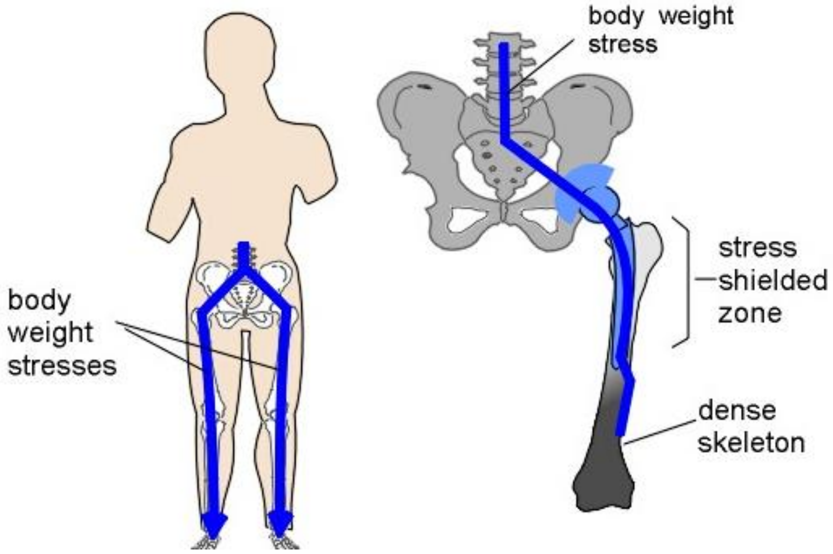

**Fig. 1-2** Scheme of stress shielding (*Surin 2005*).

Fig. 1-3 gives a brief summary of various causes for revision surgery. As a consequence, the metallic materials used for orthopedic implants especially for load bearing applications should possess excellent biocompatibility, superior corrosion resistance in body environment, excellent combination of high strength and low modulus, high fatigue and wear resistance, high ductility and be without cytotoxicity (*Long 1998*). Therefore, the new generation of biomaterials used for orthopedic implants needs to resolve these problems above and realize the following purposes:

- To remove toxic elements;

- To decrease the elastic modulus;

- To improve biocompatibility;

- To possess good mechanical properties.

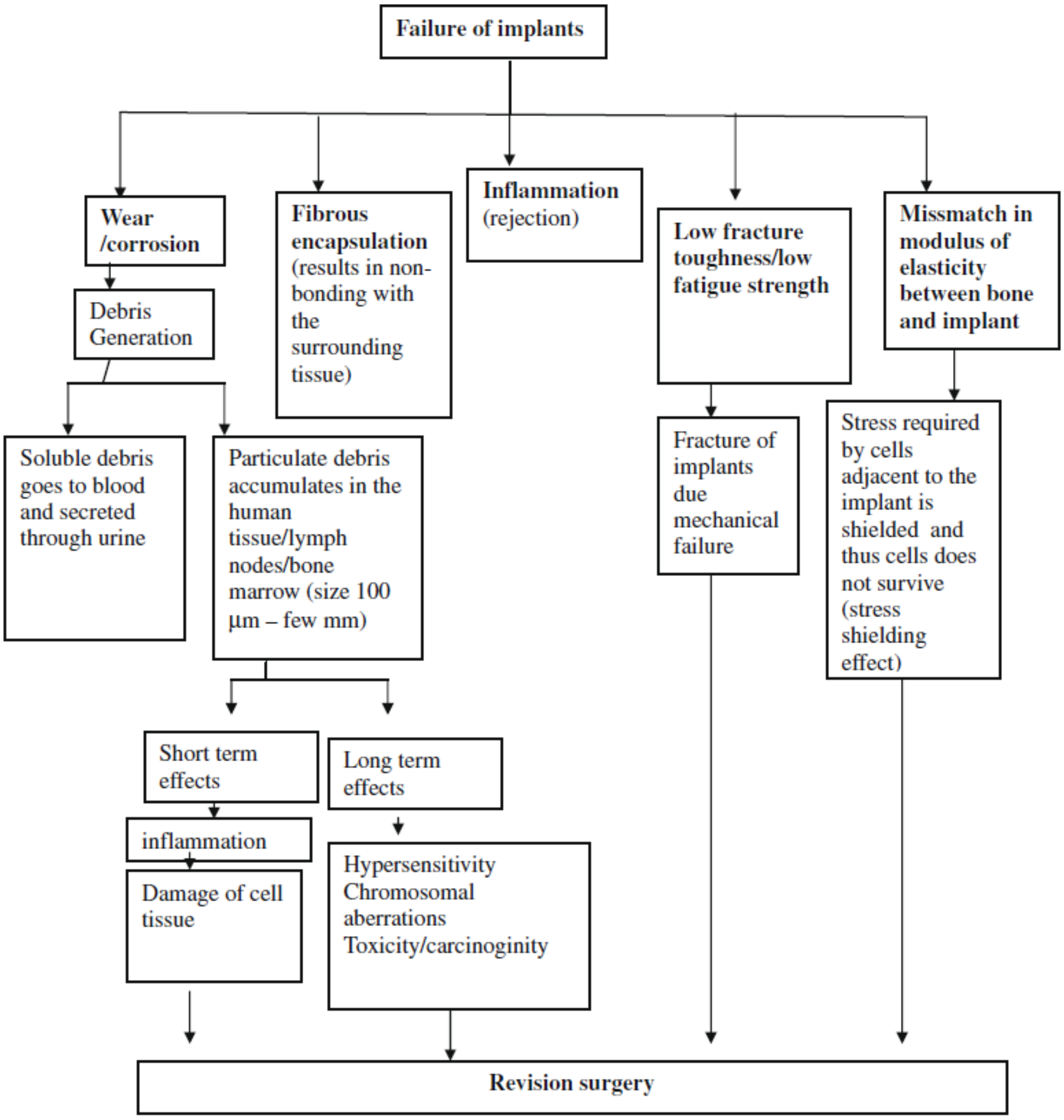
Failure of implants
Wear /corrosion
Debris Generation
Soluble debris goes to blood and secreted through urine
Particulate debris accumulates in the human tissue/lymph nodes/bone marrow (size 100 µm – few mm)
Short term effects
inflammation
Damage of cell tissue
Long term effects
Hypersensitivity Chromosomal aberrations Toxicity/carcinoginity
Fibrous encapsulation (results in non-bonding with the surrounding tissue)
Inflammation (rejection)
Low fracture toughness/low fatigue strength
Fracture of implants due mechanical failure
Missmatch in modulus of elasticity between bone and implant
Stress required by cells adjacent to the implant is shielded and thus cells does not survive (stress shielding effect)
Revision surgery

**Fig. 1-3** Various causes for revision surgery (*Geetha 2009*)

## 2.2 Low modulus metastable β Ti alloys

Judging from the above requirements, titanium alloys stand out due to a combination of excellent biocompatibility and good properties such as high strength, low density, relative low elastic modulus and excellent corrosion resistance.

Especially, the β-Ti alloys obtained through addition of β-stabilizing elements exhibit a substantially lower modulus and thus attract attention (*Niinomi 2002-2003 a,b*). Based on the selection of non-toxic alloying element, the titanium alloys reported recently are binary Ti-Nb, Ti-Mo, Ti-Ta and Ti-Zr systems; tenary Ti-Ta-Zr, Ti-Nb-Hf, Ti-Nb-Ta, Ti-Nb-Zr, Ti-Nb-Mo and Ti-Nb-Sn systems; as well as quaternary Ti-Nb-Ta-Zr system and so on.

Table 1-2 presents the elastic modulus of recently investigated commercial β-Ti alloys compared with Co-based alloys, stainless steels and other double phases Ti-based alloys (*Long 1998*). The modulus of stainless steel and Co-Cr-Mo alloys are around 200-230GPa. The introduction of α/β double phases Ti alloys decreased the modulus further to 110GPa. Now, recent efforts have already minimized the elastic modulus down to 55GPa in the Ti-35Nb-5Ta-7Zr (TNTZ) alloy but this value is still almost twice than that of bone. Amongst these research and development, it has been found that non-toxic new β-Ti alloys for biomedical applications can also show superelasticity or shape memory effect. The superelastic or shape memory characteristics are expected to guide new applications of metallic materials not only in medical fields but also in other fields.

**Table 1-2** Orthopaedic alloys developed and/or utilized as orthopaedic implants and their mechanical properties (E=elastic modulus, YS=yield strength, UTS=ultimate tensile strength) (*Long 1998*).

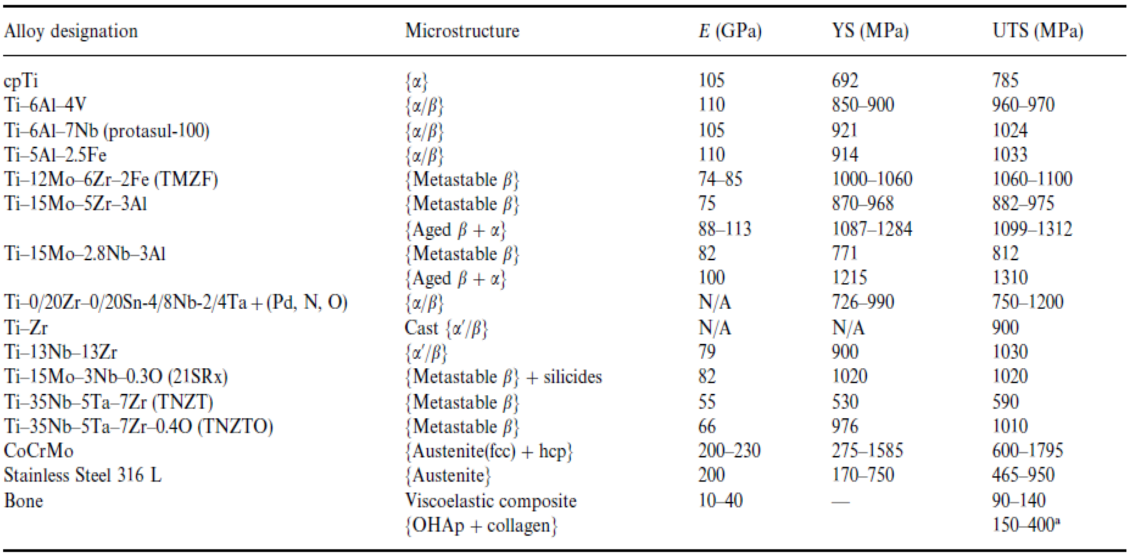

| Alloy designation | Microstructure | $E$ (GPa) | YS (MPa) | UTS (MPa) |
|---|---|---|---|---|
| cpTi | $\{\alpha\}$ | 105 | 692 | 785 |
| Ti–6Al–4V | $\{\alpha/\beta\}$ | 110 | 850–900 | 960–970 |
| Ti–6Al–7Nb (protasul-100) | $\{\alpha/\beta\}$ | 105 | 921 | 1024 |
| Ti–5Al–2.5Fe | $\{\alpha/\beta\}$ | 110 | 914 | 1033 |
| Ti–12Mo–6Zr–2Fe (TMZF) | {Metastable $\beta$} | 74–85 | 1000–1060 | 1060–1100 |
| Ti–15Mo–5Zr–3Al | {Metastable $\beta$} | 75 | 870–968 | 882–975 |
|  | {Aged $\beta + \alpha$} | 88–113 | 1087–1284 | 1099–1312 |
| Ti–15Mo–2.8Nb–3Al | {Metastable $\beta$} | 82 | 771 | 812 |
|  | {Aged $\beta + \alpha$} | 100 | 1215 | 1310 |
| Ti–0/20Zr–0/20Sn-4/8Nb-2/4Ta + (Pd, N, O) | $\{\alpha/\beta\}$ | N/A | 726–990 | 750–1200 |
| Ti–Zr | Cast $\{\alpha'/\beta\}$ | N/A | N/A | 900 |
| Ti–13Nb–13Zr | $\{\alpha'/\beta\}$ | 79 | 900 | 1030 |
| Ti–15Mo–3Nb–0.3O (21SRx) | {Metastable $\beta$} + silicides | 82 | 1020 | 1020 |
| Ti–35Nb–5Ta–7Zr (TNZT) | {Metastable $\beta$} | 55 | 530 | 590 |
| Ti–35Nb–5Ta–7Zr–0.4O (TNZTO) | {Metastable $\beta$} | 66 | 976 | 1010 |
| CoCrMo | {Austenite(fcc) + hcp} | 200–230 | 275–1585 | 600–1795 |
| Stainless Steel 316 L | {Austenite} | 200 | 170–750 | 465–950 |
| Bone | Viscoelastic composite<br>{OHAp + collagen} | 10–40 | — | 90–140<br>150–400$^{a}$ |

One of these β-Ti alloys, named Ti2448 alloy, with a nominal composition of Ti-24Nb-4Zr-8Sn (wt %), was developed in 2005 (*Hao 2005*). This non-toxic low modulus β-Ti alloy exhibits the lowest elastic modulus of 42GPa while maintaining a higher strength over 850MPa. It has already undergone a compressively development, bio-safety examination, implants part design and manufacturing, *in vivo* tests and clinical trials, and has a great potential to be a prominent material for hard tissue substitute.

# 3. Physical metallurgy of titanium

## 3.1 Pure titanium

### 3.1.1 Basic properties of pure titanium

Titanium is the fourth most abundant structural metal in the earth's crust at a level of about 0.6%. It is a transition metal belonging to Group IV of the periodic table of elements. Its atomic number is 22 and mass number is 47.867 with the electronic configuration of $1s^2\,2s^2\,2p^6\,3s^2\,3p^6\,3d^2\,4s^2$. The incomplete 3d shell enables it to form solid solutions with most substitutional elements located in its vicinity in the periodic table (*Collings 1984*). Some basic characteristics and properties of titanium are listed in Fig. 1-3 and compared to other structural metallic materials based on Fe, Ni and Al.

**Table 1-3** Some basic characteristics and properties of titanium compared to other structural metallic materials based on Fe, Ni and Al (*Lütjering 2007*).

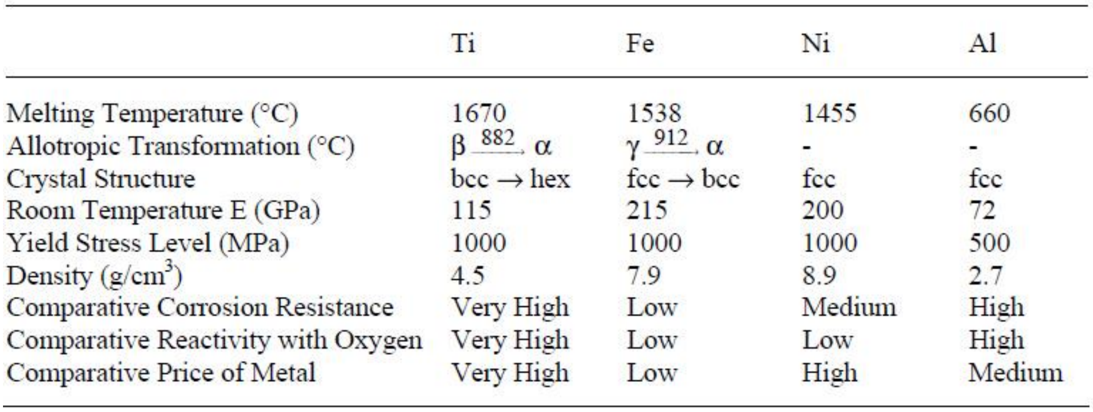

| | Ti | Fe | Ni | Al |
|---|---|---|---|---|
| Melting Temperature (°C) | 1670 | 1538 | 1455 | 660 |
| Allotropic Transformation (°C) | $\beta \xrightarrow{882} \alpha$ | $\gamma \xrightarrow{912} \alpha$ | - | - |
| Crystal Structure | bcc → hex | fcc → bcc | fcc | fcc |
| Room Temperature E (GPa) | 115 | 215 | 200 | 72 |
| Yield Stress Level (MPa) | 1000 | 1000 | 1000 | 500 |
| Density (g/cm$^3$) | 4.5 | 7.9 | 8.9 | 2.7 |
| Comparative Corrosion Resistance | Very High | Low | Medium | High |
| Comparative Reactivity with Oxygen | Very High | Low | Low | High |
| Comparative Price of Metal | Very High | Low | High | Medium |

Although titanium has the highest strength/density ratio, its application is still confined to some limited area because of its high price. This high price mainly results from the high reactivity of titanium with oxygen that requires inert atmosphere or vacuum during its production process. On the other hand, the high reactivity of titanium with oxygen leads to the immediate formation of oxide layer, which is rather stable and adherent when exposed to air. Subsequently, the superior corrosion resistance of titanium in various kinds of aggressive environments, especially in aqueous acid environment can be achieved due to this passivation layer.

Therefore, titanium is a kind of metal possessing specific high strength, low density, high melting temperature and excellent corrosion resistivity.

### 3.1.2 Equilibrium phases in pure titanium

Fig. 1-4a presents the pressure-temperature phase diagram of pure titanium (*Petry 1991*). Based on it, pure Ti exhibits an allotropic phase transformation at 882 $^{o}$C, changing from β phase with body-centered cubic (bcc) structure at higher temperature to α phase with hexagonal closed packed (hcp) structure at lower temperature. Furthermore, raising the pressure stabilizes the ω phase with a hexagonal structure (*Sikka 1982*). According to different content of interstitial and substitutional elements in pure Ti, the exact phase transformation temperature from α phase to β phase can be strongly influenced (*Ouchi 1998*). Fig 1-4b shows that the increasing d-orbital occupancy from left to right in the periodic table increases the temperature range of stability of β phase seen the increasing $T_m$-$T_o$ difference. Therefore, addition of elements located in group V and group VI can change the phase transformation temperature to a higher temperature range.

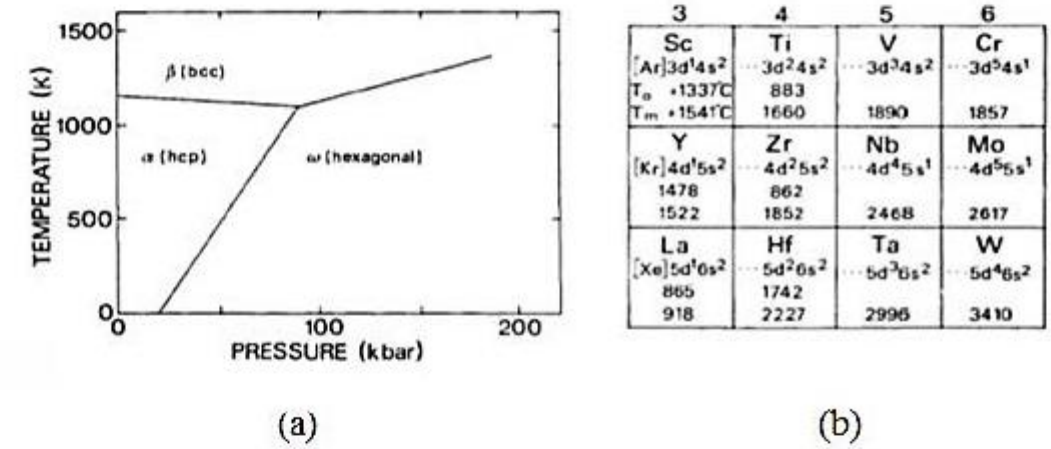

| 3 | 4 | 5 | 6 |
|---|---|---|---|
| Sc<br>[Ar]$3d^1 4s^2$<br>$T_o$ •1337°C<br>$T_m$ •1541°C | Ti<br>$3d^2 4s^2$<br>883<br>1660 | V<br>$3d^3 4s^2$<br>1890 | Cr<br>$3d^5 4s^1$<br>1857 |
| Y<br>[Kr]$4d^1 5s^2$<br>1478<br>1522 | Zr<br>$4d^2 5s^2$<br>862<br>1852 | Nb<br>$4d^4 5s^1$<br>2468 | Mo<br>$4d^5 5s^1$<br>2617 |
| La<br>[Xe]$5d^1 6s^2$<br>865<br>918 | Hf<br>$5d^2 6s^2$<br>1742<br>2227 | Ta<br>$5d^3 6s^2$<br>2996 | W<br>$5d^4 6s^2$<br>3410 |

(a) (b)

**Fig. 1-4** (a) The pressure-temperature phase diagram of pure-Ti and (b) the periodic table around Ti (*Petry 1991*).

Fig. 1-5a shows the lattice cell of α phase (space group N$^{o}$ 194, P6$_3$/mmc), indicating the lattice parameters are:

a =0.295nm, c=0.468nm, where c/a ratio=1.587.

The three most densely packed types of lattice plane are also indicated, which are {10-10} prismatic planes, (0002) basal planes and {10-11} first-order pyramidal planes. The three a1, a2 and a3 axes are the most close-packed directions with the indices <11-20>.

Fig.1-5b illustrates the lattice cell of β phase (space group N$^{o}$ 229, Im-3m) with the parameter:

a=b=c=0.332nm.

Similarly, one variant of the six most densely packed {110} lattice planes is signed with shadow. The close-packed direction for bcc crystal are the four <111> directions.

Depending on cooling rate, the transformation between β and α phases can be controlled by a conventional diffusional process including nucleation and growth or diffusionless martensitic process. The crystallographic orientation relationship follows the Burgers relationship (*Burgers 1934*):

$$\{110\}_\beta \ // \ \{0002\}_\alpha$$

$$<111>_\beta \ // \ <11\text{-}20>_\alpha$$

This relationship was firstly studied by Burgers in zirconium and then confirmed in titanium (*Newkirk 1953, Williams 1954*). According to the Burgers relationship, a bcc crystal can transform to 12 equivalent hexagonal variants that have different orientations with regard to the parent β crystal. These relationships are of significance because they show that slip compatibility is possible between transformed α and retained β phases. Indeed, when slip initiates in co-oriented α lamellae, the retained β ribs between the lamellae are not effective barriers to slip extension (*Castany 2008, Wanhill 2012*).

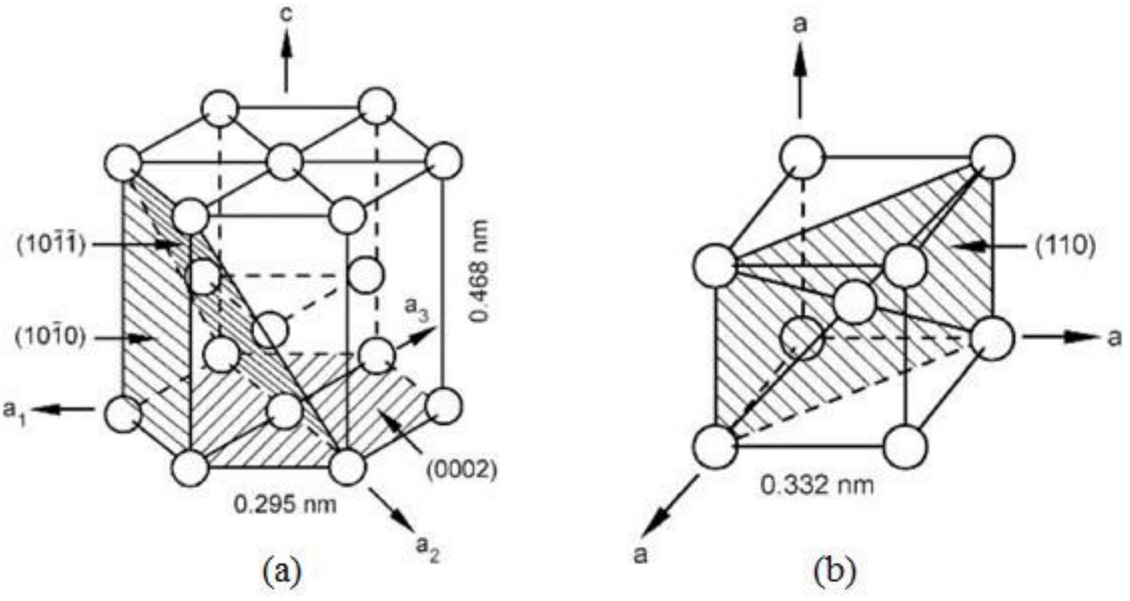

**Fig. 1-5** Lattice cell of α phase and of β phase.

Except the two most common equilibrium phases above, there are still some intermetallic and ordered phases that have been observed in titanium, such as B2 phase in Ti-Ni alloys (*Kauffman 1997, Duerig 2006*), $\alpha_2$ phase in Ti-6wt.% Al alloy and γ phase in Ti-Al alloys (*Boyer 1994*).

## 3.2 Titanium alloys

### 3.2.1 Elements addition in titanium alloys

Depending on their influence on α/β transformation temperature, the alloying elements in titanium can be classified into α or β-stabilizing elements.

The substitutional element of Al and the interstitial elements of O, N and C are all strong α-stabilizers. These elements can increase the transus temperature with increasing solute contents, as shown in the schematic phase diagram in Fig. 1-6a. Aluminum is the most widely used alloying element in titanium alloys, since it can increase the transus temperature and lead to strengthening effect due to large solubility in both α and β phases. Oxygen is sometime used to obtain a desirable strength via solid solution strengthening effect, but nitrogen and carbon are usually impurities.

The β-stabilizing elements are actually divided into β-isomorphous elements and β eutectoid forming elements depending on different binary phase diagrams. These two kinds of phase diagrams are shown schematically in Fig. 1-6b and 1-6c. The elements of Mo, V, Nb and Ta are the most widely used isomorphous ones. But Cr, Fe Cu and Si belong to the eutectoid elements. Finally, attention should be paid on H, which is also a kind of eutectoid element (*San-Martin 1987*).

Additionally, there are other elements like Zr, Hf and Sn called neutral element, because of their very slight influence on the transformation temperature.

As the α-stabilizing element of Al and β-stabilizing element of Mo are archetypical. It is accepted widely to describe a multi-component Ti-based alloy in terms of its equivalent Al and Mo contents according to the following expressions (*Collings 1984, Boyer 1994*):

$$[\mathrm{Al}]_{eq}=[\mathrm{Al}]+[\mathrm{Zr}]/3+[\mathrm{Sn}]/3+10[\mathrm{O}]$$

$$[\mathrm{Mo}]_{eq}=[\mathrm{Mo}]+[\mathrm{Ta}]/5+[\mathrm{Nb}]/3.6+[\mathrm{W}]/2.5+[\mathrm{V}]/1.25+1.25[\mathrm{Cr}]+1.25[\mathrm{Ni}]+1.7[\mathrm{Mn}]+1.7[\mathrm{Co}]+2.5[\mathrm{Fe}]$$

Where “[*X*]” indicates the concentration of element X in weight percent in the alloy. It can be said that the efficacy of the β-stabilizing element progressively increases in the following order: Ta, Nb, W, V, Mo, Cr, Ni, Mn, Co and Fe.

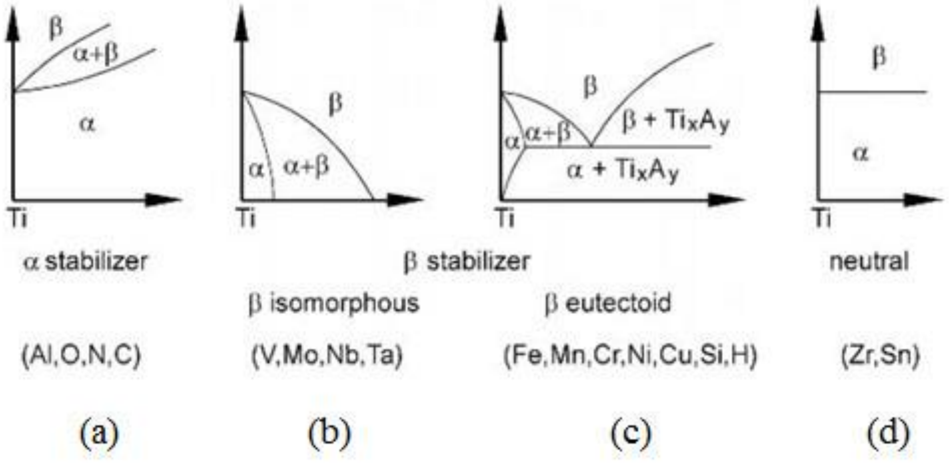
β
α+β
α
Ti
β
α
α+β
Ti
β
α
α+β
β + TixAy
α + TixAy
Ti
β
α
Ti
α stabilizer
β stabilizer
neutral
β isomorphous
β eutectoid
(Al,O,N,C)
(V,Mo,Nb,Ta)
(Fe,Mn,Cr,Ni,Cu,Si,H)
(Zr,Sn)
(a)
(b)
(c)
(d)

**Fig. 1-6** Effect of alloying elements on phase diagrams of titanium alloys (schematically).

### 3.2.2 Classification of titanium alloys

According to different alloying additions and present phases in the microstructures, Ti alloys are classified conventionally into three different categories: α alloys, α+β alloys, and β alloy (which can be divided into stable β and metastable β alloys).

Fig. 1-7 presents the classification of Ti-alloys based on the chemical composition and Table 1-4 gives some examples of the main commercial titanium alloys.

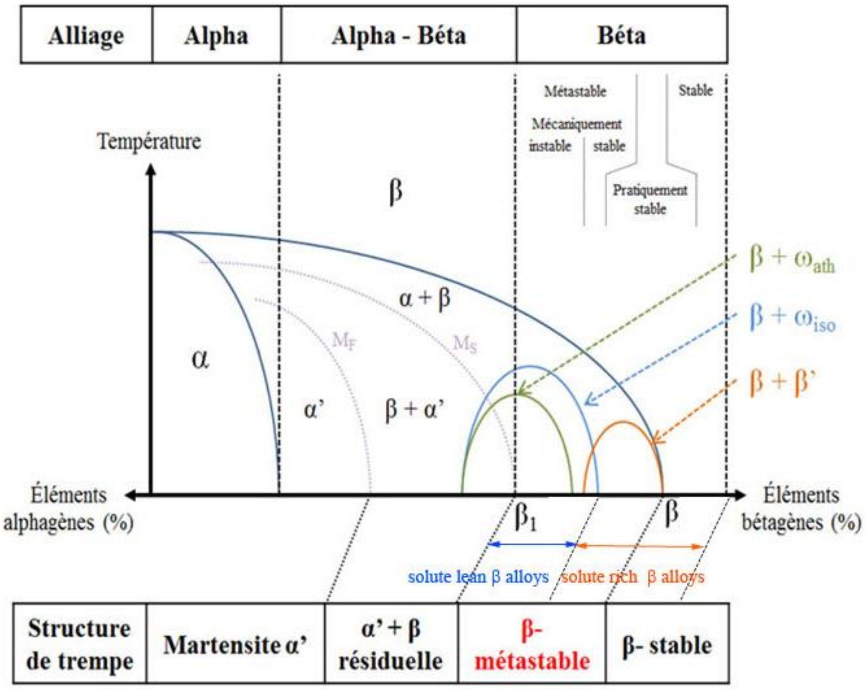
Alliage
Alpha
Alpha - Béta
Béta
Métastable
Stable
Mécaniquement
instable
stable
Pratiquement
stable
Température
β
α + β
α
MF
MS
α'
β + α'
β + ωath
β + ωiso
β + β'
Éléments
alphagènes (%)
Éléments
bétagènes (%)
β1
β
solute lean β alloys
solute rich β alloys
Structure
de trempe
Martensite α'
α' + β
résiduelle
β-
métastable
β- stable

**Fig. 1-7** Classification of Ti-alloys based on the chemical composition (schematically).

**Table 1-4** The main commercial titanium alloy (*Collings 1984*).

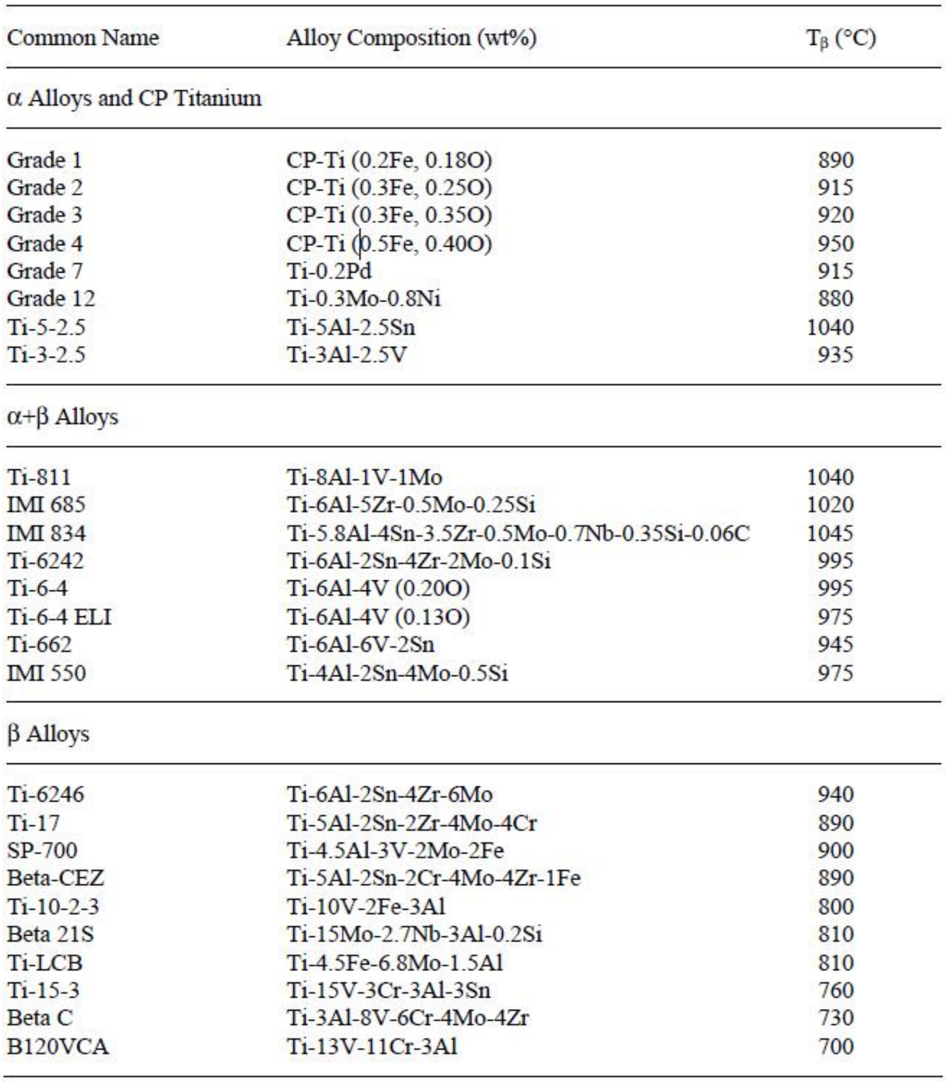

| Common Name | Alloy Composition (wt%) | $T_\beta$ (°C) |
|---|---|---|
| α Alloys and CP Titanium | | |
| Grade 1 | CP-Ti (0.2Fe, 0.18O) | 890 |
| Grade 2 | CP-Ti (0.3Fe, 0.25O) | 915 |
| Grade 3 | CP-Ti (0.3Fe, 0.35O) | 920 |
| Grade 4 | CP-Ti (0.5Fe, 0.40O) | 950 |
| Grade 7 | Ti-0.2Pd | 915 |
| Grade 12 | Ti-0.3Mo-0.8Ni | 880 |
| Ti-5-2.5 | Ti-5Al-2.5Sn | 1040 |
| Ti-3-2.5 | Ti-3Al-2.5V | 935 |
| α+β Alloys | | |
| Ti-811 | Ti-8Al-1V-1Mo | 1040 |
| IMI 685 | Ti-6Al-5Zr-0.5Mo-0.25Si | 1020 |
| IMI 834 | Ti-5.8Al-4Sn-3.5Zr-0.5Mo-0.7Nb-0.35Si-0.06C | 1045 |
| Ti-6242 | Ti-6Al-2Sn-4Zr-2Mo-0.1Si | 995 |
| Ti-6-4 | Ti-6Al-4V (0.20O) | 995 |
| Ti-6-4 ELI | Ti-6Al-4V (0.13O) | 975 |
| Ti-662 | Ti-6Al-6V-2Sn | 945 |
| IMI 550 | Ti-4Al-2Sn-4Mo-0.5Si | 975 |
| β Alloys | | |
| Ti-6246 | Ti-6Al-2Sn-4Zr-6Mo | 940 |
| Ti-17 | Ti-5Al-2Sn-2Zr-4Mo-4Cr | 890 |
| SP-700 | Ti-4.5Al-3V-2Mo-2Fe | 900 |
| Beta-CEZ | Ti-5Al-2Sn-2Cr-4Mo-4Zr-1Fe | 890 |
| Ti-10-2-3 | Ti-10V-2Fe-3Al | 800 |
| Beta 21S | Ti-15Mo-2.7Nb-3Al-0.2Si | 810 |
| Ti-LCB | Ti-4.5Fe-6.8Mo-1.5Al | 810 |
| Ti-15-3 | Ti-15V-3Cr-3Al-3Sn | 760 |
| Beta C | Ti-3Al-8V-6Cr-4Mo-4Zr | 730 |
| B120VCA | Ti-13V-11Cr-3Al | 700 |

### 3.2.2.1 α alloys

The main commercial α-titanium alloys are listed in Table 4 consisting of various grades of commercially pure (CP) titanium and α alloys. The four grades for CP titanium represent their different oxygen content from 0.18% (grade 1) to 0.4% (grade 4) that leads to an increase of the yield strength resulting from the solid solution hardening effect of oxygen. Depending on the cooling rates, the microstructure can be composed of equiaxed α, widmanstatten lath-like α phase or martensitic α′ phases. These alloys are non-heat treatable alloys having moderate strength, good toughness, superior high temperature creep, oxidation resistance and weldability (*Boyer 1994*). What is worth mentioning is that the α alloys can tolerate a small amount of β phase (2-5%) upon cooling from the β phase field with addition of Mo and V, which are called near-α alloys. The small amount of β phase in the near-α alloys is useful for better controlling the recrystallized α grain size and improving mechanical properties. Compared to pure titanium with different grades, the near-α alloys exhibit some advantages like improved tensile strength, workability and heat treatability which broaden the application of α alloys (*Collings 1984*).

### 3.2.2.2 α+β alloys

The group of α+β alloys contains a limited quantity of β-stabilizers and α-stabilizers. The addition of α-stabilizer is used to strengthen the α phase, while β-stabilizers allow the β phase to be retained at room temperature after cooling from β or α+β phase fields. Seen from the phase diagram in Fig. 1-7, the α+β alloys take the range in the phase diagram from the α/α+β phase boundary up to the intersection of the $M_s$-line with room temperature. Therefore, the α+β alloys have a α' martensitic transformation upon fast cooling from the β phase field to room temperature. Some commercial α+β alloys are listed in Table 1-4. The most used α+β alloy is the Ti-6Al-4V alloy containing 15 vol. % of β phase in equilibrium at 800$^{o}$C.

The mechanical properties of α+β alloys depend on the relative amount and distribution of α and β phases (*Semiatin 1997*). These variables are controlled by appropriate heat treatment and/or thermo-mechanical processing. In terms of microstructure, there can be fully lamellar structures, fully equiaxed structures or so-called bi-modal microstructures. These different microstructures are obtained through a certain process route shown in Fig. 1-8.

For fully lamellar microstructures shown in Fig. 1-8a, after the first step of homogenization above β transus, the deformation process can be done by forging or rolling, either in the β phase field or in the α+β phase field. The third step of recrystallization is usually kept at a temperature slightly higher than the β transus to control the β grain size. The cooling rate from the β phase field after recrystallization is a crucial parameter determining the width of the α-lamellae. The final step of annealing is a stabilization treatment that aims essentially to form an equilibrium structure, such as fully developed secondary α plates.

The bi-modal microstructure is shown in Fig. 1-8b. The process route is also divided into four steps: homogenization in the β phase field, deformation in the α+β phase field, recrystallization in the α+β phase field and finally annealing treatment for stress removing and grain growth.

The fully equiaxed structure shown in Fig. 1-8c, can be obtained through two methods. The first one is the same process route for obtaining the bi-modal microstructure; the only difference is the final step extended until the equiaxed primary α grains stops growing and forms “triple-points”. The other method for developing the fully equiaxed microstructure is to decrease the recrystallization temperature in order to obtain high volume fraction of α phase.

Generally speaking, the two phase α+β alloys offer a wide range of combinations of strength, toughness and high temperature properties that makes them attractive in wide ranging aerospace and other fields demanding high specific properties to temperature of about 600 °C.

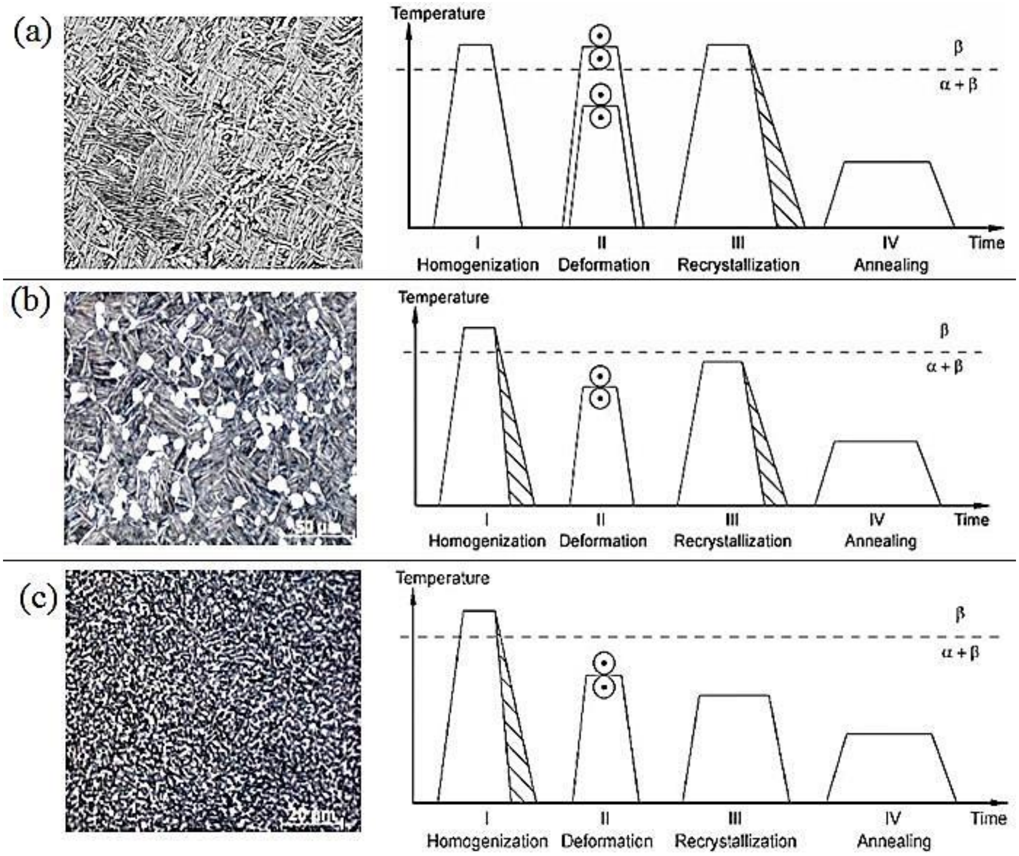
(a)
Temperature
β
α + β
I
Homogenization
II
Deformation
III
Recrystallization
IV
Annealing
Time
(b)
Temperature
β
α + β
50 μm
I
Homogenization
II
Deformation
III
Recrystallization
IV
Annealing
Time
(c)
Temperature
β
α + β
20 μm
I
Homogenization
II
Deformation
III
Recrystallization
IV
Annealing
Time

**Fig. 1-8** (a) Fully lamellar microstructure and its processing route, (b) bi-modal microstructure and its processing route and (c) fully equiaxed microstructure and its processing route in α+β titanium alloys (schematically) (*Lütjering 1998*).

### 3.2.2.3 β alloys

When sufficient β stabilizing elements are added into titanium, β alloys can be produced. Actually, the β alloys include stable β alloys and metastable β alloys. In Fig. 1-7, the metastable β alloys lie in the equilibrium α+β region of the phase diagram and stable β alloys locates in the β single phase field.

✓ **Stable β alloys**

If more content of β-stabilizing elements (>27% $[\mathrm{Mo}]_{eq}$) is added into titanium, the β/α transus temperature can be decreased below room temperature. After cooling to room temperature, β phase remains stable, thus stable β alloys can be formed. It is not surprising that the percentage of β alloys is now steadily increasing due to the attractive properties, such as heat treatability, wide and unique range of strength/weight ratios, deep hardening potential and inherent ductility. In addition, they possess superior fatigue resistance as compared to α+β alloys. These alloys can be predicted to appear in aerospace, power plant, sporting goods, automotive and biomedical health applications.

- ✓ **Metastable β alloys**

The metastable β alloys are characterized by non-martensitic transformation upon fast cooling from the β phase field. In another words, the metastable β phase can be retained to room temperature by quenching from the β phase field. However, α phase can precipitated from the metastable β phases as very fine size in the subsequent annealing process below β-transus temperature, resulting in much higher yield stress levels. This type of β alloys is generally more easily cold workable than the α+β alloys, heat treatable and has good corrosion resistance. Therefore, it is not surprising that the application of metastable β alloys has been slowly increasing in recent years (*Weiss 1998*).

According to Fig. 1-7, the phase transformation and phase decomposition in metastable β alloys is much more complex. Some non-equilibrium phases like α″ martensitic phase, athermal and isothermal ω phase can appear. The processing route, its corresponding microstructure and phase decomposition for metastable β alloys will be detailed later in section 3.2.3 after a brief introduction of these non-equilibrium phases.

### 3.2.3 Non-equilibrium phases in metastable β titanium alloys

The phase transformation proceeds via two kinds of modes: diffusive and displacive (*Roy 1973, Banerjee 1994*). The former type involves breaking of the bonds of atoms with their neighbors and re-establishment of bonds to form a new configuration in place of the pre-existing one. Such a process requires thermal activated atomic diffusion, which comprises random atomic jumps and disturbs atomic coordination. Typical examples include spinodal decomposition, vapour-phase deposition, crystal growth during solidification and grain growth in single-phase and two-phase systems (*Maraldi 2012*).

The latter one can be explained by a homogeneous distortion and shuffling of lattice planes (*Banerjee 2007*). Cooperative movements of a large number of atoms in a diffusionless way accomplish the structural change in displacive transformations. Different from the reconstructive transformation, the displacive movements do not require thermal activation and cannot, therefore, be suppressed by quenching (*Banerjee 1997*).

The α and β phases in titanium mentioned before are equilibrium phases. However, non-equilibrium or metastable phases are of great interest in titanium alloys. Two important examples of such phases are the α″ martensitic phase and the athermal ω phase; both are formed through athermal displacive transformations.

### 3.2.3.1 The martensitic α″ phase

The word "martensite", named after Dr. A. Martens, was originally adopted by metallurgists to define the acicular structure found after quenching carbon steel that was thought to be responsible for the outstanding hardness of the material, but it can also refer to any crystal structure which is formed by displacive transformation. The α″ martensitic transformation relates to cooperative movement of atoms by shear process in titanium alloys. Actually, there are two martensitic phases in titanium alloys: α′ martensite with a hexagonal structure and α″ orthorhombic martensite depending on different content of β-stabilizing elements (*Moffat 1988*).

- ✓ **Crystal structure**

In metastable β alloys, the displacive martensitic α″ phase was firstly found by Bagariatski in 1958 (*Bagaryatskii 1958b*). In fact, the martensitic α″ phase can be divided into athermal type denoted as $\alpha''_{ath}$ formed during quenching and stress induced type denoted as SIMα″. The lattice parameters of α″ phase (space group N$^o$ 63, Cmcm) are dependent on the alloy composition. They are approximately (*Duerig 1982, Qazi 2005, Brown 1964, Murray 1987*):

$$a \approx 0.315\text{nm}, \qquad b \approx 0.485\text{nm}, \qquad c \approx 0.464\text{nm}.$$

The atom positions in are:

$$(0, 0, 0), \qquad (1/2, 1/2, 0), \qquad (0, 1\text{-}2y, 1/2), \qquad (1/2, 1/2\text{-}2y, 1/2)$$

Where the value of y depends on the alloy composition (*Mornirolli 1973*).

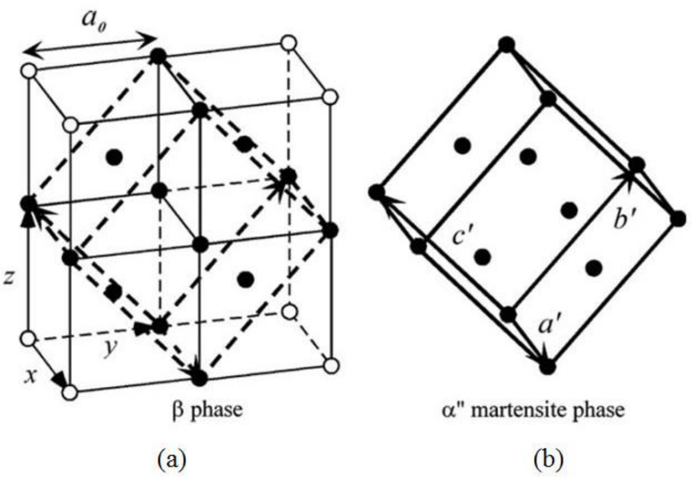

**Fig. 1-9** A schematic illustration exhibiting lattice correspondence between β and α" phases.

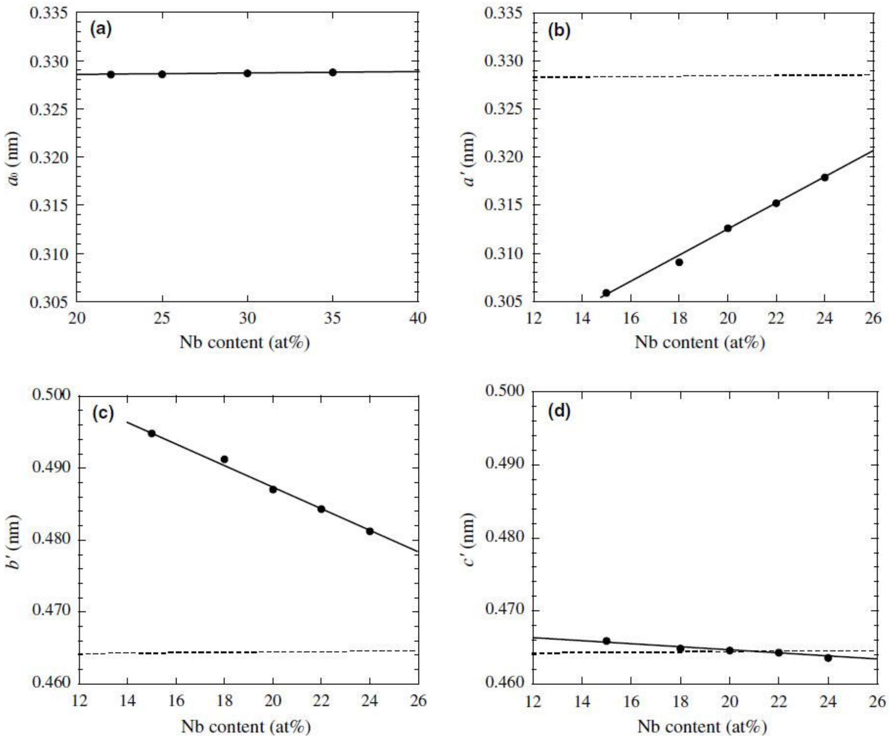

**Fig. 1-10** Nb content dependence of the lattice constants of the β and α″ phases in quenched Ti–(15-35)Nb alloys (*Kim 2006*).

A schematic of the crystal structures for α″ phase and the parent β phase are shown in Fig. 1-9 (*Kim 2006*). However, the cell parameters of α″ phase vary with the alloy composition. Some examples can be found in the quenched Ti-(15-35) at. % Nb (Fig. 1-10), Ti–(1-30) at. % Ta alloys, and Ti-(1-30) at. % Nb-3Al alloys (*Kim 2006, Dobromyslov 2009, Inamura 2007*).

### ✓ Orientation relationship between α″ and β phases

The formation of α″ phase follows the relationship below:

$$(110)_{\beta} \,//\, (001)_{\alpha''} \qquad [11\bar{1}]_{\beta} \,//\, [110]_{\alpha''}$$

Specifically, during the martensitic transformation process, the three principal axes of orthorhombic crystal $[100]_{\alpha''}$, $[010]_{\alpha''}$, and $[001]_{\alpha''}$ are derived from certain orientations in β crystal, shown as follows:

$$[100]_{\alpha''} - <100>_{\beta} \qquad [010]_{\alpha''} - <01\bar{1}>_{\beta} \qquad [001]_{\alpha''} - <011>_{\beta}$$

Hence, six lattice correspondence variants can be defined from the orientation relationship, and these were designated as V1, V2, V3, V4, V5 and V6 in Table 1-5 (*Chai 2009*).

**Table 1-5** Six lattice correspondence variants derived from the β and α″ crystals.

| Variant | $[\mathbf{100}]_{\alpha''}$ | $[\mathbf{010}]_{\alpha''}$ | $[\mathbf{001}]_{\alpha''}$ |
|---|---|---|---|
| V1 | $[100]_{\beta}$ | $[011]_{\beta}$ | $[0\bar{1}1]_{\beta}$ |
| V2 | $[100]_{\beta}$ | $[0\bar{1}1]_{\beta}$ | $[0\bar{1}\bar{1}]_{\beta}$ |
| V3 | $[010]_{\beta}$ | $[101]_{\beta}$ | $[10\bar{1}]_{\beta}$ |
| V4 | $[010]_{\beta}$ | $[10\bar{1}]_{\beta}$ | $[\bar{1}0\bar{1}]_{\beta}$ |
| V5 | $[001]_{\beta}$ | $[110]_{\beta}$ | $[\bar{1}10]_{\beta}$ |
| V6 | $[001]_{\beta}$ | $[\bar{1}10]_{\beta}$ | $[\bar{1}\bar{1}0]_{\beta}$ |

### ✓ Morphology of α″ phase

The α″ phase in metastable β alloys is known to be acicular which can be directly observed with techniques of OM, EBSD and TEM. There are several examples of the morphology of α″ phase in Fig. 1-11 (*Besse 2011, Chai 2009, Bertrand 2014, Inamura 2007*).

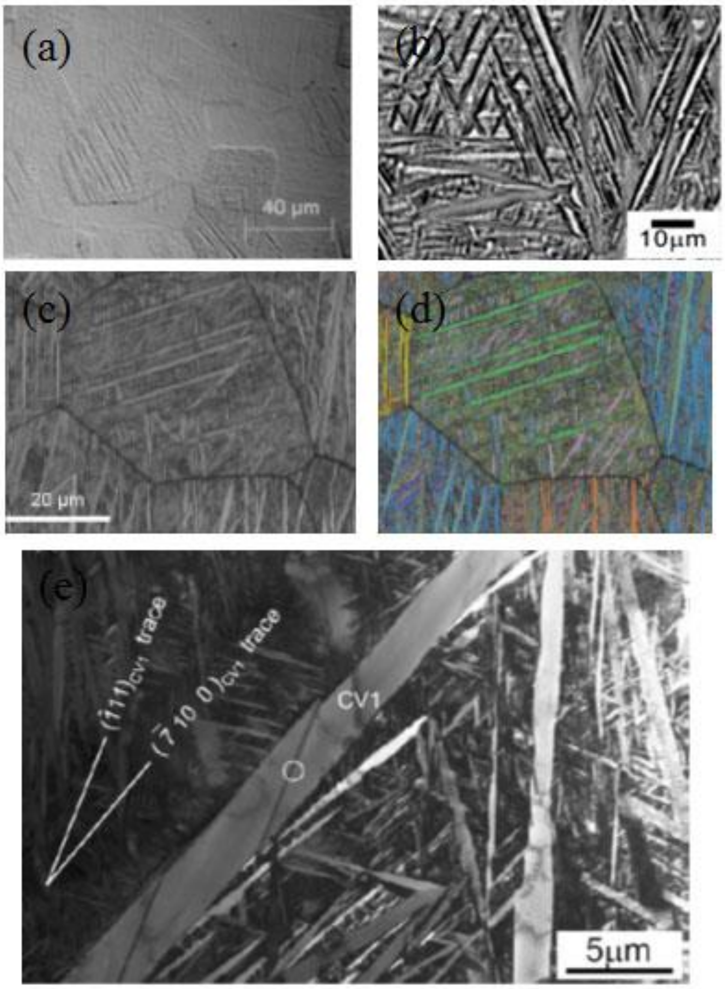

**Fig. 1-11** (a) Optical micrographs showing the microstructure of α″ phase in quenched Ti-23N-0.7Ta-2Zr alloy (*Besse 2011*), (b) Optical micrographs showing the self-accommodation microstructure of α″ phase in quenched Ti-24Nb (*Chai 2009*), (c) EBSD maps of water-quenched Ti-25Ta-20Nb alloy (*Bertrand 2014*), (d) the acicular corresponding α″ phase indexed with Euler angles and (e) bright field image of fully transformed α″ phase quenched Ti-23Nb-3Al alloy (*Inamura 2007*).

### 3.2.3.2 The ω phase

The so-called ω phase was encountered firstly by Frost et al. in 1954 (*Frost 1954*). They found some aged β titanium alloys were unexpectedly brittle. Subsequently, careful X-ray diffraction obtained from these alloys showed that the ω phase appeared as tiny coherent precipitates, which has a hexagonal structure (*Silcock 1958*) resulting from the alternate collapse of $\{111\}_\beta$ planes (*Sikka 1982*, *Fontaine 1988*). Since then, the ω phase has been found in numerous alloy systems like Ti, Zr and Hf alloyed with other d-rich elements, and has received extensive experimental as well as theoretical attention in order to explain its complex morphology (*Collings 1984, Fukui 2004, Dammak 1999, Ping 2006, Xing 2008a*), its effect on physical properties such as ductility, superconductivity (*Collings 1974*) and the mechanism of formation from the parent β phase (*Sikka 1982*).

Based on different mechanisms, the ω phase can be formed under three conditions at ambient pressure (*Banerjee 2006*):

(1) When the titanium alloy contains just high enough β-stabilizing elements, instead of martensitic α″ phase, another metastable athermal ω phase can be formed by rapid cooling from the β-phase field, denoted as $\omega_{ath}$. The athermal ω phase is represented by a green narrow region in the metastable phase diagram of titanium (Fig. 1-7). This phase cannot be suppressed however fast may be the quench rate.

(2) Isothermal aging for higher β-stabilizing content in the temperature range of 373-773K leads to the formation of isothermal omega phase, denoted as $\omega_{iso}$. After the ω structures are formed, β stabilizing elements are continuously rejected from the ω-phase particles during aging, and these particles thus stabilized (*Duerig 1980*). However, by increasing temperature and/or aging time, the size of this $\omega_{iso}$ phase particles increases. This phase acts also as nucleation sites and can transform to equilibrium α phase during subsequent aging treatment.

(3) Deformation at room temperature and application of high pressure would induce the formation of ω phase. Some studies showed the formation of stress induced ω phase in Ti-Cr alloys (*Bagariatskii 1958a*), Ti-V alloys (*Brotzen 1955, Kuan 1975*). Other studies also presented the evidences of ω phase formed in pressure (*Jamieson 1963, Bundy 1965*).

(4) Irradiation in the temperature range 303-573K can also induce ω phase (*Dammak 1999*).

### ✓ Crystallography

The crystal structure of the ω phase has been determined by X-ray, neutron and electron diffraction to be hexagonal with space group $N^o$ 191, P6/mmm shown in Fig. 1-12. The lattice parameters are approximately (*Jamieson 1963, Kutsar 1973*):

$$a=b\approx 0.462\text{nm}, \qquad c\approx 0.282\text{nm}.$$

The three equivalent positions of atoms in the cell are:

$$(0, 0, 0), \qquad (2/3, 1/3, 1/2), \qquad (1/3, 2/3, 1/2).$$

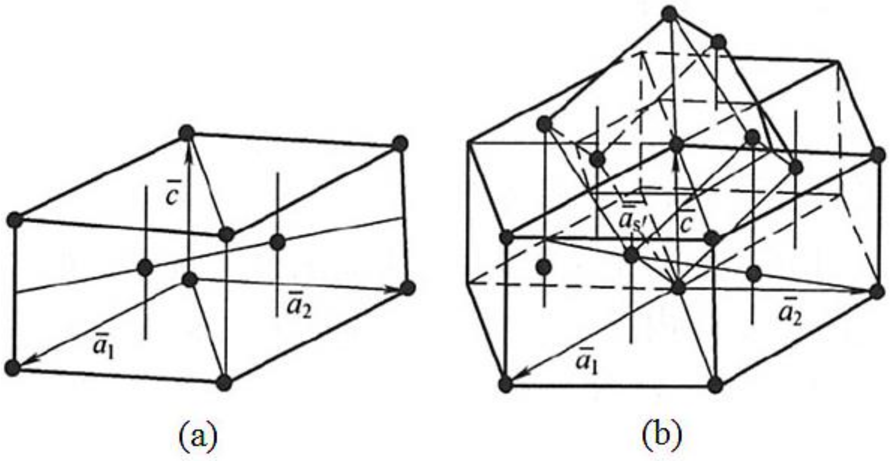

**Fig.1-12** (a) Unit cell of hexagonal ω phase and (b) lattice correspondence between ω and β phases.

### ✓ The relationship between ω phase and β phase

Fig. 1-13 give a schematic lattice to explain the formation mechanisms of the ω phase from the parent β phase, showing a set of {111} planes in the bcc lattice, and the ω lattice obtained by collapsing one pair of planes to the intermediate position leaving the next plane unaltered (*Sikka 1982*). Although the mechanism of formation of ω phase is a displacive type for $\omega_{ath}$ phase while diffusional atom movements are involved for $\omega_{iso}$ phase, the lattice collapse mechanism shown in Fig. 10 remains operative in all the cases. As a result, the observed orientation relationship between the beta and the omega crystals is independent on the type of omega phase (*Dey 2004*):

$$< 111 >_{\beta} // < 0001 >_{\omega} \qquad \{1\bar{1}0\}_{\beta} // \{11\bar{2}0\}_{\omega}$$

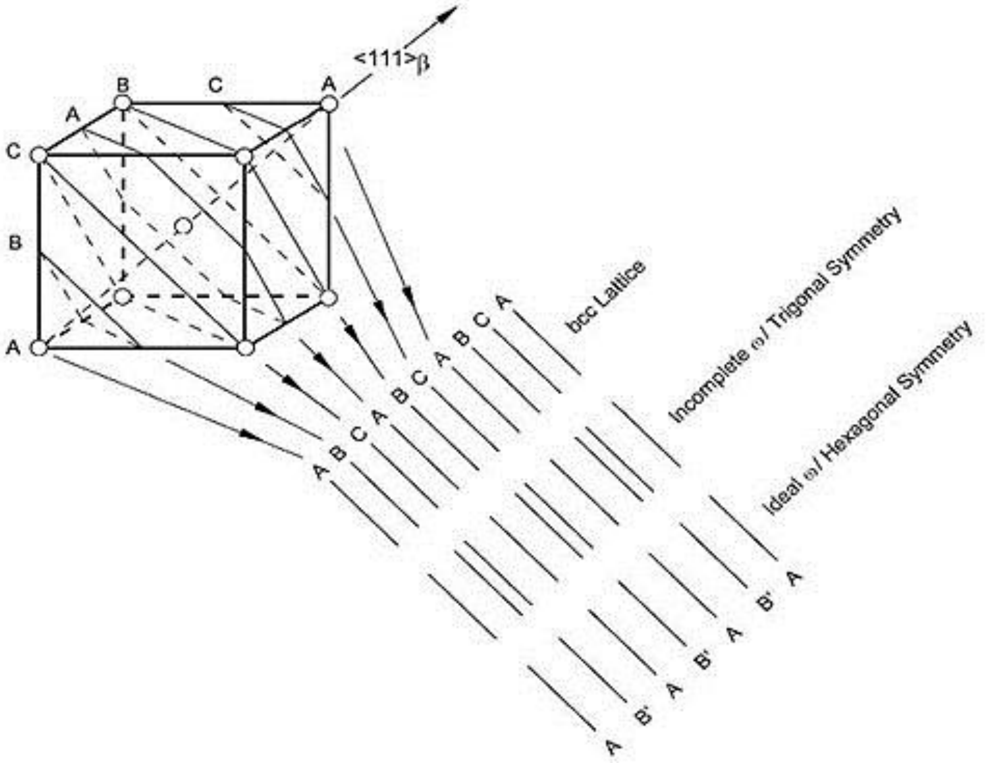
<111>β
A
B
C
A
C
B
A
A B C A B C A B C A
bcc Latice
Incomplete ω / Trigonal Symmetry
Ideal ω / Hexagonal Symmetry
A B' A B' A B' A

**Fig.1-13** Representation of the phase transformation from β to ω phases: the B and C hexagonal planes collapse and the A planes remain unchanged (*Collings 1984, Dammak 1999*).

### ✓ Morphology of ω phase

The morphology of ω phase can be modified depending on different mechanisms. Generally speaking, the $\omega_{iso}$ phase can be ellipsoidal or cuboidal with a larger particle size: Fig. 1-14a and Fig. 1-14b (*Collings 1984*), and the $\omega_{ath}$ phase particles exhibit an ellipsoidal shape with 2-10nm in diameter as illustrated in Fig. 1-14c (*Fukui 2004*).. For the ω phase obtained via shock pressure or external stress, it appears as plate shape (Fig 1-14e and Fig. 1-14f (*Xing 2008*)), while ω phase formed under irradiation has a particulate morphology ranging 1-5nm.As an example, Fig. 1-14d presents the ω phase in titanium irradiated by uranium ions (*Dammak 1999*).

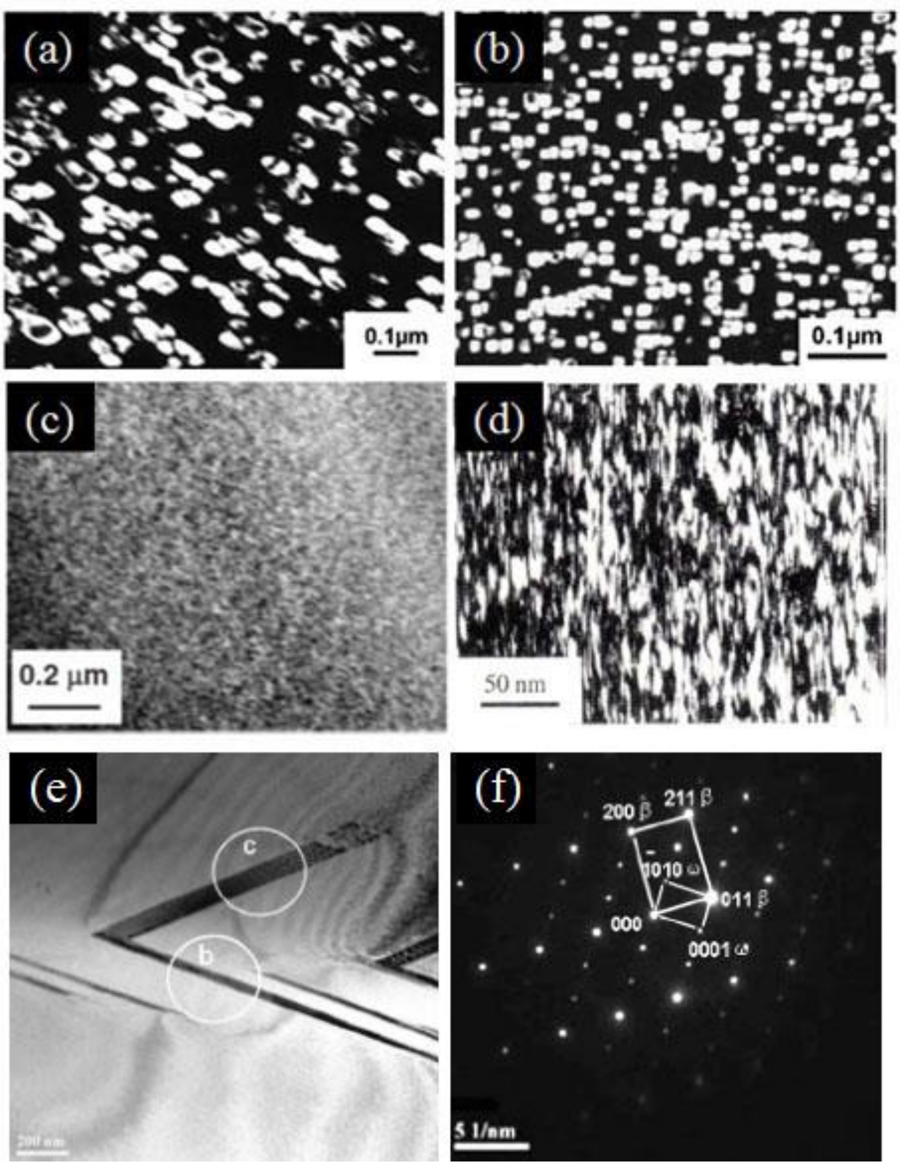

**Fig. 1-14** (a) Dark field micrograph of ellipsoidal $\omega_{iso}$ precipitates in Ti-16Mo alloy aged 48h at 450 °C, (b) Dark field micrograph of cuboidal $\omega_{iso}$ precipitates in Ti-8Fe alloy aged 4h at 400°C (*Collings 1984*), (c) Bright field micrograph of ellipsoidal $\omega_{ath}$ precipitates in Ti-Nb-Al alloy solution treated at 1000°C for 30min followed by quenching into water (*Fukui 2004*), (d) Dark field micrograph obtained using $(001)_{\omega}$ spot in Titanium irradiated at 20K with 2.2GeV uranium ions (*Dammak 1999*), (e) Bright field micrograph of stress-induced plate-shaped ω phase at room temperature in solution treated Ti-23Nb-0.7Ta-2Zr-1.2O at % alloy and (f) the corresponding diffraction pattern of image marked with “c” in (g) (*Xing 2008*).

- ✓ **Hardening effect of ω phase**

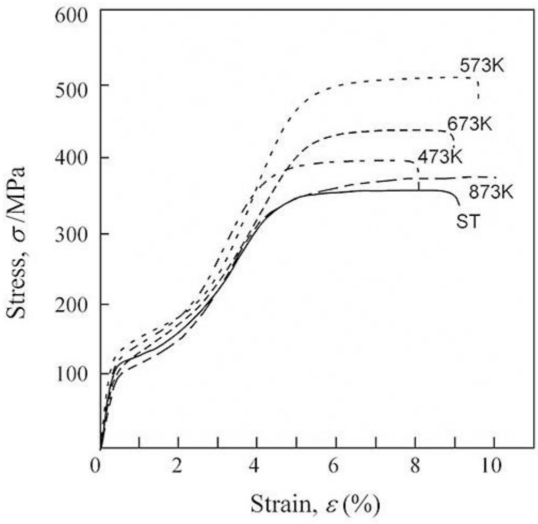

**Fig. 1-15** Stress-strain curves of a solution-treated specimen (ST) and specimens aged at various temperatures between 473 and 873K for 3.6ks for the Ti-26 at% Nb alloy (*Kim 2006*).

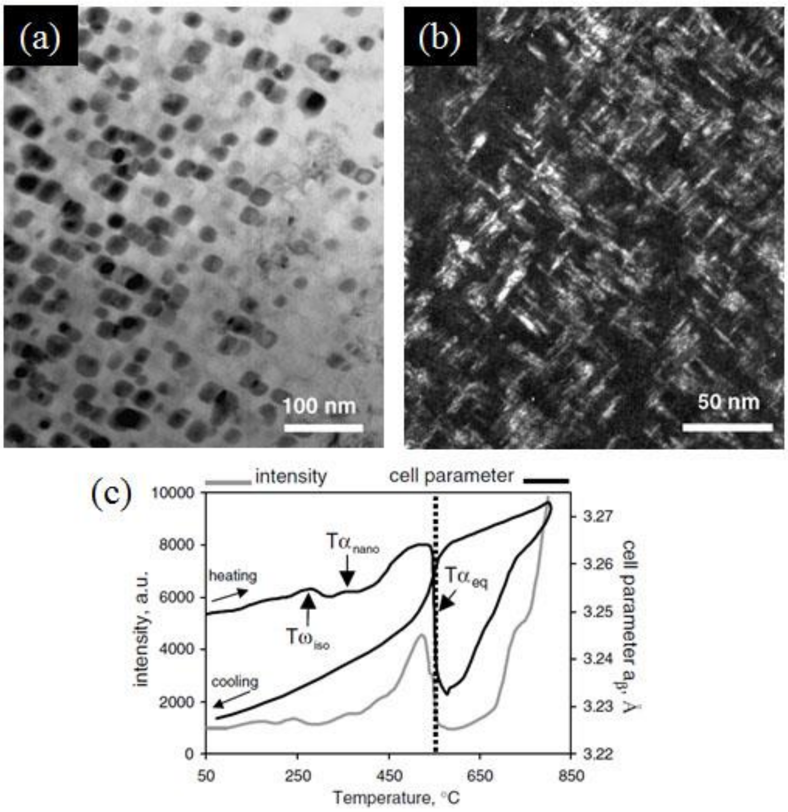
(a)
100 nm
(b)
50 nm
(c)
intensity
cell parameter
10000
8000
6000
4000
2000
0
intensity, a.u.
heating
cooling
Tα nano
Tω iso
Tα eq
50
250
450
650
850
Temperature, °C
3.27
3.26
3.25
3.24
3.23
3.22
cell parameter a_β, Å

**Fig. 1-16** (a) Bright field TEM image showing the $\omega_{iso}$ precipitates in Ti-6Mo-5Ta-4Fe alloy annealing at 300℃ for 1h, (b) Dark field TEM image showing the $\alpha_{nano}$ nano-precipitates in the following annealing at 400℃ for 1h and (c) Neutron diffraction intensity (grey curve) and crystallographic cell parameter (black curve) variations of the β (110) peak on heating (*Gloriant 2008*).

It is accepted widely that the $\omega_{iso}$ phase with small size is precipitated coherently and thus can be sheared by the moving dislocations, which results to the formation of intense, localized slip bands leading to the early crack nucleation and low ductility. Therefore, this kind of microstructures containing $\omega_{iso}$ precipitates is usually avoided in commercial β titanium alloys.

However, the precipitation of $\omega_{iso}$ phase obtained on purpose by an intermediate annealing at 473-873K can increase the critical stress for slip deformation, which in turn is an effective method to improve superelasticity in Ti-Nb alloy as shown in Fig. 1-15 (*Kim 2006*).

It is also reported that a step aging treatment can be used to firstly precipitate evenly distributed $\omega_{iso}$ phase as precursors and favorable nucleation sites for homogeneously distributed small α platelet precipitates (*Prima 2000, Gloriant 2008*). The results shown in Fig.1-16 demonstrate this effective method (*Gloriant 2008*).

## 4. Martensitic transformation and shape memory alloys

Certain metallic materials, after an apparent plastic deformation, can return to their original shape when heated. And the same material, in a certain temperature range, can be strained up to several percent and then would return to their original shape when unloaded (*Stöckel 2000*). These unusual effects are so called shape memory and superelasticity (elastic shape memory), which derive from the occurrence of a specific martensitic phase transformation responding to the temperature or load. These alloys are thus generally called shape memory alloys (SMAs).

The SMAs was firstly discovered by Arne Ölander in Cd-Au alloy on the basis of metallurgical observations and resistivity changes in 1932 (*Ölander 1932*). Later, Chang and Read named the “shape memory effect” to describe the thermo-elastic behavior of Cu-Zn alloy in 1951 (*Chang 1951*). But only after the shape memory effect was found in Ni-Ti alloys (Nitinol) in 1963, it began to gain a great popularity (*Buehler 1963, Kauffman 1997*).

As the origin of peculiarities for SMAs, the martensitic transformation has already been introduced in views of crystal structure and morphology based on titanium alloys in the previous section. However, due to the historical terminology, the different crystalline structures in martensitic transformation were also called austenite (such as the β phase in β-Ti alloy) or martensite (such as the α″ phase in β-Ti alloy), which will be inherited readily in this chapter in accordance with idioms in other SMAs.

## 4.1 Characteristic temperatures of martensitic transformations

In stress-free conditions, some phase transformation temperatures (also called "critical temperatures" or "characteristic temperatures") can be identified: *Mf*-martensite finish temperature, *Ms*-martensite start temperature, *As*-austenite start temperature, *Af*-austenite finish temperature. The order of temperature is *Mf <Ms<As<Af*. The phase composition for SMAs is generally expressed in terms of the volume fraction of martensite ($\zeta$). Fig. 1-17 just shows a plot of volume fraction of martensite as a function of temperature.

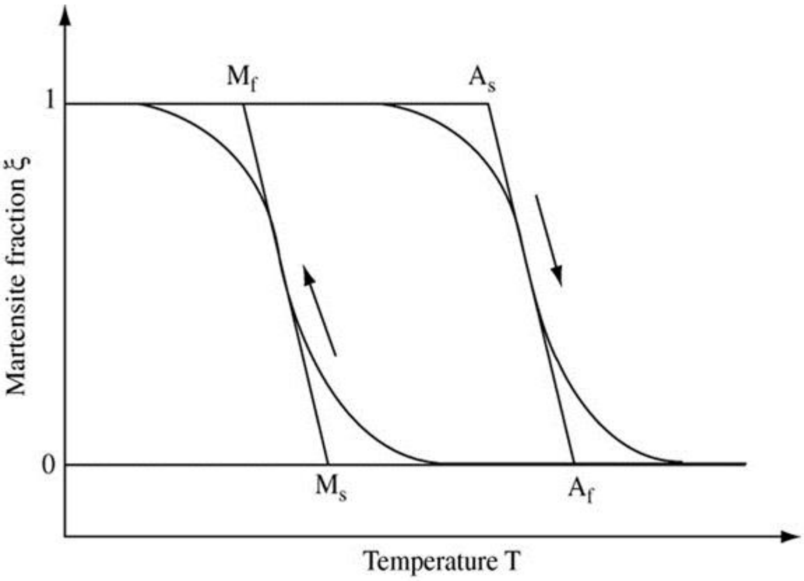

**Fig. 1-17** Schematic representation of the hysteresis loop indicating the characteristic temperature of martensitic transformation.

It can be seen from Fig. 1-17, upon cooling, that the SMAs will start from a single phase composition of 100% austenite for a temperature higher than *Af*, to reach a condition of coexistence of both martensite and austenite in different proportions, and finally obtain 100% martensite for a temperature lower than *Mf*. When heating the alloy, opposite process occurs.

## 4.2 Shape memory effect and superelasticity

On the basis of these characteristic temperatures, the shape memory alloys can be actually separated into two categories as shown in Fig. 1-18 according to different macroscopic mechanical behavior or strain-stress curves (*Barbarino 2014*) because the shape memory effect and superelasticity are dependent on the temperature of the test. When the applied ambient temperature *T<Mf*, the SMAs exhibit the shape memory

effect, while when the applied temperature *T*>*Af*, the SMAs exhibit the superelasticity.

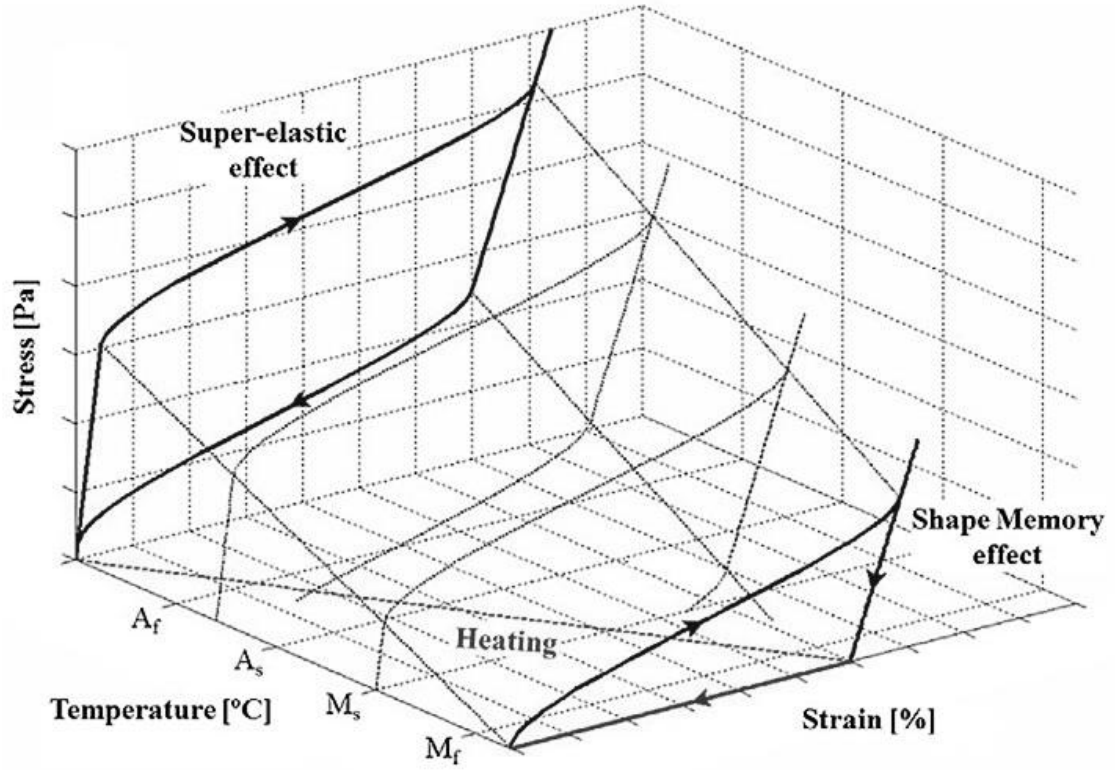

**Fig. 1-18** Different SMA strain-stress behaviors depending on ambient temperature, showing the shape memory effect when the temperature is lower than *Mf* and superelasticity at the temperature high than *Af* (*Barbarino 2014*).

### 4.2.1 Twinned and detwinned martensite

Before discussing the different mechanical behaviors between shape memory effect and superelasticity, two kinds of martensite modes together with austenite are need to be described:

(1) The twinned martensite (M), characterized by a twinned multi-variants structure schematically shown in Fig. 1-19b. This crystallographic structure keeps a twinning relationship among the adjacent martensitic variants to minimize the misfit with the austenitic phase. When the SMA is cooled down from the austenitic domain, all the possible variants of martensite are formed in one grain of austenite leading to a multi-twinned microstructure without any change in volume;

(2) The detwinned martensite (S), characterized by a typical detwinned mode with a single-variant structure shown in Fig. 1-19c. The formation of such detwinned martensite will result to a macroscopic deformation (ε).

The detwinning process of martensite is of importance (*Chopra 2002*). When the SMA is loaded above the yield point with an original state of multi-variant martensite phase, the detwinned crystal planes gradually unfold the lattice in order to accommodate the strain without achieving significant atomic displacements which is different from the conventional plastic deformation predominated by dislocation movements. Moreover, for multi-variant twinned martensite, it consists of a dense array of crystal planes which arranges an opposite orientation with each other. This twinned arrangement can exhibit a relative high mobility resulting in low elastic modulus and being a good source of damping dissipation.

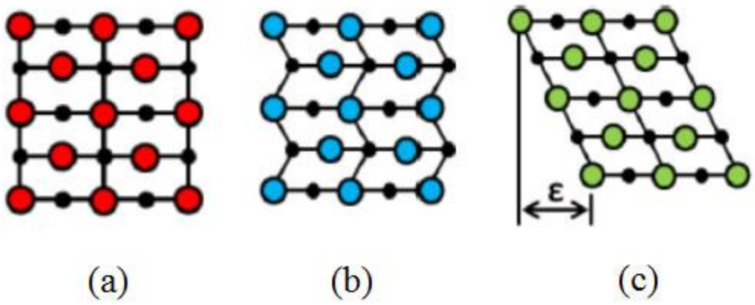

**Fig. 1-19** The schematic crystalline structures of (a) austenite, (b) twinned martensite with multi-variants and (c) detwinned martensite with single-variant (*Barbarino 2014*).

## 4.2.2 Shape memory effect

Based on the above variation of crystalline structure, the internal mechanism of shape memory effect can be further explained with the schematic strain-stress curves in Fig. 17. The premise of exhibiting shape memory effect for SMAs is the temperature lower than $Mf$ ($T<Mf$), the original structure for SMAs is thus multi-variants twinned martensite. With increasing applied stress, the following steps occur:

(1) The initial loading results to the elastic deformation of twinned multi-variants martensite;

(2) When increasing the applied stress higher than $\sigma^{MS}$, the detwinning process occurs where the multi-variant martensite transforms to a single-variant martensite, and the $\sigma^{MS}$ is the critical stress triggering the M → S transformation;

(3) Once the multi-variants martensite are detwinned to single-variants martensite, the increasing applied stress leads to the linear elastic deformation of single-variant martensite, where $\varepsilon_y^S$ is the single-variant martensite yield strain and $\sigma_y^S$ is the single-variant martensite yield stress;

(4) Then releasing the applied stress, only the elastic strain of single-variant

martensite is recovered but a large permanent strain is left;

(5) The residual strain can be thus completely recovered by an additional thermal loading $\Delta T$, which means the increase of temperature up to *Af*. Therefore, the transformation from single-variant martensite to austenite is realized leading to a total recovery of the strain. When the material is cooled down again, the shape is kept identical by the formation of a multi-twinned martensite microstructure.

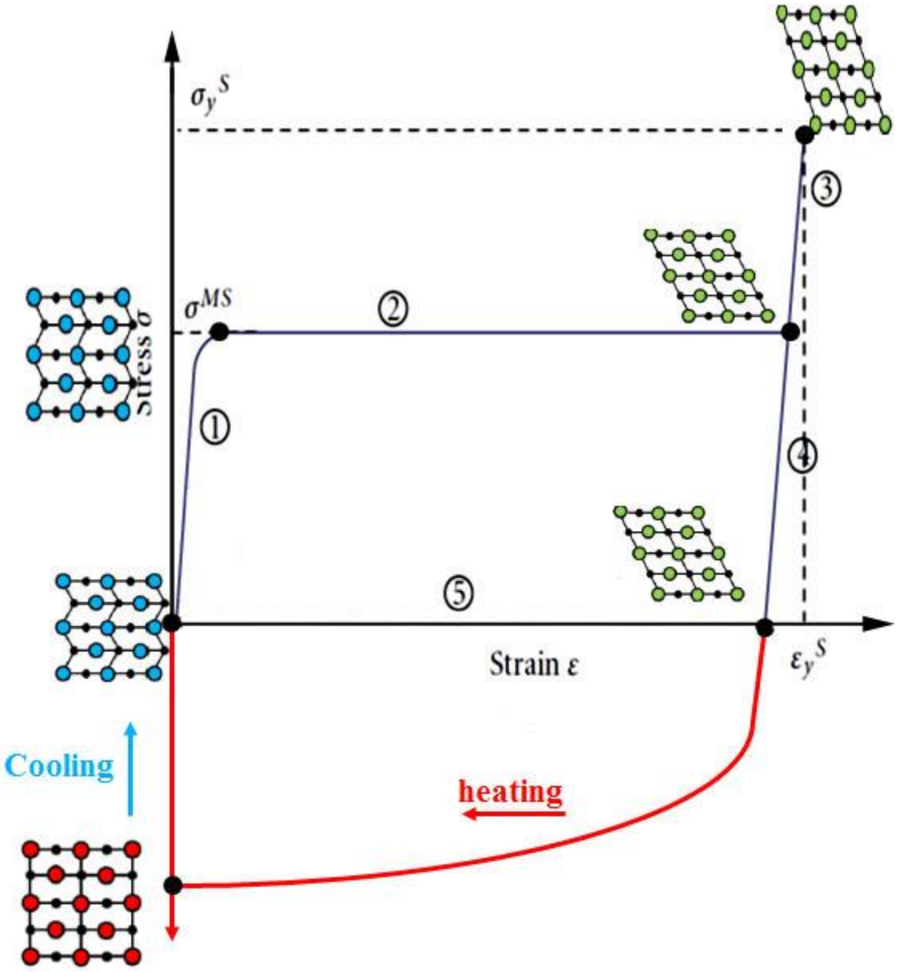

**Fig. 1-20** Shape memory effect ($T \leq Mf$) (*Chopra 2002*).

### 4.2.3 Superelasticity

The superelasticity can be observed for a SMA mechanically deformed at a temperature higher than *Af* ($T>Af$). As the temperature is above *Af*, the initial phase composition is 100% austenite. Fig. 1-21 represents the schematic strain-stress curves for superelastic alloys.

(1) The initial applied stress leads to the elastic deformation of austenite;

(2) With increasing the applied stress higher than $\sigma^{AS}$, the austenite transforms to

single-variant martensite showing a plateau on the curve, where the $\sigma^{AS}$ is the critical stress triggering the A → S transformation. It can be noticed that in some superelastic alloys, the martensite is first formed in a twinned manner (2 variants only) and is detwinned during the plateau;

(3) At the end of the plateau, the elastic deformation of the single-variant martensite occurs which cause a new linear behavior if the stress continually increases, where $\varepsilon_y^S$ is the single-variant martensite yield strain and $\sigma_y^S$ is the single-variant martensite yield stress;

(4) The elastic deformation of single-variant martensite can be totally recovered when releasing the stress;

(5) Because the martensite is not stable under the condition *T>Af*, the inverse transformation from 100% single-variant martensite to 100% austenite can take place when the load is removed to zero leading to a total recovery of the strain; $\sigma^{SA}$ is the critical stress triggering the S → A transformation.

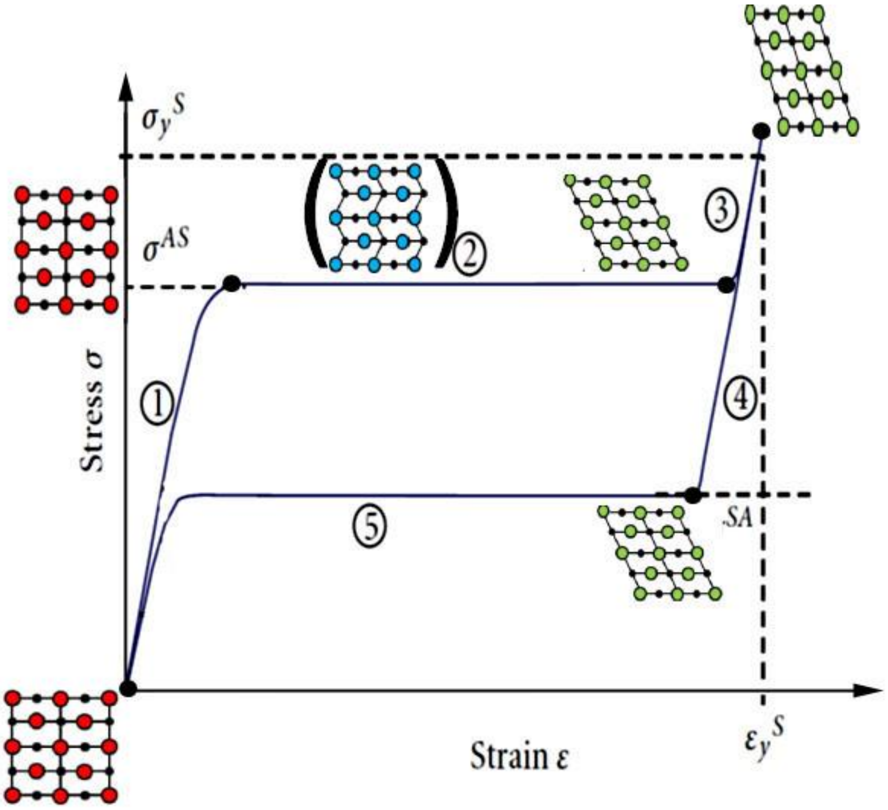

**Fig. 1-21** Superelasticity ($T \geq Af$) (*Chopra 2002*).

## 4.3 The development of Ti-Nb-based shape memory alloys

A large quantity of SMAs were developed in the last fifty years, such as Cu-Al-Ni, Cu-Sn, Ni-Al, Fe-Pd, Fe-Pt and Mn-Cu systems. The Cu-based alloys and Ni-Ti alloys have so far been suitable for commercial exploitation. But in terms of the biomedical applications, the Ti-based alloys deserve more investigations with consideration of biocompatibility.

### 4.3.1 Binary Ti-Nb alloys

As early as in 1964, A.R.G. Brown has already reported the characteristics of Ti-Nb (x=0-20 at %) alloy system including characteristic temperature *Ms* and X-ray diffraction patterns (*Brown 1964*). Recently, D.L. Moffat, T. Inamura and H.Y. Kim systematically investigated the mechanical properties, shape memory effect and superelastic behavior in binary Ti-Nb alloys, with the Nb content varying from 15 at% to 70 at% (*Moffat 1988, Inamura 2007, Kim 2004, Kim 2006*).

Fig. 1-22a presents the *Ms* depending on the Nb content, it reveals that *Ms* decreases by 40K with a 1 at. % increase of Nb content for Ti-(20-28)Nb alloys (*Kim 2006*). In this section, all compositions are given in at. %. Additionally, *Ms* becomes lower than room temperature when the Nb content increases more than 25.5 at. %, this result is in accord with the mechanical behaviors shown in in Fig. 1-22b (*Kim 2004*). For Ti-(22-25)Nb alloys subjected to solution treatment in β phase field, there is $\alpha''_{ath}$ phase resulting to the shape memory effect. Whereas for Ti-(25.5-27)Nb alloys, the metastable β phase existing in the quenched state leads to superelasticity. Finally, the Ti-(28-29)Nb β stable alloys show neither shape memory effect nor superelastic behavior.

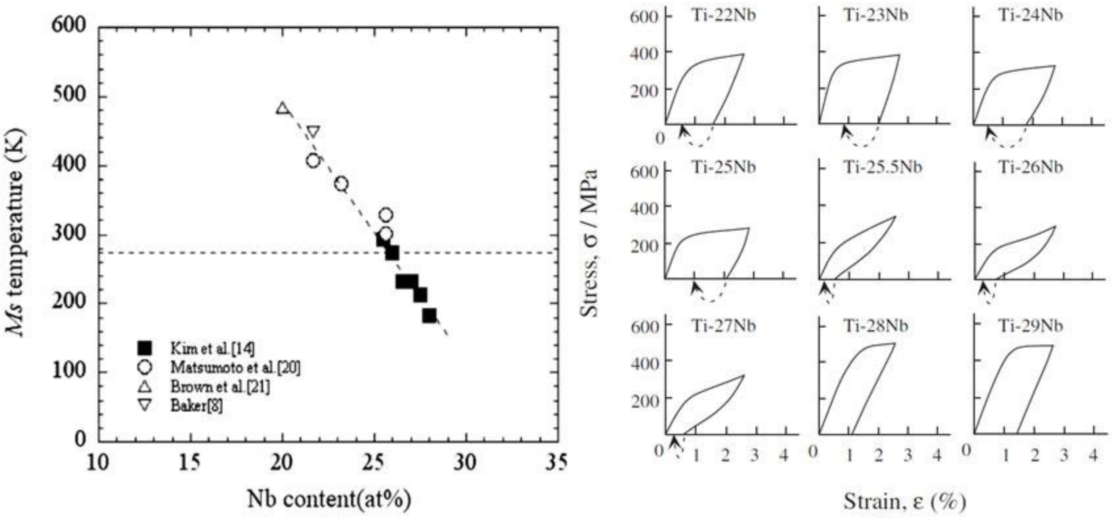

(a) (b)

**Fig. 1-22** (a) Dependence of *Ms* temperature on the content of Nb (at. %) (*Kim 2006*) and (b) stress-strain curves under loading and unloading for Ti-(22-29) at.% Nb alloys (*Kim 2004*).

In order to evaluate the superelasticity and investigate the effect of aging treatment on superelasticity, the solution-treated superelastic Ti-26Nb alloy with an original phase composition of $\beta+\omega_{ath}$ were subjected to different aging treatment (at 473K-873K for 3.6K) (*Kim 2006*). The results revealed the precipitation of $\omega_{iso}$ phase with an increasing size and volume fraction when the aging temperature increased from 473 to 573 K. However, further increasing the aging temperature above 673 K resulted in a decrease of the size and volume fraction of the ω phase. These $\omega_{iso}$ particles with size of 15-40nm could increase the critical stress for dislocation slip which subsequently results in a better recovery strain and stable superelasticity. The maximum recovered strain was revealed to be 4.2% obtained for solution treated Ti-26Nb alloy followed by aging treatment at 673K for 3.6ks.

## 4.3.2 Ternary Ti-Nb-X (X=O, N, Al) alloys

With increasing content of interstitial elements such as oxygen and nitrogen, the martensitic transformation can be suppressed and, concomitantly, the critical stress for plastic deformation increases. This increase of the critical stress for plastic deformation can thus lead to a strengthening of the superelasticity.

J.I. Kim reported the effects of oxygen on the shape memory behavior of Ti-22 Nb-O (at. %) alloy (*Kim 2005*). Fig. 1-23a gives the details of mechanical tensile curves with the oxygen content increasing from 0, 0.5%, 1.0% 0, 1.5%, to 2.0%. It is clearly known that the Ti-22Nb alloy has a fully $\alpha''_{ath}$ microstructure in the as-quenched state and therefore shows obvious shape memory effect at room temperature. However, addition of more than 1.0% of oxygen changes the mechanical behavior. The shape memory effect and superelasticity are observed in the Ti-22Nb-(0-0.5)O alloys and the Ti-22-Nb-(1.0-1.5)O alloys, respectively. Further analysis revealed that the *Ms* temperature decreased by 160K with 1 at.% increase of oxygen content. The same results can be found in shape memory Ti-24Nb alloys (at.%) with addition of 0.5 % oxygen or nitrogen (*Ramarolahy 2012*), but the results prove that nitrogen is a slightly weaker inhibitor of the martensitic transformation compared to oxygen.

The Ti-26Nb alloy (at. %) which has a fully metastable β phase microstructure behaves superelasticity at room temperature, and can also be modified by oxygen addition. Fig. 1-23b shows the mechanical behaviors of Ti-26Nb-O (at. %) alloys with different oxygen content varying between 0 and 1.0 at. % deformed at different temperature (*Nii 2010*). The critical stress for inducing the martensitic transformation is shown to increase to higher value that also proves the strong inhibition effect of oxygen on martensitic transformation. Contrarily to conventional superelastic β titanium alloys such as binary Ti-Nb alloys, the martensitic transformation is proposed to be confined in nanodomains in the high oxygen content β titanium alloys, such as Ti-23Nb-1.0O (at. %), Ti-26Nb-1.0O (at. %) and Ti-23Nb-2Zr-0.7Ta-1.2O (at. %) (*Tahara 2011*, *Nii 2010, Kim 2013*). This random nanosized modulated domains are thought to be responsible for suppressing the long-range martensitic transformation and be the mechanism of superelasticity in this class of alloys.

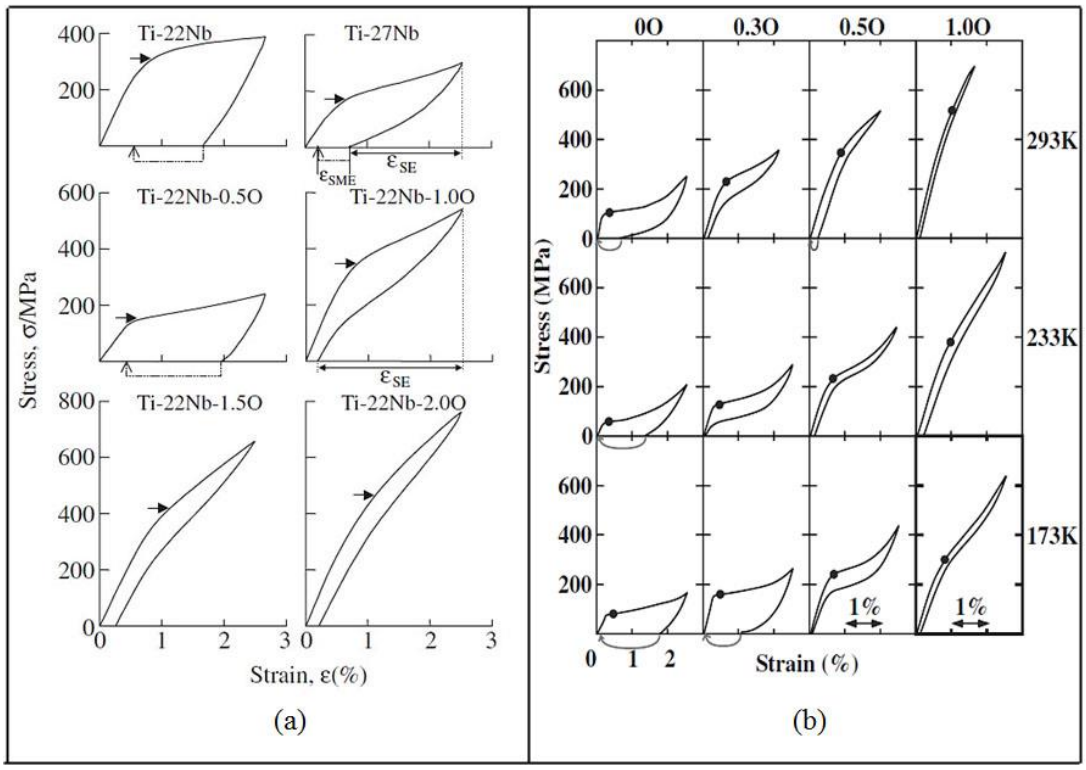

**Fig. 1-23** (a) Strain-stress curves of Ti-22 at.%Nb alloy with different addition of oxygen content varying from 0-2.0 at.% compared to Ti-27Nb alloy, showing the suppression effect of oxygen addition on martensitic transformation (*Kim 2005*) and (b) Strain-stress curves of Ti-26 at. %Nb alloy with different addition of oxygen content from 0-1.0 at.% deformed at different temperature (*Nii 2010*).

**Table 1-6** Characteristic temperatures of Ti-Nb-Al (at. %) alloys.

| Alloy | *Mf* | *Ms* | *As* | *Af* |
|---|---|---|---|---|
| Ti-16Nb-3Al | 474K | 521k | 534K | 589K |
| Ti-18Nb-3Al | 394K | 441K | 454K | 509K |
| Ti-23Nb-3Al | 194K | 241K | 254K | 309K |
| Ti-24Nb-3Al | 154K | 201K | 214K | 269K |

Except oxygen and nitrogen, aluminum is also added into Ti-Nb-based alloy (*Fukui 2004, Inamura 2010, Hosoda 2006*). The characteristic temperatures of these alloys can be resumed in Table 1-6. It can be known from Table 6, there is only the Ti-24Nb-3Al alloy exhibiting the *Af* lower than room temperature, which displays thus superelasticity with a microstructure containing $\omega_{ath}$ phase. By comparison with the binary Ti-24Nb alloy, one can conclude that aluminum is also a martensitic transformation inhibitor.

Furthermore, an investigation of crystallographic orientation dependence of superelasticity on the Ti-24Nb-3Al alloy revealed the largest superelastic strain of 4.7% was observed when the tensile direction was parallel to the $<110>_\beta$ whereas only 1.3% was observed along $<111>_\beta$. The similar conclusion that the strong texture of RD// <110> leads to a best superelasticity was also demonstrated in Ti-22Nb-6Ta (at.%) alloy (*Miyazaki 2006*) as shown in Fig. 1-24.

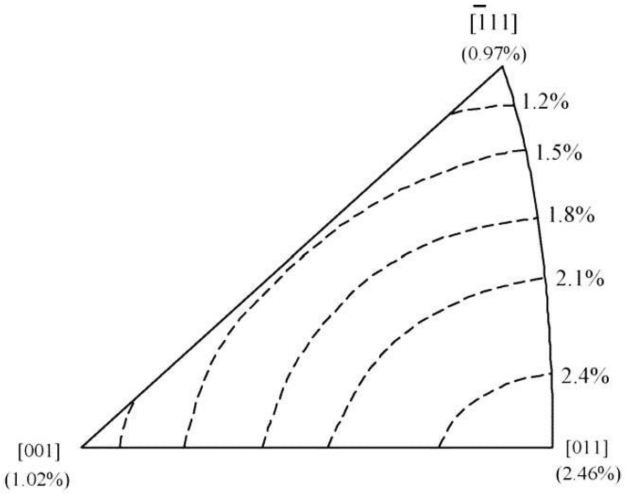

**Fig. 1-24** Orientation dependence of the calculated transformation strain associated with the martensitic transformation from the β to α″ for the Ti–22Nb–6Ta (at.%) alloy (*Miyazaki 2006*).

## 4.3.3 Quaternary Ti-Nb-Ta-Zr alloy

In the last decades, a β-type Ti-based alloy called *Gum metal*, with a nominal composition of Ti-23Nb-2Zr-0.7Ta-1.2O (at.%) has been developed and attracted considerable attention due to some “super” properties, such as high strength, low Young’s modulus, superelasticity and superplasticity at room temperature (*Saito 2003, Kim 2013*).

It has been claimed that a certain amount of oxygen addition larger than 0.7 at.% and substantial cold working, in additional to low β stability with an electron/atom ratio of about 4.24, a bond order of about 2.87 and a d-electron orbital energy of 2.45eV, are required to exhibit multiple super properties (*Saito 2003, Ikehata 2004, Hwang 2005, Furuta 2005, Kuramoto 2006a, b*). Saito et al. firstly explained these properties with unconventional deformation mechanisms such as “nanodisturbances” and “giant faults”. However, evidences of other deformation mechanisms involving dislocation slip (*Guo 2008, Withey 2010, Xing 2008b, Yang 2010, Besse 2011, Castany 2011*), twinning (*Yang 2010, Xing 2008, Yang 2008*), SIMα″ (*Talling 2009*) and nanodomain formation (*Kim 2013*) were found by other researchers. Therefore, the mechanism of deformation of such an alloy is still in debate.

# 5. Ti-24Nb-4Zr-8Sn alloy

Ti-24Nb-4Zr-8Sn alloy (wt. %, abbreviated as Ti2448) is a low Young’s modulus, high strength, good corrosion resistivity and high recoverable strain alloy, designed for biomedical applications but can actually be used for multifunction. Young’s modulus below 50GPa with 3.3% recoverable strain (*Hao 2005, 2006, 2007b*) is realized directly after hot-working (*Li 2011*), and tensile strength of 1150 MPa can be achieved through α-ageing treatment. In-vivo trials show also excellent biocompatibility (*Zheng 2009*).

In this section, the alloy designation will be introduced, after what an exploration of the effect of heat treatment and the elastic and plastic deformation mechanisms will be tried to be clarified. Finally, unresolved problems will be listed that can be set as the target of the thesis.

## 5.1 Alloy designation

### 5.1.1 Primary consideration

When designing a new biomedical β-Ti alloy, besides excluding elements that show toxic effect on human body, the primary consideration is to reduce the elastic modulus while maintaining good mechanical properties. However, how to reduce the modulus of alloy?

For most water-quenched binary titanium alloys stabilized by varying amounts of group IV or V transition metals, the Young's modulus (*E*) of the resulting microstructure depends much on the solute concentration. Two examples are shown in Fig.1-25a for Ti-Nb alloys and in Fig. 1-25b for Ti-Mo alloys, respectively (*Collings 1980*). In this diagram, the value of *E* actually depends on two competing process. The first one is the variation of *E* caused by variation in the volume fraction of phases with different Young's moduli. And the second one is the variation of intrinsic Young's moduli of each phase, as a function of concentration of β stabilizer.

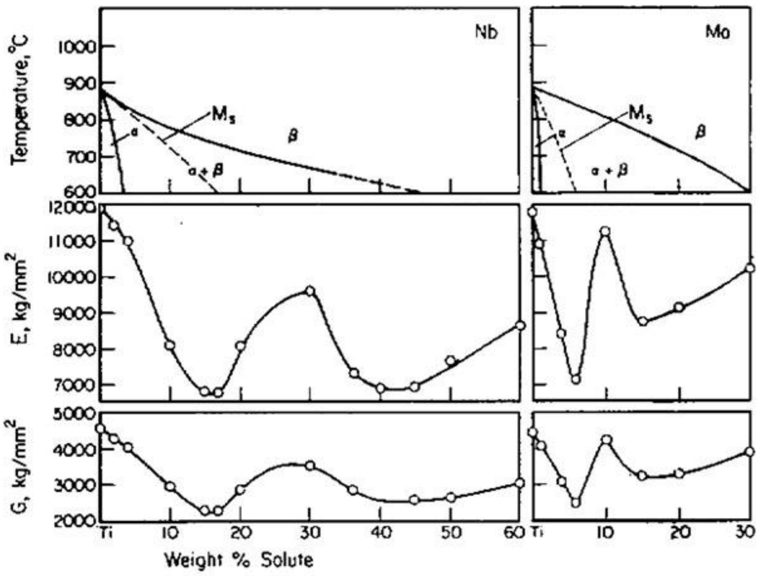

(a) (b)

**Fig. 1-25** (a) Variation of average Young's modulus in binary Ti-Nb alloys and Ti-Mo (b) alloys in relation to the quenched microstructure (*Collings 1980*).

Seen from Fig. 1-25, in the binary titanium alloys containing sufficiently high concentrations of β stabilizing elements, for example Ti-Nb alloys with approximately 40 wt. % niobium, the β phase can be retained to room temperature by fast cooling which shows a general lower modulus compared to α phase. The modulus composition dependence of Ti-Nb alloy can be discussed in three parts: 0-15%, 15-40% and 40-60%. In the range of 40-60%, the *E* value of β phase increases with increasing Nb content, showing a lowest value of 70GPa for 40% Nb. And an unusual peak in *E* at about 30% of Nb is related to the $\omega_{ath}$ phase transformation. The steep decline in modulus from 0 to 15% Nb results from the formation of α″ martensite, which can also be proved by the decline of *E* for metastable β phase with occurrence of SIM α″ phase during loading. The similar pattern can be found for the average shear modulus *G* in the bottom of Fig. 1-25.

Based on these discussions, there are three strategies to reduce the elastic modulus:

(1) The alloying additions must avoid the formation of $\omega_{ath}$ phase as it is not only responsible for the peak in elastic modulus but also regarded as highly undesirable due to its embrittling effects.

(2) The alloying should ideally depress the *Ms* to below room temperature so that the SIM α″ transformation could occur upon loading for a decrease of modulus.

(3) The alloying scheme must be able to further reduce the intrinsic elastic modulus of the β phase.

## 5.1.2 Alloy design

The stability of bcc β phase is linked to the shear constant $C'=(C_{11}-C_{12})/2$ (*Zener 1947*), which represents the {110}<1-10> cubic shear moduli and can be used to calculate all the Young's modulus and shear modulus shown in the following expressions (*Wortman 1965*). Additionally, the valence electrons per atom ratio (e/a) also has a relationship with C′, that is displayed in Fig. 1-26 (*Collings 1980, Tane 2008*).

$$E_{110}=\left\{\frac{(C_{11}+C_{12})}{(C_{11}-C_{12})(C_{11}+2C_{12})}+\frac{1}{4}\left(\frac{1}{C_{44}}-\frac{2}{C_{11}-C_{12}}\right)\right\}^{-1}$$

$$E_{111=}\left\{\frac{(C_{11}+C_{12})}{(C_{11}-C_{12})(C_{11}+2C_{12})}+\frac{1}{3}\left(\frac{1}{C_{44}}-\frac{2}{C_{11}-C_{12}}\right)\right\}^{-1}$$

$$E_{100}=\frac{(C_{11}-C_{12})(C_{11}+2C_{12})}{C_{11}+C_{12}}$$

$$G_{100}=C_{44}$$

$$G_{110}=\frac{C_{11}-C_{12}}{2}$$

$$G_{111}=\frac{3C_{44}(C_{11}-C_{12})}{C_{11}-C_{12}+4C_{44}}$$

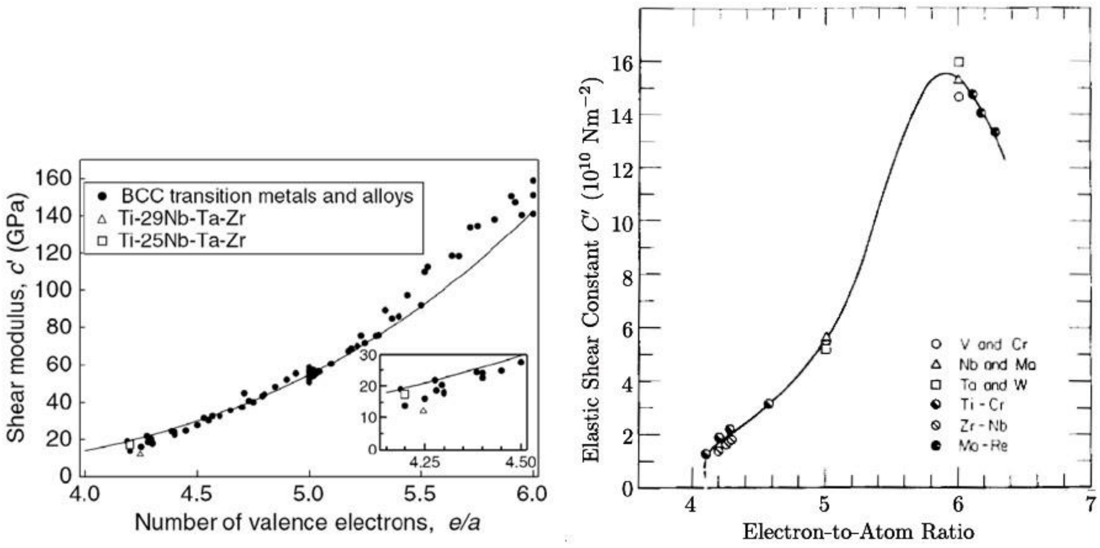

(a) (b)

**Fig. 1-26** Shear constant $c'$ of bcc metals as a function of valence electrons and the solid line denotes the $c'$ calculated by theory (*Collings 1980, Tane 2008*).

It can be seen from the formulas shown above that the lower value of shear constant $c'$ corresponds to lower value of both Young's modulus and shear modulus. Whereas in Fig. 1-25, the variation in $c'$ forms a continuous function of e/a, from the highly stable Cr, Mo, W $\beta$ phases in group VI (e/a=6) with $c'$ =150GPa down to the low solute limit to $\beta$ stability at e/a=4.15-4.20 with $c'$ =10-20GPa. For example, the newly developed $\beta$ type Ti-29Nb-Ta-Zr, Ti-25Nb-Ta-Zr and Ti-23Nb-0.7Ta-2Zr-O gum metal are all lied in the low solute limit region, which show relatively low Yong's modulus.

According to these observations, Hao et al. employed the Ti-24 wt. % Nb system to develop a new $\beta$ titanium alloy, in which the e/a value is about 4.15 nearly approaching the minimum limit. Further addition of Zr and Sn is used in order to effectively suppress the $\omega_{ath}$ phase and $\alpha''$ martensitic transformation but maintaining the e/a=4.15 unchanged. The Ti-24Nb-4Zr-8Sn alloy was finally developed after investigations on the microstructure and phase optimization (*Hao 2007b, Li 2008*).

## 5.2 Elastic properties of single crystal

Single crystals of Ti2448 alloy were fabricated successfully using an optical floating-zone furnace (*Zhang 2010a*). Using the single crystals, the anisotropic elastic constants were investigated. Several kinds of resonant methods gave consistent elastic constants of $C_{11}$, $C_{12}$ and $C_{44}$ of 57.2, 36.1 and 35.9GPa respectively. Further, according to the Wortman's formulas, Young's modulus of 27.1, 56.3 and 88.1GPa and shear modulus of 34.8, 11.0 and 14.6GPa along the different orientations of <100>,

<110> and <111> can be obtained, respectively. Zhang has reported the comparison of these elastic constants with the other β type biomedical alloys (*Zhang 2011a*).

The deformation behavior of single crystal shows anisotropy in Fig. 1-27. For the crystal along <100> direction, the pure elastic region can be extended to a strain as high as 2.5% but a slight non-linear elasticity is observed. The deformation behavior of crystal with <110> direction has an apparent double yielding, which indicates the SIM α″ occurs; a maximum recoverable strain of 4.0% can thus be obtained. For the crystal with <111> direction, the deformation behavior is more conventional with a maximum elastic strain of only 0.8% which is much smaller than the other orientations. The Young's moduli are $E_{<100>}$=25.9GPa, $E_{<110>}$=55.4GPa and $E_{<111>}$=86.1GPa measured from the tensile curves in Fig. 1-27, which are in accord with the theoretical calculations.

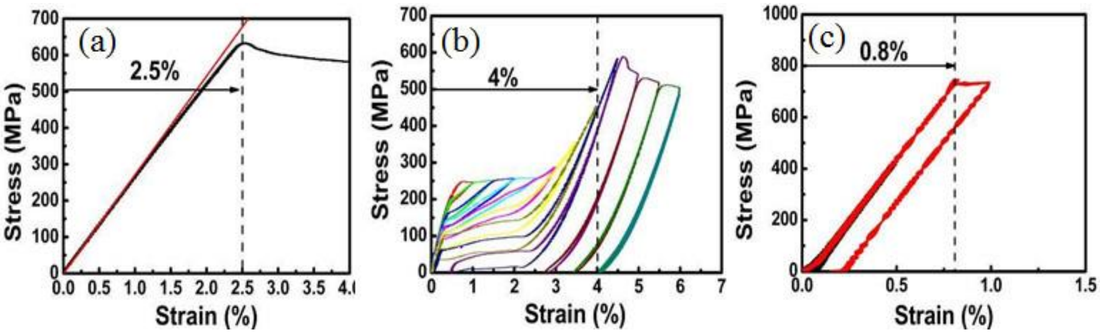

**Fig. 1-27** The deformation behavior of Ti2448 single crystal along different orientation (a) <100>, (b) <110> and (c) <111> (*Zhang 10a, Zhang 2011a*).

Therefore, it was concluded that the <100> crystal exhibits a low modulus of 25.9GPa, high strength of 631MPa, good ductility of 73% and medium elastic strain of 2.5%, which may be useful for orthopedic implant applications (*Zhang 2010a*). A superelasticity of 4.0% via SIM α″ transformation was also observed along <110> direction.

## 5.3 Superelasticity depending on processing route

The microstructure of the polycrystalline Ti2448 alloy can be extremely refined through severe plastic deformation. The microstructures and corresponding cyclic tensile curves after hot forging, warm rolling and hot rolling are shown in Fig. 1-28a ,b and c, respectively.

For the as-hot forged state in Fig. 1-28a, the Ti2448 alloy has a fully-β phase microstructure with grain size of 1μm and a maximum recoverable strain of 2.6% can be obtained. Compared with warm rolling in Fig. 1-28b, although the grain size was increased after hot rolling in Fig. 1-28c, similar maximum recoverable strain of 3.3% can be realized.

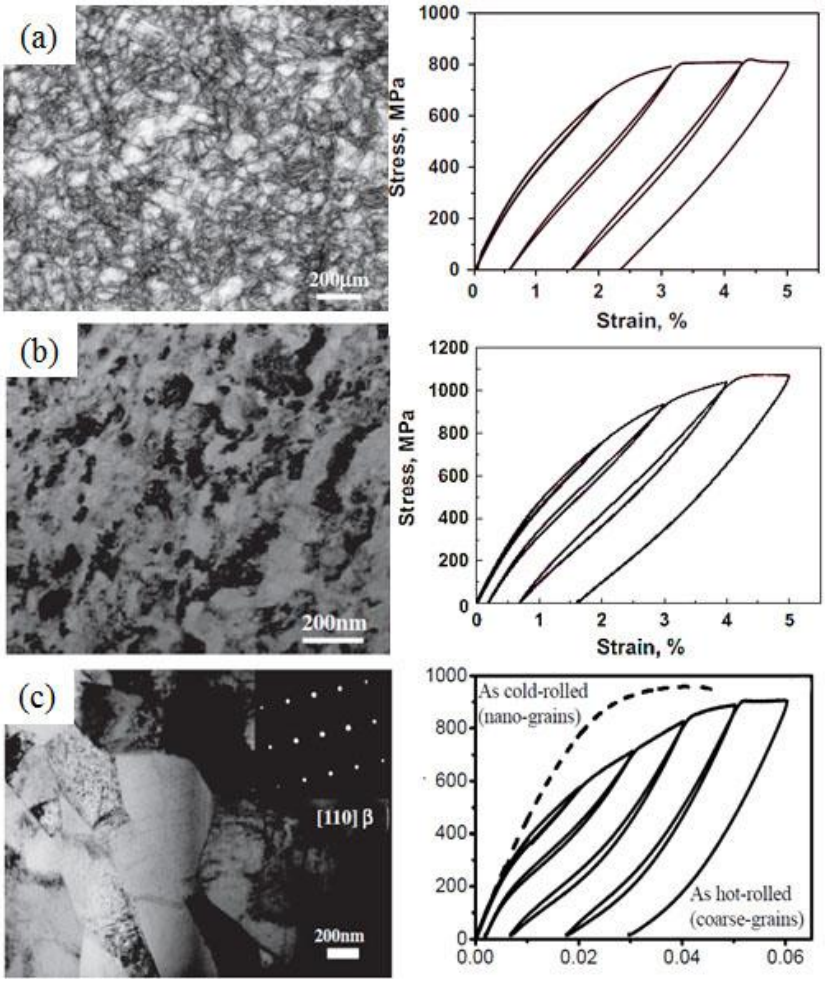

**Fig.1-28** (a, b) Microstructure and cyclic tensile curves of as hot-forged Ti2448 alloy at 1123K (*Hao 2012*), (c, d) as warm-rolled Ti2448 alloy at 473-673K (*Hao 2012, Zhang 2011c*) and (e, f) as hot-rolled Ti2448 alloy at 1073K (*Zhang 2011b, Li 2008*).

The critical stress for inducing the SIMα″ phase can be measured at 250MPa for all different heat treated superelastic Ti2448 alloys. This result is consistent with the value of the single crystal along <110> direction, which indicates the strongly developed <110> texture along rolling direction. The slight difference of maximum recoverable strain can be attributed to different grain sized depending on heat treatment.

## 5.4 Effect of heat treatment on microstructure and mechanical properties

Annealing at 550-850 ℃ for 10 minutes followed by water quenching has been conducted on as-cold rolled Ti2448 alloy. The X-ray diffraction reveals that the precipitation of α phase only occurs below the annealing temperature of 650℃. The microstructure in Fig. 1-29 presents the grain size increases with the annealing temperature, from less than 100nm at 550℃, 600nm at 650℃ to approximately 10μm at 700℃.

A second step of annealing at 450℃ for 1h and 4h, respectively, were also conducted on Ti2448 alloy subjected firstly to annealing at 750℃ for 10 minutes; the corresponding microstructures are shown in Fig. 1-30. Apparently, the α phase nucleates firstly at grain boundaries of β phase. When the aging time increases, the nucleation and growth of α phase happens inside β grain.

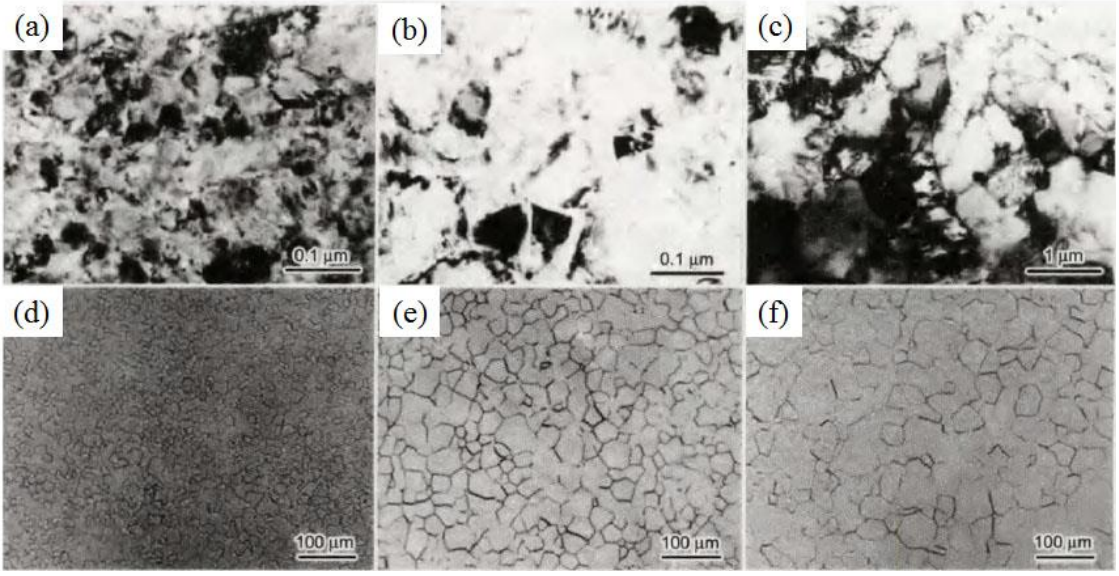

**Fig. 1-29** Microstructure of cold-rolled sheet after solution treatment at (a)550°C, (b)600°C, (c)650°C, (d)700°C, (e)750°C, (f)800°C and (g)850°C for 10 minutes followed by water quenching (*Cui 2008*).

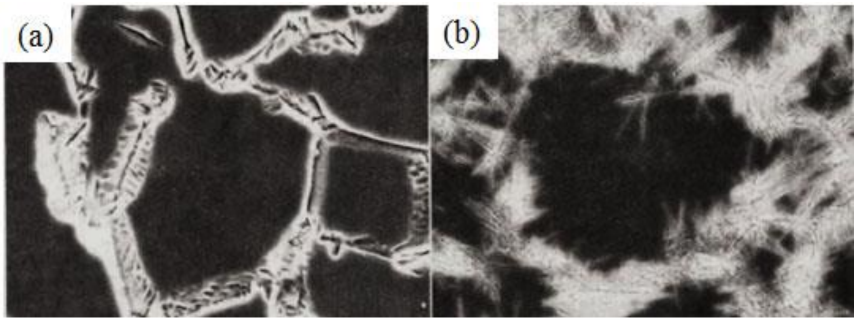

**Fig. 1-30** The SEM microstructures of cold-rolled sheet after annealing at 750°C for 10 minutes and then aged at (a) 450°C for 1 hour and (b) 450°C for 4 hours (*Cui 2008*).

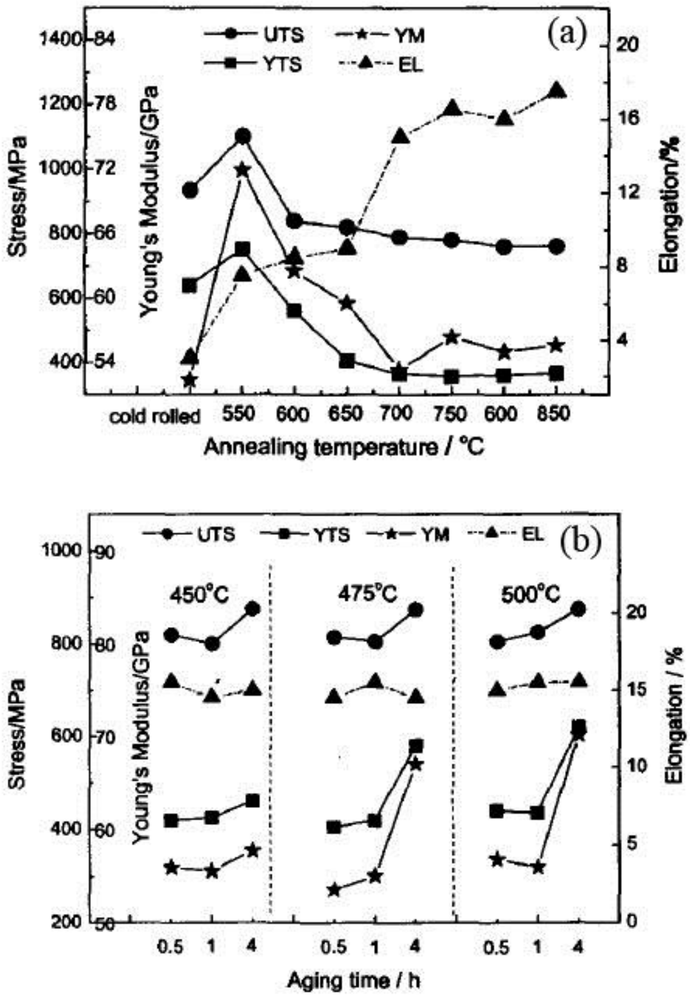

**Fig. 1-31** (a) Effects of annealing at 550-800°C for 10 minutes followed by water quenching and (b) effects of second annealing at 450 -500°C conducted on the alloy subjected at 750°C for 10 minutes, where UTS, YTS, YM and EL represents ultimate tensile strength, yielding tensile strength, Young's modulus and elongations (*Cui 2008*).

Different grain size and phase composition lead to the complex mechanical response shown in Fig 1-31, where the ultimate tensile strength, yielding tensile strength, Young's modulus and elongation were plotted. Fig. 31a and Fig 31b display the mechanical properties of alloys subjected to annealing at 550-850 ℃ for 10 minutes and the secondly annealing at 450 ℃, respectively. Actually, the fluctuation of curve in Fig. 31a is caused by contrary effects of two competing process, which are volume fraction of α phase and grain sizes. Firstly, tensile strengths are increased after annealing at 550 ℃ with comparison to as-cold rolled state; the reason comes from the stronger positive effect of α phase precipitation than the negative effect of increasing β grains. The decreasing tendency of tensile strength and Young's modulus thereafter is due to higher volume fraction and increasing grain size of β phase, which also explain the better ductility obtained after high temperature annealing.

In terms of the second annealing step at 450-500 ℃, annealing for short time (0.5-1h) has slight influence on the mechanical properties (Fig 1-30b). However, with increasing the annealing time to 4h, the strengths and Young's modulus increase apparently. In addition, with increasing the annealing temperature, the yielding strength and Young's modulus can be increased to a higher level.

## 5.5 Corrosion resistance

The corrosion resistance of annealed Ti2448 alloy has been evaluated in aerated PBS (phosphate buffered solution) for simulating the human body fluid with comparison to CP Ti and Ti-6Al-4V alloy. The potentiodynamic polarization curves are shown in Fig. 1-32 (*Bai 2012*).

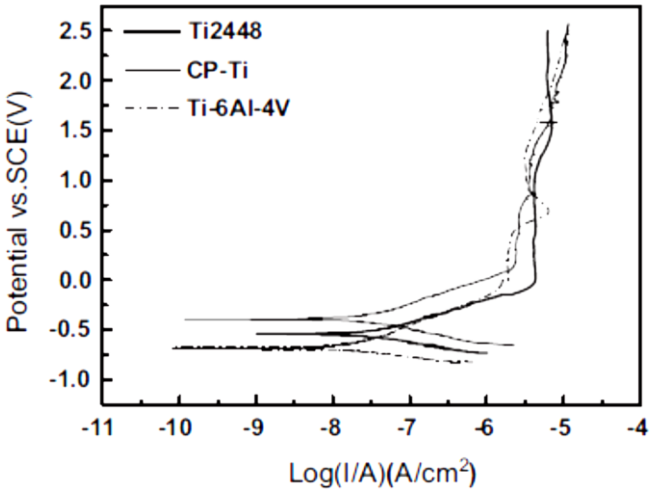

**Fig. 1-32** Potentiodynamic polarization curves in the PBS solution at 37°C ( *Bai 2012*).

It is clear all the samples exhibit a typical active-passive characteristic. The corrosion potentials ($E_{corr}$) can be estimated from these curves as -0.53, -0.39 and -0.69 V (vs. SCE) for the Ti2448 alloy, CP-Ti and Ti-6Al-4V alloy, respectively. The corrosion current densities ($I_{corr}$) were obtained by Tafel analysis using both anodic and cathodic branches of the polarization curves. Therefore, The Ti2448 alloy presents a good passivation performance and its corrosion rate is comparable to that of CP-Ti and Ti-6Al-4V alloy.

## 5.6 Fatigue properties

The stress-controlled high-cycle fatigue (HCF) properties and the strain-controlled low-cycle fatigue properties (LCF) for the as-hot rolled Ti2448 alloy were evaluated (*Zhang 2010b, Zhang 2011b*).

### 5.6.1 High-cycle fatigue

The HCF tests were performed under a sinusoidal cyclic waveform loading with frequency of 20 Hz and R of 0.3, 0.1 and -1, where the value of R is the stress ratio, defined as the value of minimum peak stress divided by the maximum peak stress on the applied loading wave. The cyclic stress-response curves (S-N) of as-hot rolled Ti2448 alloy HCF tested at room temperature are presented in Fig. 1-32a. The fatigue limit varies with the value of R, revealed to be 427MPa, 375MPa and 225MPa under stress ratio of 0.3, 0.1 and -1, respectively. This difference is due to different stress states.. In addition, the annealed state (SA), that underwent a historical process of hot rolling+700 ℃/30min+water quenching+ 400 ℃/24h, has a better HCF property caused by precipitation of α phase during the low temperature annealing treatment.

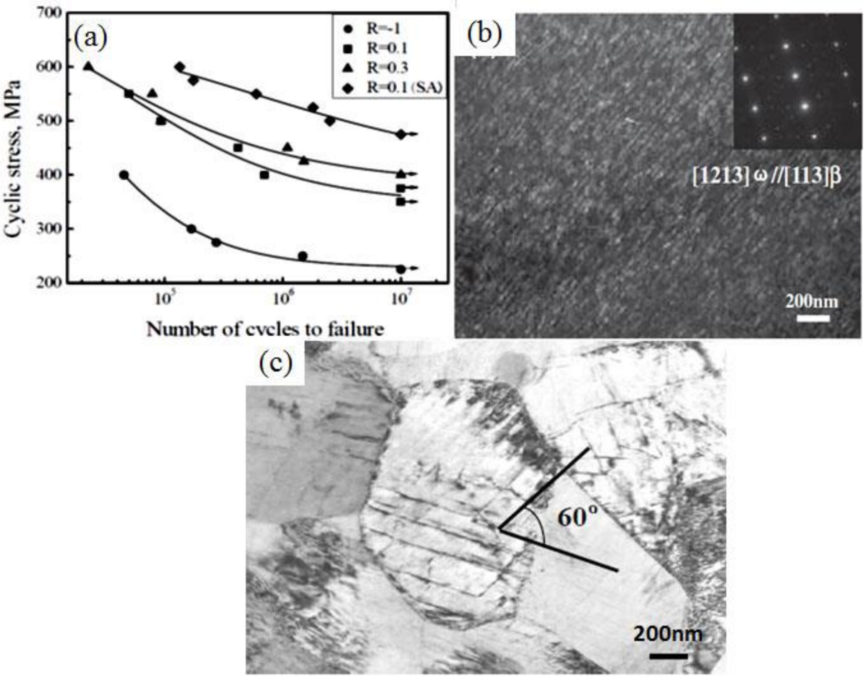

**Fig. 1-33** (a) S-N curves of as-hot rolled and aged Ti2448 (SA) alloy HCF tested at room temperature, (b) Dark field image of stress-induced ω phase in the as-hot rolled Ti2448 at the condition of R=0.1, σ=500MPa and $N_f$=92001 and (c) R=-1, σ=250MPa and $N_f$=$10^7$(*Zhang 2010b, Zhang 2011b*).

The characteristic microstructures at different conditions are typically shown in Fig. 1-33b and c. There are stress-induced ω phase and dislocations slip. It seems that stress-induced ω phase occurs at higher loading condition whereas only dislocations are involved at lower loading condition.

### 5.6.2 Low-cycle fatigue

The LCF tests were performed under a triangular waveform straining with frequency of 0.5Hz and R of 0.1, 0.3 and -1. The parameter of R is here defined as the value of minimum peak strain divided by the maximum peak strain on the applied strain wave. The strain-controlled LCF properties of both as-hot rolled Ti2448 alloy and Ti-40Nb-13Ta-5Zr alloy (TNTZ) at different strain ratios are displayed in the form of plots of strain amplitude against the number of reversals to failure in Fig. 1-34a. The fatigue resistance of Ti2448 alloy in the low-cycle regime enhances with the increase in the strain ratio. Comparing with TNTZ alloy, Ti2448 alloy shows much stronger fatigue resistance (R=0.1). For example, at cyclic strains between 0.25% and 2.5%, Ti2448 exceeds $5\times10^4$ cycles without failure whereas TNTZ alloy withstands just $2\times10^2$cycles. The plastic deformation in the fatigued Ti2448 alloy involves dislocation slip and stress-induced α″ phase transformation (Fig. 1-34b and c).

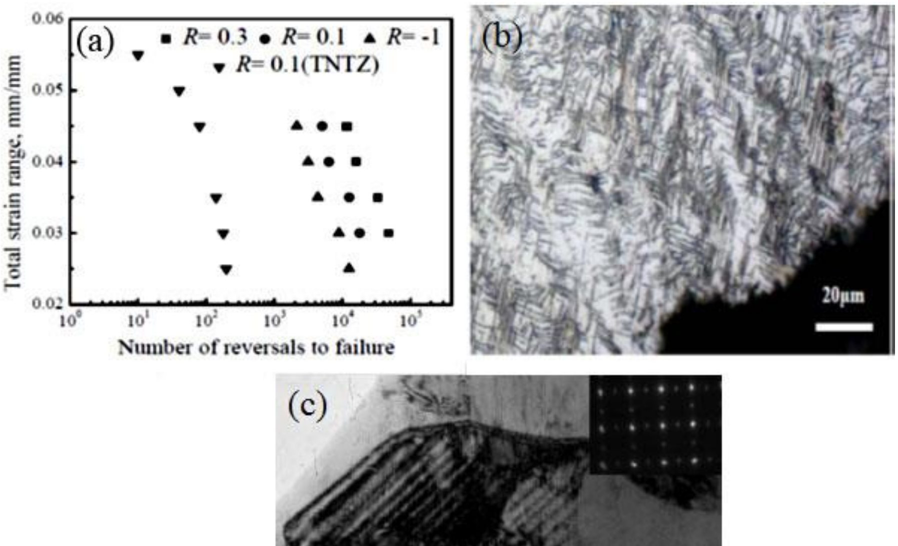

**Fig. 34** (a) S-N curves of as-hot rolled and TNTZ alloys LCF tested at room temperature; (b) optical microstructure showing the slip bands near the fracture surface and (c) TEM observation of aggregated SIMα″ phase at the condition of R=-1, $\varepsilon_t$=4% (*Zhang 2010b, Zhang 2011b*).

## 5.7 Biocompability

In order to test the biocompatibility of Ti2448 alloy, surface modification with calcium phosphate coating has been done (*Zheng 2007, Zheng 2009*). Then *in vitro* cell tests on rabbit osteoblast show these modified surfaces improved considerably the cell proliferation (*Tao 2009*). Further, extensive *in vivo* tests and clinical trials have been conducted in the past few years in order to investigate the correlation of elastic matching between bone and implant to the healing of fractured bone. According to Guo *et al.* (*Guo 2009*), intramedullary nails made of Ti2448 were implanted in New Zealand white rabbits in order to study the bone healing and stability of implants. The results show that the low modulus of Ti2448 alloy leads to significant improvement in new bone formation in fractured rabbit tibiae as compared with the control group made of ($\alpha$+$\beta$) type Ti-6Al-4V EIL alloy. Additionally, clinical trials of implant parts made of Ti2448, such as bone plates, nails, and spinal fixtures, have all been conducted (*Yang 2011*). Results revealed that the Ti2448 alloy is biocompatible.

## 5.8 Unresolved problems

Since the Ti2448 alloy was developed as a biomedical titanium alloy based on the combination of first principle computations of alloying effects and physical metallurgy principles, extensive investigation on properties, microstructure and clinical trials have been conducted. However, some underlying mechanisms, especially elastic and plastic mechanisms remain a problem under debates.

The observed non-linear elasticity, which was firstly thought to be the result of easy crystal distortion due to much-weakened atomic bond (*Hao 2007a*) and incipient kind bands (*Hao 2007a*), was later explained with three reversible deformation mechanisms: nano-disturbances reversible dislocation loops and martensitic transformation (*Cui 2009*). In recent years, the technique of *in situ* synchrotron high-energy X-ray scattering was employed: the results show the occurrence of nano-saled stress-induced reversible martensitic transition is the intrinsic mechanism of the peculiarity (*Liu 2013*).

The highly localized plasticity, characterized by a relative easily nanostructuration, is also under investigation and can result to ultra-fine grain size material. The previous studies on the Ti2448 alloy with ultra-fine grain size showed that this microstructure can lead to different response to mechanical (*Li 2011*), fatigue (*Zhang 2011*), biocompatibility properties (*Hao 2008*). However, the reason of the plastic nanostructured microstructure is still unknown.

# References

Bagariatskii Y.A., Tagunova T.V., Nosova G.I., *Problemy metallovedenija i fisika*, metallov, **5**, p210, 1958a.

Bagaryatskii Y.A., Nosova G.I., Tagunova T.V., *law of formation of metastable phase in titanium alloys*, Doklady Akad, Nauk S.S.S.R., **122**, p593, 1958b.

Bai Y., Li S.J., Prima F., Hao Y.L., Yang R.. *Electrochemical corrosion behavior of Ti-24Nb-4Zr-8Sn alloy in a simulated physiological environment*. Applied Surface Science, **258**, p4035, 2012.

Banerjee S., Johnson W.C., Howe J.M., Laughlin D., Soffa W.A. (Eds.), *Solid- Solid Phase Transformations in Inorganic Materials*, TMS, Warrendale, PA, p861, 1994.

Banerjee S., Tewari R., Mukhopadhyay P., *Coupling of displacive and replacive ordering*. Progress in Materials Science, **42**, p109, 1997.

Banerjee S., Mukhopadhyay P., *Phase Transformations-examples from Titanium and Zirconium Alloys*. Pergamon Materials Series, **12**, p3, 2007.

Barbarino S., Saavedra Flores E.I., Ajaj R.M., Dayyani I., Friswell M.I., *Topical Review: A review on shape memory alloys with applications to morphing aircraft.* Smart Materials and Structures, **23**, p063001, 2014.

Bertrand E., Castany P., Gloriant T., *An alternative way to orient the parent phase in the cubic/orthorhombic martensitic transformation of titanium shape memory alloys*. Scripta Materialia, **83**, 41, 2014.

Besse M., Castany P., Gloriant T., *Mechanisms of deformation in gum metal TNTZ-O and TNTZ titanium alloys: A comparative study on the oxygen influence*. Acta Materialia, **59**, p5982, 2011.

Boyer R., Welsch G., Collings E. W., *Materials Properties Handbook: Titanium Alloys,* ASM International, 1994.

Brotzen F.R., Harmon F.L., Troiano A.R., *Decomposition of Beta Titanium*. Trans. TMS-AIME, **203**, p413, 1955.

Brown A.R.G., Clark D., Eastabrook J., Jepson J.S., *The Titanium–Niobium System*. Nature (London), **201**, p914, 1964.

Buehler W.J., Gilfrich J.V., Wiley R.C., *Effect of low-temperature phase changes on the mechanical properties of alloys near composition TiNi*. Journal of Applied Physics, **34**, 1475, 1963.

Bundy F.P., *Formation of New Materials and Structures by High-Pressure Treatment. Irreversible Effects of High Pressure and Temperature on Materials*. ASTM, Special technical publication, **374**, p52, 1965.

Burgers W.G., *on the process of transition of the cubic-body-centered modification into the hexagonal-close-packed modification of ziroconium*. Physica, **1**, p561, 1934.

Castany P., Pettinari-Sturmel F., Douin J., Coujou A., *In situ transmission electron microscopy deformation of the titanium alloy Ti–6Al–4V: Interface behavior*, Materials Science and Engineering A, 483-484, p719, 2008.

Castany P., Besse M., Gloriant T., *Dislocation mobility in gum metal β-titanium alloy studied via in situ transmission electron microscopy*, Physical Review B **84**, p020201, 2011.

Chai Y.W., Kim H.Y., Hosoda H., Miyazaki S., *Self-accommodation in Ti-Nb shape memory alloys*. Acta Materialia, **57**, p4054, 2009.

Chang L.C., Read T.A., *Plastic deformation and diffusionless phase changes in metals—the gold–cadmium beta phase*. AIME Transactions, **189**, p47, 1951.

Chopra I., *Review of state of art of smart structures and integrated systems.* AIAA Journal, **40**, 2145, 2002.

Collings E.W., *Anomalous electrical resistivity, bcc phase stability, and superconductivity in Titanium-Vanadium alloys*, Physical review B, **9**, p3989, 1974.

Collings E.W., *The metal physics of titanium alloys.* Titanium ’80 Science and Technology, **13**, p77, 1980.

Collings E.W., *The Physical Metallurgy of Titanium Alloys*. American Society for Metals, Metals Park, OH, 1984.

Cui J.P., Hao Y.L., Li S.J., Sui M.L., Li S.X., Yang R.. *Reversible movement of homogeneously nucleated dislocations in a β-titanium alloy*. Physical Review Letters, **102**, p045503, 2009.

Cui T.C., Li S.J., Hao Y.L., Yang R., *Effects of heat treatments on microstructure and mechanical properties of cold-rolled Ti2448 alloy*. Chinese Journal of Materials Research, **22**, p225, 2008.

Ping D.H., Cui C.Y., Yin F.X., Yamabe-Mitarai Y., *TEM investigations on martensite in a Ti-Nb-based shape memory alloy*, Scripta Materialia, **54**, p1305, 2006.

Dammak H., *Study of the irradiation induced α-ω phase transformation in titanium: kinetics and mechanism*. Philosophical Magazine A, **79**, p147, 1999

Dey G.K., Tewari R., Banerjee S., Jyoti G., Gupta S.C., Joshi K.D., Sikka S.K.. *Formation of a shock deformation induced omega phase in Zr20Nb alloy*. Acta materiallia, **52**, p5243, 2004.

Dobromyslov A.V., Dolgikh G.V., Dutkevich Ya., Trenogina T.L., *Phase and Structural Transformations in Ti–Ta Alloy*s. The Physics of Metals and Metallography, **107**, p502, 2009.

Duerig T.W., Terlinde G.T., Williams J.C., *The omega phase reaction in titanium alloys*. Titanium’80 Science & Technology - Proceedings of the 4th International Conference on Titanium, **2**, p1299, 1980.

Duerig T.W., Albrecht J., Richter D., Fischer P., *Formation and Reversion of Stress Induced Martensite in Ti-10V-2Fe-3Al*. Acta Metallurgica, **30**, p2161, 1982.

Duerig T.W., *Some unsolved aspects of Nitinol.* Materials Science and Engineering A, Proceedings of the International Conference on Martensitic Transformations, **438-440**, p69, 2006

Fontaine D.de., *Simple models for the omega phase transformation*, Metallurgical Transaction A, **19**, p169, 1988.

Frost P.D., Parris W.H., Hirsch L.I., Doing J.R., Schwartz C.M., *This isothermal transformation of titanium-chromium alloys*. Transactions of the American Society for Metals, **46**, p231, 1954.

Fukui Y., Inamura T., Hosoda H., Wakashima K., Miyazaki S., *Mechanical Properties of a Ti-Nb-Al Shape Memory Alloy*, Materials Transactions, **45**, p1077 , 2004.

Furuta T., Kuramoto S., Hwang J., Nishino K., Saito T., *Elastic deformation behavior of Multi-functional Ti-Nb-Ta-Zr-O alloys*. Materials Transactions, **46**, p3001, 2005.

Geetha M., Singh A.K., Asokamani R., Gogia A.K., *Ti based biomaterials, the ultimate choice for orthopaedic implants-A review*. Progress in Materials Science, **54**, p397, 2009.

Gloriant T., Texier G., Sun F., Thibon I., Prima F., Soubeyroux J.L., *Characterization of nanophase precipitation in a metastable $\beta$ titanium-based alloy by electrical resistivity, dilatometry and neutron diffraction*. Scripta Materialia, **58**, p271, 2008.

Guo W.Y., Xing H., Sun J., Li X.L., Wu J.S., Chen R.. *Elovlution of microstructure and texture during recrystallization of the cold-swaged Ti-Nb-Ta-Zr-O alloy*. Metallurgical and materials transaction A, **39**, p672, 2008.

Guo Z., Fu J., Zhang Y.Q., Hu Y.Y., Wu Z.G., Shi L., Sha M., Li S.J., Hao Y.L., Yang R., *Early effect of Ti-24Nb-4Zr-7.9Sn intramedullary nails on fractured bone*. Materials Science and Engineering C, **29**, p963, 2009.

Gutkin M.Y., Ishizaki T., Kuramoto S., Ovid’ko I.A., *Nanodisturbances in deformed gum metal*.

Acta Materialia, **54**, p2489, 2006.

Gutkin M.Y., Ishizaki T., Kuramoto S., Ovid'ko I.A., Skib N.V., *Giant faults in deformed gum metal*. International Journal of Plasticity, **24**, p1333, 2008.

Hao Y.L., Li S.J., Sun S.Y., Zheng C.Y., Hu Q.M., Yang R., *Super-elastic titanium alloy with unstable plastic deformation*. Applical Physics Letters, **87**, p091906, 2005.

Hao Y.L., Li S.J., Sun S.Y., Yang R., *Effect of Zr and Sn on Young's modulus and superelasticity of Ti-Nb-based alloys*, Materials Science and Engineering A, **441**, p112 , 2006.

Hao Y.L., Li S.J., Sun B.B., Sui M.L., Yang R., *Ductile titanium alloy with low Poisson's ratio*, Physical Review Letter, **98**, p216405, 2007a.

Hao Y.L., Li S.J., Sun S.Y., Zheng C.Y., Yang R., *Elastic deformation behaviour of Ti-24Nb-4Zr-7.9Sn for biomedical applications*, Acta Biomaterial, **3**, p277, 2007b.

Hao Y.L., Zhang Z.B., Li S.J., Yang R., *Microstructure and mechanical behavior of a Ti-24Nb-4Zr-8Sn alloy processed by warm swaging and warm rolling*. Acta Materialia, **60**, p2169, 2012.

Hermawan H., Ramdan D., Djuansjah Joy R. P., *Metals for Biomedical Applications, Biomedical Engineering - From Theory to Applications*, publisher: In Tech, August 29, p411, 2011.

Hosoda H., Kinoshita Y., Fukui Y., Inamura T., Wakashima K., Kim H.Y., Miyazaki S., *Effects of short time heat treatment on superelastic properties of a Ti-Nb-Al biomedical shape memory alloy*. Materials Science and Engineering A, **438-440**, p870, 2006.

Huiskers R., Weinans H., Rietbergen B. Van., *The relationship between stress shielding and bone resorption around total hip stems and the affects of flexible materials.* Clinical Orthopaedics Related Research, **274**, p124, 1992.

Hwang J., Kuramoto S., Furuta T., Nishino K., Saito T., *Phase-stability dependence of plastic deformation behavior in Ti-Nb-Ta-Zr-O alloys*. Journal of Materials Engineering and Performance, **14**, p747, 2005.

Ikehata H., Nagasako N., Furuta T., Fukumoto A., Miwa K., Saito T., *First-principles calculations for development of low elastic modulus Ti alloys*. Physical Review B, **70**, p174113, 2004.

Inamura T., Kim J.I., Kim H.Y., Hosoda H., Wakashima K.. Miyazaki S., *Composition dependent crystallography of a″-martensite in Ti-Nb-based β-titanium alloy.* Philosophical Magazine, **87**, p3325, 2007.

Inamura T., Yamamoto Y., Hosoda H., Kim H.Y., Miyazaki S., *Crystallographic orientation and stress-amplitude dependence of damping in the martensite phase in textured Ti-Nb-Al shape memory alloy*. Acta Materialia , **58**, p2535, 2010.

Jamieson J.C., *Crystal Structures of Titanium, Zirconium, and Hafnium at high pressures*. Science, **140**, p72, 1963.

Kauffman B.G., Mayo I., *The Story of Nitinol: The Serendipitous Discovery of the Memory Metal and Its Applications*. The Chemical Educator, **2**, p1, 1997.

Kim H.Y., Satoru H., Kim J.I., Hosoda H., Miyazaki S., *Mechanical properties and shape memory behavior of Ti-Nb alloys*. Materials Transaction, **45**, p2443, 2004.

Kim J.I., Kim H.Y., Hosoda H., Miyazaki S., *Shape Memory Behavior of Ti-22Nb-(0.5-2.0)O(at%) Biomedical Alloys*. Materials Transactions, **46**, p852, 2005.

Kim H.Y., Ikehara Y., KIM J.I., Hosoda H., Miyazaki S., *Martensitic transformation, shape memory effect and superelasticity of Ti – Nb binary alloys*. Acta Materialia, **54**, p2419, 2006.

Kim H.Y., Wei L., Kobayashi S., Tahara M., Miyazak S., *Nanodomain structure and its effect on abnormal thermal expansion behavior of a Ti-23Nb-2Zr-0.7TA-1.2O alloy*. Acta Materialia, **61**, p4874, 2013.

Kuan T.S., Ahrens R.R., Sass S.L., *The stress induced omega phase transformation in Ti-V alloys*. Metallurgical Transaction A, **6**, p1767, 1975.

Kuramoto S., Furuta T. , Hwang J.H., Nishino K., Saito T., *Elastic properties of gum metal*. Materials Science and Engineering A, **442**, p454, 2006a.

Kuramoto S., Furuta T., Hwang J.H., Nishino K., Saito T., *Plastic deformation in a multifunctional Ti-Nb-Ta-Zr-O alloy*. Metallurgical and Materials Transactions A, **37**, p657662, 2006b.

Kurtz S., Ong K., Lau E., Mowat F., Halpern M., *Projections of primary and revision hip and knee arthroplasty in the United States from 2005 to 2030.* The Journal of Bone and Joint Surgery, **89**, p780, 2007.

Kutsar A.R., German V.N., Nosova, G.I. *The $\alpha$-$\omega$ transformation in titanium and zirconium in shock waves.* Doklady AN SSR, **213**, p81, 1973.

Li S.J., Cui T.C., Li Y.L., Hao Y.L., Yang R., *Ultrafine-grained $\beta$-type titanium alloy with nonlinear elasticity and high ductility*. Applied Physics Letters, **92**, p043128 2008.

Li S.J., Jia M.T., Prima F., Hao Y.L., Yang R., *Improvements in nonlinear elasticity and strength by grain refinement in a titanium alloy with high oxygen content*. Scripta Materialia, **64**, p1015, 2011.

Li T., Morris J.W., Nagasako N., Kuramoto S., Chrzan D.C., *“Ideal” engineering alloys*, Physical Review Letters, **98**, p105503, 2007.

Liu J.P., Wang Y.D., Hao Y.L., Wang Y.Z., Nie Z.H., Wang D., Ren Y., Lu Z.P., Wang J.G., Wang H.L., Hui X.D., Lu N., Kim M.J., Yang R., *New Intrinsic Mechanism on Gum-Like Superelasticity of Multifunctional Alloys*, Scientific Reports, **3**, p2156. 2103.

Long M., Rack H.J., *Titanium alloys in total joint replacement-a materials science perspective*. Biomaterials, **19**, p1621, 1998.

Lütjering G., *Influence of processing on microstructure and mechanical properties of ($\alpha$+$\beta$) titanium alloys.* Materials Science and Engineering A, **243**, p32, 1998.

Lütjering G., Williams J.C., *Titanium (Engineering Materials and Processes)*, Second ed., Springer, Berlin, p15, 2007.

Maraldi M., Molari L., Grandi D., *A unified thermodynamic framework for the modelling of diffusive and displacive phase transitions*. International Journal of Engineering Science, **50**, p31, 2012.

Miyazaki S., Kim H.Y., Hosoda H., *Development and characterization of Ni-free Ti-base shape memory and superelastic alloys*, Materials Science and Engineering A, **438-440**, p18, 2006

Moffat D.L., Larbeliestier D.C., *The competition between martensite and omega in quenched Ti-Nb alloys*. Metallurgical Transactions A, **19**, p1677, 1988.

Mornirolli J.P., Gantois M., *Etude des conditions de formation de la phase omega dans les alliages titane-niobium et titane-molybdène*, Mémoires Scientifiques de la Revue de Métallugie, **11**, 1973.

Morris Jr J.W., Hanlumyuang Y., Sherburne M., Withey E., Chrzan D.C., Kuramoto S., Hayashi Y., Hara M., *Anomalous transformation-induced deformation in <110> textured gum metal*. Acta Materialia, **58**, p3271, 2010.

Murray J. L., *Phase Diagram of Binary Titanium Alloys*, ASM, Metals Park, Ohio, 1987, p88, 1987.

Nag S., Banerjee R., Fraser H.L., *Microstructural evolution and strengthening mechanisms in Ti-Nb-Zr-Ta, Ti-Mo-Zr-Fe and Ti-15Mo biocompatible alloys*. Materials Science and Engineering C, **25**, p357, 2005.

Newkirk J.B., Geisler A.H., *crystallographic aspects of the beta to alpha transformation in titanium*. Acta Metallurgica, **1**, p370, 1953.

Nii Y., Arima T., Kim H.Y., Miyazaki S, *Effect of randomness on ferroelastic transitions: Disorder-induced hysteresis loop rounding in Ti-Nb-O martensitic alloy*. Physical Review B, **82**, p214104, 2010.

Niinomi M., *Recent Metallic Materials for Biomedical Applications*. Metallurgical and Materials Transactions A, **33**, p477, 2002.

Niinomi M., *Fatigue performance and cyto-toxicity of low rigidity titanium alloy, Ti-29Nb-13Ta-4.6Zr*. Biomaterials, **24**, p2673, 2003a.

Niinomi M., *Recent research and development in titanium alloys for biomedical applications and healthcare*. Science and Technology of Advanced Materials, **4**, p445, 2003b.

Ölander A., *An electrochemical investigation of solid cadmium-gold alloys.* Journal of the American Chemical Society, **54**, p3819, 1932.

Ouchi C., Iizumi H., Mitao S., *Effect of ultra-high purification and addition of interstitial elements on properties of pure titanium and titanium alloy*. Materials Science and Engineering A, **243**, p186,1998.

Petry W., Heiming A., Trampenau J., Alba M., Herzig C., Schober H. R., Vogl G., *Phonon dispersion of the bcc phase of group IV metals. I. bcc titanium*. Physical Review B, **43**, p10933, 1991.

Prima F., Vermaut P., Ansel D., Debuigne J.. *ω precipitation in a beta metastable titanium alloy*, resistometric study. Materials Transactions, JIM, **41**, p1392, 2000.

Qazi J.I., Marquardt B., Allard L.F., Rack H.J., *Phase transformations in Ti-35Nb-7Zr-5Ta-(0.06-0.68)O alloys*. Materials Science and Engineering C, **25**, p389, 2005.

Ramarolahy A., Castany P., Prima, F. Laheurte P., Péron I., Gloriant T., *Microstructure and mechanical behavior of superelastic Ti-24Nb-0.5O and Ti-24Nb-0.5N biomedical alloys*. Journal of the mechanical behavior of biomedical materials, **9**, p83, 2012.

Roy R., *A syncretist classification of phase transitions*. Proceedings of the Conference on Phase Transitions and Their Applications in Materials Science, University Park, Pennsylvania, May 23-25, p13, 1973.

S. Banerjee, R. Tewari, and G. K. Dey (2006). *Omega phase transformation- morphologies and mechanisms*. International Journal of Materials Research, **97**, p963, 2006.

Saito T., Furuta T., Hwang J.H., Nishino K., Kuramoto S., Suzuki N., et al. *Multifunctional Alloys Obtained via a Dislocation-Free Plastic Deformation Mechanism*. Science, **300**, p464, 2003.

San-Martin A., Manchester F.D., *The H-Ti (Hydrogen-Titanium) System*. Bulletin of Alloy Phase Diagrams, **8**, p30, 1987.

Semiatin S.L., Seetharaman V., Weiss I., *The thermomechanical processing of alpha/beta titanium alloys*. JOM, **49**, p33, 1997.

Sikka S.K., Vohra Y.K., Chidambaram R., *Omega phase in materials*. Progress in materials science, **27**, p245, 1982.

Silcock J.M., *An X-ray examination of the omega phase in TiV, TiMo and TiCr alloys*. Acta Metallurgica, **6**, p481, 1958.

Stöckel D., *The shape memory effect, phenomenon, alloys*. Proceedings: Shape Memory Alloys for Power Systems EPRI, p1, 1995.

Surin H.B.V., *Stress shielding effect of the shaft component*, Available at: http://www.bananarepublican.info/Stress_shielding.htm, 2005.

Tahara M., Kim H.Y., Inamura T., Hosoda H., Miyazaki S., *Lattice modulation and superelasticity in oxygen –added β-Ti alloys*. Acta Materialia, **59**, p6208, 2011.

Talling R.J., Dashwood R.J., Jackson M., Kuramoto S., Dye D., *Determination of (C11-C12) in Ti-36Nb-2Ta-3Zr-0.3O (wt.%) (Gum metal)*. Scripta Materialia, **59**, p669, 2008.

Talling R.J., Dashwood R.J., Jackson M., Dye D., *On the mechanism of superelasticity in gum metal*. Acta Materialia, **57**, p1188, 2009.

Tane M., Nakano T., Hagihara K., Umakoshi Y., Niinomi M., Nakajima H., *Peculiar elastic behavior of Ti-Nb-Ta-Zr single crystals*. Acta Materialia, **56**, p2856, 2008.

Tao X.J., Li S.J., Zheng C.Y., Fu J., Guo Z., Hao Y.L., Guo Z.X., *Synthesis of a porous oxide layer on a multifunctional biomedical titanium by micro-arc oxidation*, Materials Science and Engineering C, **29**, p1923, 2009.

Wan Z., Dorr L. D., Woodsome, T. Ranawat A., Song M., *Effect of stem stiffness and bone stiffness on bone remodeling in cemented total hip replacement*. The Journal of Arthroplasty, **14**, p149, 1999.

Wanhill R., Barter S., *Fatigue of beta processed and beta Heat-treated titanium alloys*. Springer Briefs in Applied Sciences and Technology, p5, 2012.

Weiss I., Semiatin S.L., *Thermomechanical processing of beta titanium alloys—an overview*. Materials Science and Engineering A, **243**, p46, 1998.

Williams A.J., Cahn R.W., Barrett C.S., *The crystallography of the β-α transformation in titanium.* Acta Metallurgica, **2**, p117, 1954.

Williams D.F., *Definitions in biomaterials*. Proceedings of a consensus conference of the European society for biomaterials, Vol. 4. Chester, England, March 3-5 1986. New York: Elsevier, 1987.

Withey E.A., Minor A.M., Chrzan D.C., Morris Jr. J.W., Kuramoto S., *The deformation of gum metal through in situ compression of nanopillars*. Acta Materialia **58**, p2652, 2010.

Wortman J.J., Evans R.A., *Young's Modulus, Shear Modulus, and Poisson's Ratio in Silicon and Germanium*. Journal of Applied Physics, **36**, p153, 1965.

Xing H., Sun J., *Mechanical twinning and omega transition by 111{112} shear in metastable β titanium alloy*. Applied Physics Letters, **93**, p031908, 2008a.

Xing H., Sun J., Yao Q., Guo W.Y., Chen R., *Origin of substantial plastic deformation in Gum metals*. Applied Physical Letters, **92**, p151905 , 2008b.

Yang R., Hao Y.L., Li S.J., *Development and Application of Low-Modulus Biomedical Titanium Alloy Ti2448*. Metals for Biomedical Applications, Biomedical Engineering - Trends in Materials Science, publisher: In Tech, January 08, p225, 2011.

Yang Y., Li G.P., Cheng G.M., Wang H., Zhang M., Xu F., Yang K., *Stress-introduced α″ martensite and twinning in a multifunctional titanium alloy*. Scripta Materialia, **58**, p9 , 2008.

Yang Y., Wu S.Q., Li G.P., Lu Y.F., Yang K., Ge P., *Evolution of deformation mechanisms of Ti-22.4Nb-0.73Ta-2Zr-1.34O alloy during straining*. Acta Materialia, **58**, 2778, 2010.

Zener C., *Contribution to the theory of beta-phase alloys*. Physical Review, **71**, p846, 1947.

Zhang Y.W., *Elastic and plastic deformation of Ti2448 single crystals*, Doctorate Dissertation, Institute of Metal Research, Chinese Academy of Sciences, Shenyang, 2010a.

Zhang S.Q., Investigation of fatigue behavior of Ti2448 alloy, Doctorate Dissertation, Institute of Metal Research, Chinese Academy of Sciences, Shenyang, 2010b.

Zhang Y.W., Li S.J., Obbard E.G., Wang H., Wang S.C., Hao Y.L., Yang R., *Elastic properties of Ti-24Nb-4Zr-8Sn single crystals with bcc crystal structure*. Acta Materialia, **59**, p3081, 2011a.

Zhang S.Q., Li S.J., Jia M.T., Prima F., Chen L.J., Hao Y.L., Yang R.. *Low-cycle fatigue properties of a titanium alloy exhibiting nonlinear elastic deformation behavior*. Acta Materialia, **59**, p4690, 2011b

Zhang Z.B., *The preparation and fatigue properties of ultrafine grained Ti2448 alloy*, Maser

Dissertation, Institute of Metal Research, Chinese Academy of Sciences, Shenyang, 2011c.

Zheng C., *An investigation on the biocompatibility of Ti-24Nb-4Zr-8Sn alloy*, Ph.D. Thesis, Institute of Metal Research, Chinese Academy of Sciences, Shenyang , 2009.

Zheng C.Y., Li S.J., Tao X.J., Hao Y.L., Yang R., *Calcium phosphate coating of Ti-Nb-Zr-Sn titanium alloy*. Materials Science and Engineering C, **27**, p824, 2007.

# Chapter II: Material and methods

# 1. Material and preparation of samples

A hot-forged cylinder of Ti-24Nb-4Zr-8Sn (wt.%) alloy with diameter of 55 mm was used as raw material in this work. The chemical composition of the alloy is given in Table 2-1.

**Table 2-1** Chemical composition of hot forged Ti2448 (wt.%).

| Nb | Zr | Sn | O | Ti |
|---|---|---|---|---|
| 23.9 | 4.05 | 8.22 | 0.16 | Bal. |

Hot-forged slice-cut samples were directly multi-pass cold rolled without intermediate annealing to reach the final thickness of 0.5 mm. According to different initial thicknesses of the samples used, three reduction rates calculated using the equation as follows, were obtained: 40% (moderate), 80% (intermediate) and 94% (high).

$$\tau = \frac{(e_{initial} - e_{final})}{e_{initial}} \times 100\%$$

For each reduction rate, two thermal treatments were performed: on the one hand, cold rolled specimens were solution treated under high vacuum at 900 ℃ for 30 minutes followed by water quenching (solution treated state, ST); on the other hand, cold rolled specimens were thermally “flash treated” at 700 °C for 3 minutes followed by air cooling (flash treated state, FT). The two different thermo-mechanical processing routes of the as-hot forged Ti2448 alloy are shown in Fig. 2-1. And the solution treatment was carried out on the vacuum furnace shown in Fig. 2-2 (*Besse 2010*).

After thermal treatments, all samples were cleaned in an acid solution made of 50% HF and 50% HNO3 (in volume) to remove any oxidation layer. Each sample is labeled as CR*XX*%-ST and CR*XX*%-FT depending if a solution treatment (ST) or a flash thermal treatment (FT) was performed and where *XX*% mentions the applied cold rolling reduction rate.

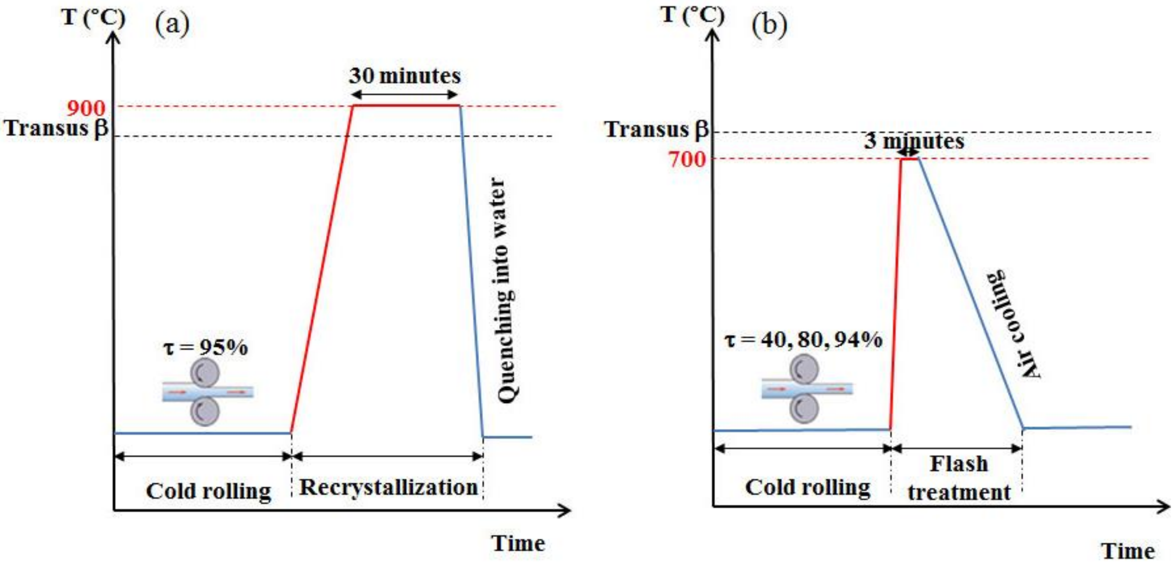
T (°C)
(a)
30 minutes
900
Transus β
Quenching into water
τ = 95%
Cold rolling
Recrystallization
Time
T (°C)
(b)
Transus β
3 minutes
700
τ = 40, 80, 94%
Air cooling
Cold rolling
Flash treatment
Time

**Fig. 2-1** The two different thermo-mechanical processing routes of the as-hot forged Ti2448 alloy (a) ST and (b) FT

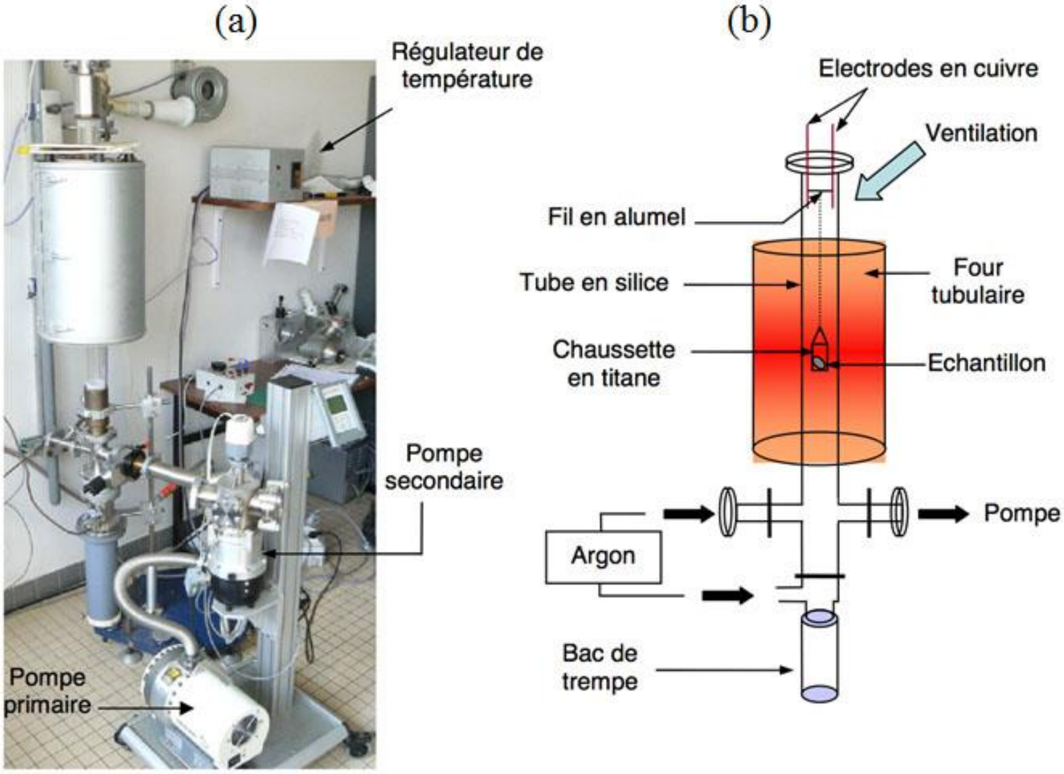
(a)
Régulateur de température
Pompe secondaire
Pompe primaire
(b)
Electrodes en cuivre
Ventilation
Fil en alumel
Tube en silice
Four tubulaire
Chaussette en titane
Echantillon
Argon
Pompe
Bac de trempe

**Fig. 2-2** The vacuum furnace for solution treatment (a) the photograph and (b) schematic one (*Besse 2010*).

# 2. Mechanical tests

## 2.1 Conventional tensile tests

Mechanical properties were estimated by conventional tensile tests with a strain rate of $10^{-4}$ $s^{-1}$ on an INSTRON 3369 tensile machine that is shown in Fig. 2-3. Normalized flat tensile specimens with 3mm×15mm×0.5mm gauge dimensions were used (Fig. 2-4). The tensile direction was chosen parallel to the rolling direction. An extensometer indicated particularly in Fig. 2-3 was used to ensure the accuracy of real strain.

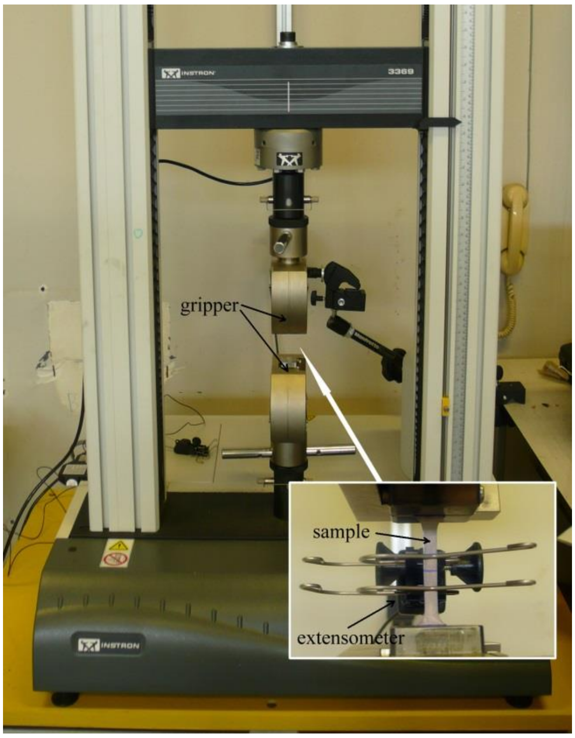
INSTRON
3369
gripper
sample
extensometer
INSTRON

**Fig. 2-3** Tensile test machine (INSTRON 3369) (*Sun 2009*).

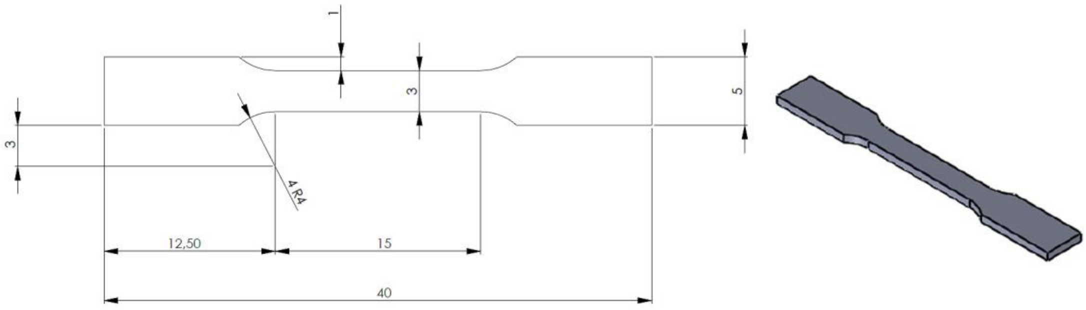
1
3
5
3
4 R4
12,50
15
40

**Fig. 2-4** The gauged dimensions of the specimens for tensile test (*Bertrand 2011*).

## 2.2 Cyclic tensile tests

The superelasticity was characterized by cyclic loading-unloading tensile tests on the INSTRON 3369 tensile machine with the same strain rate of $10^{-4}$ $s^{-1}$: the strain was increased by steps of 0.5% until an elongation of 5% and each step was followed by a total release of the stress. The tensile direction of the specimens was also chosen parallel to the rolling direction. The tensile specimens used have the same shape described in the previous paragraph.

The superelasticity is evaluated by the value of recoverable strain on every cycle of cyclic tensile tests. Fig. 2-5 displays the schematic of one cycle on a cyclic tensile curve. According to the Fig. 2-5, different strains, which compose the total applied strain, can be measured (*Grosdidier 2000*). The $\varepsilon_{res}$, $\varepsilon_{se}$, $\varepsilon_{e}$ and $\varepsilon_{rec}$ represent the residual strain, the superelastic strain due to the SIM transformation, the elastic strain and the total recoverable strain, respectively. Therefore, the recoverable strain used to characterize the superelasticity at any applied strain is the sum of pure elastic strain and superelastic strain.

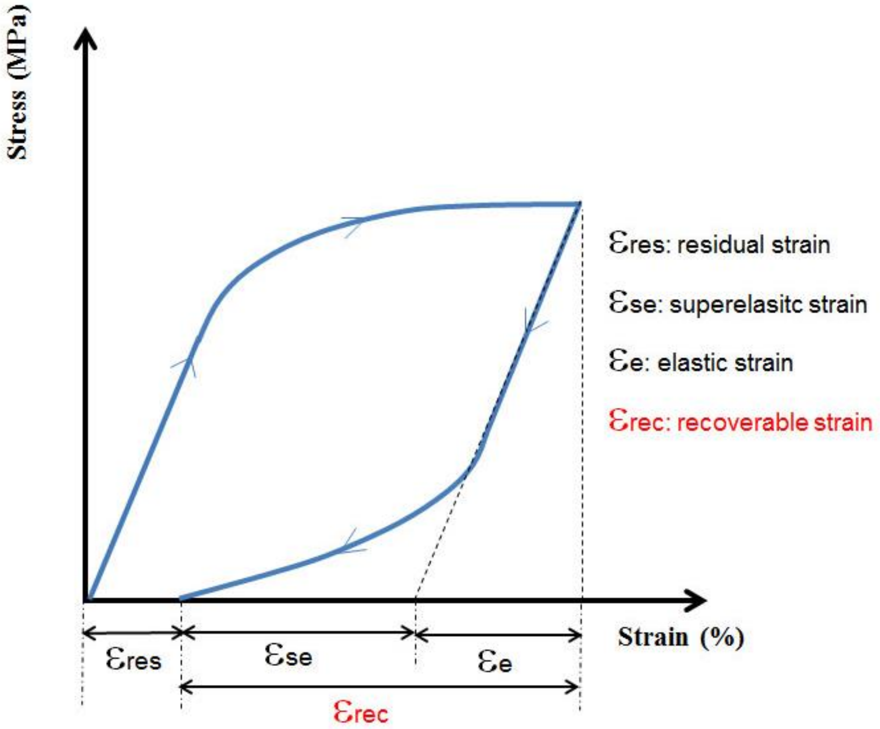

**Fig. 2-5** Illustration of one cycle on a cyclic tensile curve to interpret different strains.

# 3. Microstructural characterizations

## 3.1 Optical microscopy

In order to observe microstructure, the specimens were mechanically prepared and finally polished with colloidal silica suspension. And then each specimen was etched by a solution composed of 8% HF, 15% $HNO_3$ and 77% $H_2O$ to reveal the microstructure and finally observed by an optical Leica microscope.

*In situ* optical microstructural observation under tensile test was conducted on a CSM machine equipped with an optical microscope. The sample with 3mm×15mm×0.5mm gauge dimensions was polished to a “mirror” condition and strained with a $10^{-1}$ $s^{-1}$ rate.

## 3.2 X-ray diffraction

The principle of X-ray diffraction is based on Bragg’s law:

$$2d_{hkl}\sin\theta = n\lambda$$

Where the variable $d_{hkl}$ is the distance between parallel atomic layers in a crystal, the variable $\theta$ is the angle between the incident beam and the diffracting atomic planes, the variable $\lambda$ is the wavelength of the incident X-ray beam and $n$ is an integer. This law expresses a X-ray wave interference phenomenon, commonly known as X-ray diffraction (XRD), and is a direct evidence for the periodic atomic structure of crystals.

In the present work, the XRD was done on a Philips PW3710 system with Cu-$K_{\alpha1}$ radiation ($\lambda$ = 0.154060 nm) shown in Fig. 2-6. Through identification of position for each reflection peak, the phase composition in the Ti2448 alloy can be known.

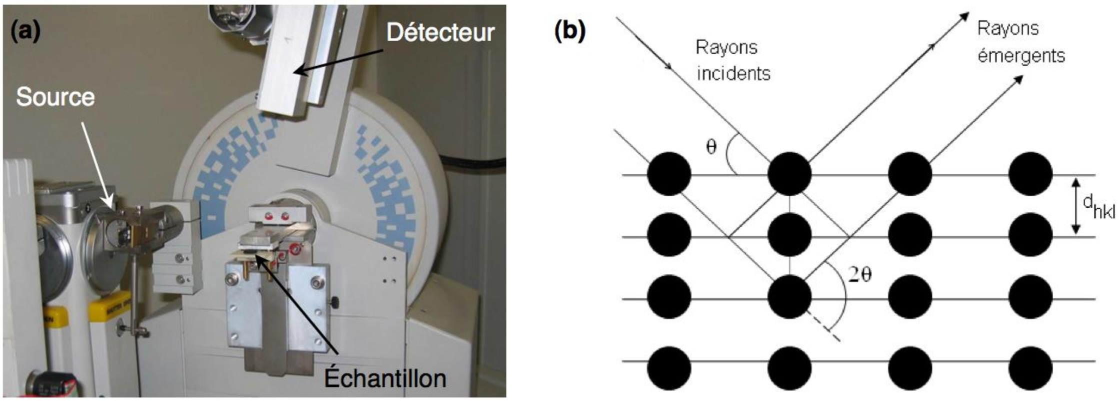

**Fig. 2-6** (a) The powder diffractometer Philips PW3710 system and (b) the schematic explanation of the principle for XRD (*Besse 2010*).

## 3.3 Crystallographic texture

### 3.3.1 Definition of crystallographic texture

In a polycrystalline material, the crystallographic orientation of the grains can be distributed randomly with respect to each other, or they can be oriented to a certain preferential direction. If there is a preferred orientation, then we say that the material has a *crystallographic texture*. There are several ways for representing texture, like pole figure (PF), inverse pole figure (IPF) and orientation distribution function (ODF), those can be transformed mutually into another.

The basic one is the pole figure illustrated in Fig. 2-7. As shown on this figure, a pole figure is simply a stereogram with its axes defined by an external frame of reference with particular *hkl* poles plotted onto it from all of the crystallites in the polycrystalline (*ToiTPoMS 2009*). Typically, the external frame is defined by the normal direction, the rolling direction, and the transverse direction in a sheet (ND, RD and TD respectively). A pole figure for a polycrystalline aggregate shows completely random orientation, while if the material shows a degree of texture, the resultant pole figure will show an accumulation of poles at specific directions.

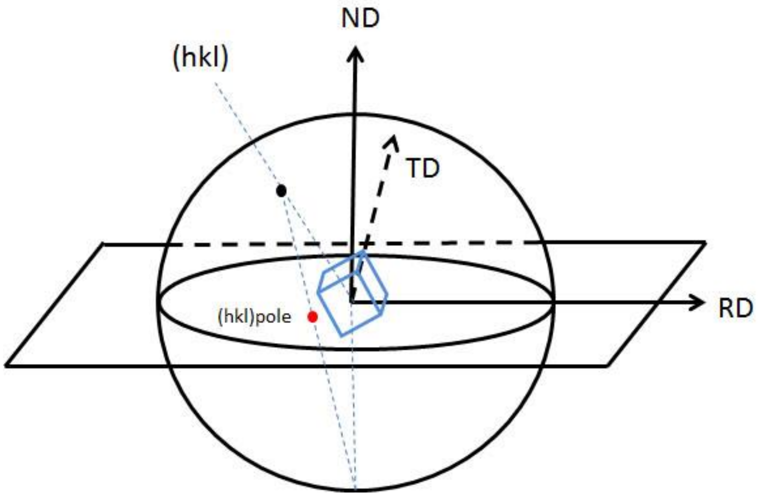

**Fig. 2-7** Schematic illustration of (hkl) pole figure

Instead of PF plotting crystal orientations with respect to an external frame of reference, IPF can be produced which show the RD, TD and ND with respect to the crystallographic axes. Differently from both PF and IPF, the ODF describes the crystal orientation relative to the Euler space ($\varphi_1$, $\phi$, $\varphi_2$). The different three Euler angles define the difference in orientation between the crystal axes and the external frame of reference axes. The ODFs are then constructed by combining the data from several pole figures via complex mathematics and could display the texture components in the Euler space.

In the present work, the texture will be presented with ODFs. Fig. 2-8a displays the Euler space containing important texture components and fibers for bcc alloys. It can be seen in Fig.2-8b, the main texture components lie in two lines in the section with a constant value of $\varphi_2$=45°, which are called α fiber (<110>//RD) and γ fiber (<111>//ND). Table 2-2 lists the primary fibers and their meanings in bcc metals and alloys (*Randle 2000*).

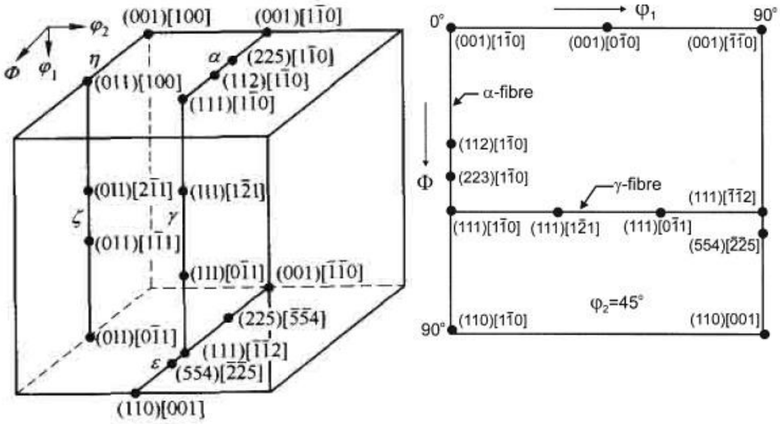
φ2
Φ
φ1
(001)[100]
(001)[11̄0]
η
α
(225)[11̄0]
(011)[100]
(112)[11̄0]
(111)[11̄0]
(011)[21̄1]
(111)[12̄1]
ζ
γ
(011)[1̄1̄1]
(111)[01̄1]
(001)[1̄1̄0]
(225)[5̄54]
(011)[01̄1]
(111)[1̄1̄2]
ε
(554)[2̄2̄5]
(110)[001]
0°
φ1
90°
(001)[11̄0]
(001)[01̄0]
(001)[1̄1̄0]
α-fibre
(112)[11̄0]
Φ
(223)[11̄0]
γ-fibre
(111)[1̄1̄2]
(111)[11̄0]
(111)[12̄1]
(111)[01̄1]
(554)[2̄2̄5]
φ2=45°
90°
(110)[11̄0]
(110)[001]

**Fig. 2-8** (a) Euler space and texture components for bcc alloys; (b) location of important texture components in the section of $\varphi_2$ =45°(*Randle 2000*).

**Table.2-2** Characteristic fibers in bcc metals and alloys.

| Fiber name | Fiber axis |
|---|---|
| α-fiber | <110> parallel to RD |
| γ-fiber | <111> parallel to ND |
| η-fiber | <001> parallel to RD |
| ζ-fiber | <011> parallel to ND |
| ε-fiber | <011> parallel to TD |
| θ-fiber | <001> parallel to ND |

### 3.3.2 Principle of texture measurement

The most common method of measuring texture uses X-ray diffraction with an apparatus known as a four-angle diffractometer or an *Eulerian cradle*. The source of X-rays and the detector are oriented so that a particular value of $2\theta$ is specified (Fig. 2-9). This allows for a single Bragg reflection to be measured. The stage of the cradle is tilted and rotated systematically, so that all angular orientations of the sample are investigated. When the specified lattice plane of a crystallite fulfils the Bragg's condition, the detector will record the reflection (*ToiTPoMS 2009*). For a polycrystalline material, the intensity of detected X-rays will increase when there are more crystallites in a specific orientation. The intensity for a given orientation is thus proportional to the volume fraction of crystallites with that specific orientation. Areas of high and low intensity suggest a preferred orientation, while constant intensity at all angles would occur in a random polycrystalline aggregate.

The X-rays diffractometer used to measure texture in the lab and the schematic *Eulerian cradle* are shown in Fig. 2-9. The step size used for the data acquisition is 5 ° for advancement of any axe. The ODFs were calculated with the raw data of the most important three pole figures (110), (200) and (211) after applying corrections for background and defocusing. Contoured plots of ODF were delineated for constant $\varphi_2$ sections in the volume of the reduced Euler space ($0^\circ < \varphi_1, \phi, \varphi_2 < 90^\circ$).

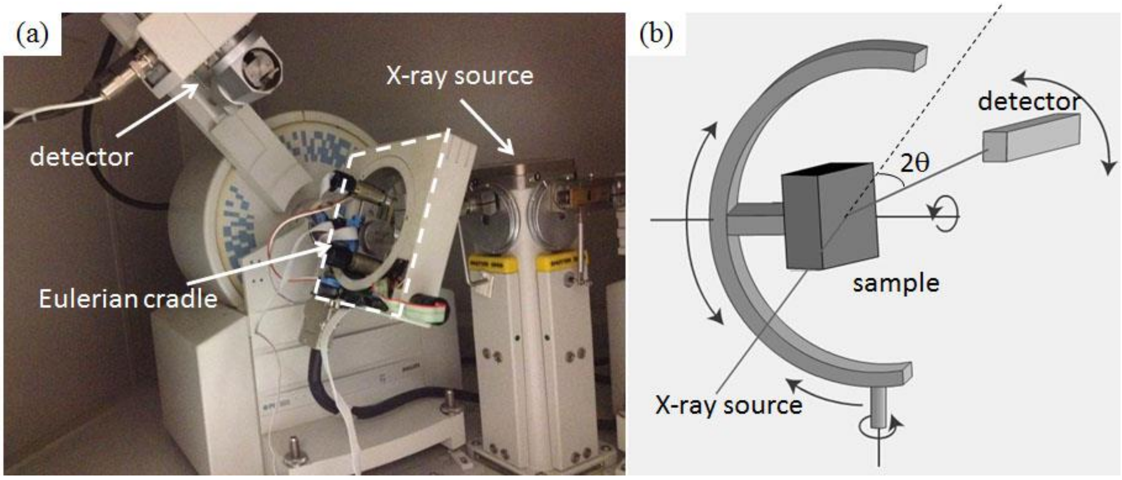

**Fig. 2-9** (a) The powder diffractometer for texture (Philips PW3710) and (b) schematic Eulerian cradle (*Wikimedia, 2006*).

## 3.4 Electron backscattered diffraction

An alternative method of texture determination is that of electron backscattered diffraction (EBSD) using a scanning electron microscope (SEM). Within a single grain, the electron beam is fixed at a point on the surface. At particular angles the beam is diffracted, so that there is a change in the intensity of the reflection measured. This leads to the formation of a *backscattered Kikuchi pattern* made up of *Kikuchi lines.* The location and symmetry of the backscattered Kikuchi pattern allows specific bands of Kikuchi lines to be indexed unambiguously. The indexed patterns are used to determine the orientation of the grain within typically an experimental error of ±2 ° (*ToiTPoMS 2009*).

In the present work, for the EBSD measurement, a flat and polished sample is placed in the scanning electron microscope chamber at a highly tilted angle (~70 ° from horizontal) to increase the contrast in the resultant electron backscattered diffraction pattern. Fig. 2-10 presents the schematic principle of formation of the Kikuchi lines in EBSD. Some of the electrons entering the sample backscatter and may escape. As these electrons leave the sample, they may exit at the Bragg’s condition related to the spacing of the periodic atomic lattice planes of the crystalline structure and diffract. These diffracted electrons can escape the material and are detected with a phosphor screen used to collect reflected data. The orientation at each pixel in the obtained image is then represented by a different color. Each colored pixel is defined by a single EBSD measurement. The colors can be separated into their red, green, and blue constituents by fractal analysis. The orientation of the crystal can be determined from the key. Each grain orientation is thus described with reference to an external frame of reference (*ToiTPoMS 2009*).

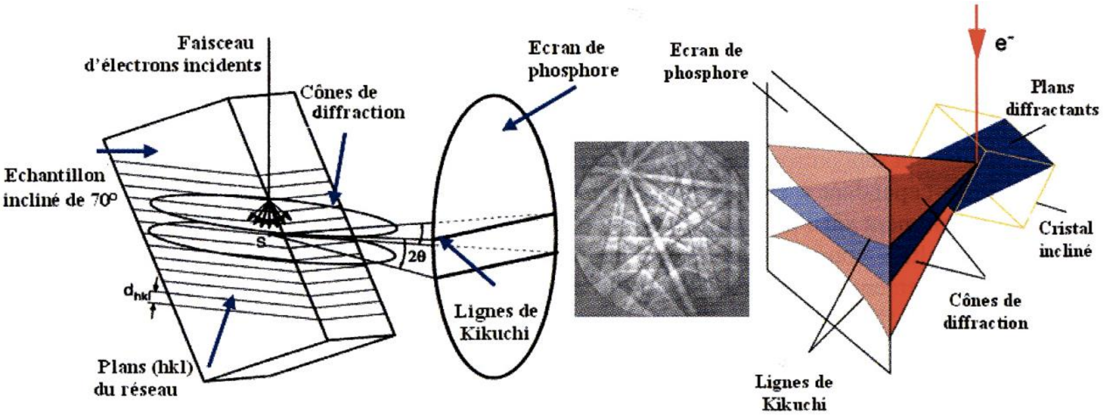
Faisceau
d'électrons incidents
Cônes de
diffraction
Echantillon
incliné de 70°
S
$d_{hkl}$
2θ
Plans (hkl)
du réseau
Ecran de
phosphore
Lignes de
Kikuchi
Ecran de
phosphore
e⁻
Plans
diffractants
Cristal
incliné
Cônes de
diffraction
Lignes de
Kikuchi

**Fig. 2-10** The principle of formation of the Kikuchi lines in EBSD technique (*Brisset 2008*).

## 3.5 Transmission electron microscopy

Transmission electron microscopy (TEM) observations were made using a JEOL 2100 microscope operating at 200kV. Thin foils for TEM were prepared by an electro-polishing technique in a solution of 6% perchloric acid and 94% methanol (vol.%). Disks of 3mm diameter were firstly mechanically cut and polished to a thickness of 150 μm, then twin-jet polished at 253-263K. Twin-jet polishing was stopped before perforation to leave a thickness of ~ 10μm. Final step of thinning was finished by ion milling with a Fischione 1010 Model.

## 4. *In situ* synchrotron X-ray diffraction

Synchrotron radiation is one of the brightest lights on earth. It is the single most powerful tool available to X-ray crystallographers and made of X-ray beams generated in large machines called synchrotrons. These machines accelerate electrically charged particles, often electrons, to nearly the speed of light, and then whip them around a huge, hollow metal ring. The largest component of each synchrotron is its electron storage ring. This ring is actually not a perfect circle, but a many-sided polygon. At each corner of the polygon, precisely aligned magnets bend the electron beam, forcing it to stay in the ring. Each time the electrons' path is bent, they emit bursts of energy in the form of electromagnetic radiation. Because particles in a synchrotron are hurtling at nearly the speed of light, they emit intense radiation, including lots of high-energy X-rays (*ESRF 2014*).

*In situ* synchrotron X-ray diffraction (SXRD) under cyclic tensile test was conducted on beam line ID31 at the European Synchrotron Radiation Facility (ESRF, Grenoble, France). The ID31 offers a high-resolution incident X-ray beam ($\lambda$=0.040002106nm). Nine-channel multi-analyzer installed as detectors are used to collect scanning data over the angular range 2-14 °, with a scanning step of 0.005 °. This in-situ cyclic tensile test under SXRD was realized on tensile specimen (gauge width of 3mm and a thickness of 0.5mm) with increments of 0.5% until 5.0% and then increments of 1.0% until 10%. SXRD scans were then obtained after each increment for both loading and unloading conditions. Fig. 2-11 shows the SXRD diffractometer on beam line ID31 at ESRF and schematic illustration of sample stage for in situ SXRD cyclic tensile test.

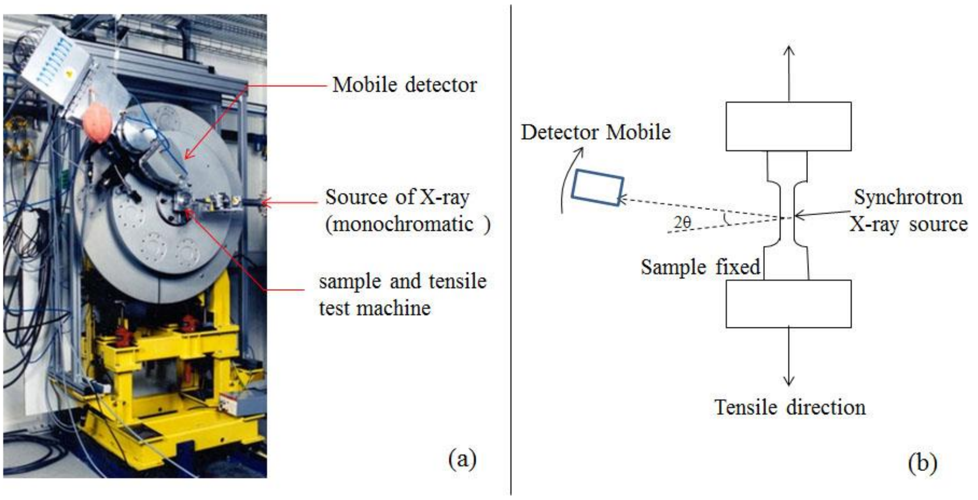

**Fig. 2-11** (a) The SXRD diffractometer on beam line 31 at ESRF and (b) schematic illustration of sample stage for *in situ* SXRD cyclic tensile test.

# 5. Dynamic mechanical analysis

## 5.1 Principle of dynamic mechanical analysis

The dynamic mechanical analysis (DMA) can be simply described as applying an oscillating force to a sample and analyzing the response of the material to that applied force. The DMA supplies an oscillatory force, causing a sinusoidal stress applied to the sample, which generates a sinusoidal strain. By measuring both the amplitude of the deformation at the peak of the sine wave and the lag between the stress and strain sine waves, quantities like the modulus, the viscosity and the damping can be calculated. Fig. 2-12a gives the schematic illustration of principle of DMA (*Menard 2008*).

The modulus measured in DMA is, however, not exactly the same as the Young's modulus of the classic stress–strain curve (Fig. 2-12b). Young's modulus is the slope of a stress–strain curve in the initial linear region, wheras in DMA, a complex modulus ($E^*$), an elastic modulus ($E'$), and an imaginary (loss) modulus ($E''$) are calculated from the material response to the sine wave. These different moduli allow better characterization of the material, because we can now examine the ability of the material to return or store energy ($E'$), to its ability to lose energy ($E''$), and the ratio of these effects (tan δ), which is called damping factor. All these relationships are shown in Fig. 2-12c.

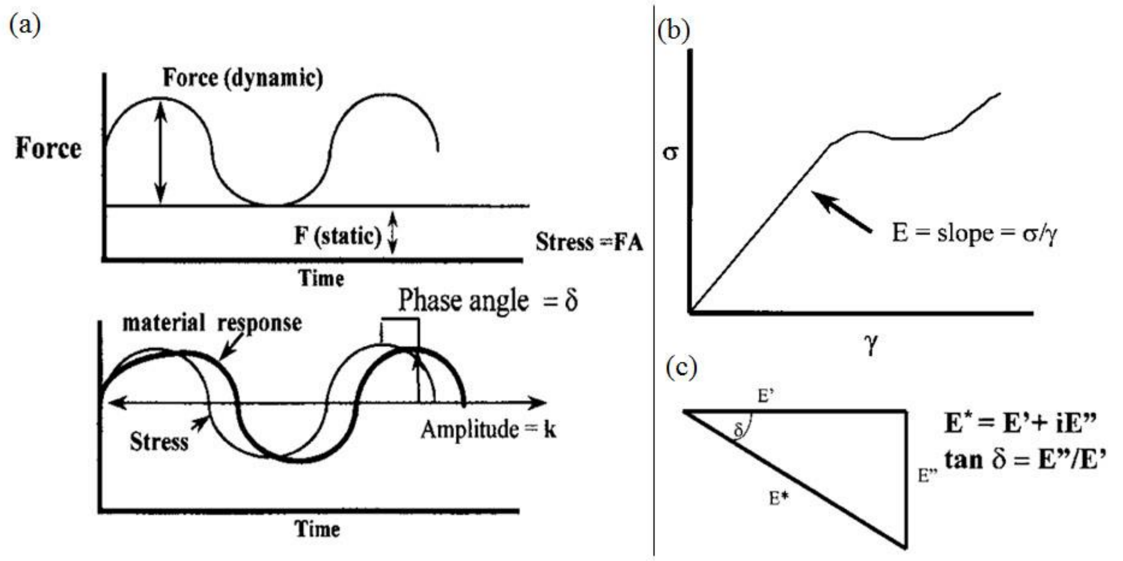

**Fig. 2-12** (a) The principle of dynamic mechanical analysis, (b) the measurement of Young's modulus on a classic stress–strain curve and (c) schematic illustration of relationships for DMA experiment (*Menard 2008*).

## 5.2 DMA tests

The DMA tests in the present work were done with a Metravib DMA50 machine in tensile mode shown in Fig. 2-13a. Samples for DMA (Fig. 2-13b) were cut with a low-speed diamond wire saw (Fig. 2-13c).

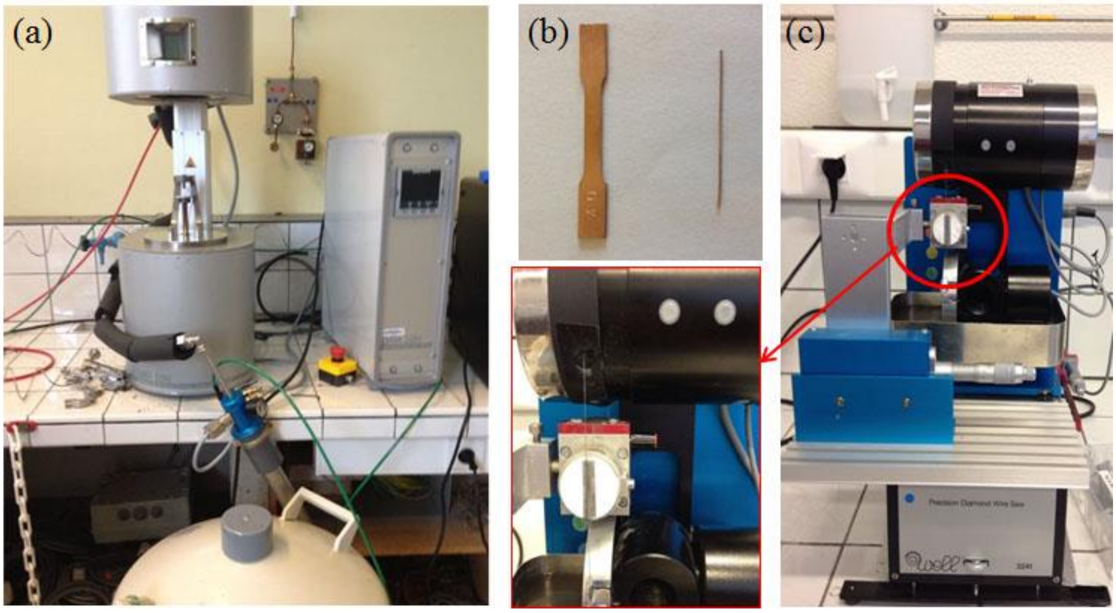

**Fig. 2-13** (a) The Metravib DMA50 machine, (b) the specific sample used for DMA test with comparison to the conventional tensile sample and (c) the low-speed diamond wire saw.

The thermal cycle was chosen between -150 ℃ and 50 ℃ with a rate of 5 ℃/min. The frequency of the sinusoidal dynamic mechanical solicitation is 1 Hz and the dynamic/static ratio for the applied stress was kept at $\sigma_{dyn}/\sigma_{stat}=1/4$. The tests were performed with the tensile direction parallel to the rolling direction for different static stress values: 120, 160, 200, 240 and 280MPa. Two important characteristic parameters of DMA: storage modulus (E′) and damping factor (Tanδ) as a function of temperature can be obtained by this method. The determination of characteristic martensitic temperatures is based on intersection of tangents and will be describe more precisely in chapter 4.

# References

Bertrand E., *Elaboration et caractérisation d'alliages biocompatibles Ti-Ta-Nb présentant des propriétés superélastiques et à mémoire de forme*. Thèse de doctorat, Institut National des Sciences Appliquées de Rennes, 2011.

Besse M., *Elaboration et caractérisation d'alliages à base de titane de type Gum Metals en vue d'adapter leurs propriétés superélastiques aux applications biomédicales*. Thèse de doctorat, Institut National des Sciences Appliquées de Rennes, 2010.

Brisset F., *Microscopie électronique à balayage et Microanalyses*, EDP Sciences, 2008.

ESRF, 2014, available online: http://www.esrf.eu/

Grosdidier T., Philippe M.J., *Deformation induced martensite and superelasticity in a β-metastable titanium alloy*. Materials Science and Engineering A, **291**, p218, 2000.

Menard K.P., *Dynamic mechanical analysis: a practical introduction*. CRC press, 2008.

Randle V., Engler O.. *Introduction to texture analysis: macrotexture, microtexture and orientation mapping*. 2000.

Sun F., *Alliages nanostructurés : cas des amorphes à base d'aluminium et des beta-métastables à base de titane*. Thèse de doctorat, Institut National des Sciences Appliquées de Rennes, 2009.

ToiTPoMS-TLP-Library, *Crystallographic Texture*. 2009, available on line:
http://www.doitpoms.ac.uk/tlplib/crystallographic_texture/index.php.

Wikimedia, *Diffractometre berceau Euler*, 2006, available on line:
http://commons.wikimedia.org/wiki/File:Diffractometre_berceau_Euler.png

# Chapter III: Primary investigations on the superelasticity of the Ti2448 alloy

# 1. Introduction

The Ti-24Nb-4Zr-8Sn alloy (Ti2448 for short) is a new β-type multifunctional alloy (body-centered cubic structure, bcc). This alloy displays interesting properties such as high strength, low elastic modulus, high ductility, superelastic property and good biocompatibility. In previous works, different kinds of thermo-mechanical treatments were used for the processing of the alloy (cold deformation, hot rolling and warm rolling) (*Hao 2005, Hao 2007a, Hao 2007b, Li 2008, Li 2011, Hao 2012*). Thanks to these investigations, a superelasticity of about 3.3% was obtained (*Hao 2007b, Li 2008, Li 2011, Hao 2012*), which is much higher than the values usually obtained with binary Ti-Nb alloys (*Kim 2006a, Kim 2006b, Ramarolahy 2012*). Moreover, "flash treatments" (thermal treatment at 600℃ for 6min for example) carried out on the as-cold rolled Ti-based alloy allow to further enhance the superelastic property, combined with a very high strength in that case (*Sun 2010*). These properties were recently correlated to the reduced grain size, which is due to the strong applied plastic deformation combined with the following rapid recrystallization treatment in the β phase field (*Sun 2010*). Furthermore, intense plastic deformation is known to induce strong crystallographic texture, which can also influence the mechanical properties and, in the present case, the superelastic behavior of the Ti2448 alloy. As for example, texture evolution after warm rolling was previously investigated in detail in a β titanium alloy (*Sander 2008*) and it was evaluated that the superelastic recovery strain is maximized for grains strained along $<110>$ direction (*Kim 2006b*). Consequently, a control of the texture can also be used in order to improve the superelasticity of β titanium alloys (*Kim 2006b, Bertrand 2013*).

In this chapter, different cold rolling reduction rates: moderate (40%), intermediate (80%) and high cold rolling reduction rates (94%) were employed in the Ti2448 alloy in order to vary the crystallographic texture in its solution treated (ST) and flash thermal treated (FT) states.

The mechanical properties and superelasticity were firstly evaluated by tensile test. Then, optical microscopy and X-ray diffraction were used to characterize the microstructures. In the end, different textures obtained by changing the cold rolling reduction rate and the following thermal treatment (solution treatment or flash thermal treatment) were evidenced. The influence of the resulting texture on the related mechanical properties (tensile strength, Young's modulus, superelastic recovery strain) was investigated in detail.

The main content of this chapter was published in *Journal of Alloys and Compounds 2014;* ***591****: 85* (*Yang 2014*).

## 2. Mechanical properties

Mechanical properties were estimated by conventional tensile tests with a strain rate of $10^{-4}$ $s^{-1}$. Fig. 3-1 displays the tensile curves obtained after solution treatment (ST, 900°C/30min) and flash treatment (FT, 700°C/3min). The method of slope of tangent for the linear elastic range on the stress-strain curve was adopted to obtain incipient Young's modulus. The mechanical characteristics determined from tensile curves in Fig. 3-1 (ultimate tensile strength/UTS, incipient Young's modulus/E, elongation at fracture/e) are concluded in Table 3-1.

**Table 3-1** Mechanical properties of solution treated and flash thermal treated Ti2448 alloy after different cold rolling rates.

| Reduction rate/% | Elongation at rupture/% | | Ultimate tensile strength/MPa | | Young's modulus/GPa | |
|---|---|---|---|---|---|---|
| | ST | FT | ST | FT | ST | FT |
| CR40% | 10 | 9 | 873 | 944 | 58 | 58 |
| CR80% | 12 | 8 | 868 | 954 | | |
| CR94% | 13 | 9 | 877 | 990 | | |

From the conventional tensile curves (Fig.3-1a and 3-1b), a double yielding phenomenon associated to the superelastic property of this alloy is clearly observed, suggesting that SIM α" transformation has occurred. For both thermal treatments, no influence of reduction rate on mechanical properties can be noticed, except for the CR 94%-FT sample, where a slight increase of 50MPa in ultimate tensile strength can be observed. However, a strengthening effect is observed after the flash thermal treatment (Fig.3-1b) since higher ultimate tensile strength is obtained by comparison to the solution treated alloy. Elongation at rupture was evaluated to lie between 8 and 12 % and no clear difference in ductility was observed whatever the thermo-mechanical process applied. Similarly, the Young's modulus is independent on the thermo-mechanical process.

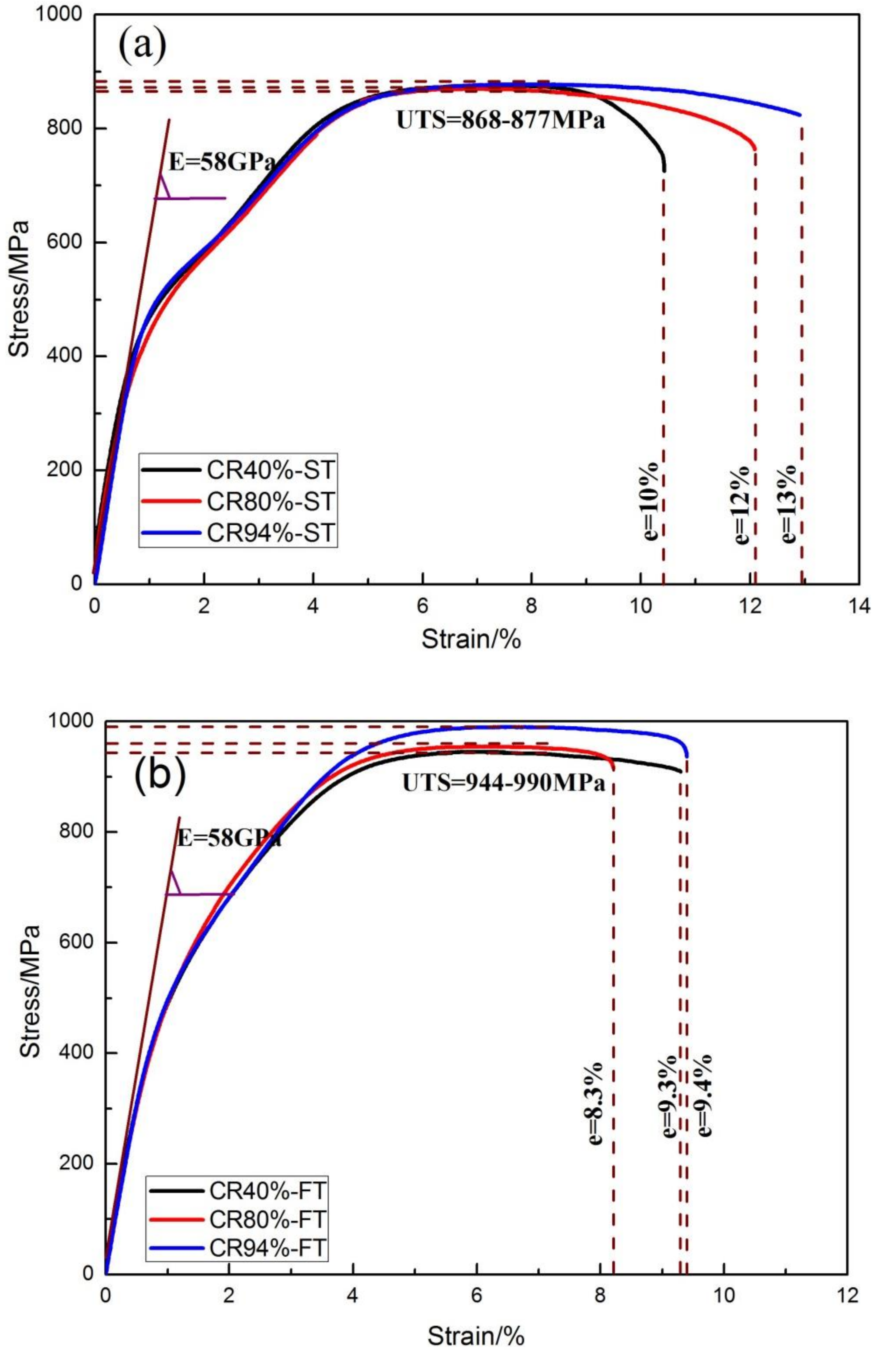

**Fig. 3-1** Strain-stress curves of Ti2448 alloy after (a) solution treatment and (b) flash treatment with different cold rolling rates.

## 3. Superelasticity depending on thermal treatment

The cyclic stress-strain curves, between 0 and 5% of strain with an increment of 0.5%, are given in Fig.3-2a for ST alloy and Fig. 3-2b for FT alloy, respectively.

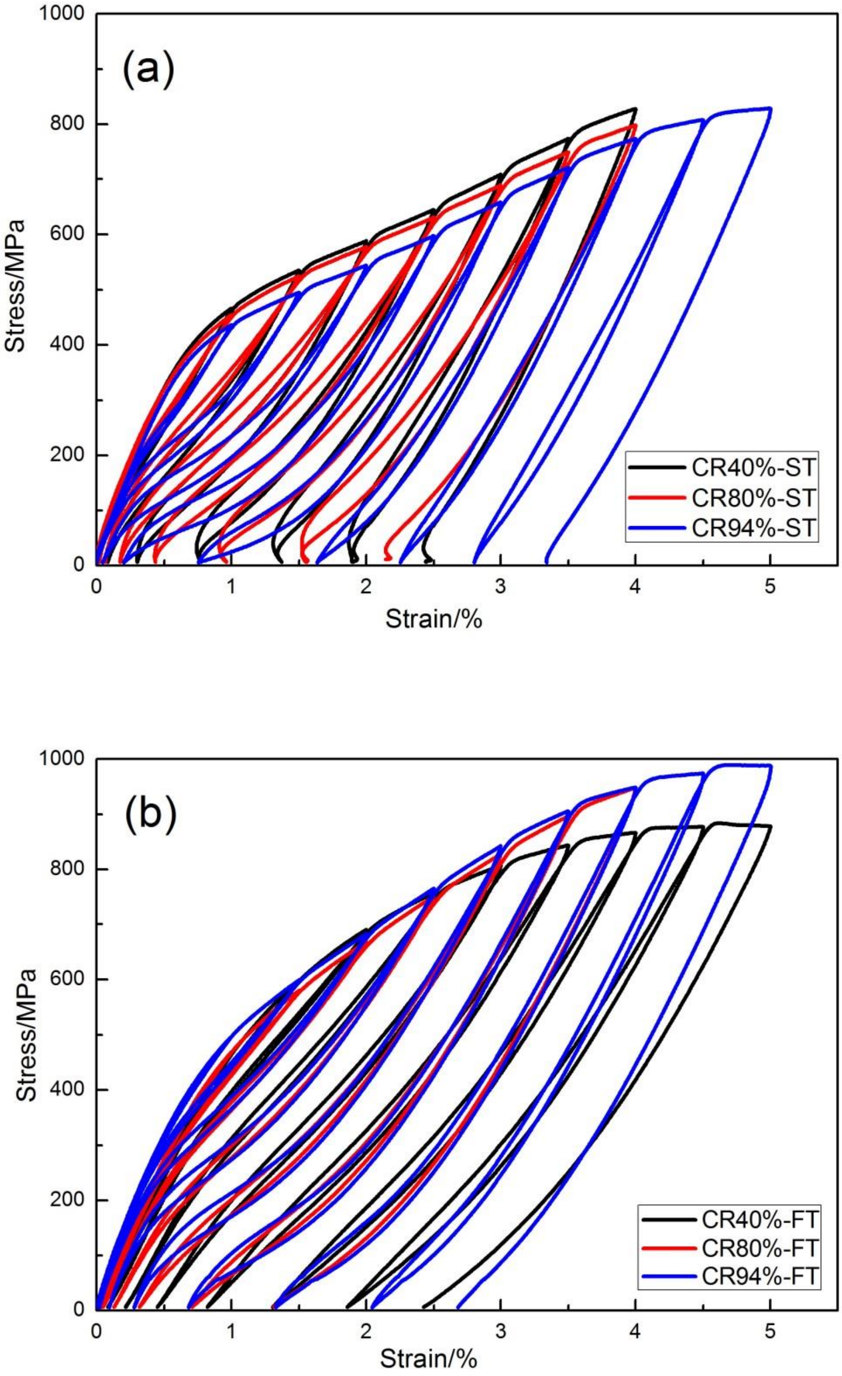

**Fig. 3-2** Strain-stress curves of Ti2448 alloy after (a) solution treatment and (b) flash treatment with different cold rolling rates.

As it can be seen, all tensile curves show a hysteresis between loading and unloading, which is due to the stress-induced reversible martensitic transformation. For each cycle, the recoverable strain was measurement according to the method illustrated in Fig. 2-5, and this value as a function of the applied strain has been plotted in Fig.3-3 in order to evaluate the evolution of the elastic recovery.

From the Fig. 3-3, the most important influence is due to the thermal treatment. Indeed, the highest recoverable strain (2.75%) is obtained for flash treated samples while 2% maximum is reached for solution treated specimens (at 3.5% of applied strain). It seems that the maximum recoverable strain is enhanced by the reduction rate as well, particularly for the solution treated samples.

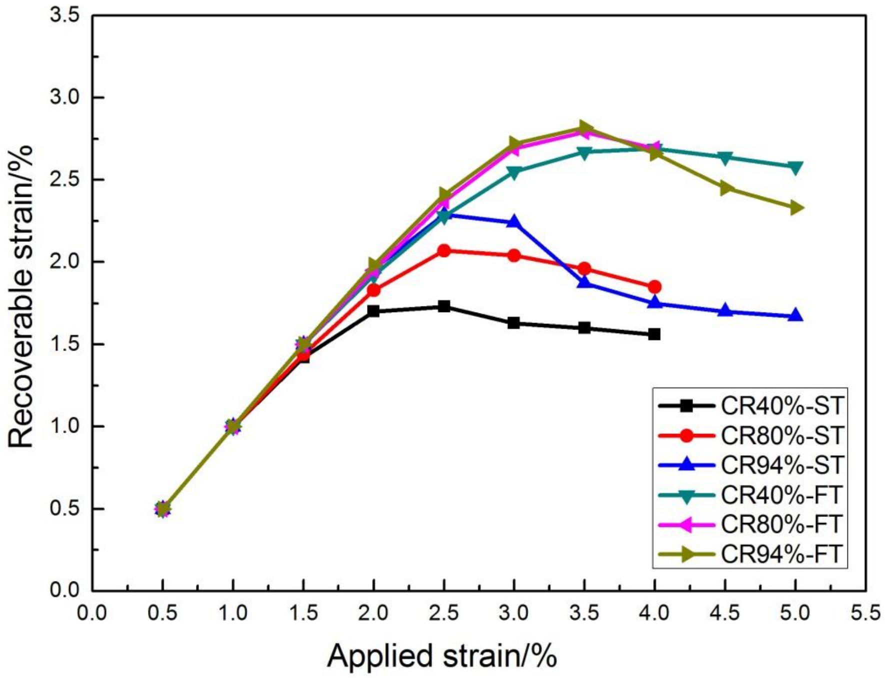

**Fig. 3-3** Variation of recovery strain for different thermo-mechanical conditions of the Ti 2448 alloy.

# 4. Microstructural characterization

## 4.1 X-ray diffraction

The X-ray diffraction patterns of Ti-24Nb-4Zr-8Sn alloy are shown in Fig. 3-4. Whatever the cold rolling reduction rate and the thermal treatment applied, only a full-recrystallized β phase microstructure was obtained. Indeed, (110), (200), (211), and (220) peaks of the body-centered cubic (bcc) β phase are observed. The lattice parameter of β phase is calculated to be close to 0.3292nm, which is consistent with the results published previously for the Ti2448 alloy (*Hao 2006*).

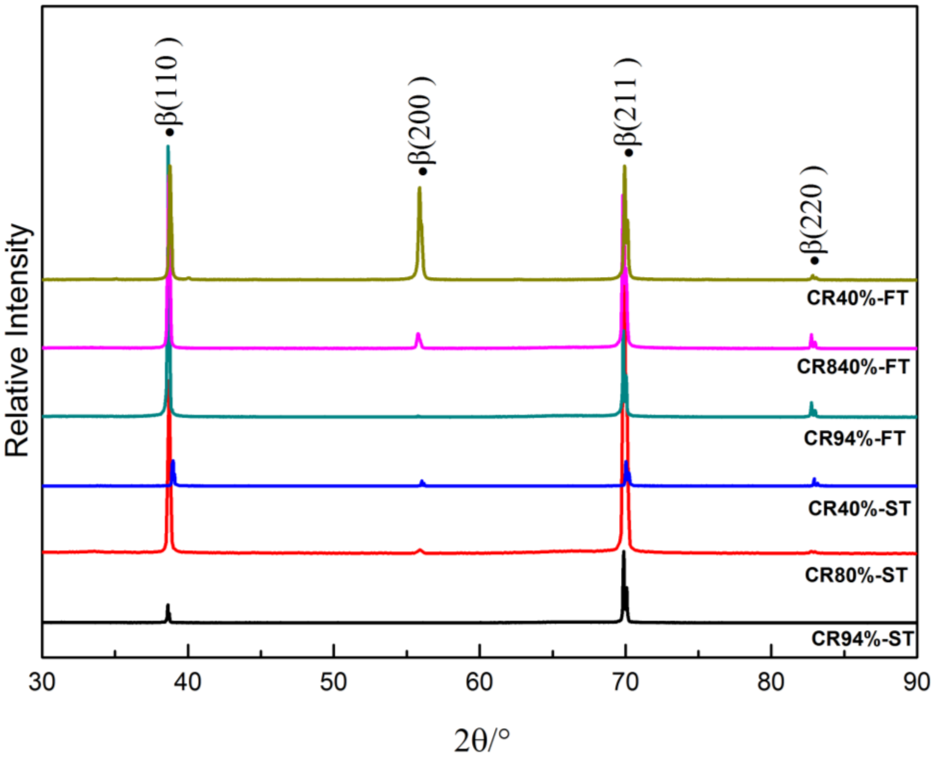

**Fig. 3-4** XRD profiles of Ti2448 alloy after different thermo-mechanical treatments.

## 4.2 Optical microstructure

The microstructures of Ti2448 alloy after ST and FT were shown in Fig. 3-5. According to the phase analysis on Fig. 3-4, these microstructures consist of only equiaxed β-grains after solution treatment (Fig. 3-5a to 3-5c) with an average grain size of 60 μm for CR40% and 50 μm for both CR80% and CR94%. After flash thermal treatment, optical micrographs reveal similar microstructures for each cold rolling rate with smaller grains whose size is measured lesser than 10 μm (Fig. 3-5d to 3-5f). However, the TEM observations show that the true grain size is smaller than what is observed in optical micrographs for the flash thermal treated alloy (*Yang 2014*). The grain size is thus observed to be independent of the applied cold rolling rate and the microstructures are similar: for example, the inserted TEM bright-field image inside the Fig. 3-5f illustrates the microstructure with sub-micron grains of the CR94%-FT specimen. For each thermal treatment (ST or FT), the grain size is thus almost independent of the cold rolling rate.

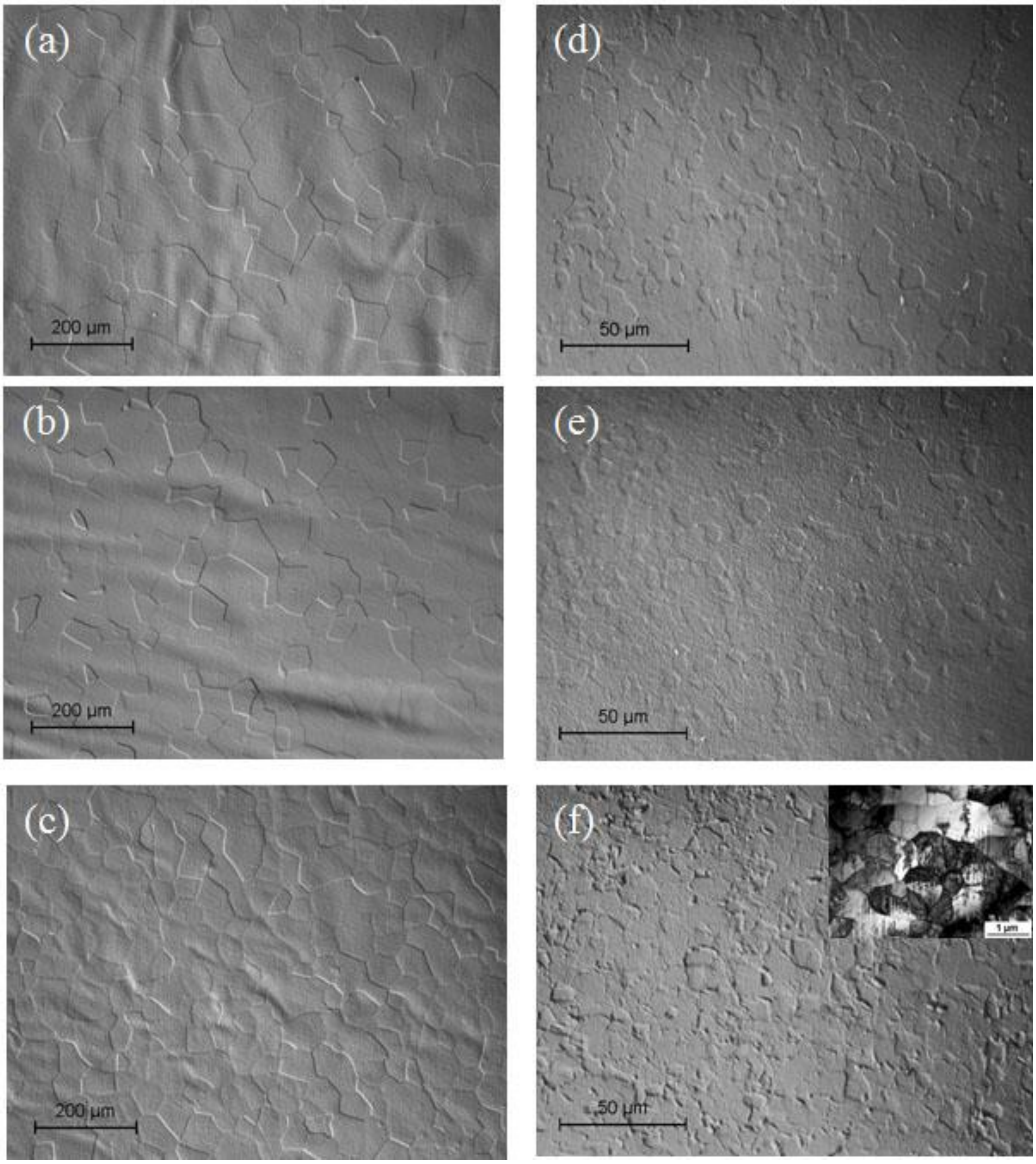

**Fig. 3-5** Optical micrographs of Ti2448 after different cold rolling rates and solution treatment ST (a) CR40%-ST, (b) CR80%-ST, (c) CR94%-ST, (d) CR40%-FT, (e) CR80%-FT and (f) CR94%-FT and its bright-field TEM micrograph showing sub-micron grains.

Fig. 3-5 has revealed the microstructure of fully β phase before deformation. As it can be predicted from the double yielding phenomenon and superelasticity on mechanical tensile curves in Fig. 3-1 and Fig. 3-2, the SIM$\alpha''$ transformation occurs during the deformation process. In order to observe the SIM$\alpha''$ phase, the microstructures of Ti2448 alloy after deformation were shown in Fig. 3-6 for CR94%-ST alloy and CR94%-FT alloy.

For the CR94%-ST alloy after deformed to 1.5% strain, there is no visible change inside the original β grains, but some bands could be clearly observed in Fig. 3-6b and 3-6c at higher deformation strains which are thought to be related to the SIMα″ martensite. However, due to the smaller grain size under FT condition, the microstructure is still not clear to be observed as shown in Fig. 3-6d for CR94%-FT sample deformed to 5%.

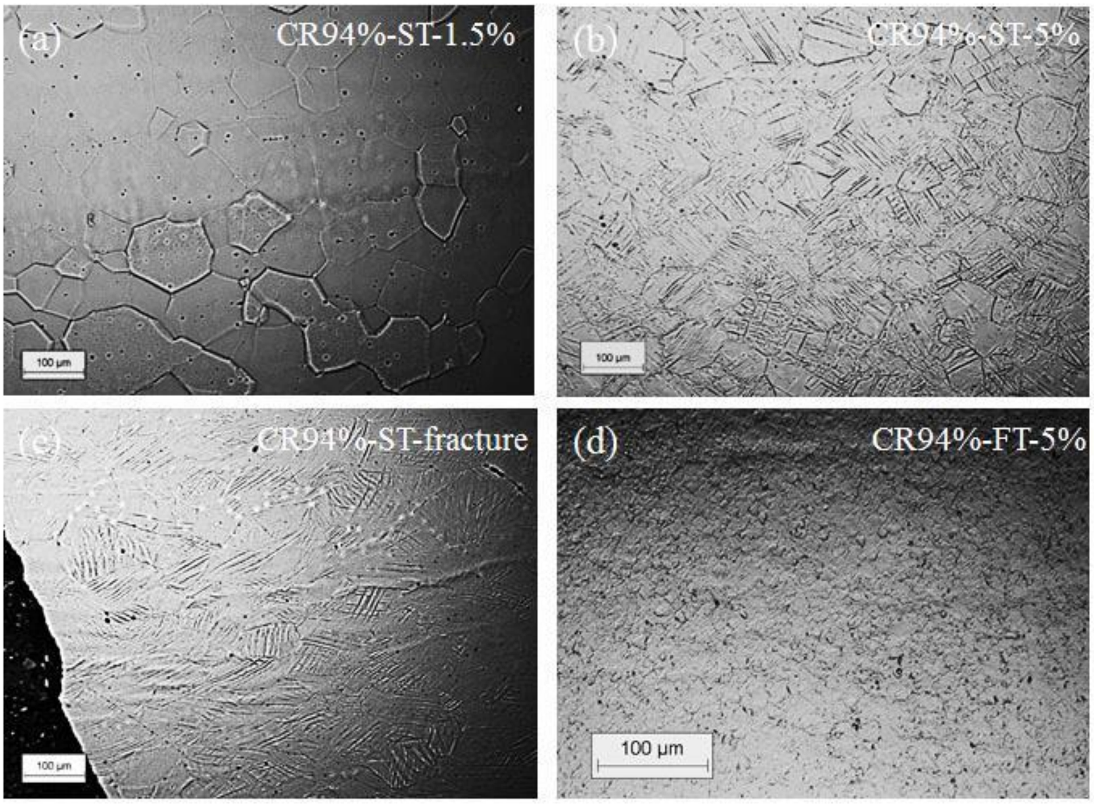

**Fig. 3-6** Optical micrographs of Ti2448 deformed to different strain rate: (a) CR94%-ST-1.5%, (b) CR94%-ST-5%, (c) CR94%-ST-fracture and (d) CR40%-FT-5%.

# 5. Texture analysis

## 5.1 Texture evolution depending on thermo-mechanical treatment

Crystallographic texture can influence the mechanical properties and, in the present case, the superelastic behavior of the Ti2448 alloy. As evidenced in Fig. 3-3, the most important influence is due to the thermal treatment, but the recoverable strain differs with the reduction rate after each thermal treatment. Especially for the solution treatment, the maximum recovery strain is enhanced by the increasing of reduction rate as well. Therefore, it is meaningful to measure the crystallographic texture and investigate the preferable texture which leads to the better superelasticity.

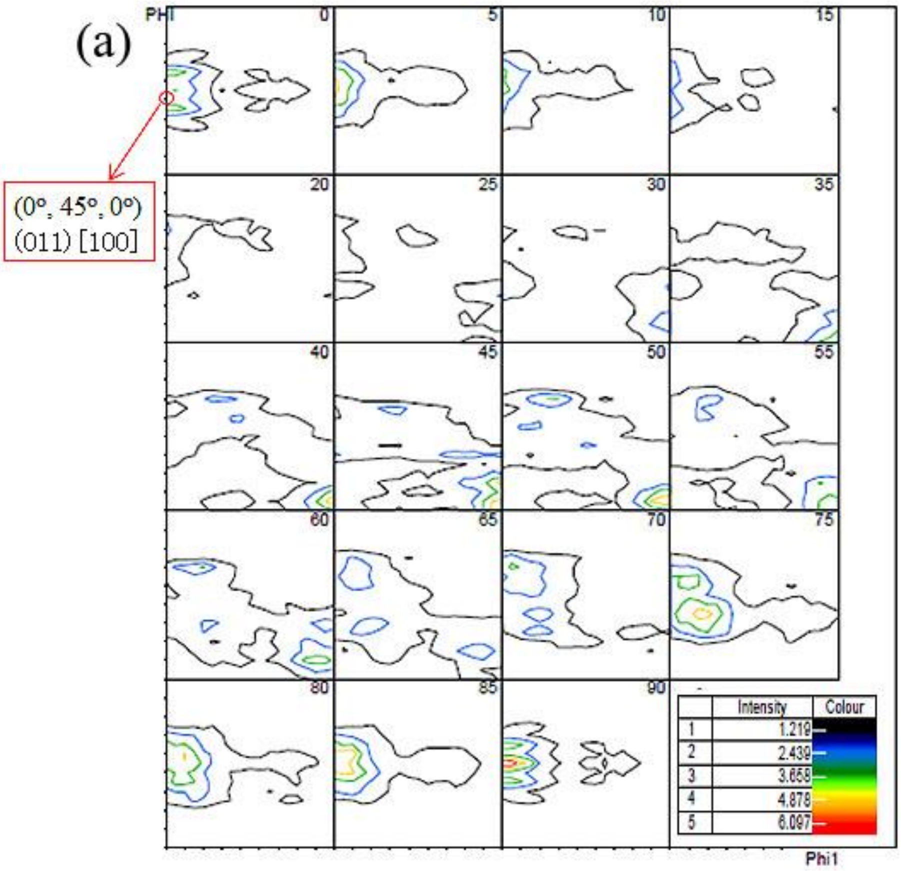
(a)
PHI
0
5
10
15
20
25
30
35
40
45
50
55
60
65
70
75
80
85
90
(0°, 45°, 0°)
(011) [100]
Intensity
Colour
1 1.219
2 2.439
3 3.658
4 4.878
5 6.097
Phi1

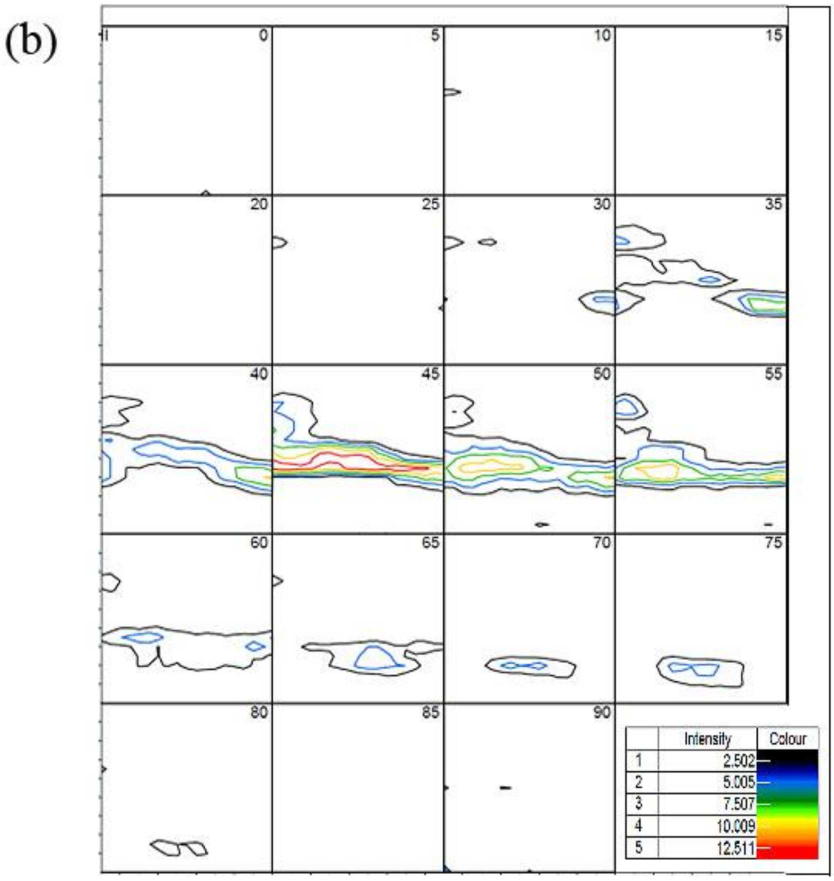
(b)
0
5
10
15
20
25
30
35
40
45
50
55
60
65
70
75
80
85
90
Intensity
Colour
1 2.502
2 5.005
3 7.507
4 10.009
5 12.511

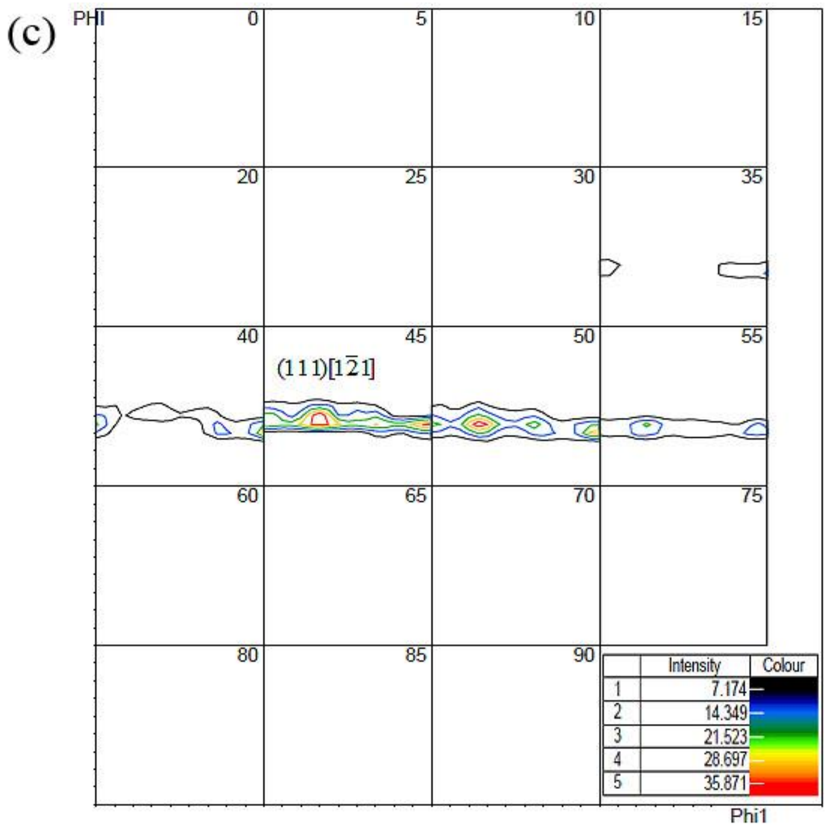

**Fig. 3-7** Constant $\varphi_2$ sections of ODF for Ti2448 alloy after different cold rolling rates followed by solution treatment: (a) 40% (b) 80% and (c) 94%.

The ODFs obtained on samples after solution treatment with different cold rolling reduction rates 40%, 80% and 94% are displayed in Fig. 3-7 from a to c, respectively. After solution treatment, the CR40%-ST sample ((Fig. 3-7a)) does not show a strong texture but the main component $(011)[100]$ (0°, 45°, 0°) highlighted with a red arrow can clearly be identified. For higher reduction rate (CR80%-ST, (Fig. 3-7b), it can be observed preferential orientations on the γ-fiber. The γ-fiber is defined as containing all orientations of $(111) < uvw >$ type and can be visible on the $\varphi_2$=45° section where $\phi$=55° with highest intensity. For more precision, the orientation densities are drawn in Fig. 3-9 with variable $\varphi_1$ angle. At intermediate cold rolling rate (Fig. 3-7b), the texture concentrates mainly on the γ-fiber, which means all the grains are oriented so that the $(111)$ plane of the grains is parallel to the surface of the sample. This γ-fiber is commonly observed in bcc alloys (*Raabe 1993*, *Hölscher 1994*, *Raabe 1995*) and was recently observed in β-titanium alloys after high deformation reduction rates (*Sander 2008*). At high cold rolling rate (Fig.3-7c) the same observation can be got, but the component $(111)[1\bar{2}1]$ appears prominent on this same fiber.

(a)

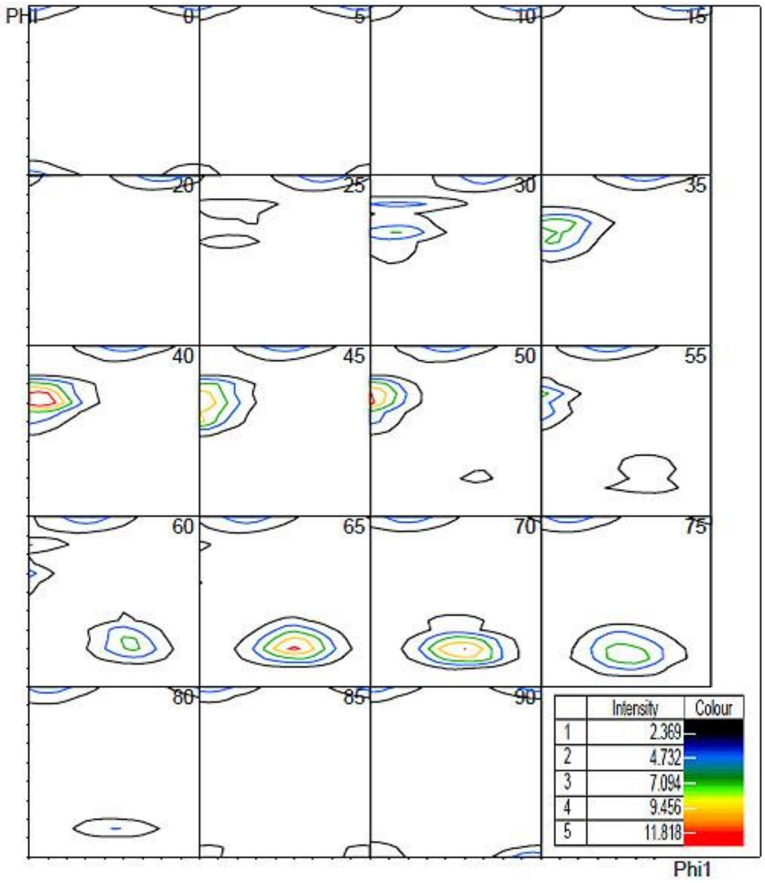
PHI
0
5
10
15
20
25
30
35
40
45
50
55
60
65
70
75
80
85
90
Intensity
Colour
1 2.369
2 4.732
3 7.094
4 9.456
5 11.818
Phi1

(b)

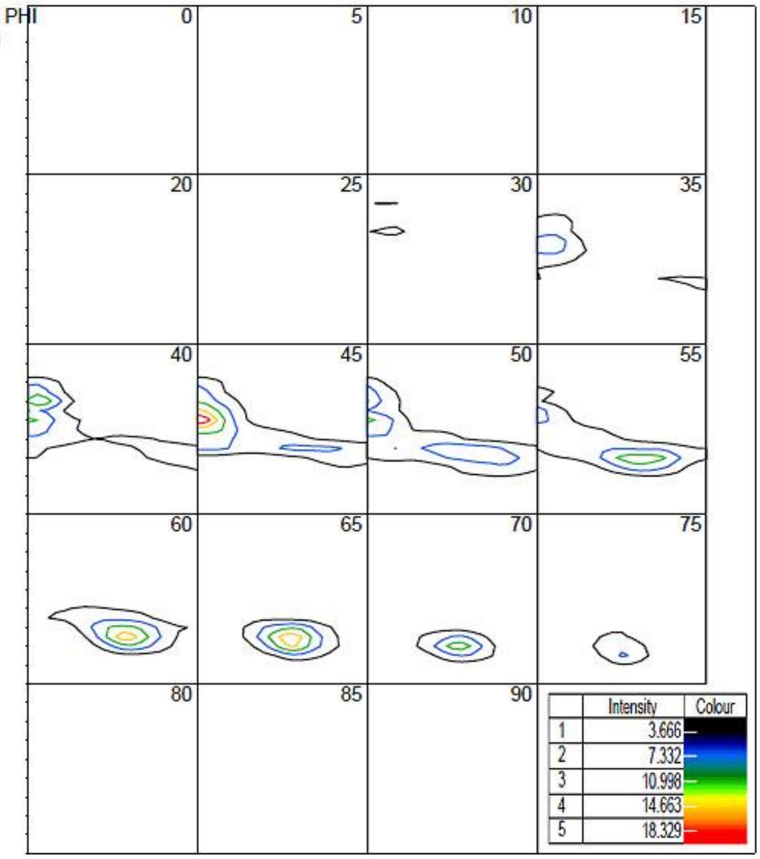
PHI
0
5
10
15
20
25
30
35
40
45
50
55
60
65
70
75
80
85
90
Intensity
Colour
1 3.666
2 7.332
3 10.998
4 14.663
5 18.329

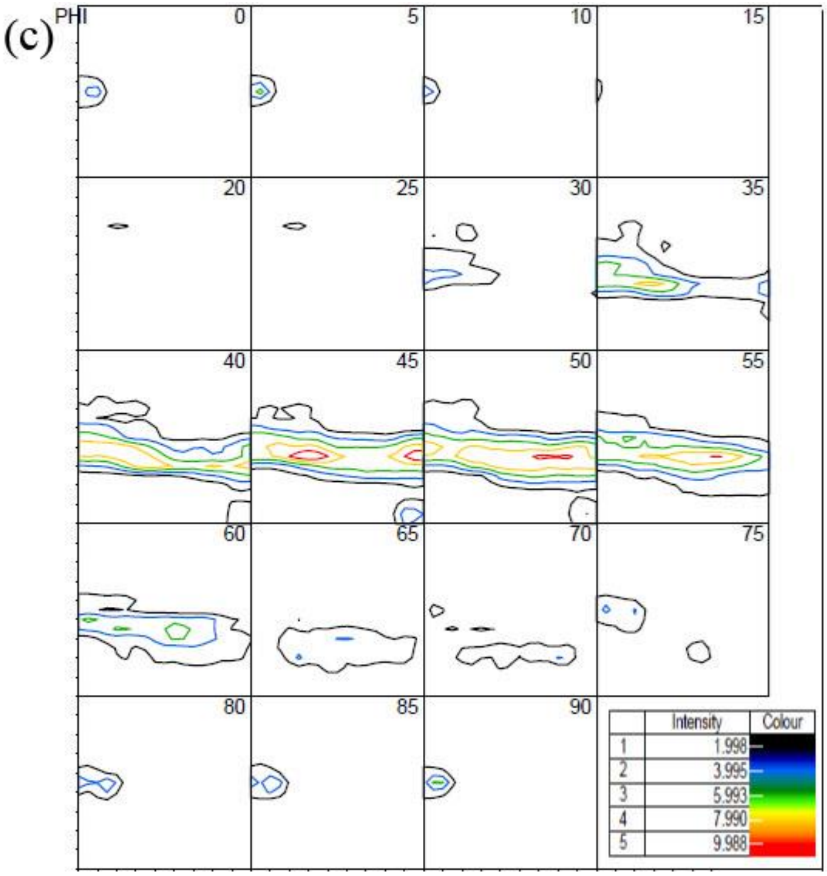

**Fig. 3-8** Constant φ2 sections of ODF for Ti2448 alloy after different cold rolling rates followed by flash treatment: (a) 40% (b) 80% and (c) 94%.

After flash thermal treatment, the lowest cold rolling rate (CR40%-FT, Fig.3-8a) exhibits a clear texture corresponding mainly to $(211)[0\bar{1}1]$ (50°, 66°, 63°). With the CR80%-FT sample (Fig. 3-8b), this orientation remains but orientations along the γ-fiber are also observed as the same shown in the solution treated samples. For the CR94%-FT, only orientations of the γ-fiber are observed (Fig. 3-8c). It seems that higher the reduction rate is, stronger is the γ-fiber as seen on Fig. 3-9 wherein the intensity of orientations along this fiber increases with the cold rolling rate. For both thermal treatments, the main component of the γ-fiber is $(111)[1\bar{2}1]$ after high cold rolling rate, but with a stronger intensity for the solution treated samples.

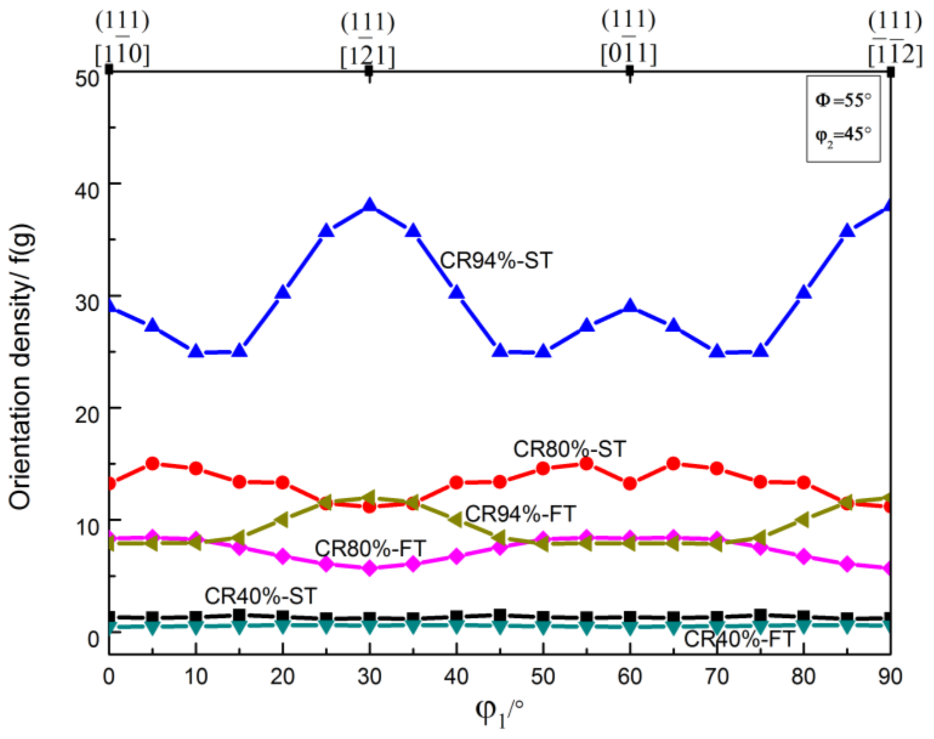

**Fig. 3-9** Orientations distributed along the $\phi$=55° line on $\varphi_2$=45° sections of ODF observed in specimens after different thermo-mechanical treatments illustrating the presence of γ-fiber.

## 5.2 Superelasticity dependence on texture

For solution treated samples, an increase of the superelasticity is observed at high cold rolling rates (Fig. 3-3). It was shown previously that the recoverable strain due to the reversible martensitic transformation is maximum when the grains are orientated with $<110>$ direction parallel to the tensile direction (*Kim 2006b*). In the present ST samples, this optimal condition is fulfilled only at higher cold rolling rates (80% and 94%) since the $(111)[1\bar{1}0]$ orientation is lied on the γ-fiber. The increase of the superelasticity in ST samples can thus be linked to the higher amount of grains processing the appropriated orientation.

For the flash thermal treated samples, no change in superelasticity is observed whatever the cold rolling rate (Fig. 3-3). Consequently, the texture change observed from 40% to 94% of reduction rate does not influence the superelastic recovery strain. This is due to the fact that, for each cold rolling rate, there are always a significant amount of grains possessing the favorable orientation of $(211)[0\bar{1}1]$ or $(111)[1\bar{1}0]$ along the γ-fiber (Fig. 3-8). As a consequence, the change in texture does not influence the strain recovered by the martensitic transformation.

By comparing the FT and ST samples, a strong increase of the superelasticity is observed as previously mentioned (Fig. 3-3). At least for both higher cold rolling rates (80% and 94%), it is clear that this increase cannot be attributed to the texture as both samples exhibit the same γ-fiber texture but a different recovery strain. This increase for the FT samples can thus rather be due to the reduced grain size as reported in previous work (*Sun 2010*) and (*Sun 2011*). Indeed, the stress-induced martensite can be trapped by dislocations, which can impede a total reversion during the unloading. An increase of the critical stress of dislocation slip, obtained by a smaller grain size, can thus improve the superelastic behavior of FT samples.

## 6. Conclusion

Texture evaluation and its relationship with superelasticity have been investigated for the Ti2448 alloy with three cold rolling reduction rates (40%, 80% and 94%) and two following thermal treatments (ST and FT) in this work. The main conclusions are:

(1) For ST samples, the main orientation is $(011)[100]$ at moderate cold rolling rate (40%) whereas a γ-fiber texture is observed at higher cold rolling rates (80% and 94%) with the $(111)[1\bar{2}1]$ orientation as a main component (CR94%-ST).

(2) For FT samples, a γ-fiber texture with the $(111)[1\bar{2}1]$ main component is observed at intermediate (80%) and high (94%) cold rolling rates. But a clear texture corresponding mainly to $(211)[0\bar{1}1]$ is obtained after a moderate cold rolling rate (40%).

(3) FT samples exhibit higher ultimate tensile strength than ST samples due to a smaller grain size. Young’ modulus and elongation at rupture are shown to be independent of the applied thermo-mechanical process and thus of the texture, contrarily to superelasticity.

(4) Superelasticity of ST samples increases with the cold rolling rate in relation with the texture change. Indeed, the amount of grains orientated to give the highest recovery strain, which is with $< 110 >$ directions along the tensile direction, increases with the cold rolling rate.

(5) Superelasticity of FT samples is not influenced by the texture change due to the variation of cold rolling rate because the amount of grains orientated to give the highest recovery strain does not vary significantly.

(6) FT samples exhibit better superelasticity than ST samples. For both higher cold rolling rates (80% et 94%), the higher superelastic properties observed with the FT samples cannot be correlated to the texture but are clearly due to the grain refinement.

# References

Bertrand E., Castany P., Gloriant T., *Investigation of the martensitic transformation and the damping behavior of a superelastic Ti-Ta-Nb alloy*. Acta Materialia, **61**, p511, 2013.

Hao Y. L., Li S. J., Sun B.B., Sui M.L., Yang R., *Ductile Titanium Alloy with Low Poisson's Ratio*. Physical Review Letters, **98**, p216405, 2007a.

Hao Y.L., Li S.J., Sun S.Y., Yang R., *Effect of Zr and Sn on Young's modulus and superelasticity of Ti–Nb-based alloys.* Materials Science and Engineering A, **441**, p112, 2006.

Hao Y.L., Li S.J., Sun S.Y., Zheng C.Y., Hu Q.M., Yang R., *Super-elastic titanium alloy with unstable plastic deformation*. Applied Physics letters, **87**, p091906, 2005.

Hao Y.L., Li S.J., Sun S.Y., Zheng C.Y., Yang R., Elastic deformation behavior of Ti-24-Nb-4Zr-7.9Sn for biomedical applications. Acta Biomater, **3**, p277, 2007b.

Hao Y.L., Zhang Z.B., Li S.J., Yang R., *Microstructure and mechanical behavior of a Ti–24Nb–4Zr–8Sn alloy processed by warm swaging and warm rolling*. Acta Materialia, **60**, p2169, 2012.

Hölscher M., Raabe D., Lücke K., *Relationship between rolling textures and shear textures in Fcc and Bcc metals*. Acta Metallurgica et Materialia , **42**, p879, 1994.

Kim H.Y., Ikehara Y., Kim J.I., Hosoda H., Miyazaki S., *Martensitic transformation, shape memory effect and superelasticity of Ti-Nb binary alloys*. Acta Materialia, **54**, p2419, 2006a.

Kim H.Y., Sasaki T., Okutsu K., Kim J.I., Inamura T., Hosoda H., Miyazaki S., *Texture and Shape Memory Behavior of Ti-22Nb-6Ta Alloy*. Acta Materialia, **54**, p423, 2006b.

Li S.J., Cui T.C., Li Y.L., Hao Y.L., Yang R., *Ultrafine-grained beta-type titanium alloy with nonlinear elasticity and high ductility*. Applied Physics letters, **92**, p043128, 2008.

Li S.J., Jia M.T., Prima F., Hao Y.L., Yang R., *Improvements in nonlinear elasticity and strength by grain refinement in a titanium alloy with high oxygen content*. Scripta Materialia., **64**, p1015, 2011.

Raabe D., Lücke K., *Texture of ferritic stainless steels*. Materials Science and technology, **9**, p302, 1993.

Raabe D., *textures of strip cast and hot rolled ferritic and austenitic stainless steel*. Materials Science and technology, **11**, p461, 1995.

Ramarolahy A., Castany P., Prima F., Laheurte P., Péron I., Gloriant T., *Microstructure and mechanical behavior of superelastic Ti-24Nb-0.5O and Ti-24Nb-0.5N biomedical alloys.* Journal of the Mechanical Behavior of Biomedical Materials, **9**, p83, 2012.

Sander B., Raabe D., *Texture inhomogeneity in a Ti-Nb-based β-titanium alloy after warm rolling and recrystallization*. Materials Science and Engineering A, **479**, p236, 2008.

Sun F., Hao Y.L., Nowak S., Gloriant T., Laheurte P., Prima F., *A thermo-mechanical treatment to improve the superelastic performances of biomedical Ti–26Nb and Ti–20Nb–6Zr (at.%) alloys*. Journal of the Mechanical Behavior of Biomedical Materials, **4**, p1864, 2011.

Sun F., Nowak S., Gloriant T., Laheurte P., Eberhardt A., Prima F., *Influence of a short thermal treatment on the superelastic properties of a titanium-based alloy*. Scripta Materialia, **63**, p1053, 2010.

Yang Y., Castany P., Cornen M., Thibon I., Prima F., Gloriant T., *Texture investigation of the superelastic Ti-24Nb-4Zr-8Sn alloy*. Journal of Alloys and Compounds, **85**, p591, 2014.

# Chapter IV: Characterization of the martensitic transformation by *in situ* synchrotron X-ray diffraction and dynamic mechanical analysis

# 1. Introduction

The metastable β-type Ti-24Nb-4Zr-8Sn (wt.%, Ti2448 for short) alloy was investigated in order to characterize the martensitic transformation occurring in this alloy. Indeed, due to this martensitic transformation, the Ti2448 alloy shows good superelasticity at room temperature characterized by a large recoverable strain up to 3.3% (*Hao 2007, Hao 2005, Li 2008*). This recoverable strain is much higher than that observed in the conventional Ti-6Al-4V alloy and in other binary Ti-Nb superelastic alloys (*Tahara 2009, Tobe 2013*). Thus, the good mechanical properties of the Ti-24Nb-4Zr-8Sn alloy, including high strength (>800MPa), low modulus (approx. 50GPa) and the superelasticity mentioned above enable it to be used as bone substitutes (implants or prostheses) for biomedical applications.

With this alloy, the superelastic (or pseudoelastic) behavior is obtained when the quenched microstructure is composed of the metastable β phase at room temperature. In such case, a stress-induced martensitic (SIM) transformation between the austenitc β phase (bcc) and the martensitic α″ phase (orthorhombic) occurs and large elastic recovery (superelasticity) can be obtained once the mechanical stress is released due to the fact that this SIM transformation is fully reversible. By tensile tests, the superelastic effect can be highlighted by the presence of a stress plateau on the tensile curve presenting thus a characteristic double-yielding behavior (See Chapter 3 for more details).

In superelastic alloys, the study of the SIM transformation is challenging due to its reversibility after the release of the stress. That is why *in situ* experiments are needed to characterize the SIM transformation under loading conditions. For example, conventional *in situ* X-ray diffraction (XRD) studies were performed on binary Ti-26Nb or Ti-13Nb-4Mo alloys (at. %) and allowed the detection of the SIM α″ phase transformation under loading conditions (*Tahara 2009, Al-Zain 2011*). However, it is difficult to separate the main peaks belonging to β and α″ phases because of the relatively longer wavelength and the presence of both $K_{\alpha1}$ and $K_{\alpha2}$ wavelengths of conventional X-ray sources used in laboratories. In order to avoid these limitations, synchrotron X-ray diffraction (SXRD) can be used because of the combination of a shorter wavelength and a better monochromaticity. Thus, SXRD appears to be a very efficient method to characterize such SIM transformation and was never used to study the Ti2448 alloy in which superelasticity is predominantly due to this mechanism. Furthermore, martensitic transformations are usually described using characteristic temperatures such as martensite start, martensite finish, austenite start and austenite finish temperatures, respectively denoted $M_s$, $M_f$, $A_s$ and $A_f$ (*Lovey 1999, Otsuka 2005*). These temperatures can be evaluated by dynamic mechanical analysis (DMA) for different applied static stresses, and the martensitic transformation is thus generally highlighted by a drop of the dynamic elastic modulus corresponding to an increase of the damping factor tan δ (*Liu 1997, Mercier 1979*).

The objective of this chapter is to characterize the martensitic transformation occurring in the Ti2448 alloy by both *in situ* synchrotron radiation X-ray diffraction (SXRD) and dynamic mechanical analysis (DMA). Two kind of sample CR94%-ST and CR94%-FT (abbreviated as ST and FT sample due to fixed cold rolling reduction of 94%) were employed for comparison in this study.

The main content of this chapter was submitted to *Acta Materialia* (*Yang 2015*).

## 2. Microstructure and mechanical properties

The microstructures of the Ti2448 alloy observed by optical microscopy are remembered in Fig. 4-1 for the solution treated alloy (ST, Fig. 4-1a) and for the flash treated alloy (FT, Fig. 4-1b), respectively. The grain sizes after ST and FT were evaluated to be about 50 μm and less than 1, respectively (see Chapter 3).

Fig. 4-2 displays the conventional and cyclic tensile curves for the ST (Fig. 2a) and FT (Fig. 2b) conditions. On these tensile curves, a double yielding phenomenon associated with the superelastic effect was observed, suggesting that the SIM transformation has occurred for both ST and FT conditions. The critical stress to induce the SIM transformation was measured to be 414MPa for ST and 440MPa for FT, respectively. The highest recoverable strain of 2.75% is obtained for the FT while 2.3% maximum is reached for the ST. The higher value of recoverable strain for FT sample was attributed to grain refinement (*Yang 2014*).

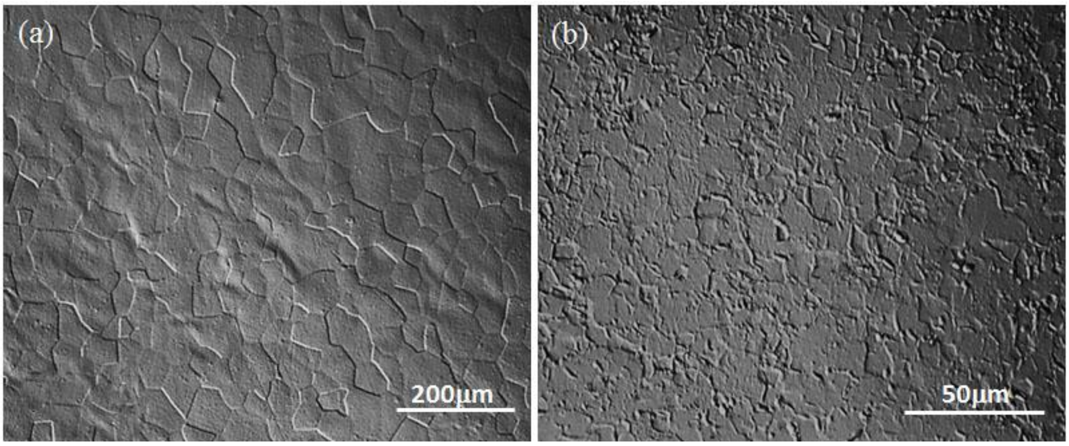

**Fig. 4-1** Optical microstructure of Ti2448 alloy after different thermal treatment: (a) solution treatment at 900°C for 30min and (b) flash treatment at 700°C for 3min.

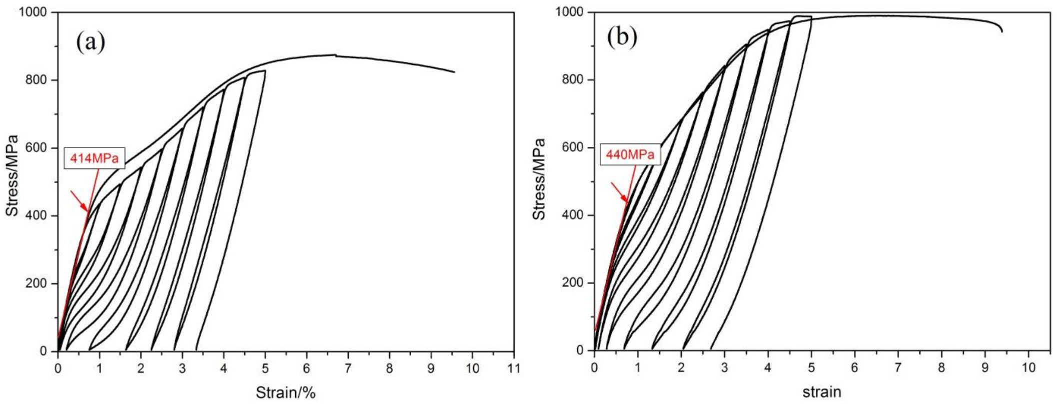

**Fig. 4-2** Conventional and cyclic tensile strain-stress curves for Ti2448 alloy after (a) solution treatment at 900°C for 30min and (b) flash treatment at 700°C for 3min.

# 3. *In situ* synchrotron X-ray diffraction

## 3.1 Indexation of whole spectrum

For obtaining a direct evidence of the SIM transformation and further the crystallographic information of both β and α″ phases during all the deformation stages, the *in situ* SXRD during cyclic loading/unloading tensile tests were conducted. The whole angle range spectra at 0% strain and after 10% strain are firstly displayed in Fig. 4-3a for the ST sample and Fig. 4-3b for the FT sample, respectively. Before any deformation, both ST and FT samples display only the β phase and its typical diffraction peaks: $(110)_{\beta}$, $(200)_{\beta}$, $(211)_{\beta}$ and $(220)_{\beta}$ as shown in Fig. 4-3a and Fig. 4-3b. But after being deformed up to 10%, the diffraction peaks $(020)_{\alpha''}$, $(002)_{\alpha''}$, $(111)_{\alpha''}$, $(021)_{\alpha''}$, $(022)_{\alpha''}$, $(131)_{\alpha''}$, $(113)_{\alpha''}$, $(040)_{\alpha''}$ and $(004)_{\alpha''}$ of the martensitic α″ phase are well detected in both ST and FT samples, which coexist with residual β phase. Thus, stress-induced martensitic transformation was clearly evidenced for both ST and FT alloys.

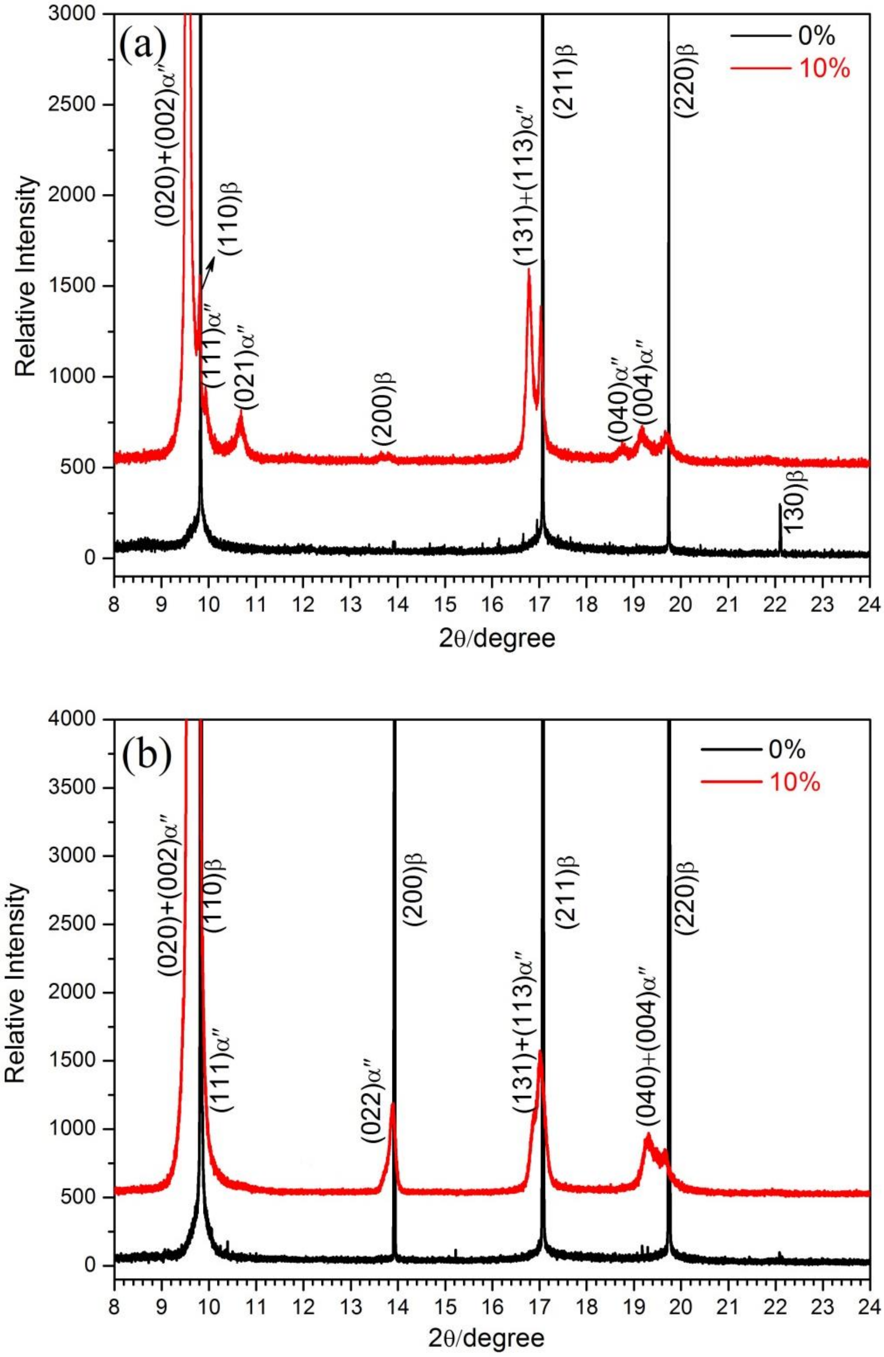

**Fig. 4-3** *In situ* SXRD spectra of Ti2448 alloy before deformation and after to be deformed at 10% of strain for ST (a) and FT (b).

## 3.2 Evolution of partial spectra with applied strains

In order to characterize more precisely the SIM transformation, Fig. 4-4 displays the SXRD patterns obtained during the *in situ* cyclic tensile tests: on the ST sample after loading (Fig. 4-4a) and after each unloading (Fig. 4-4b), on the FT sample after loading (Fig. 4-4c) and after each unloading (Fig. 4-4d). The different strains reached are indicated beside the spectra. In these figures, only the partial spectra in the angle range 8 º-11.5 ° around the main $(110)_{\beta}$ peak, where the most intense peaks are present, are showed. From Fig. 4a, the $(020)_{\alpha''}$, $(111)_{\alpha''}$, $(021)_{\alpha''}$ peaks start to be visible from 1.5% of strain and their intensities continue to increase as the applied strain increases. At the same time, the $(110)_{\beta}$ peak intensity decreases meaning that the SIM transformation has occurred on loading in the ST alloy. After unloading (Fig. 4b), it can be clearly observed that all the martensitic α″ phase could be transformed back to the β phase as the $(110)_{\beta}$ peak intensity is recovered while the α″ peaks disappear.

The SIM transformation and its reversibility is also evidenced in the FT alloy (Fig. 4-4c and 4-4d) with the difference that in this case, the SIM transformation seems to start later as the α″ peaks start to be visible at about 2% on loading. These values are in good agreement with the tensile curves results (Fig. 4-2).

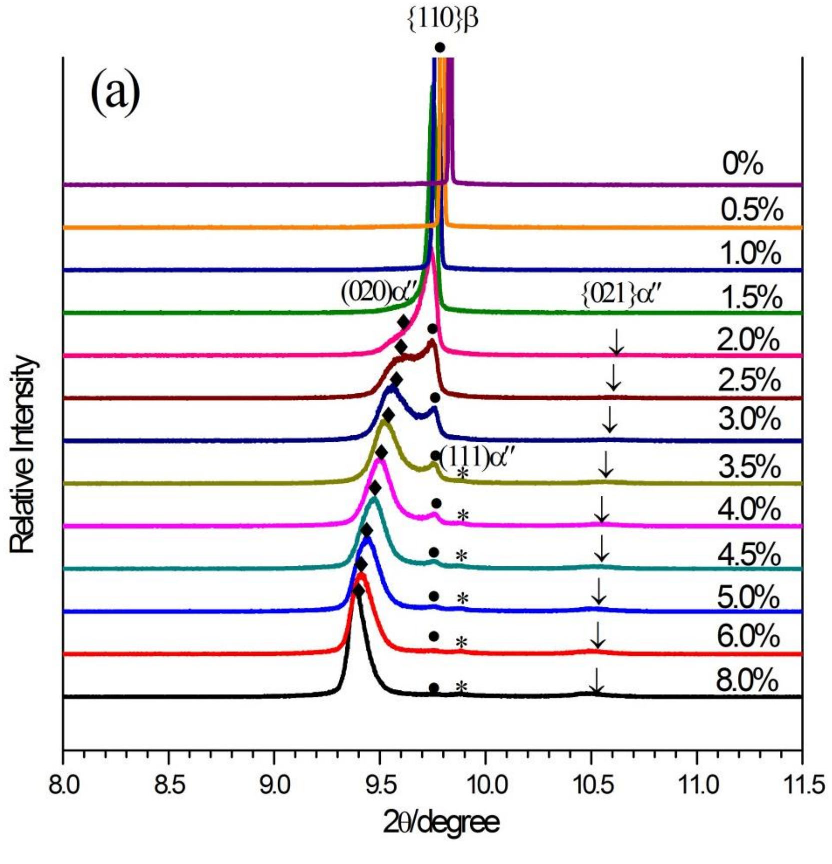

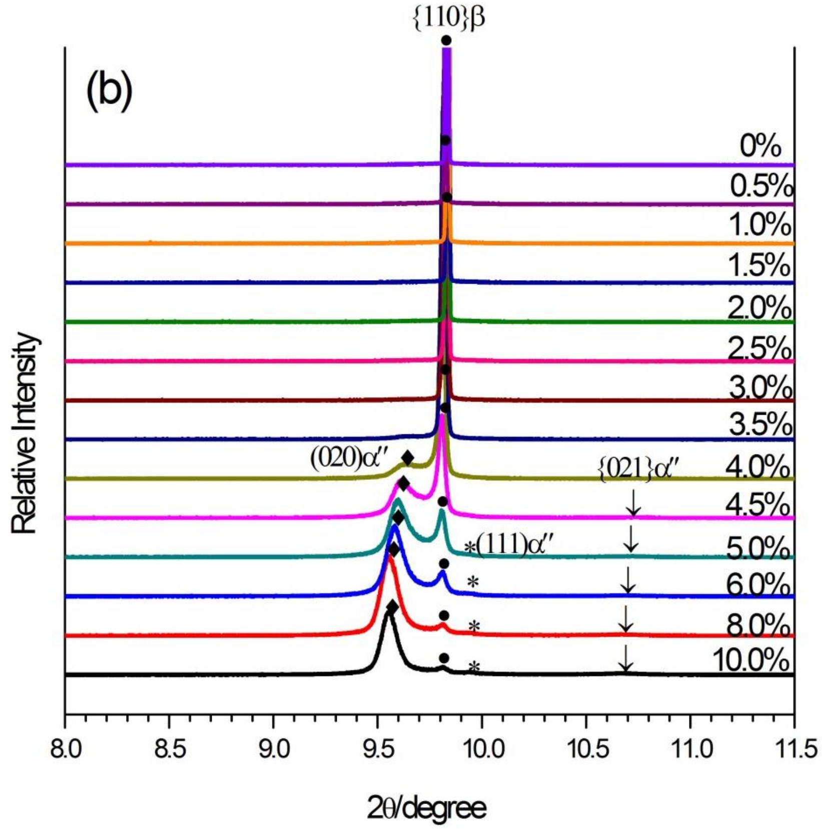
{110}β
(b)
0%
0.5%
1.0%
1.5%
2.0%
2.5%
3.0%
3.5%
(020)α″
{021}α″
4.0%
4.5%
(111)α″
5.0%
6.0%
8.0%
10.0%
Relative Intensity
8.0
8.5
9.0
9.5
10.0
10.5
11.0
11.5
2θ/degree

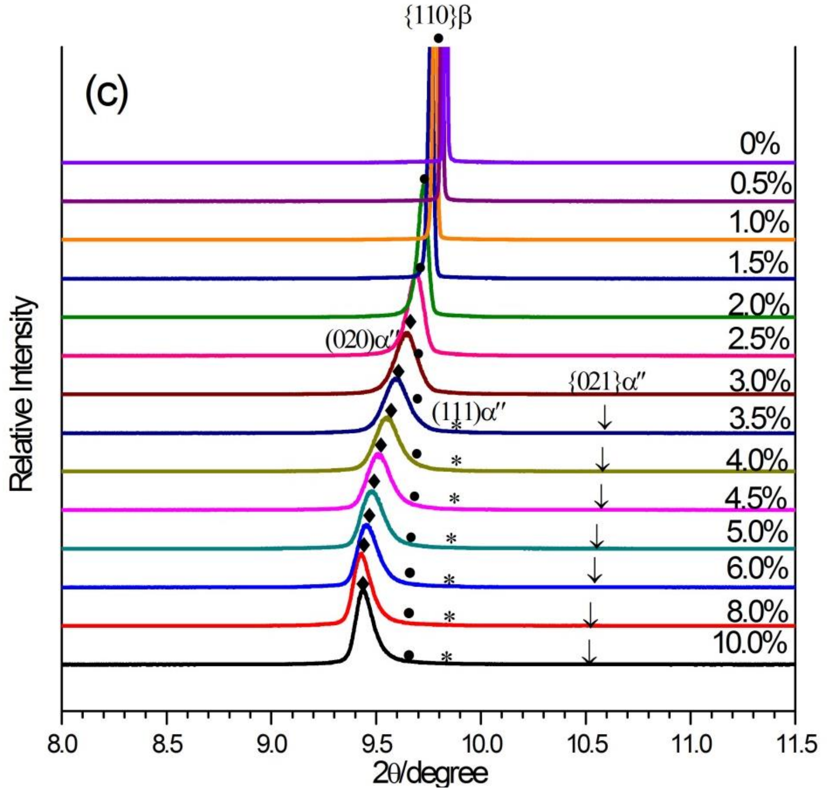
{110}β
(c)
0%
0.5%
1.0%
1.5%
2.0%
(020)α″
2.5%
{021}α″
3.0%
(111)α″
3.5%
4.0%
4.5%
5.0%
6.0%
8.0%
10.0%
Relative Intensity
8.0
8.5
9.0
9.5
10.0
10.5
11.0
11.5
2θ/degree

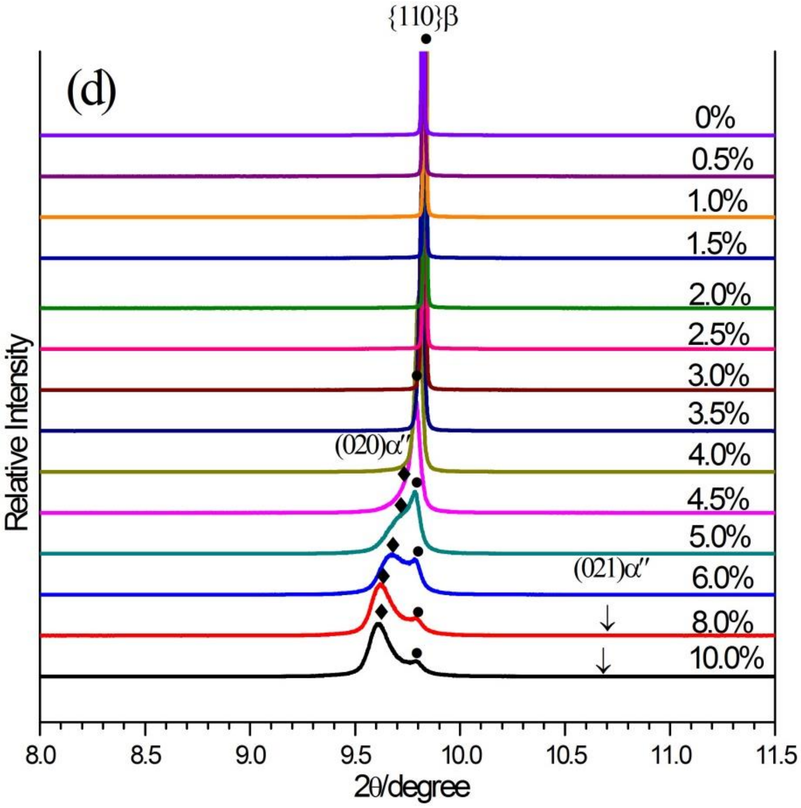

**Fig. 4-4** The partial *in situ* SXRD spectra for Ti2448 alloy on loading and after unloading for different applied strains: (a) on loading for ST sample, (b) on the corresponding unloading for ST sample, (c) on loading for FT sample and (d) on the corresponding unloading for FT sample.

## 3.3 Measurement of cell parameters

### 3.3.1 Cell parameters under loading condition

From the loading spectra (Fig. 4-4a and 4-4c), it can also be observed a clear shift to the lower angles of the α″ and β peaks due to cell parameter variations. Thus, from each SXRD spectrum, the angular positions of all peaks were determined to evaluate the different cell parameters and their variations under loading. The evolution of these cell parameters ($a_{\beta}$, ,$a_{\alpha''}$, $b_{\alpha''}$ and $c_{\alpha''}$) were plotted as a function of the applied percentage strain for ST alloy (Fig. 4-5a) and FT alloy (Fig. 4-5b), respectively. These figures will be discussed later through comparison with tensile curves.

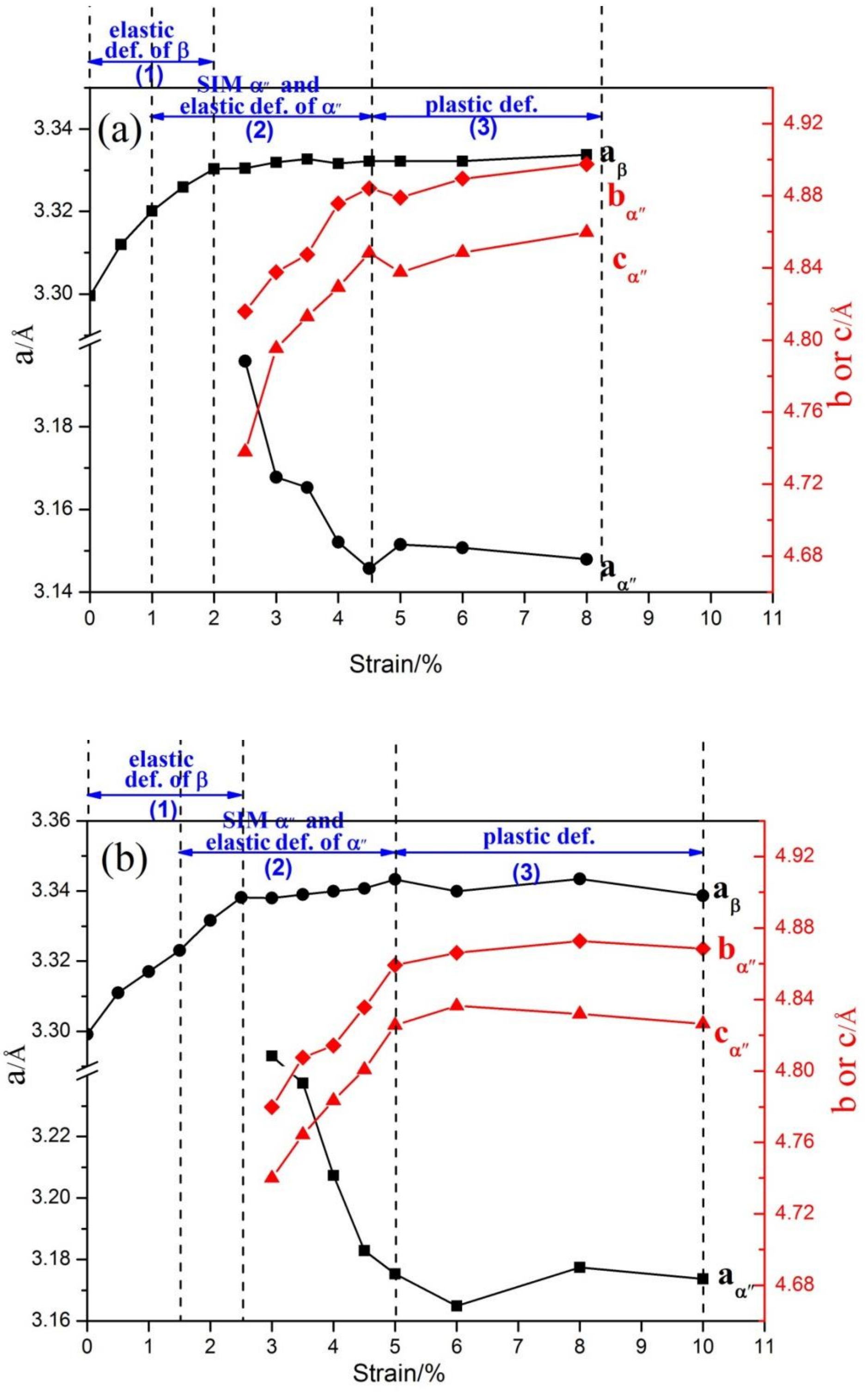

**Fig. 4-5** The calculated cell parameters of the β phase and α″ phase under loading condition for Ti2448 alloy after: (a) solution treatment at 900°C for 30min and (b) flash treatment at 700°C for 3min.

### 3.3.2 Cell parameters under unloading condition

From the unloading spectra (Fig. 4-4b and 4-4d), the angular positions of all peaks were determined to evaluate the different cell parameters and their variations under unloading. The evolution of these cell parameters ($a_{\beta}$, ,$a_{\alpha''}$, $b_{\alpha''}$ and $c_{\alpha''}$) were plotted as a function of the applied percentage strain for ST alloy (Fig. 4-6a) and FT alloy (Fig. 4-6b), respectively. It can be seen that there is nearly no variation under unloading whatever the deformation process.

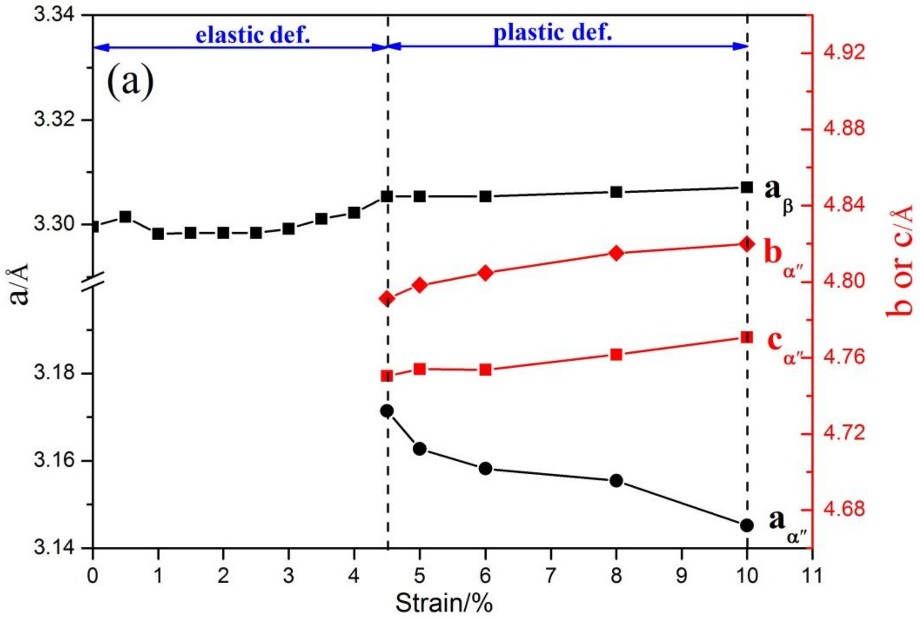

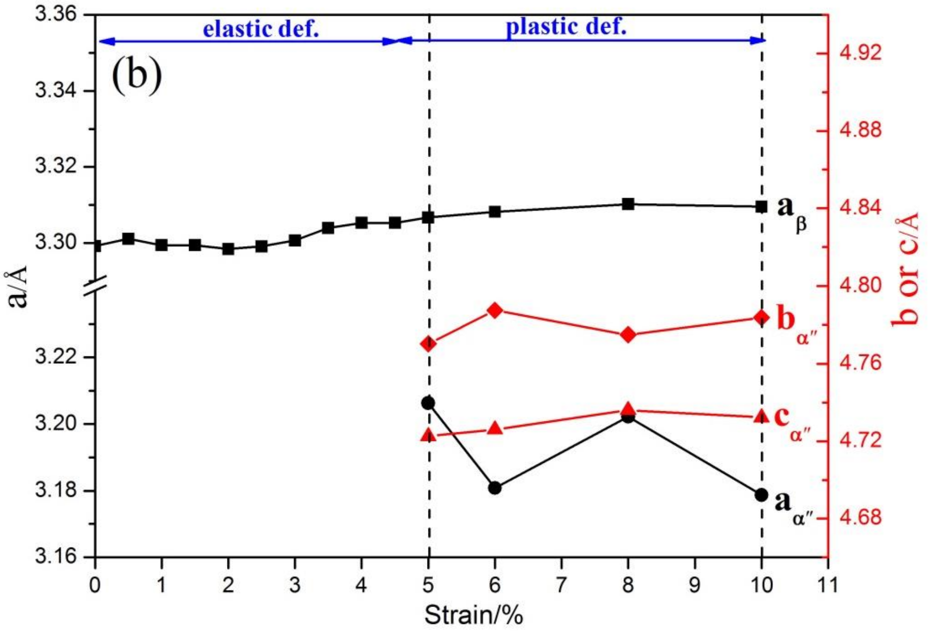

**Fig. 4-6** The calculated cell parameters of the β phase and α″ phase under unloading condition for Ti2448 alloy after: (a) solution treatment at 900°C for 30min and (b) flash treatment at 700°C for 3min.

# 4. Dynamic mechanical analysis

## 4.1 Determination of characteristic temperatures

Two important characteristic parameters: storage modulus (E′) and damping factor (Tanδ) as a function of temperature can be obtained by DMA. Fig. 4-7 displays the evolution of the E′ and the Tanδ curves upon cooling and heating as a function of temperature under an applied stress of 160MPa on Ti2448 alloy after ST, as well as the methods used to determine these characteristic temperatures.

In order to characterize the martensitic transformation in the present case, the martensite start ($M_s$) and austenite finish ($A_f$) temperatures can be evaluated on the E′ curves. The characteristic temperature of $M_s$ is the point at which the change of slope on the E′ curves occurs, and also corresponds exactly to the initial increasing point on Tanδ curve upon cooling, while the $A_f$ is determined on E′ curves upon heating. Other detected characteristic temperatures are $M_{max}$ and $A_{max}$, which correspond to the maximum SIMα″ transformation. With this method, all the characteristic temperature $M_s$, $M_{max}$, $A_f$, and $A_{max}$ can be obtained

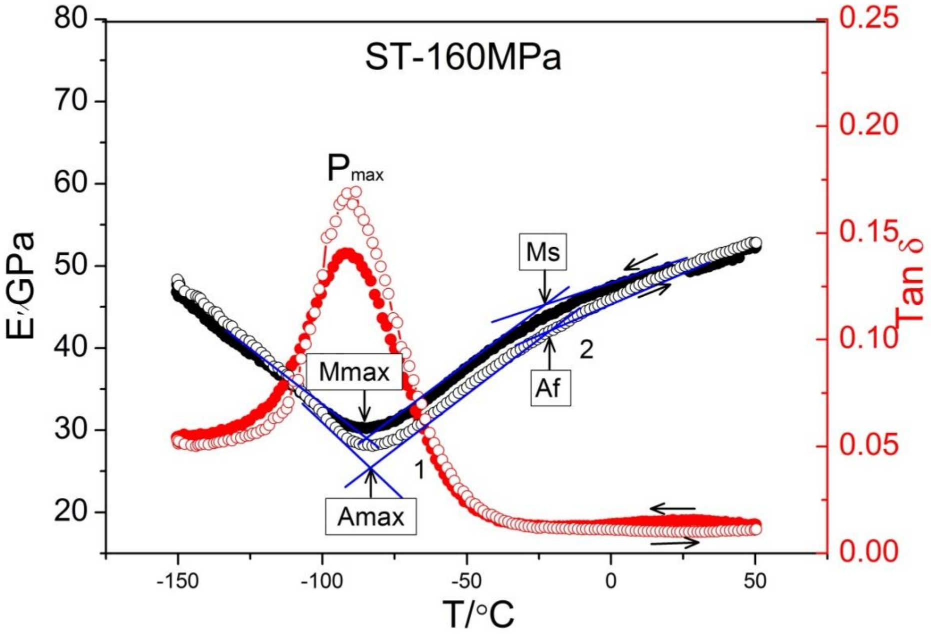

**Fig. 4-7** Storage modulus and damping factor (in black and red, respectively) under an applied stress of 160MPa during cooling and heating (in solid and open circles, respectively) for Ti2448 alloy after solution treatment (ST).

## 4.2 Evolution of storage modulus curves and damping factor curves depending on applied stresses

Fig. 4-8 displays the evolution of the storage modulus (E′) and the damping factor (Tanδ) upon cooling and heating as a function of temperature under various applied stresses for Ti2448 alloy after ST (Fig. 4-8a) and after FT (Fig. 4-8b). On these figures, E′ curves are also presented in black and Tanδ curves in red. On cooling, E′ and Tanδ curves are also represented with solid circles, while on heating, they are represented with open circles. The applied static stress ($\sigma_{stat}$) was initially fixed at 160MPa and then was subsequently increased by 40MPa after each temperature cycle until 280MPa on the same specimen. All the figures show that both the martensitic transformation on cooling and the austenitic transformation on heating are characterized by a decrease of the storage modulus and an increase of the damping factor. Thus, modulus drops and damping peaks are clearly observed.

From the DMA experiments, the martensitic transformation is particularly well highlighted by the Tanδ curve. This kind of damping peak was commonly observed in other shape memory alloys such as Ni-Ti (*Mazzolai 2007, Van Humbeeck 2003*), Ti-Nb based alloys (*Bertrand 2013, Yin 2006*) and Cu-Al-Ni alloys (*Suresh 2008*). It is well known that the reversible SIM transformation, which is accompanied by the movements of coherent austenite/martensite interfaces, can induce mechanical energy dissipation and thus constitutes an important damping source (*Van Humbeeck 2003*). Consequently, a clear damping peak is observed in the present case and its maximum ($P_{max}$) corresponds more or less to $M_{max}$. The high value of damping factor Tanδ (0.2-0.25) due to the SIM α″ transformation in the Ti2448 alloy (Fig. 4-8) shows a superior damping capacity by comparison with the other β-type Ti-Ta-Nb (*Bertrand 2013*) and Ti-Nb-Al (*Inamura 2010*) alloys under the same tensile mode under 1Hz frequency. On the other hand, higher damping capacity is observed for the ST sample by comparison with the FT sample. This is caused by the larger β grain size observed in ST that permits longer distance mobility of the α″/β interfaces.

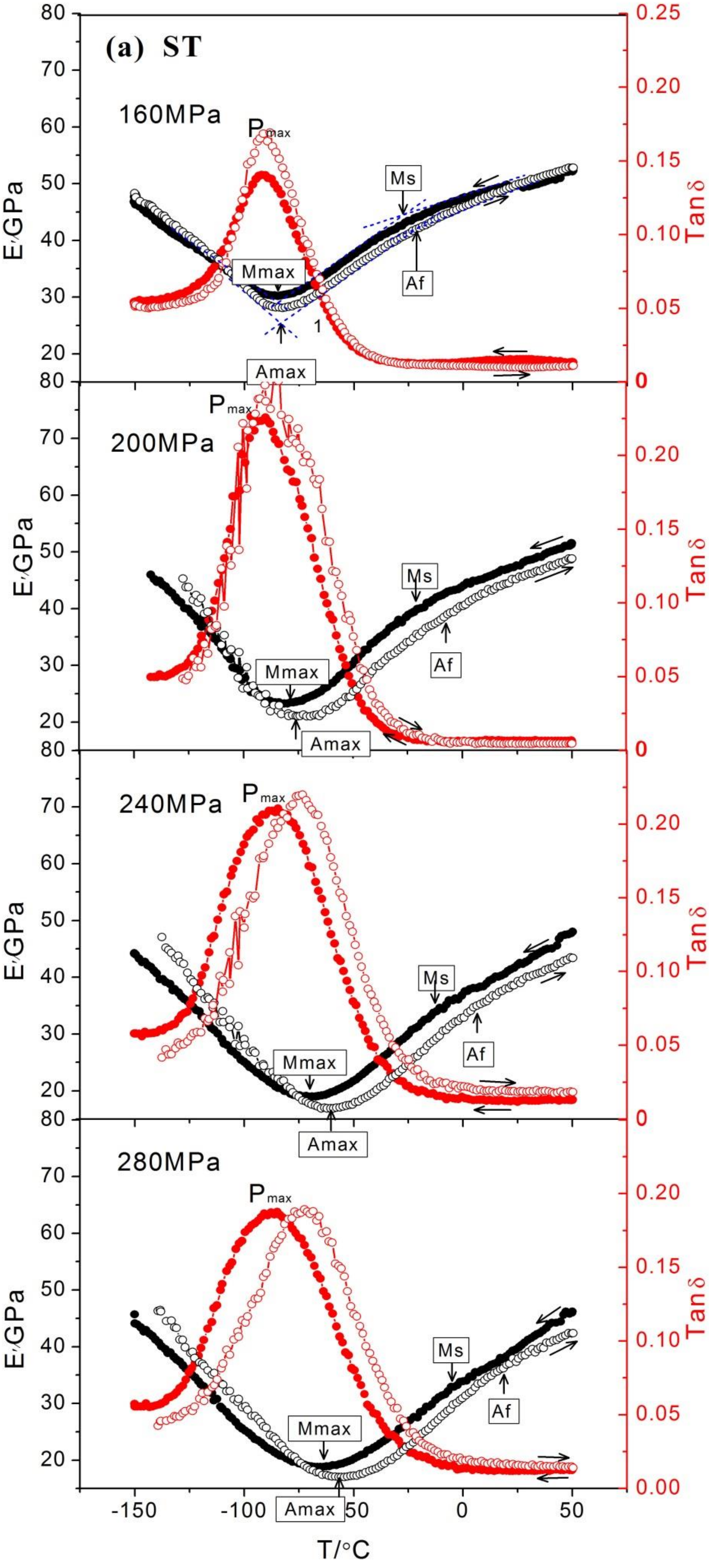
(a) ST
160MPa
200MPa
240MPa
280MPa
Pmax
Ms
Af
Mmax
Amax
1
E′/GPa
Tanδ
T/°C
80
70
60
50
40
30
20
0.25
0.20
0.15
0.10
0.05
0
0.00
-150
-100
-50
0
50

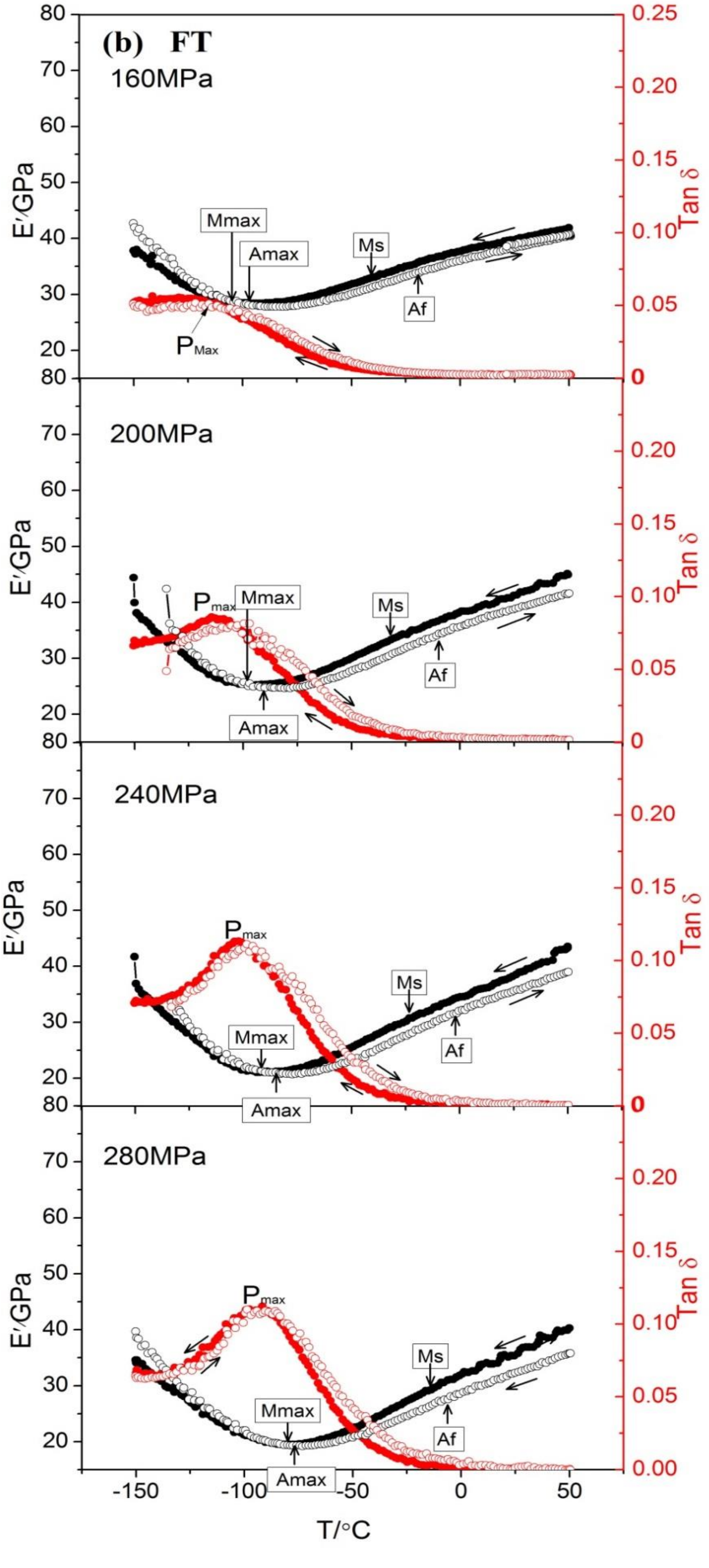
(b) FT
160MPa
200MPa
240MPa
280MPa
Mmax
Amax
Ms
Af
P_Max
P_max
E′/GPa
Tan δ
T/°C
80
70
60
50
40
30
20
0.25
0.20
0.15
0.10
0.05
0
0.00
-150
-100
-50
0
50

**Fig. 4-8** Storage modulus and damping factor (in black and red, respectively) evolutions as a function of the $\sigma_{stat}$ during cooling and heating (in solid and open circles, respectively) for Ti2448 alloy after different thermal treatment: (a) solution treatment at 900°C for 30min and (b) flash treatment at 700°C for 3min.

It has to be mentioned that the $M_f$ and $A_s$ temperatures cannot be clearly detected in the present case. This is due to the fact that the damping peak includes also the contribution of martensite/martensite interfaces movement as it was explained in a recent work (*Bertrand 2013*). The hysteretic movement of twin boundaries between martensite variants is another important damping source to dissipate mechanical energy that can overlap the movements of the austenite/martensite interfaces (*Van Humbeeck 2003*). That is also for this reason that the position of $P_{max}$ does not correspond exactly to the $M_{max,}$ especially under high applied stress.

## 4.3 Characteristic temperatures depending on applied stresses

All the detected characteristic temperatures $M_s$, $M_{max}$, $A_f$, and $A_{max}$ were plotted here as a function of the applied stress in Fig. 4-9 for ST alloy (Fig. 4-9a) and for FT alloy (Fig. 4-9b). As shown, a quite good linear fitting can be obtained in good agreement with the Clausius-Clapeyron relationship. It can be found that the slope is 0.19K/MPa for $M_s$ and $M_{max}$, 0.32K/MPa for $A_f$ and 0.24K/MPa for $A_{max}$ for the ST sample. On the other hand, all the slopes were found to be 0.20-0.22 K/MPa for the FT sample.

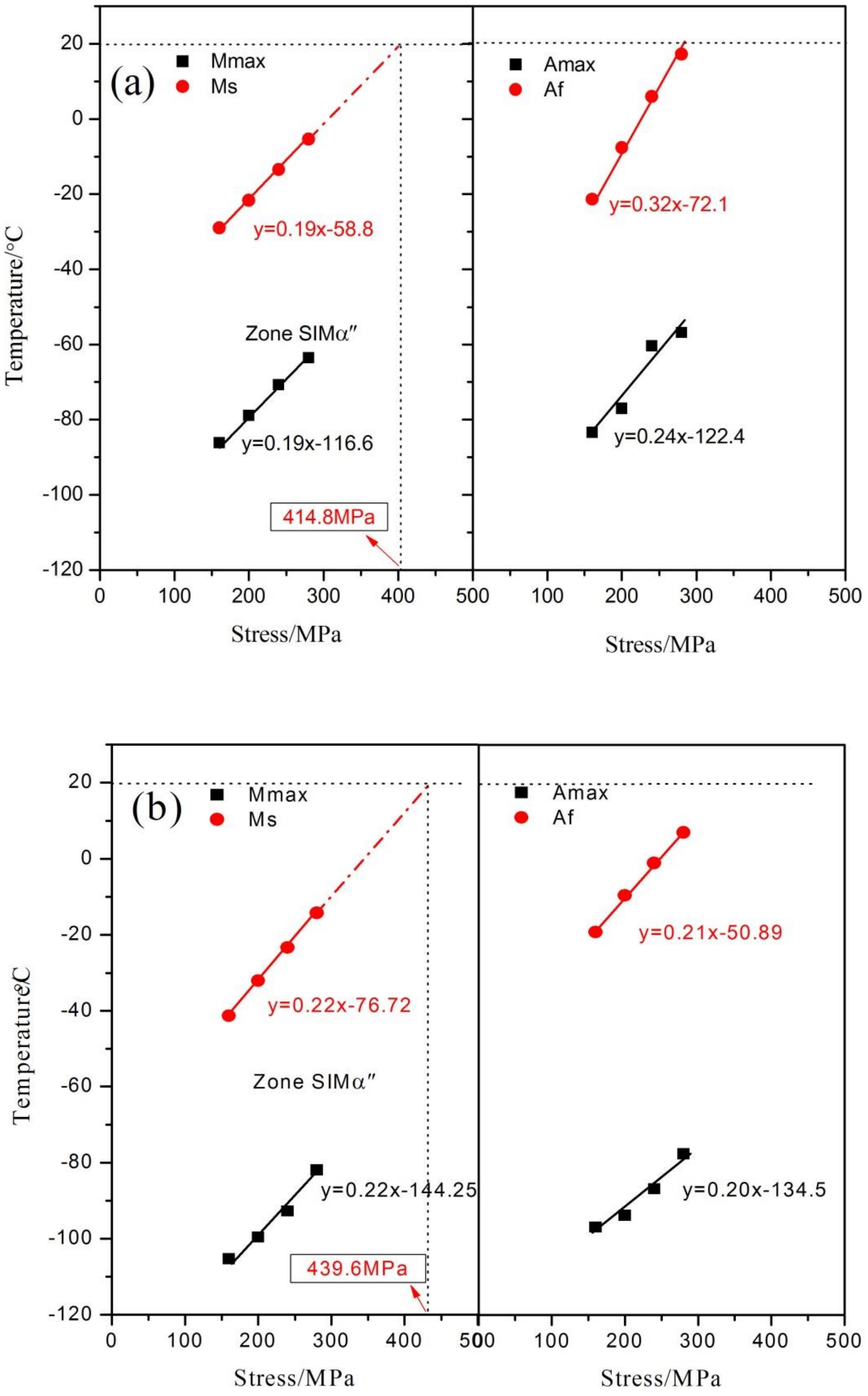

**Fig. 4-9** Characteristic temperatures of $M_s$, $M_{max}$, $A_f$ and $A_{max}$ as a function of the applied static stresses $\sigma_{stat}$ for Ti2448 alloy after different thermal treatment: (a) solution treatment at 900°C for 30min and (b) flash treatment at 700°C for 3min.

# 5. Comparison between SXRD, DMA and tensile curves

From the evolution of the different cell parameters on loading determined by SXRD (Fig. 4-5), it can be observed firstly that the β phase is elastically deformed in the 0%-2.0% strain range (Fig. 4-5a) and in the 0-2.5% strain range (Fig. 4-5b) for ST and FT alloys, respectively. As shown, the $a_\beta$ increases from 3.30 Å to 3.33 Å (in ST alloy) and from 3.30 to 3.34Å (in FT alloy). On the other hand, once the α″ phase appears, this phase is observed to be elastically deformed up to 4.5% for ST and 5% for FT, respectively. This elastic deformation is clearly observed to be accommodated by an increase of the $b_{\alpha''}$ and $c_{\alpha''}$ parameters and by a decrease of the $a_{\alpha''}$ parameter. These observations are in agreement with the tensile curves. Consequently, from both SXRD analysis and tensile tests, a three-step deformation sequence can be established as follows: firstly, the β phase is elastically deformed up to around 1.5-2% of strain in the ST alloy (2-2.5% for FT alloy); secondly, the deformation is accommodated by the SIMα″ transformation, which is elastically deformed up to 4.5% in ST (5% in FT); from this value, both residual β phase and α″ phase start to be deformed plastically.

From the tensile curves obtained at room temperature (Fig. 4-2), the critical stress inducing the SIM α″ transformation was found to be 414MPa for ST sample and 440MPa for FT sample, respectively. From the DMA analyses, the critical stress inducing the SIM α″ transformation at room temperature can also be obtained by extrapolating the data plotted in Fig. 4-9 (dot-lines). Indeed, at 20 ℃ the critical stress corresponding to the $M_s$ value was found to be 415MPa for ST sample and 440MPa for FT sample, respectively, as it is indicated on Fig. 4-9a and 4-9b. These critical stress values coincide perfectly with those obtained by tensile tests meaning that DMA analysis and mechanical tensile tests are in very good agreement.

In this chapter, the SIM α″ transformation could be clearly evidenced by tensile tests, SXRD and DMA. However, the SIM α″ phase morphology could not be observed in the present study although great efforts have been done by using transmission electron microscopy (TEM). Indeed, only the β phase was observed by TEM. One reason can be due to the fact that it is well known that spontaneous strain relaxation occurs during the preparation of the thin TEM specimens and consequently the SIM α″ phase could have been transformed back to the β phase (*Lütjering G 2007*).

Another reason can be linked with very recent works concerning the presence of nanodomains in this kind of alloy (*Liu 2013*), which were first reported by Miyazaki et al. (*Kim 2013, Tahara 2011*). As reported, nanodomains consist of nanosized modulated domain structure distributed homogeneously and randomly in the β phase and acted as obstacles for the long-range martensitic transformation. Consequently, nanodomains observation by conventional TEM remains tricky and high resolution

TEM investigations are required for such characterization.

## 6. Conclusions

In this work, the martensitic transformation occurring in the superelastic Ti-24Nb-4Zr-8Sn alloy was investigated by tensile tests, *in situ* synchrotron X-ray diffraction (SXRD) and dynamic mechanical analysis (DMA). The SXRD results clearly showed the diffraction peaks related to the $\alpha''$ and $\beta$ phases and their evolution under loading and unloading conditions, have highlighted the reversible stress-induced martensitic (SIM) transformation. Consequently, a three steps deformation sequence was established from both SXRD analysis and tensile test characterization. On the other hand, the characteristic temperatures related to the martensitic transformation under different applied stresses have been determined from the storage modulus and the damping curves by DMA analysis. A very good accordance concerning the critical stress inducing the martensitic transformation was obtained by comparing the results obtained from SXRD, DMA and tensile tests. A brief of conclusions can be made as follows:

(1) By *in situ* SXRD, the typical diffraction peaks of the $\beta$ and $\alpha''$ phases during loading and unloading were clearly observed and the reversible transformation between the $\beta$ phase and the SIM $\alpha''$ phase was evidenced for both ST and FT states. On the other hand, variations of the $\beta$ and $\alpha''$ cell parameters were characterized in both loading and unloading conditions.

(2) From both SXRD analysis and tensile tests, a three steps deformation sequence could be established as follows: firstly, the $\beta$ phase is elastically deformed up to around 1.5-2% of strain in the ST alloy (2-2.5% for FT alloy); secondly, the deformation is accommodated by the SIM $\alpha''$ transformation, which is elastically deformed up to 4.5% in ST (5% in FT); from this value, both residual $\beta$ phase and $\alpha''$ phases start to be deformed plastically.

(3) From the DMA experiments, clear damping peaks were observed and the characteristic temperatures detected ($M_s$, $M_{max}$, $A_f$, and $A_{max}$) were plotted as a function of the applied stress. A quite good linear fitting could be obtained in agreement with the Clausius-Clapeyron relationship.

(4) A very good accordance concerning the critical stress inducing the martensitic transformation was obtained by comparing the results obtained from SXRD, DMA and conventional tensile tests.

# References

Al-Zain Y., Kim H.Y., Koyano T., Hosoda H., Nam T.H., Miyazaki S., *Anomalous temperature dependence of the superelastic behavior of Ti–Nb–Mo alloys*. Acta Materialia, **59**, p1464, 2011.

Bertrand E., Castany P., Gloriant T., *Investigation of the martensitic transformation and the damping behavior of a superelastic Ti-Ta-Nb alloys*. Acta Materialia, **61**, p511, 2013.

Hao Y.L., Li S.J., Sun B.B., Sui M.L., Yang R., *Ductile titanium alloy with low Poisson's ratio*. Physical Review Letter, **98**, p216405, 2007

Hao Y.L., Li S.J., Sun S.Y., Zheng C.Y., Hu Q.M., Yang R., *Super-elastic titanium alloy with unstable plastic deformation*. Applical Physics Letters, **87**, p091906, 2005.

Kim H.Y., Wei L., Kobayashi S., Tahara M., Miyazak S., *Nanodomain Structure and Its Effect on Abnormal Thermal Expansion Behavior of a Ti-23Nb-2Zr-0.7Ta-1.2O Alloy*. Acta Materialia, **61**, p4874, 2013.

Li S.J., Cui T.C., Li Y.L., Hao Y.L., Yang R., *Ultrafine-grained β-type titanium alloy with nonlinear elasticity and high ductility*. Applied Physics Letters, **92**, p043128, 2008

Liu J.P., Wang Y.D., Hao Y.L., Wang Y.Z., Nie Z.H., Wang D., Ren Y., Lu Z.P., Wang J.G., Wang H.L., Hui X.D., Lu N., Kim M.J., Yang R., *New Intrinsic Mechanism on Gum-Like Superelasticity of Multifunctional Alloys*, Scientific Reports; **3**, p2156, 2013.

Liu Y., Van Humbeeck J., Stalmans R., Delaey L., *Some aspects of the properties of NiTi shape memory alloy*. Journal of Alloys and Compounds, **247**, p115, 1997.

Lovey F.C., Torra V., *Shape memory in Cu-based alloys: phenomenological behavior at the mesoscale level and interaction of martensitic transformation with structural defects in Cu-Zn-Al*. Progress in Materials Science, **44**, p189, 1999.

Lütjering G., Williams J.C., *Titanium*. (2nd ed.)Springer-Verlag, Berlin, p141, 2007.

Mazzolai F.M., Biscarini A., Coluzzi B., Mazzolai G., Villa E., Tuissi A., *Low frequency internal friction of hydrogen-free and hydrogen-doped NiTi alloys*. Acta Materialia; **55**, p4243, 2007.

Mercier O., Melton K.N., De Préville Y., *Low-frequency internal friction peaks associated with the martensitic phase transformation of NiTi*. Acta Metallurgica, **27**, p1467, 1979.

Otsuka K., Ren X., *Physical metallurgy of Ti–Ni-based shape memory alloys*. Progress in Materials Science, **50**, p511, 2005.

Suresh N., Ramamurty U., *Aging response and its effect on the functional properties of Cu-Al-Ni* *shape memory alloys*. J Alloys Compd, **449**, p113, 2008;.

Tahara M., Kim H.Y., Hosoda H., Miyazaki S., *Cyclic deformation behavior of a Ti–26 at.% Nb alloy*. Acta Materialia, **57**, p2461, 2009.

Tahara M., Kim H.Y., Inamura T., Hosoda H., Miyazaki S., *Lattice modulation and superelasticity in oxygen-added beta-Ti alloys*. Acta Materialia, **59**, p6208, 2011.

Tobe H., Kim H.Y., Inamura T., Hosoda H., Nam T.H., Miyazaki S., *Effect of Nb content on deformation behavior and shape memory properties of Ti-Nb alloys*. Journal of Alloys and Compounds, **577S**, pS435, 2013.

Van Humbeeck J., *Damping capacity of thermoelastic martensite in shape memory alloy*. Journal of Alloys and Compounds, **355**, p58, 2003.

Yang Y., Castany P., Cornen M., Thibon I., Prima F., Gloriant T., *Texture investigation of the superelastic Ti-24Nb-4Zr-8Sn alloy*. Journal of Alloys and Compounds, **591**, p58, 2014.

Yang Y., Castany P., Cornen M., Prima F., Li S.J., Hao Y.L., Gloriant T., *Characterization of the martensitic transformation in the superelastic Ti-24Nb-4Zr-8Sn alloy by in situ synchrotron X-ray diffraction and dynamic mechanical analysis*, Acta Materialia, **88**, p25, 2015.

Yin F., Iwasaki S., Ping D., Nagai K., *Snoek-type high damping alloys realized in β-Ti alloys with high oxygen solid solution*. Advanced Materials, **18**, p1541, 2006.
ter 2011; 59: 6208.

# Chapter V: Plastic deformation mechanisms in the Ti2448 alloy

# 1. Introduction

## 1.1 Stress-induced martensitic $\alpha''$ phase

Stress-induced martensitic (SIM) transformation between austenic $\beta$ phase (bcc) and martensitic $\alpha''$ phase (orthorhombic) is known to be the origin of superelasticity in metastable $\beta$ titanium alloys, characterized by a large pseudo-elastic recovery strain. The present investigated Ti-24Nb-4Zr-8Sn (wt. %, Ti2448 for short) alloy, exhibits the superelastic behavior with the as-quenched microstructure composed of fully metastable $\beta$ phase at room temperature (*Hao 2005, Hao 2007, Yang 2014*). With this alloy, the maximum recoverable strain of 3.3 % can be obtained combining good mechanical properties. Indeed, the SIM transformation has already been clearly evidenced in the Ti2448 alloy by techniques of *in situ* synchrotron X-ray diffraction (SXRD) and dynamic mechanical analysis (DMA) (*Chapter 4, Yang 2015*).

Concerning the microstructural evidences, the needle-like SIM $\alpha''$ phase could be observed by TEM in some deformed metastable $\beta$ titanium alloys, such as Ti-35Nb-2Ta-3Zr (wt. %) (*Wang 2008*), Ti-40Nb (wt. %) alloy (*Ping 2008*), Ti-26Nb and Ti-20Nb-6Zr (at. %) alloys (*Sun 2011*), Ti-12Mo (wt. %) alloy (*Sun 2013*), Ti-24Nb-0.5O and Ti-24Nb-0.5N alloys (at. %) (*Ramarolahy 2012*). What is worth noting is, the SIM $\alpha''$ phase can form as single variant or twinned variants. Examples of the twinned variants were found in Ti-16Nb-10Zr (at. %) (*Zhang 2013*), Ti-12Mo (wt. %) (*Sun 2013*) and Ti-40Nb (wt. %) alloys (*Ping 2008*). However, the twinning elements of the SIM $\alpha''$ phase were not mentioned clearly. Furthermore, there are still cases where the SIM $\alpha''$ phase is tricky to be captured such as in the present Ti2448. The reason of failure to observe the SIM $\alpha''$ phase can be attributed to the unstable character of SIM $\alpha''$ phase which could have been transformed back to the $\beta$ phase easily via spontaneous strain relaxation during the preparation of thin foils for TEM observation (*Lütjering 2007*). Under this circumstance, the investigation of SIM $\alpha''$ phase could resort to the crystallographic analysis of the corresponding $\beta$ phase which was relaxed from the SIM $\alpha''$ phase.

## 1.2 Lattice correspondence between $\beta$ and $\alpha''$ phases

According to the phenomenological theory of martensite crystallography (PTMC) (*Lieberman 1955, Klostermann 1972, Wayman 1994*), the martensitic transformation from the $\beta$ phase to $\alpha''$ phase keeps a strict crystallographic relationship which provides a useful method to presume the orientation of $\alpha''$ phase based on the known orientation of β phase. The schematic of the crystal structures of the β phase and α″ phase was shown in Fig. 1-9 (*Kim 2006*). The lattice correspondence during the SIM transformation between β and α″ phases can be expressed as follows:

$$[100]_{\alpha''} - [100]_{\beta},\ [010]_{\alpha''} - [01\bar{1}]_{\beta},\ [001]_{\alpha''} - [011]_{\beta}$$

Therefore, six variants of martensitic α″ phase can be derived, and these were designated as V1, V2, V3, V4, V5 and V6 in Table 1-5 (*Chai 2009*). Based on these crystallographic relationships, the crystallographic orientation of the six variants of α″ phase can be deduced from the crystallographic orientation of the corresponding β phase.

## 1.3 Crystallographic theory of twinning

Taking the possibility of forming twinned α″ phase into consideration, the crystallographic theory of twining needs to be illustrated. Fig. 5-1a represents a sphere cut from a single crystal (*Cahn 1953*). In the classic theory of deformation twinning, the original lattice is re-orientated by atom displacements which are equivalent to a simple shear of the lattice points, or of some integral fraction of these points (*Christian 1995*). For a specific twin, there are four essential elements denoted $K_1$, $K_2$, $\eta_1$ and η in Fig. 5-1a. $K_1$ is the twinning plane or invariant plane; $\eta_1$ is the direction of shear. Any point above $K_1$ moves parallel to $\eta_1$ through a distance proportional to its own height above $K_1$. The magnitude of shear s is defined as the distance through which a point at distance unity from $K_1$ moves; it is always such that each atomic plane parallel to $K_1$ moves relatively to the neighboring plane through a distance which is considerable less than the repeated distance along $\eta_1$. There is a second undistorted plane or reciprocal plane $K_2$, apart from the $K_1$, which remains unchanged after twinning. After twinning, $K_2$ still makes an angle 2ϕ with $K_1$. The plane including $\eta_1$ and normal to $K_1$ is called the plane of shear. The line of intersection of $K_2$ with the plane of shear is the direction $\eta_2$.

Due to the essential point about twinning that the symmetry and structure of the crystal is the same after twinning as it is beforehand mentioned, twins are classified as type I ($\eta_2$ and $K_1$ are rational, but $\eta_1$ and $K_2$ can be irrational) and type II ( $\eta_1$ and $K_2$ are rational, but $\eta_2$ and $K_1$ can be irrational). The type I and type II are illustrated in Fig. 5-1b and c, respectively. Thus, the orientation of the new twin lattice relative to the original lattice is a mirror reflection regarding $K_1$ plane for a type I twin and is a rotation of $180^o$ around $\eta_1$ for a type II twin (*Cahn 1953*). It is also possible for all four elements $K_1$, $K_2$, $\eta_1$ and $\eta_2$ to be rational, this kind of twin is thus called compound twin and is the more probable for the higher crystal symmetry, such as in cubic and hexagonal metals. The type I and type II are more common for less high crystal symmetry, like in orthorhombic uranium phase (*Cahn 1951, Frank 1953*).

As there are very few reports about the twinning elements of orthorhombic SIM α″ phase, the well investigated twinning elements for orthorhombic uranium will be taken as references because of the strong similarity of both structures that have the same space group and similar positions of atoms (*Cahn 1951, Frank 1953, Cahn 1953, Crocker 1965, Field 2009*). Table 5-1 presents the top priority twinning elements for the orthorhombic uranium (*Cahn 1951, Frank 195*3), which have been clearly evidenced by both theoretical calculations and experimental observations.

**Table 5-1** Most frequently observed twinning modes in orthorhombic uranium.

| K1 | K2 | η1 | η2 | Type |
|---|---|---|---|---|
| $(\mathbf{130})$ | $(1\bar{1}0)$ | $[3\bar{1}0]$ | $[110]$ | Compound |
| $(\mathbf{1\bar{7}2})$ | $(112)$ | $[312]$ | $[3\bar{7}2]$ | Type II |
| $(\mathbf{112})$ | $(1\bar{7}2)$ | $[3\bar{7}2]$ | $[312]$ | Type I |
| $(\mathbf{121})$ | $(1\bar{4}1)$ | $[3\bar{2}1]$ | $[311]$ | Type I |

In this study, solution treated alloy and flash treated alloy with a prior cold rolling reduction rate of 94% (abbreviated as ST and FT) were both used. The microstructures of ST alloy deformed to different deformation strains (3 % and 5 %) were observed by techniques of optical microscopy, electron backscattered diffraction (EBSD) and transmission electron microscopy (TEM) in order to explore the plastic deformation mechanisms of the ST alloy. Additionally, TEM observations on FT alloy deformed to 5 % was also conducted for comparison. Therefore, this chapter is mainly focused on ST alloy except few observations on FT alloy.

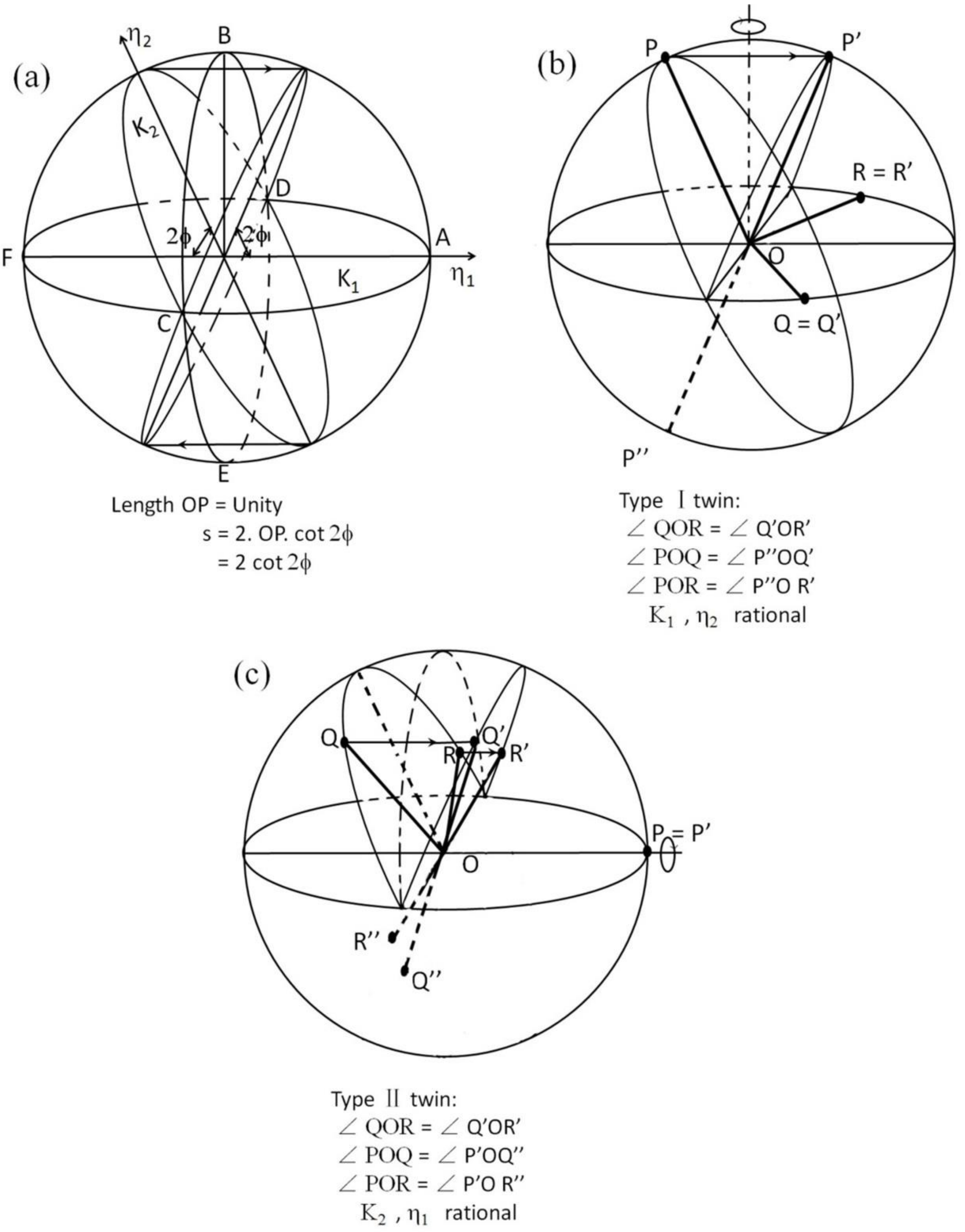
(a)
η2
B
K2
D
2ϕ
2ϕ
F
A
η1
K1
C
E
Length OP = Unity
s = 2. OP. cot 2ϕ
= 2 cot 2ϕ
(b)
P
P'
R = R'
O
Q = Q'
P''
Type I twin:
∠ QOR = ∠ Q'OR'
∠ POQ = ∠ P''OQ'
∠ POR = ∠ P''O R'
K1 , η2 rational
(c)
Q
Q'
R
R'
P = P'
O
R''
Q''
Type II twin:
∠ QOR = ∠ Q'OR'
∠ POQ = ∠ P'OQ''
∠ POR = ∠ P'O R''
K2 , η1 rational

**Fig. 5-1** (a) Four elements of a twin: the twinning and reciprocal twinning planes are $K_1$ and $K_2$, twining and reciprocal twinning directions are $\eta_1$ and $\eta_2$, respectively, (b) type I twin and (c) type II twin (*Cahn 1953*).

# 2. Experimental results

## 2.1 Tensile behavior and optical microstructure of ST alloy

Fig. 5-2 displays the conventional and cyclic tensile curves for the ST Ti2448 alloy. Elongation at rupture, ultimate tensile strength and incipient Young’s modulus were measured to be around 10 %, 877 MPa and 58 GPa, respectively. A double yielding phenomenon or a “plateau” and elastic hysteresis loops associated with the SIM transformation has occurred. In order to explore the plastic deformation mechanisms, two samples have been taken from interrupted tensile tests as indicated on the Fig. 5-2: sample A after a deformation of 3% and sample B after a deformation of 5%. The insert figure (*Yang 2015*) presents the partial SXRD profile of each sample under loading condition and after unloading. Therefore, the phase composition for sample A is α″+β under loading and only β after unloading. Similarly, the microstructure of the sample B consists mainly of α″ phase under loading and α″+β after unloading.

The optical microstructures for sample A and sample B deformed to different strains followed by stress releasing were shown in Fig. 5-3a and 5-3b, respectively. In Fig. 5-3a, the equiaxed grain with grain size of 50 μm can be observed in the sample A without any visible trace of SIM transformation due to the complete reversibility of SIM transformation as proved by the only β peaks in the insert SXRD profile in Fig. 5-2. When the applied strain increased to 5 %, quite a quantity of unknown deformation band can be observed in Fig. 5-3b for the sample B. These bands were thought to be linked with the SIM transformation as the phase composition for this sample under loading is nearly 100% of martensite.

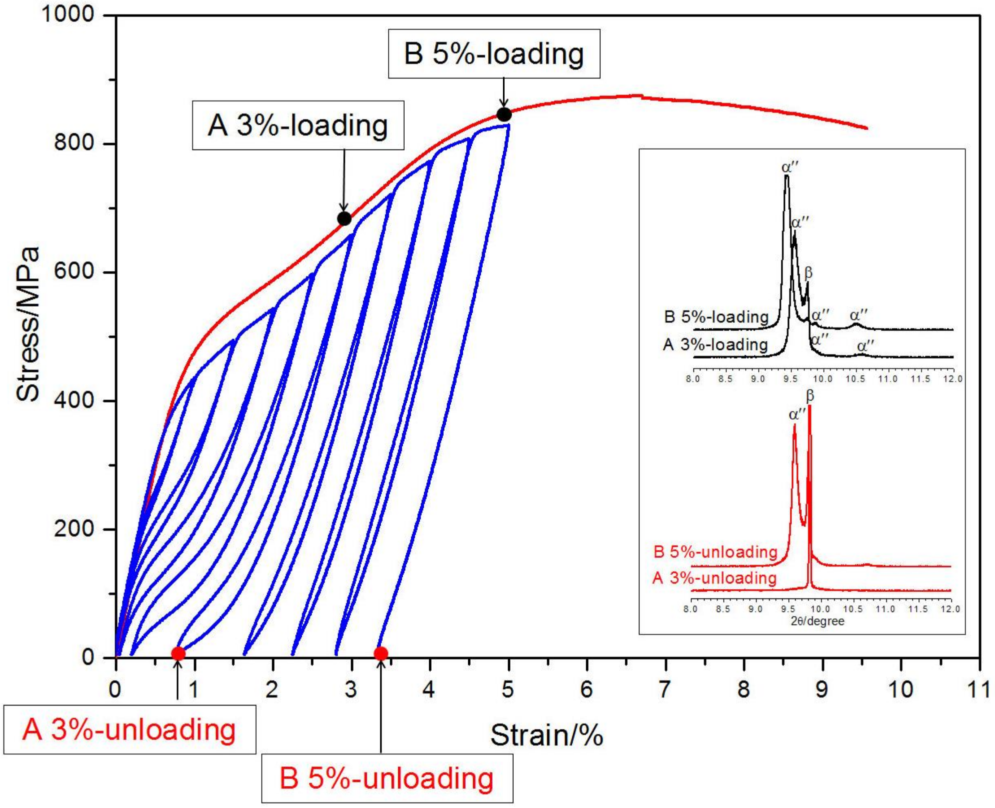

**Fig. 5-2** Conventional and cyclic tensile curves of as-quenched Ti2448 alloy with the two samples taken from interrupet tests: A after 3% strain and, B after 5% strain ; the insert figure shows the phase composition for each sample from *in situ* SXRD experiments (*Yang 2014b*).

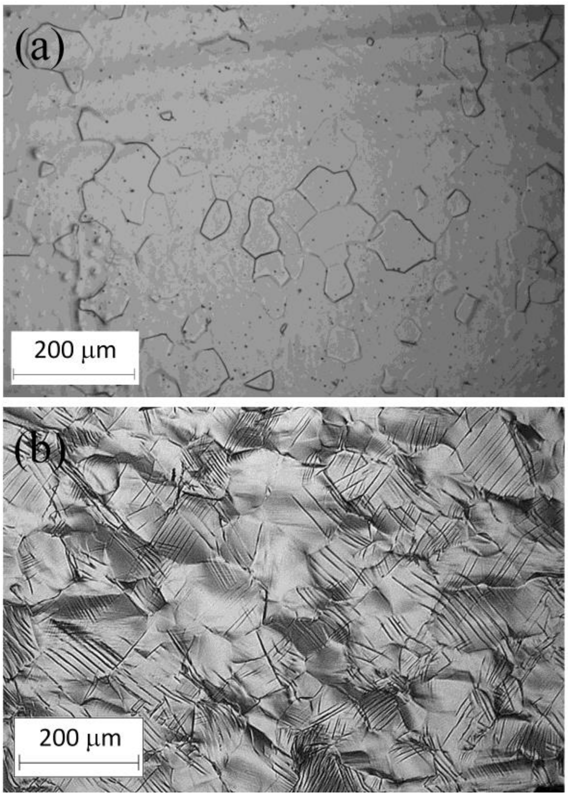

**Fig. 5-3** The optical microstructures of (a) sample A and (b) sample B.

## 2.2 EBSD analysis of ST alloy

EBSD was employed for further observation of deformation microstructures. The image quality (IQ) maps as well as [001] inverse pole figure (IPF) for sample A and sample B were shown in Fig. 5-4 and Fig. 5-5, respectively. The IQ map constructed from electron backscattered diffraction data provides useful visualizations of microstructure; its contrast could arise from a variety of factors like phase, strain, topography and grain boundaries. The IPF map includes the crystallographic orientation of each grain.

In Fig. 5-4a, the IQ map only shows grain boundaries with strong contrast in which atomic planes are not perfectly diffracting. The [001] IPF map in Fig. 5-4b reveals a strong texture of <111> // ND which is in accordance with the γ-fiber texture analyzed by XRD (*Yang 2014*). However, no martensitic phase or deformation bands can be detected on both the IQ and IPF maps for the sample A.

In Fig. 5-5, deformation bands with wideness of 1-2 μm was strongly contrasted on the IQ map (Fig. 5-5a). However, the [001] IPF (Fig. 5-5b) containing crystallographic orientations cannot provide useful information for indexation of these bands. An enlarged area in Fig. 5-5d revealed the very low indexation resolution in these bands. Compared to a similar deformation microstructure in Fig. 5-5c for another β metastable superelastic Ti-24Nb-0.5O alloy deformed to 6 % in which the {332}<113> twins was unambiguously identified by a misorientation of 50.5$^{o}$ around the <110> common direction (*Ramarolahy 2012*), the deformation bands in present Ti2448 alloy after deformation to 5 % strain was thought to contain probably a complex microstructural hierarchy.

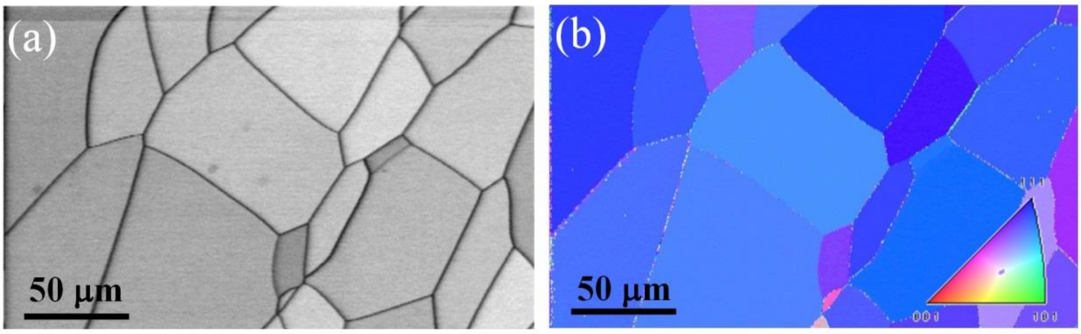

**Fig. 5-4** EBSD observations on the sample A including: (a) the image quality map and (b) the [001] inverse pole figure map with an insert of color code.

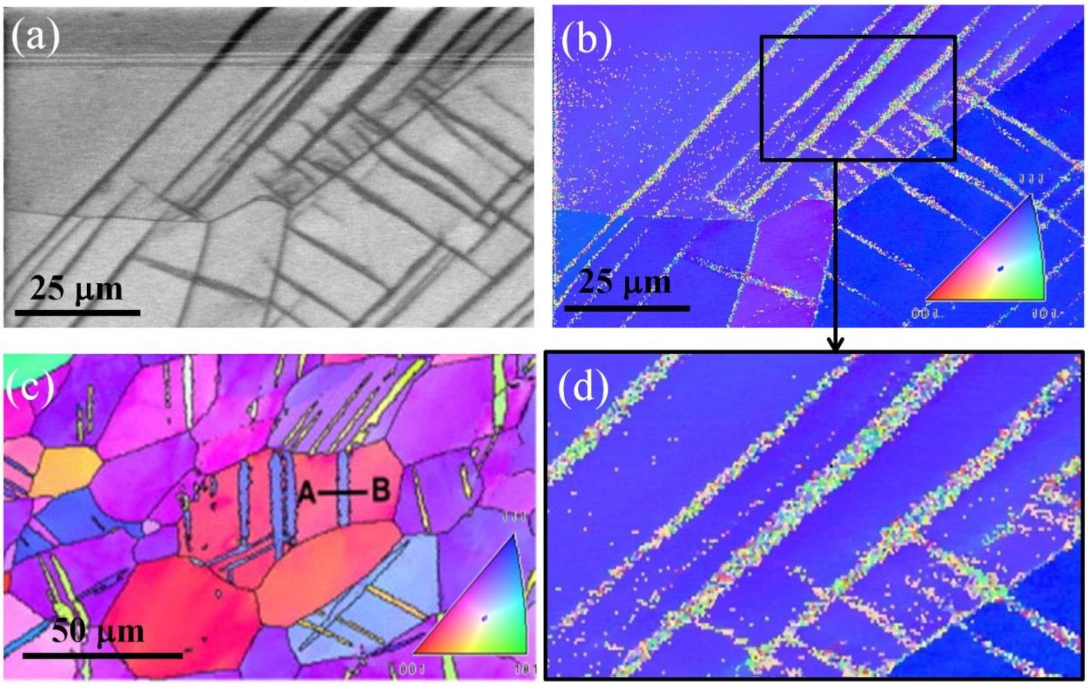

**Fig. 5-5** EBSD observations on the sample B including: (a) the image quality map, (b) the [001] inverse pole figure map, (d) an enlarged zone implying the band has a more complex structure which is different to the (c) deformation band obtained from a superelastic Ti-24Nb-0.5O alloy deformed to 6%.

## 2.3 TEM observations on the deformation twining of ST alloy

Fig. 5-6a shows a TEM bright-field image (BFI) obtained from the sample A deformed at 3% strain. A thin primary band with wideness of dozens of nanometers was observed. Fig. 5-6b shows a selected area electron diffraction pattern (SAED) taken from this region. Fig. 5-6c shows the dark-field image (DFI) highlighted with the diffraction spot encircled in Fig. 5-6b. The key diagram in Fig. 5-6d illustrated the crystallographic relationship between the primary thin band and its surrounding matrix was {332}<113> β twinning. Due to the very few quantity of such bands observed by TEM and to their small size, this kind of primary band was not visible in optical microstructure and EBSD maps.

Fig. 5-7a presents a BFI of one single deformation band with microstructural hierarchy in the sample B deformed at 5% strain. A SAED (Fig. 5-7b) obtained from this region revealed the existence of β phase and ω phase only. In order to differentiate the components, DFIs in Fig. 5-7c, Fig. 5-7d, Fig.5-7e and Fig. 5-7f were imaged with the diffraction spots marked with blue, green, red and white circles in Fig. 5-7b, respectively. For accurate description of the deformation microstructure, the four components in Fig. 5-7c, Fig. 5-7d, Fig.5-7e and Fig. 5-7f were named primary band, secondary band, matrix and interfacial ω phase, respectively. The key diagram presented in Fig. 5-7g demonstrated the {332}<113> β-twinning relationship between the primary band and secondary band which was observed frequently in deformed metastable β titanium alloys *(Oka 1978, Hanada 1984, Hanada 1986, Hanada 1987, Sun 2011, Ramarolahy 2012, Tobe 2013*). However, the crystallographic relationship between the primary band and matrix does not correspond to any well defined orientation relationship. This is most probably due to the fact that the original orientation relationship between the matrix and the primary band has been modified by the occurrence of secondary twinning.

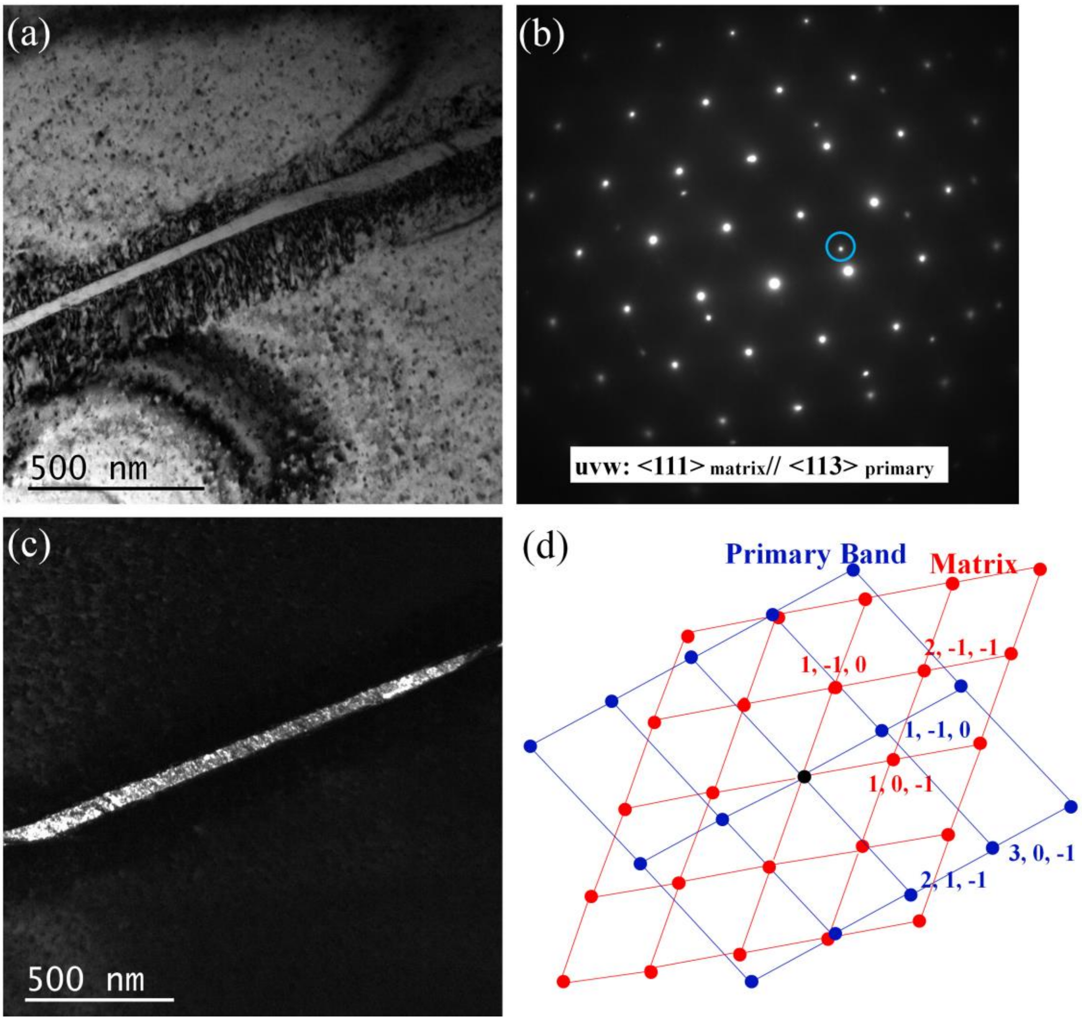

**Fig. 5-6** The TEM observations on the sample B: (a) a bright field image showing a primary deformation band, (b) the corresponding selected area electron diffraction pattern, (c) the dark field image corresponding to the blue circle surrounding spot in (b) and (d) the key diagram.

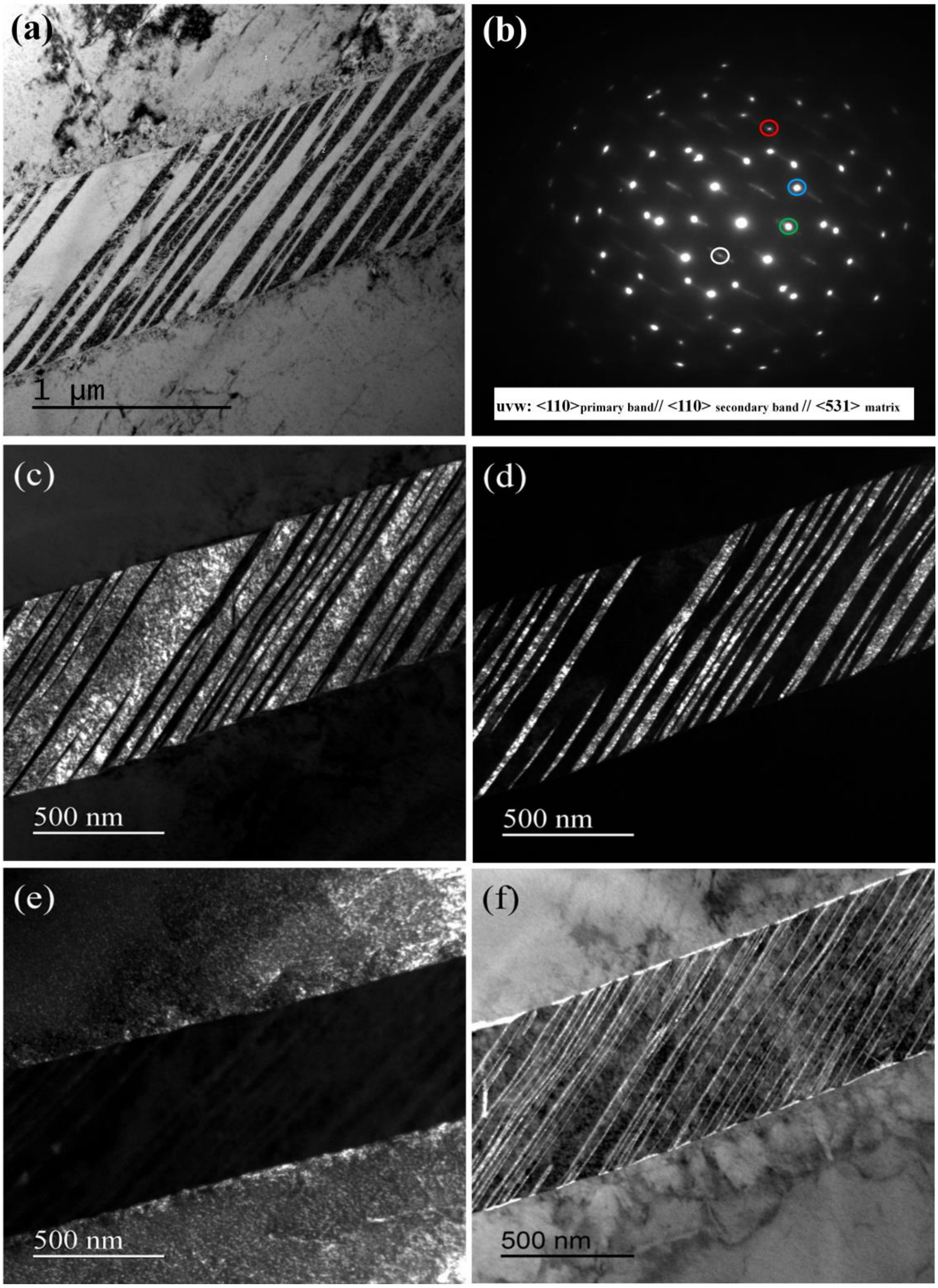
(a)
1 µm
(b)
uvw: <110>primary band// <110> secondary band // <531> matrix
(c)
500 nm
(d)
500 nm
(e)
500 nm
(f)
500 nm

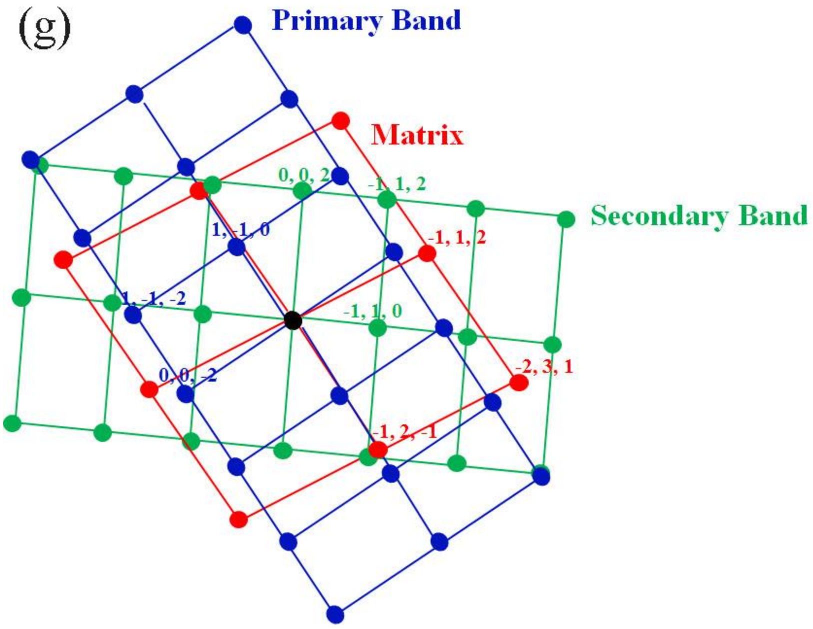

**Fig. 5-7** The TEM observations on the sample B: (a) a bright field image (BFI) presenting a complex deformation band, (b) the corresponding selected area electron diffraction pattern, (c) (d) (e) and (f) the dark field images (DFI) corresponding to the diffraction spots surrounded by blue, green, red and white circles, respectively, inside the SADP and (g) the key diagram of the SADP.

## 2.4 TEM observations of dislocations in ST and FT alloys

As a commonly-known plastic deformation mechanism, dislocation movements were also observed in metastable β titanium alloys (*Castany 2011, 2012*). In the present ST and FT Ti2448 alloy, the dislocations observation was presented in Fig. 5-8.

For the sample B of ST alloy deformed to 5% strain, some screw dislocations were observed in the β matrix between the deformation twinning bands (signified with a white arrow) in Fig. 5-8a,. For FT alloy, the original microstructure without introduction of plastic deformation shows an inhomogeneous grain size in Fig. 5-8b. After deformed to 5 % strain, SIM transformation occurred (*Yang 2015*) which could reverse completely in the TEM sample proved by Fig. 5-8c where only dislocations were left inside the grains. In addition, no twinning was observed in the FT alloy indicating an effect of the grain size on the nucleation of twins.

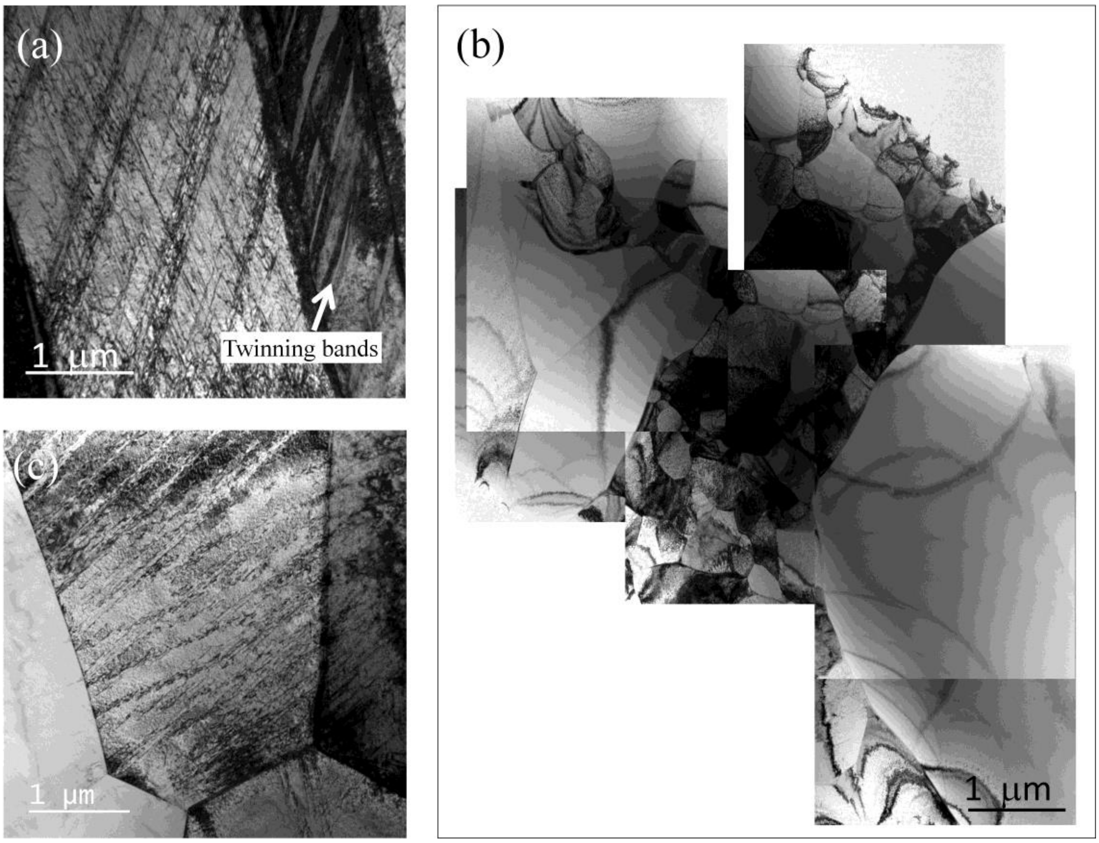

**Fig 5-8.** The TEM observations on the (a) sample B of ST alloy showing the dislocations in the β matrix between the twinning bands, (b) initial microstructure of the FT alloy showing the grain size is inhomogeneous and (c) FT alloy deformed to 5 % followed by stress release indicating there is no martensite left and no twinning bands.

# 3. Discussion

## 3.1 Determination of twinning systems in ST alloy

The SIM transformation was obviously evidenced with SXRD profiles in Fig. 5-2 for the ST Ti2448 alloy. However, only β phase and a small amount of interfacial ω phase were observed by TEM. This means the microstructure observed by TEM is not the real deformation structure but a resulting relaxed microstructure wherein all martensite has transformed back to β phase. According to that, the real deformation microstructure existing under loading condition can be tried to be determined using the orientation relationship between β and α" phases. Based on the known β orientation determined by TEM, the corresponding six variants (V1-V6) of α″ phase can thus be subsequently deduced according to the lattice correspondence shown in Fig. 1-9 and Table 1-5. This method was used for both the sample A and sample B in order to presume their deformation microstructure of the α″ phase before releasing the stress.

For the sample A (deformed at 3%), according to the TEM observations in Fig. 5-6, the crystallographic orientations of both β-matrix and β-primary band can be represented by stereographic projections of the three basic poles (1 0 0), (0 1 0) and (0 0 1) in top of Fig. 5-9a and 5-9b. For either β-matrix or β-primary, the six possible α″-variants (V1-V6) were also presented in Fig. 5-9. It is demonstrated clearly with stereographic projections that the β-matrix and β-primary band have a {332}<113> twinning relationship. The trace of the twining plane (3 -3 2) and the twining direction [-1 1 3] were indicated in Fig. 5-9. In terms of the α″-variants, several common poles have been searched between all variants. A convincing possibility was found with the relationship between V6 of β-matrix and V6 of β-primary band that corresponds to a compound {1-30}<310> twin. As mentionned previously, twinning in α" martensite was not deeply investigated and this possibility cannnot be compared with litterature. Nevertheless, uranium posses an orthorhombic phase that is very similar to α" phase in titanium ; this orthorhombic uranium phase deforms via twinnning and this {1-30}<310> twinning system is the most commnly observed, confirming the hypothesis of this twinning system. Moreover, the trace of the twining plane $(1\ -3\ 0)_{\alpha''}$ and the twining direction $[3\ 1\ 0]_{\alpha''}$ indicated in Fig. 5-9 are parallel to the twining plane $(3\ -3\ 2)_{\beta}$ and the twining direction $[-1\ 1\ 3]_{\beta}$, respectively, indicating a clear correspondence between the assumed twinning system in the α" phase and the observed twinning system in the relaxed β phase. As a conclusion, according to the SXRD profiles of sample A in Fig. 5-2, the primary band observed as {332}<113> β-twin under unloading condition had been {1-30}<310> α″-twin under loading condition.

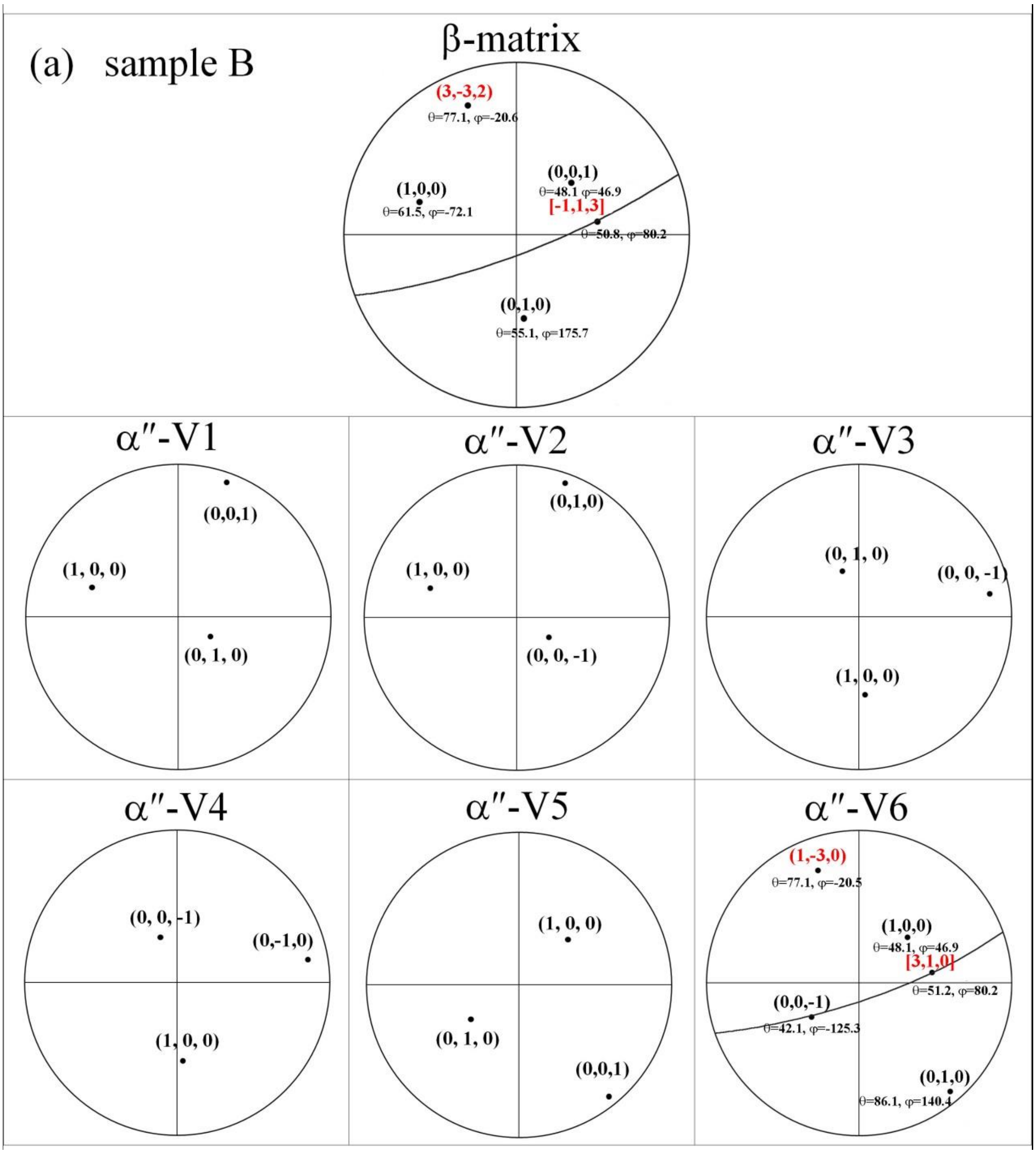
(a) sample B
β-matrix
(3,-3,2)
θ=77.1, φ=-20.6
(0,0,1)
θ=48.1 φ=46.9
(1,0,0)
θ=61.5, φ=-72.1
[-1,1,3]
θ=50.8, φ=80.2
(0,1,0)
θ=55.1, φ=175.7
α″-V1
(0,0,1)
(1, 0, 0)
(0, 1, 0)
α″-V2
(0,1,0)
(1, 0, 0)
(0, 0, -1)
α″-V3
(0, 1, 0)
(0, 0, -1)
(1, 0, 0)
α″-V4
(0, 0, -1)
(0,-1,0)
(1, 0, 0)
α″-V5
(1, 0, 0)
(0, 1, 0)
(0,0,1)
α″-V6
(1,-3,0)
θ=77.1, φ=-20.5
(1,0,0)
θ=48.1, φ=46.9
[3,1,0]
θ=51.2, φ=80.2
(0,0,-1)
θ=42.1, φ=-125.3
(0,1,0)
θ=86.1, φ=140.4

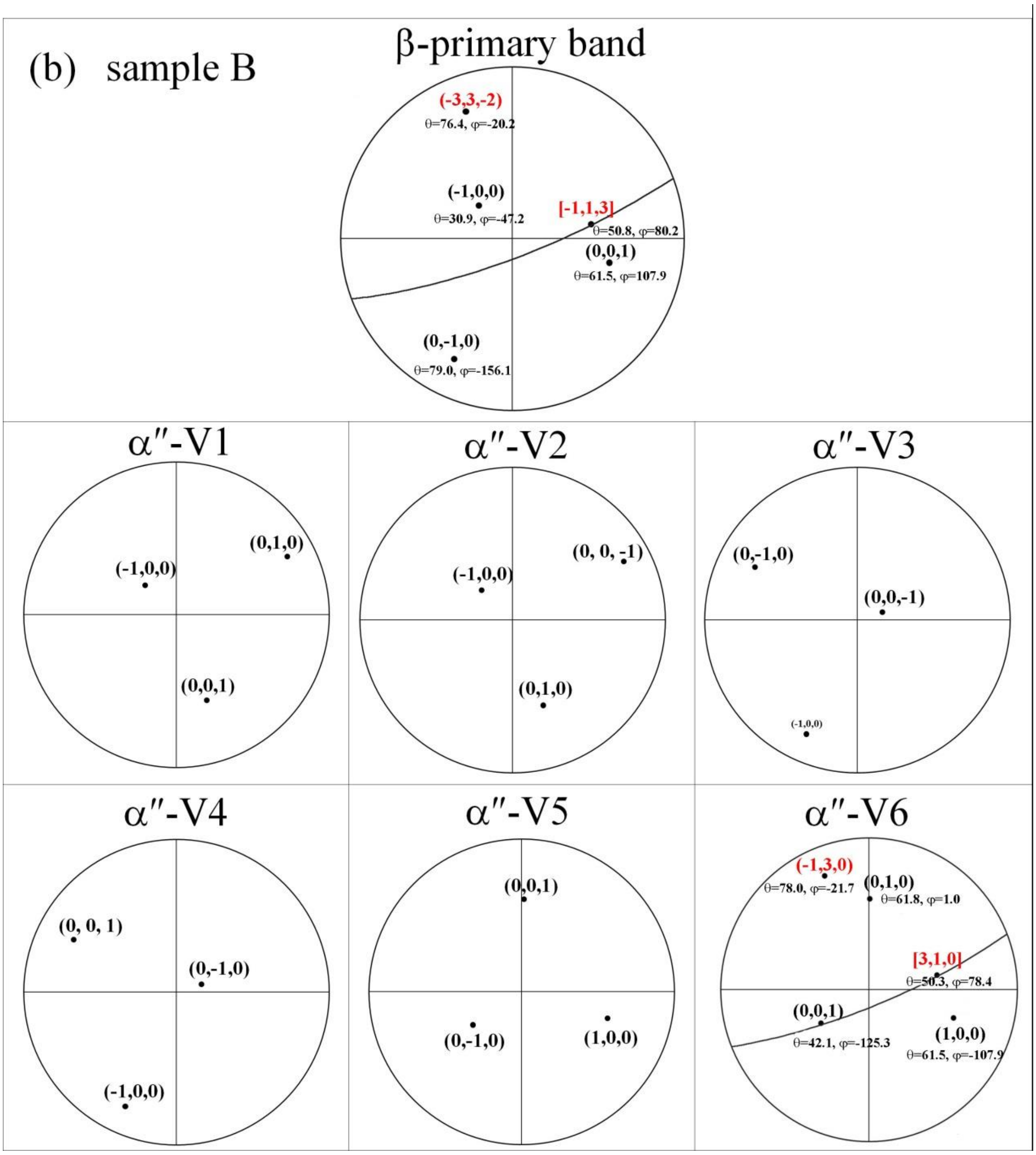
(b) sample B
β-primary band
(-3,3,-2)
θ=76.4, φ=-20.2
(-1,0,0)
θ=30.9, φ=-47.2
[-1,1,3]
θ=50.8, φ=80.2
(0,0,1)
θ=61.5, φ=107.9
(0,-1,0)
θ=79.0, φ=-156.1
α″-V1
(0,1,0)
(-1,0,0)
(0,0,1)
α″-V2
(0, 0, -1)
(-1,0,0)
(0,1,0)
α″-V3
(0,-1,0)
(0,0,-1)
(-1,0,0)
α″-V4
(0, 0, 1)
(0,-1,0)
(-1,0,0)
α″-V5
(0,0,1)
(0,-1,0)
(1,0,0)
α″-V6
(-1,3,0)
θ=78.0, φ=-21.7
(0,1,0)
θ=61.8, φ=1.0
[3,1,0]
θ=50.3, φ=78.4
(0,0,1)
θ=42.1, φ=-125.3
(1,0,0)
θ=61.5, φ=-107.9

Fig 5-9. Crystallographic orientation represented as stereographic projections used to determine the relationship between the matrix and primary band in sample A: (a) the β-matrix and its corresponding six possible variants of α″ phase (V1-V6) and (b) β-primary band and its corresponding α″ phase with six possible variants (V1-V6).

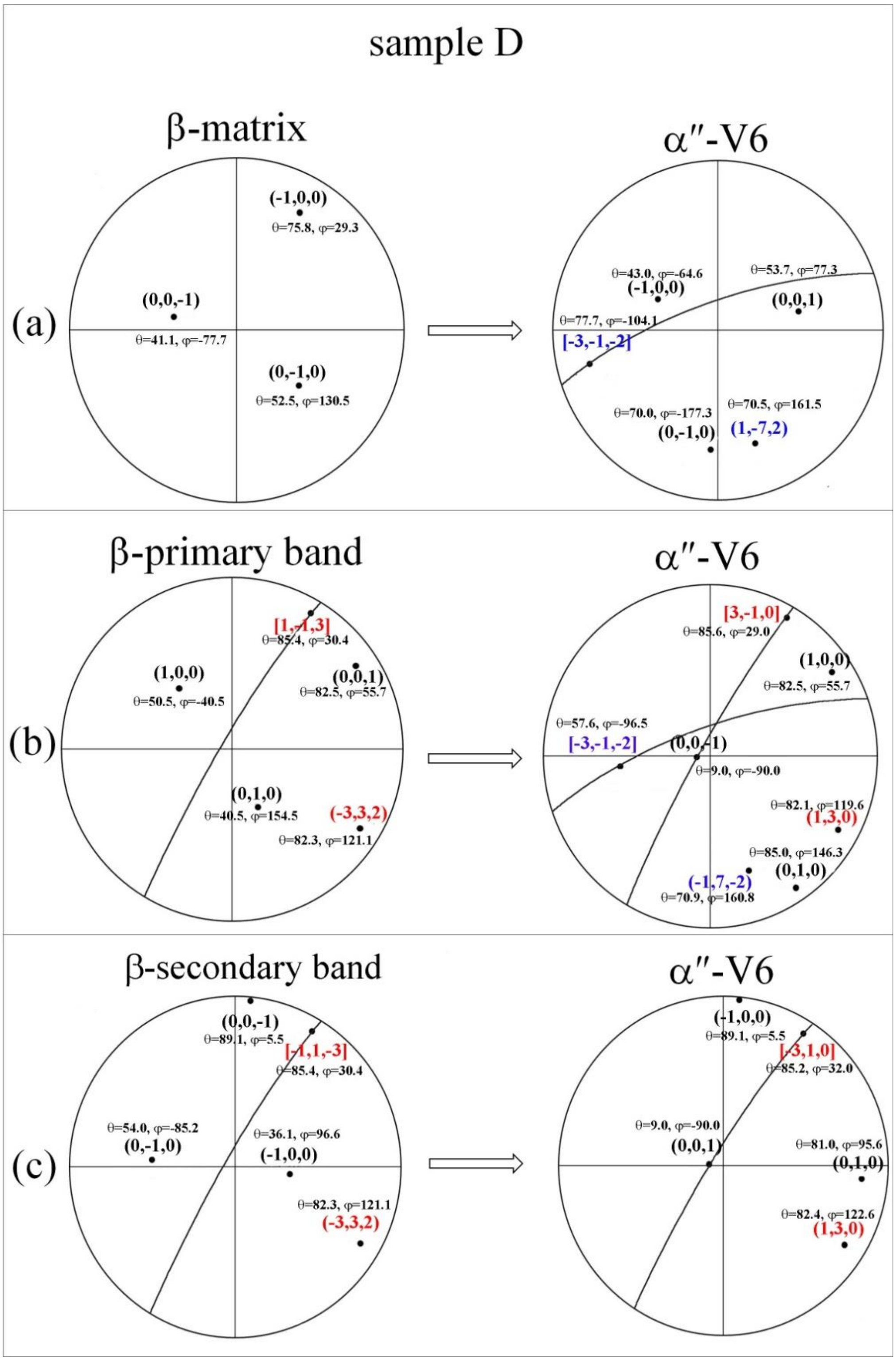
sample D
β-matrix
α″-V6
(a)
(-1,0,0)
θ=75.8, φ=29.3
(0,0,-1)
θ=41.1, φ=-77.7
(0,-1,0)
θ=52.5, φ=130.5
θ=43.0, φ=-64.6
(-1,0,0)
θ=53.7, φ=77.3
(0,0,1)
θ=77.7, φ=-104.1
[-3,-1,-2]
θ=70.0, φ=-177.3
(0,-1,0)
θ=70.5, φ=161.5
(1,-7,2)
β-primary band
α″-V6
(b)
[1,-1,3]
θ=85.4, φ=30.4
(1,0,0)
θ=50.5, φ=-40.5
(0,0,1)
θ=82.5, φ=55.7
(0,1,0)
θ=40.5, φ=154.5
(-3,3,2)
θ=82.3, φ=121.1
[3,-1,0]
θ=85.6, φ=29.0
(1,0,0)
θ=82.5, φ=55.7
θ=57.6, φ=-96.5
[-3,-1,-2]
(0,0,-1)
θ=9.0, φ=-90.0
θ=82.1, φ=119.6
(1,3,0)
θ=85.0, φ=146.3
(0,1,0)
(-1,7,-2)
θ=70.9, φ=160.8
β-secondary band
α″-V6
(c)
(0,0,-1)
θ=89.1, φ=5.5
[-1,1,-3]
θ=85.4, φ=30.4
θ=54.0, φ=-85.2
(0,-1,0)
θ=36.1, φ=96.6
(-1,0,0)
θ=82.3, φ=121.1
(-3,3,2)
(-1,0,0)
θ=89.1, φ=5.5
[-3,1,0]
θ=85.2, φ=32.0
θ=9.0, φ=-90.0
(0,0,1)
θ=81.0, φ=95.6
(0,1,0)
θ=82.4, φ=122.6
(1,3,0)

**Fig 5-10.** Crystallographic orientation represented as stereographic projections used to determine the relationship among the matrix, primary band and secondary band shown in Fig. 5 for the CR94%-ST-5.0% sample: (a) the β phase matrix and its corresponding α″ phase-V6, (b) β phase primary band and its corresponding α″ phase-V6 and (c) β phase secondary band and its corresponding α″ phase-V6.

The same method has been applied for the hierarchically twinned microstructure observed in the sample B deformed at 5%. Based on the TEM observations in Fig. 5-7, the crystallographic orientations of β-matrix, β-primary band and β-secondary band can be presented as stereographic projections in Fig. 5-10a, b and c, respectively. From thes orientations, the 6 variants of each crystal were deduced and, similarly to the sample A, only one orientation of α" phase was convincing for each crystal that is also represented in Fig. 5-10 (V6). As evidenced by SAED in TEM, the {332}<113> twinning relationship between the β-primary band and β-secondary band can be verified again with the stereographic projections in Fig. 5-10b and c. Identically for the sample A, the trace of the twining plane $(-3\ 3\ 2)_{\beta}$ and the twining direction $[1\ -1\ 3]_{\beta}$ indicated in Fig. 5-10 coincide perfectly to the trace of the twining plane $(1\ 3\ 0)_{\alpha''}$ and the twining direction $[3\ -1\ 0]_{\alpha''}$ in the α″-V6. The crystallographic orientation relationship between primary and secondary bands had thus been {130}<3-10> twinning of the α" phase before the stress was released.

Concerning the relationship between the β-matrix and β-primary band for sample B, it cannot be identified directly as twinning by TEM observations. However, the type II {1-72}<312> twinning system can be determined for their corresponding α″-V6s, that is also a commonly observed twinning system in uranium. Indeed, the trace of the twining plane $(1\ -7\ 2)_{\alpha''}$ fits well with the interface between β-matrix and β-primary band shown in Fig. 5-7. But the twinning direction and the twinning plane does not coincide exactly in both crystals and the twinning relationship can not be asserted unambiguously. This ambiguous relationship between the matrix and the primary band is most probably due to the formation of secondary twinning bands inside the primary band that deviate the original orientation of the primary band compared with the matrix. It seems thus that at least two different twinning systems operate in the α" phase of this alloy. But further investigations are needed to confirm these observations.

## 3.2 Sequence of plastic deformation in ST alloy

Schematic illustration in Fig. 5-11 was used for the interpretation of plastic deformation mechanisms. For the ST Ti2448 alloy, the initial recrystallized microstructure was composed of equiaxed grains as shown in Fig. 5-11a.

When the applied stress exceeds a critical stress, the SIM transformation occurs. Especially when the strain arrived to 3 % as shown in Fig. 5-11b, the grains are supposed to be mainly composed of a single variant of α" martensite (see SXRD results) and a martensitic α″-primary band start to be formed which has a {130}<3-10> twinning relationship with the surrounding α″-matrix variant formed subsequently in the β matrix.

Once the applied stress was released as shown in Fig. 5-11c, all the martensite variants reverse back to β phase. This martensitic α″-primary band would reverse back to a β-primary band that keeps a {332}<113> twinning relationship with the β-matrix. This microstructure corresponds thus to the one observed in Fig. 5-6.

When the applied stress increased up to 5 % strain, the number of primary bands has increased as shown in Fig. 5-11d. These expanded α″-primary bands provide an appropriate location for the nucleation and growth of α″-secondary bands. The orientation relationship between the α″-primary band and α″-secondary band is a {130}<3-10> twinning relationship while the α″-primary band and the α″-matrix variant can also exhibit a type II {1-72} <312> twinning relationship. At this tage of deformation, nearly 100% SIM transformation was realized.

When the applied stress and strain were totally released, the martensitic α″ phase reverses back to β phase completely as shown in Fig. 5-11e. The twinnig relationship between primary and secondary bands results thus in {332}<113> twinning relationship in the β phase. But the relationship between the β-primary band and β-matrix remains unclear and needs further investigations. As reported before (*Oka 1978, Hanada 1985, Hanada 1987, Sun 2013*), the stress-induced ω phase accompanying the {332}<113> deformation twin appears in the metastable titanium alloys. In the present case, the interfacial stress-induced ω phase which plays a role to relax the local internal stress and accommodate the lattice distortion was formed in all the phase boundaries.

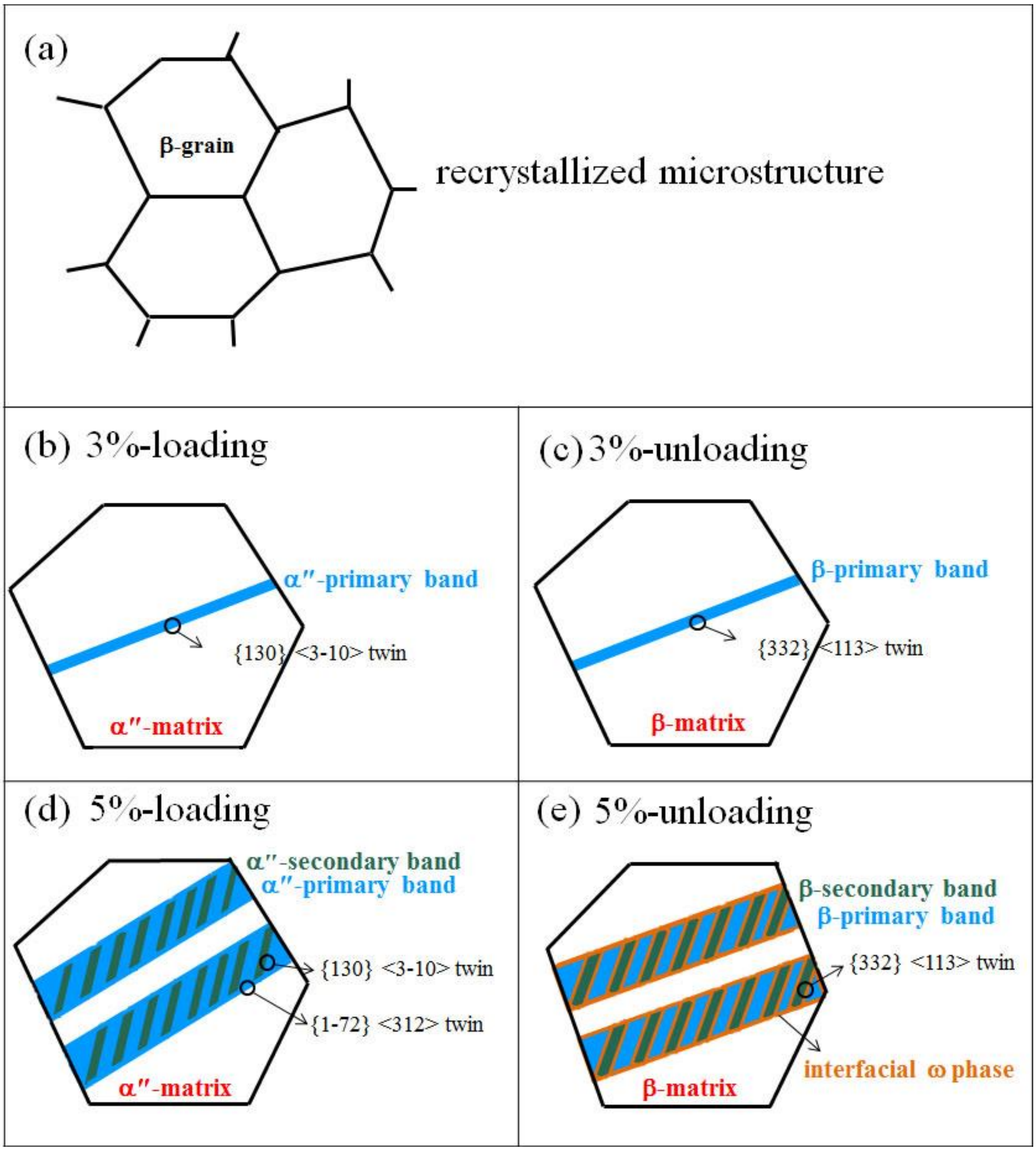
(a)
β-grain
recrystallized microstructure
(b) 3%-loading
α″-primary band
{130}<3-10> twin
α″-matrix
(c) 3%-unloading
β-primary band
{332}<113> twin
β-matrix
(d) 5%-loading
α″-secondary band
α″-primary band
{130} <3-10> twin
{1-72} <312> twin
α″-matrix
(e) 5%-unloading
β-secondary band
β-primary band
{332} <113> twin
interfacial ω phase
β-matrix

**Fig 5-11.** Schematic illustration of plastic deformation mechanisms for as-quenched STalloy.

# 4. Conclusions

In this study, the deformation microstructures of ST Ti2448 alloy were mainly investigated by EBSD and TEM. Based on them, the plastic deformation mechanisms were discussed. The following conclusions can be made:

(1) With 3 % strain, only a few amount of primary band identified to be {332}<113> β-twins appeared in the deformation microstructure under unloading condition.

(2) With 5 % strain, a lot of deformation bands composed of primary bands with

secondary bands inside and interfacial ω plates were observed for the deformation microstructure. The primary and secondary bands were revealed to be {332}<113> β-twins under unloading condition.

(3) As SXRD results proves that under loading condition, this alloy is mainly composed of α" martensite, and based on the lattice correspondence between β phase and α″ phase, the existence of compound {130}<3-10> α″-twins and type II {1-72}<312> α″-twins were identified in the deformation microstructure under loading condition. The {332}<113> β-twins were thus shown to be the result of reversibility of {130}<3-10> α″-twins.

(4) Stress induced ω phase located in the phase boundaries of deformation bands was due to the strain relaxation.

(5) The plastic deformation mechanisms of the ST Ti2448 alloy are twinning SIM α″ transformation and dislocation slip.

(6) In addition, the plastic deformation of the FT alloy is only accomodated by dislocation slip. No twinning is observed due to the smaller grain size.

## References

Cahn R.W., *Plastic deformation of alpha-uranium twinning and slip*, Acta Metallurgica, **1**, p49, 1953.

Cahn R.W., *Twinning and slip in α-uranium*, Acta Crystallographica, **4**, p470, 1951.

Castany P., Besse M., Gloriant T., *Dislocation mobility in gum metal β-titanium alloy studied via in situ transmission electron microscopy,* Physical Review B, 84, p020201, 2011.

Castany P., Besse M., Gloriant T., *In situ TEM study of dislocation slip in a metastable titanium alloy*. Scripta Materialia, **66**, p371, 2012.

Chai Y.W., Kim H.Y., Hosoda H., Miyazaki S., *Self-accommodation in Ti-Nb shape memory alloys*. Acta Materialia, **57**, p4054, 2009.

Crocker A.G., *The crystallography of deformation twinning in alpha-uranium,* Journal of Nuclear Materials, **16**, p306, 1965

Field R.D., Mccabe R.J., Alexander D.J., Teter D.F., *Deformation twinning and twinning related fracture in coarse-grained α-uranium*, Journal of Nuclear Materials, **392**, p105, 2009.

Frank F.C., *A note on twinning in alpha-uranium*, Acta Metallurgica, **1**, p71, 1952.

Hanada S., Izumi O., *Correlation of Tensile Properties, Deformation Modes, and Phase Stability in*

*Commercial β-Phase Titanium Alloys*. Metallurgical Transactions A. **18**, p265, 1987.

Hanada S., M., Izumi O., *Transmission electron microscopic observations of mechanical twinning in metastable beta titanium alloys*, Metallurgical Transactions A, **17A**, p1409, 1986.

Hanada S., Ozeki M., Izumi O., *Deformation characterisitics in β phase Ti-Nb alloys*, Metallurgical Transactions A, **16A**, p789, 1985.

Hao Y.L., Li S.J., Sun B.B., Sui M.L., Yang R., *Ductile titanium alloy with low Poisson's ratio*, Physical Review Letter, **98**, p216405, 2007.

Hao Y.L., Li S.J., Sun S.Y., Zheng C.Y., Hu Q.M., Yang R., *Super-elastic titanium alloy with unstable plastic deformation*. Applical Physics Letters, **87**, p091906, 2005.

Kim H.Y., Ikehara Y., KIM J.I., Hosoda H., Miyazaki S., *Martensitic transformation, shape memory effect and superelasticity of Ti –Nb binary alloys*. Acta Materialia, **54**, p2419, 2006.

Klostermann J.A., T*he concept of the habit plane and the phenomenological theories of the martensite transformation*. Journal of Less-Common metals, **28**, p75, 1972.

Lieberman D.S., Wechsler M.S., Read T. A., *Cubic to Orthorhombic Diffusionless Phase Change-Experimental and Theoretical Studies of AuCd*. Journal of Applied Physics, **26**, p473, 1955.

Lütjering G, Williams JC, *Titanium*. (2nd ed.)Springer-Verlag, Berlin 2007: 141

Oka M., Taniguchi Y., *{332} deformation twins in a Ti-15.5 pct V alloy*, Metallurgical Transactions A, **10A**, p651, 1979.

Ping D.H., Yamabe-Mitarai Y., Cui C.Y., Yin F.X., Choudhry M.A., *Stress-induced α" martensitic (110) twinning in β-Ti alloys*, Applied Physics Letters, **93**, p151911, 2008.

Ramarolahy A., Castany P., Prima F., Laheurte P., Peron I., Gloriant T., *Microstructure and mechanical behavior of superelastic Ti-24Nb-0.5O and Ti-24Nb-0.5N biomedical alloys*, Journal of the mechanical behavior of biomedical materials, **9**, p83, 2012.

Sun F., Hao Y.L., Nowak S., Gloriant T., Laheurte P., Prima F., *A thermo-mechanical treatment to improve the superelastic performances of biomedical Ti-26Nb and Ti-20Nb-6Zr (at.%) alloys*, Journal of the mechanical behavior of biomedical materials, **4**, p1864, 2011.

Sun F., Zhang J.Y., Marteleur M., Gloriant T., Vermaut P., Laille D., Castany P., Curfs C., Jacques P.J., Prima F., *Investigation of early stage deformation mechanisms in a metastable β titanium alloy showing combined twinning-induced plasticity and transformation-induced plasticity effects*, Acta Materialia, **61**, p6406, 2013.

Tobe H., Kim H.Y., Inamura T., Hosoda H., Miyazaki S., *Origin of {332} twinning in metastable β-Ti alloys*, Acta Materialia, **64**, p345, 2014

Wang L.Q., Lu W.J., Qin J.N., Zhang F., Zhang D., *Microstructure and mechanical properties of cold-rolled TiNbTaZr biomedical β titanium alloy*, Materials Science and Engineering A, **490**, p421, 2008.

Wayman C.M., *The phenomenological theory of martensite crystallography: interrelationships*, Metallurgical and Materials Transactions A, **25**, p1787, 1994.

Yang Y., Castany P., Cornen M., Thibon I., Prima F., Gloriant T., *Texture investigation of the superelastic Ti-24Nb-4Zr-8Sn alloy*, Journal of Alloys and Compounds, **591**, p85, 2014.

Yang Y., Castany P., Cornen M., Prima F., Li S.J., Hao Y.L., Gloriant T., *Characterization of the martensitic transformation in the superelastic Ti-24Nb-4Zr-8Sn alloy by in situ synchrotron X-ray diffraction and dynamic mechanical analysis*, Acta Materialia, **88**, p25, 2015.

# General conclusion

The new β-type metastable Ti-24Nb-4Zr-8Sn alloy exhibiting high strength, low elastic modulus, high ductility, superelastic property and good biocompatibility was investigated in this thesis. In the present work, the as-cold rolled Ti2448 alloy was subjected to two kinds of thermal treatment which are solution treatment ($900^{o}$C/30min, ST) and flash treatment ($700^{o}$C/3min, FT) for comparison. The investigations were focused on primary evaluation of mechanical and superelastic properties, characterization of martensitic transformation related to superelasticity and exploration of mechanisms of plastic deformation.

After a bibliographic review of titanium alloys used as biomaterials and a presentation of the experimental methods employed for this work in the two first chapters, the chapter 3 focused on the evaluation of mechanical properties and microstructure of the Ti2248 alloy after various thermos-mechanical treatments. The usual mechanical properties and superelasticity were primarily evaluated by conventional and cyclic tensile tests for three cold rolling reduction rates (40%, 80% and 94%) followed by ST or FT heat treatments. On the other hand, the influence of textural change, introduced by these different cold rolling reduction rates, on the mechanical properties was analyzed. Results revealed that the ultimate tensile strength was measured around 870MPa for ST alloys and 950-990MPa for FT alloys, while the incipient Young’s modulus was stabilized at 58GPa. The elongation at rupture was evaluated to lie between 8 and 12% and no clear difference in ductility was observed whatever the thermo-mechanical process applied. Generally, for each thermal treatment, no strong influence of reduction rates on mechanical properties can be therefore noticed. Contrarily, FT samples exhibit higher mechanical strength than ST samples due to a smaller grain size.

From the cyclic tensile curves, the recoverable strain was measured as a function of the applied strain in order to characterize the superelasticity. In addition, a double yielding phenomenon associated to the superelasticity as well as a hysteresis between loading and unloading were clearly observed suggesting that reversible stress-induced martensitic (SIM) transformation has occurred. Whatever the applied cold rolling reduction rate, the FT alloy exhibits better superelasticity than ST alloy, meaning that the most important influence is due to the thermal treatment. Indeed, the highest recoverable strain (2.75%) is obtained for FT alloy while 2% maximum is reached for solution treated specimens (at 3.5% of applied strain). But the maximum recoverable strain is enhanced by the reduction rate as well, particularly for the ST alloy. In order to explain these observations, texture evaluation and its effects on superelasticity were therefore investigated.

For ST alloy, the main texture component was observed to be (011)[100] at moderate cold rolling rate (40%) whereas a γ-fiber texture was observed at higher cold rolling rates (80% and 94%) with the (111)[1-21] orientation as a main component. The increase of superelasticity with the cold rolling rate for ST alloy can thus be attributed to the texture change: indeed, the amount of grains orientated to give the highest recovery strain, that is with <110> directions along the tensile direction, increases with the cold rolling rate. For FT alloy, a γ-fiber texture with (111)[1-21] main component was also observed at intermediate (80%) and high (94%) cold rolling rates. But a clear texture corresponding mainly to (211)[0-11] was obtained after a moderate cold rolling rate (40%). As a consequence, the superelasticity of FT alloy is not influenced by the texture change due to the variation of cold rolling rate because the amount of grains orientated to give the highest recovery strain does not vary significantly. Furthermore, the better superelasticity of FT alloy than ST alloy is not related to texture change but clearly due to the grain refinement because the same texture was observed for both higher cold rolling rates (80% et 94%). Therefore, the superelasticity of Ti2448 alloy can be improved by texture variation and grain refinement.

In superelastic metastable β alloys, the study of the SIM transformation is challenging due to its reversibility after the release of the stress. For this reason, *in situ* experiments by synchrotron X-ray diffraction (SXRD) which has a shorter wavelength ($\lambda$=0.040002106nm) and a better monochromaticity than conventional XRD were employed to characterize the SIM transformation during cyclic tensile tests. Dynamic mechanical analysis (DMA) was also used to investigate the characteristics of the SIM transformation as a function of both temperature and applied stress. This complete study of the SIM transformation, consisting of the chapter 4 of this manuscrit, has been conducted for both ST and FT alloys with a fixed cold rolling reduction rate of 94%.

The *in situ* cyclic tensile tests under SXRD were realized on tensile specimens with strain increments of 0.5% until 5.0% and then increments of 1.0% until 10%. SXRD scans were then obtained after each cycle of the tensile test for both loading and unloading conditions. The results clearly showed the occurrence of a SIM transformation characterized by the appearence of the typical diffraction peaks of the α'' phase: $(020)_{\alpha''}$, $(002)_{\alpha''}$, $(111)_{\alpha''}$, $(021)_{\alpha''}$, $(022)_{\alpha''}$, $(131)_{\alpha''}$, $(113)_{\alpha''}$, $(040)_{\alpha''}$, $(004)_{\alpha''}$ to the detriment of the initial $(110)_{\beta}$, $(200)_{\beta}$, $(211)_{\beta}$ and $(220)_{\beta}$ peaks belonging to β phase. The evolutions of these peaks have thus highlighted the reversibility of the SIM transformation.

Cell parameters of α'' and β phase under loading and unloading conditions were then measured according to these SXRD profiles. A three steps deformation sequence was thus established as follows: firstly, the β phase is elastically deformed up to around 1.5-2% of strain in the ST alloy (2-2.5% for FT alloy); secondly, the deformation is accommodated by the reversible SIM α″ transformation, which is elastically deformed up to 4.5% in ST (5% in FT); from this value, both residual β phase and α″ phases start to be deformed plastically.

On the other hand, martensitic transformations are usually described using characteristic temperatures such as martensite start, martensite finish, austenite start and austenite finish temperatures, respectively denoted $M_s$, $M_f$, $A_s$ and $A_f$. These temperatures were evaluated by DMA experiments under different applied static stresses from the drop of the dynamic elastic modulus and the concomitant increase of the damping factor tan δ associated to the martensitic transformation. The variation of the characteristic temperatures as a function of the applied stress shows a quite good linear fitting that is in agreement with the Clausius-Clapeyron relationship. The critical stress inducing the SIM α″ transformation at room temperature was obtained by extrapolating these data: the critical stress corresponding to the $M_s$ value of 20 ℃ was found to be 415MPa for ST alloy and 440MPa for FT alloy, respectively. These critical stress values coincide perfectly with those obtained by tensile tests meaning that DMA analysis and mechanical tensile tests are in very good agreement.

After the detailed study of the reversible SIM transformation responsible for the superelasticity, the last chapter of this thesis deals with the investigation of the mechanisms of plastic deformation in the Ti2448 alloy, with a special attention to the twinning in the ST specimens. Microstructures of the ST alloy deformed to two different deformation strains (3 % and 5 %) were observed by optical microscopy, EBSD and TEM techniques. Additionally, the TEM observation on FT alloy deformed to 5 % was also supplemented for comparison. Both optical microscopy and EBSD reveal the presence of thin deformation bands in the ST alloy. However, these bands cannot be indexed accurately by EBSD because of an apparent internal hierarchical structuration that has been confirmed by TEM.

When the ST alloy is deformed to 3% strain, the microstructure showed only a few amount of primary bands identified to be {332}<113> β-twins by TEM. But, according to the SXRD results, the microstructure of the alloy under stress is mainly composed of α" phase, that means the observed microstructure by TEM is the result of the relaxation of the martensitic microstructure under loading condition. Consequently, the twins observed in the β phase have been formed in the α" martensite. In order to determine the original twinning system in the martensitic phase, the orientation relationship between both phases has been applied to determine the six possible variants of martensitic α″ phase from the orientation of each observed β grains and twins. Regarding all the possibilities, the primary {332}<113> β-twins observed under unloading condition were determined to be {1-30}<310> α″-twins under loading condition. The {332}<113> β-twins were thus thought to be the result of reversibility of {130}<3-10> α″-twins.

When the alloy is deformed to 5% strain, the unresolved thin deformation bands observed by EBSD are determined by TEM to be complex hierarchically twinned bands composed of primary bands, secondary bands and interfacial ω plates. Similarly to the specimens deformed at 3% strain, the observed microstructure is the result of the reversion of the martensitic microstructure. By applying the orientation relationship between β and α" phases, the primary bands and secondary bands were analyzed to be {332}<113> β-twins under unloading condition which had been {130}<3-10> α″-twins previously formed under loading condition. However, an unambiguous crystallographic relationship under unloading condition cannot be determined between primary bands and matrix, most probably due to presence of secondary bands. Nevertheless, the relationship between primary bands and matrix seems to be a type II {1-72}<312> α″-twin under loading condition. The interfacial ω phase observed in all the band boundaries plays a role to relax local internal stress and accommodate the lattice distortion during the reversion from the α" phase to the β phase.

Dislocations were also observed to participate in the plastic deformation for ST alloy. However, for the FT alloy, only dislocations were detected without any observation of deformation bands. The plastic deformation of ST alloy can be concluded to be accommodated by both twinning and dislocation movements, whereas only dislocation slip operates in the FT alloy.

As a general summary, mechanical properties and microstructure were investigated in the Ti2448 alloy after several thermo-mechanical treatments. The reversible SIM transformation responsible of the superelasticity has been extensively studied by DMA and *in situ* SXRD experiments. In addition, the mechanisms of plastic deformation, especially twinning, have been also analyzed. But, as a perspective of this work, the complex twinning structures need more investigations to assert unambiguously the proposed twinning mechanisms of the α" martensite.

# Document de synthèse en français

A cause de l'augmentation de la durée de service des matériaux implantés dans le corps qui découle de l'augmentation de l'espérance de vie, la biocompatibilité des alliages métalliques utilisés dans le domaine biomédical doit être pensée à plus long terme, tant du point de vue chimique que mécanique.

Parmi les alliages métalliques utilisés dans le domaine médical, les alliages de titane se sont toujours distingués par leur excellente biocompatibilité, notamment en raison de leurs excellentes propriétés mécaniques et grâce à leur capacité à former spontanément une couche de passivation stable et bioinerte (*Geetha 2009, Long 1998*). Ils constituent un matériau de choix comme substitut osseux pour une prothèse et sont aussi implantés sous forme de plaque ou de vis. Deux des alliages de titane les plus utilisés sont le Ti-6Al-4V ou TA6V comme substitut osseux et le Ni-Ti en tant qu'alliage à mémoire de forme pour des dispositifs fonctionnels. Le Ti-6Al-4V est un alliage qui a été développé pour des applications aéronautiques, il possède d'excellentes propriétés mécaniques et une très bonne résistance à la corrosion. Cependant, les éléments d'addition utilisés, l'aluminium et le vanadium, sont réputés cytotoxiques et la présence en faible proportion de ces éléments remet en cause la biocompatibilité à long terme de cet alliage (*Nag 2005*). L'autre limitation de cet alliage est d'ordre mécanique. En effet, son module d'élasticité (114 GPa) est trop élevé par rapport à celui de l'os (environ 30 GPa). Une utilisation de cet alliage comme substitut osseux provoque alors le phénomène de « stress shielding » qui a pour conséquence une dégradation du tissu osseux situé à l'interface os/implant et une réduction de la durée de service de la prothèse (*Huiskes 1992*). Les alliages Nickel-Titane comme le Nitinol® sont des alliages intermétalliques avec une teneur en nickel proche de 50 at.%. Selon leur composition exacte et les traitements thermiques appliqués, ces alliages présentent un effet superélastique ou un effet mémoire de forme, ce qui autorise un large panel d'applications : arcs orthodontiques, cathéters, stents, agrafes à mémoire de forme, etc. Ces propriétés découlent d'une transformation martensitique thermoélastique qui peut être induite sous contrainte ou par l'effet de la température. Bien que ces alliages possèdent une bonne tenue à la corrosion, leur forte teneur en nickel, élément allergène et cytotoxique, limite leur utilisation sur de longues périodes. De plus, la combinaison d'une composition intermétallique et d'un effet superélastique ou mémoire de forme rend ces alliages extrêmement difficiles à usiner ou à mettre en forme.

De ce fait, les recherches consistant à élaborer des alliages de titane sans nickel qui présentent les caractéristiques de superelasticité et de mémoire de forme des alliages Ni-Ti ont été intensément développées ces dernières années. Dans ce domaine, les alliages de titane β-métastables, se sont avérés être les candidats les plus prometteurs. En effet, pour une teneur en éléments bétagènes judicieusement choisie, la phase β de ces alliages, qui aura été retenue préalablement par trempe, peut être transformée en martensite α″ sous l'effet d'une contrainte extérieure et donc présenter un effet superélastique tout comme les alliages titane-nickel (*Kim 2004*). De plus, l'existence de cette transformation sous contrainte contribue à abaisser le module apparent de ces alliages. Enfin, ces alliages peuvent être élaborés à partir de titane et d'éléments bétagènes parfaitement biocompatibles comme le tantale, le niobium, le zirconium ou le molybdène et sont très faciles à mettre en œuvre comme la plupart des alliages beta (*Niinomi 2002-2003 a,b*).

L'alliage superélastique biocompatible de composition Ti-24Nb-4Zr-8Sn (% massique) étudié dans le cadre de cette thèse (le Ti2448) a été développé par le groupe de Y. L. Hao à l'IMR de Shenyang en Chine. Cet alliage montre des propriétés intéressantes telles qu'un bas module élastique, une haute résistance mécanique et une ductilité relativement élevée. Lors d'études précédentes, différents traitements thermomécaniques ont été employés comme la déformation à froid, le laminage à chaud, le forgeage… (*Hao 2005, Hao 2007a, Hao 2007b*) de manière à optimiser la microstructure. Grâce à ces investigations, une élasticité recouvrable d'environ de 3,3% (due à l'effet superélastique) a été obtenue (*Li 2008, Li 2011, Hao 2012*), ce qui représente une valeur beaucoup plus élevée que les valeurs habituellement obtenues avec les alliages Ti-Nb binaires (*Kim 2006a, Kim 2006b, Ramarolahy 2012*). De plus, des traitements thermiques « flash » (traitement thermique à 600 °C pendant quelques minutes) effectués sur l'alliage écroui ont permis d'augmenter encore l'effet superélastique tout en obtenant une haute résistance mécanique (*Sun 2010*). Comme la déformation plastique intense qui a été réalisée (par laminage à froid) sur l'alliage est connue pour potentiellement induire une forte texture cristallographique (*Sander 2008*), celle-ci peut grandement influencer les propriétés mécaniques de l'alliage Ti2448. Des travaux récents ont en effet montré que l'élasticité recouvrable est maximisée pour une texture de direction < 110 > dans les microstructures β équiaxes issues d'alliages Ti-Nb et Ti-Ta-Nb (*Kim 2006b, Bertrand 2013*).

Dans ce travail de thèse, 3 différents taux de réduction par laminage à froid ont été réalisés : laminage modéré (40% de réduction par rapport à l'épaisseur initiale), intermédiaire (80%) et élevés (94%) sur l'alliage Ti2448 qui a été ensuite remis en solution (état ST, solution treated, à 900 °C pendant 30 min) ou qui a ensuite été traité « flash » (état FT, flash treated, à 700°C pendant 3 min) afin d'obtenir des textures cristallographiques différentes. Les propriétés mécaniques et l'élasticité recouvrable pour chaque état ont été dans un premier temps évalués par essais de traction. L'alliage Ti2448 β métastable présente d'excellentes propriétés mécaniques avec une résistance relativement élevée (>800MPa), un bas module d’élasticité (58GPa), et une déformation élastique recouvrable pouvant atteindre 3.3 %. Les courbes de traction obtenues sont présentées sur la figure 1.

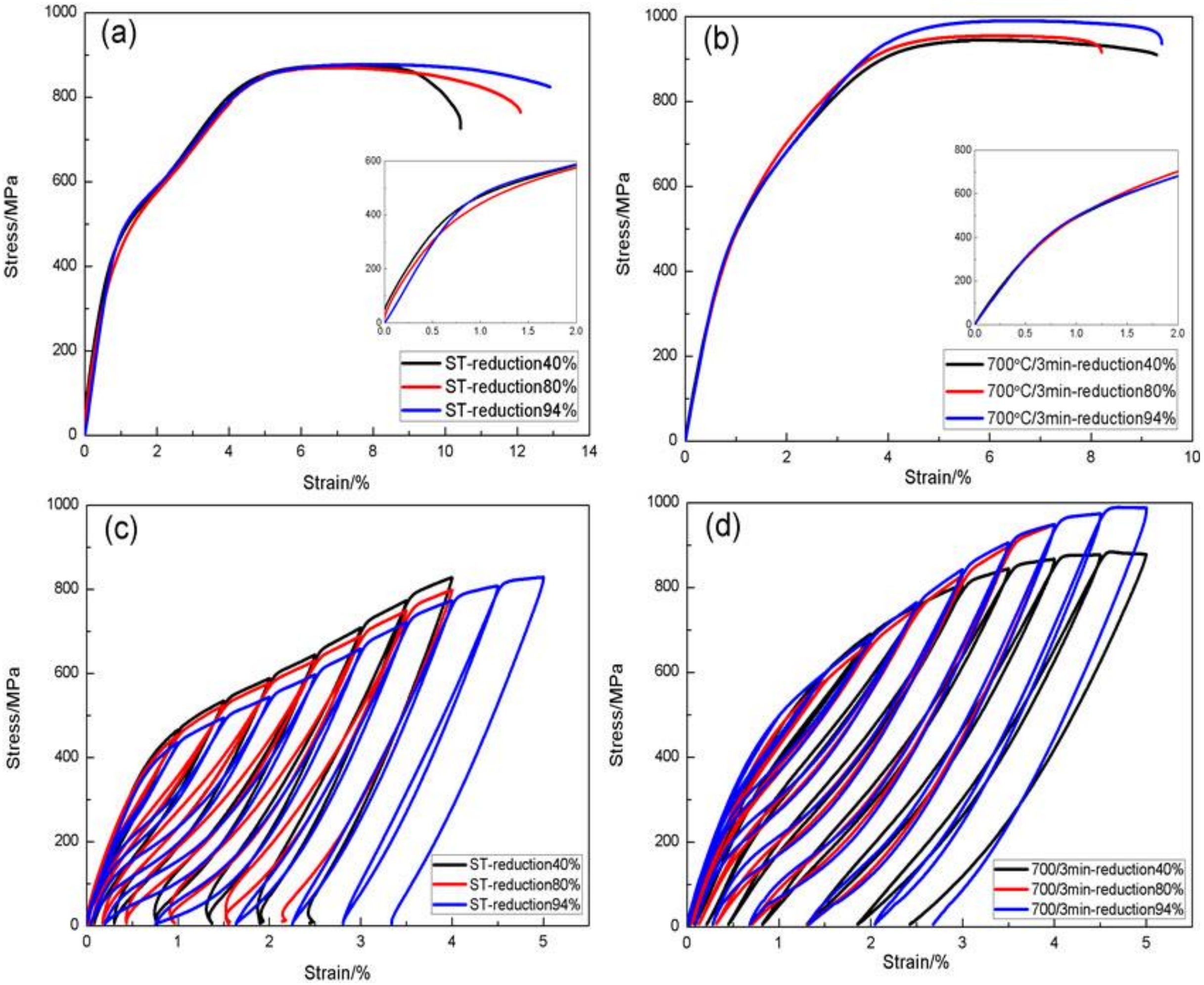

Figure 1 : Courbes de traction conventionnelles et cycliques obtenues sur l’alliage Ti2448 à l’état ST (900°C/30min) (a) et (d) et à l’état FT (700°C/3min) (b) et (d)

Concernant les microstructures et les différentes textures qui ont été caractérisées par microscopie optique, par EBSD et par diffraction des rayons X à l’aide d’un berceau d’Euler pour l’obtention de figures de pôle. Un exemple de distribution des orientations cristallographiques obtenue à partir des ODF en DRX sur l’alliage Ti2448 est présentée sur la figure 2.

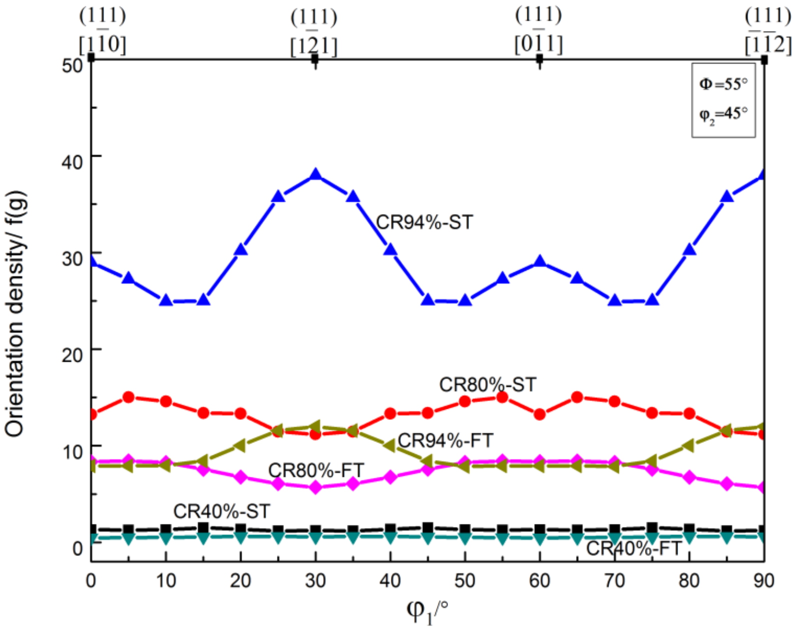

Figure 2 : Distribution des orientations à partir des ODF obtenus sur l'alliage Ti2448 selon le traitement thermo-mécanique appliqué et illustratant la présence de la fibre de texture γ.

A partir des expériences qui ont été menées, les conclusions suivantes ont pu être proposés (*Yang 2014*) :

(1) Pour l'alliage Ti2448 à l'état ST, l'orientation cristallographique principale est $(011)[100]$ pour le taux de laminage modéré (40%) tandis que la texture de fibre γ est observée pour les taux de laminage plus élevés (80% and 94%) avec comme composante d'orientation majoritaire $(111)[1\bar{2}1]$ clairement identifiée pour l'état ST-94%.

(2) Pour l'état FT, la texture de fibre γ est également obtenue avec $(111)[1\bar{2}1]$ comme composante principale dans le cas des forts taux de laminage (80% et 94%) alors qu'une texture correspondant à l'orientation principale $(211)[0\bar{1}1]$ est observée pour le taux de laminage modéré (40%).

(3) Les alliages traités FT possèdent une résistance mécanique plus élevée que les alliages traités ST. Ceci est dû à une taille de grain β beaucoup plus réduite suite aux traitements FT. Les différents taux de laminage effectués et donc les différentes textures conférées ne semblent pas avoir d'influence sur les caractéristiques conventionnelles de traction comme le module, la limite d'élasticité, la résistance maximum ou à rupture.

(4) La texture semble par contre avoir une forte influence sur les propriétés de superélasticité dans le cas des alliages traités ST. L'élasticité recouvrable augmente avec le taux de laminage à froid en relation avec l'évolution de la texture. En effet, plus les grains β sont orientés selon la direction $< 110 >$ qui est également la direction de traction, plus l'élasticité recouvrable est importante.

(5) Dans le cas des alliages traités FT, la superélasticité ne semble pas être affectée par la

texture probablement dû au fait que la quantité de grains β qui sont orientés favorablement ne varie pas de manière significative avec le taux de laminage.

(6) Les alliages traités FT possèdent une meilleure élasticité recouvrable que les alliages traités ST, notamment ceux qui ont été plus fortement laminés (80% et 94%). Cette bonne propriété de superélasticité est plutôt à mettre au crédit de la taille de grain réduite qu'aux effets de texture.

Pour les alliages superélastiques, l'étude de la transformation martensitique induite sous contrainte (SIM) reste problématique du fait de sa réversibilité une fois la contrainte relachée. C'est pourquoi des méthodes de caractérisation *in situ* sous sollicitations mécaniques s'avèrent nécessaires. Par exemple, des études *in situ* sous charge menées en diffraction des rayons X conventionnelle (XRD) ont été réalisées sur les alliages binaires de Ti-26Nb ou de Ti-13Nb-4Mo et ont permis de détecter les contraintes critiques de transformation martensitique β vers α″ (*Tahara 2009, Al-Zain 2011*). Cependant, une réelle quantification s'avère très problématique avec les sources conventionnelles RX utilisées dans les laboratoires et il est très difficile d'indexer les phases β et α″, notamment à cause de la longueur d'onde qui n'est pas assez courte pour séparer les pics. Dans ce cas, la solution est d'utiliser le rayonnement synchrotron qui possède une longueur d'onde beaucoup plus petite et une bien meilleure monochromaticité. Ainsi, des caractérisations *in situ* en traction par diffraction sous rayonnement synchrotron (SXRD) se sont montrées être très efficace afin de caractériser une telle transformation sous contrainte et n'a jamais été menée jusqu'à présent sur l'alliage β-métastable Ti2448 superélastique. Comme les transformations martensitiques se produisant dans les alliages à mémoire de forme sont habituellement décrites par la connaissance des températures caractéristiques : Ms (martensitic start), Mf (martensitic finish), As (austenitic start) et Af (austenitic finish), il est important qu'elles puissent être déterminées (*Lovey 1999, Otsuka 2005*). La DMA (Dynamic Mechanical Analysis) est une technique qui peut être utilisée efficacement afin de déterminer ces températures de transformation martensitique dans les alliages à mémoire de forme Le principe d'une mesure en analyse mécanique dynamique consiste à appliquer une sollicitation mécanique statique ou dynamique par l'intermédiaire d'un excitateur électrodynamique et mesurer la réponse du matériau étudié, l'analyse étant réalisée en fonction de la température. La sollicitation peut être imposée soit en force, soit en déplacement ; la mesure du paramètre laissé libre constitue alors la réponse du matériau. La représentation habituelle des courbes dynamiques en DMA consiste à tracer le module (appelé aussi module dynamique ou module de stockage) ainsi que la tangente du déphasage (facteur d'amortissement) en fonction de la température (*Liu 1997, Mercier 1979, Bertrand 2013*).

Un important objectif de cette thèse a donc été de caractériser les transformations se produisant dans l'alliage Ti2448 a la fois par diffraction des rayons X sous rayonnement synchrotron sous sollicitation mécanique (SXRD) *in situ* et par analyse mécanique dynamique (DMA) sous différentes contraintes statiques. Deux états pour l'alliage Ti2448 ont été utilisés : l'état ST après avoir appliqué un taux de réduction par laminage à froid de 94% (CR94%-ST) et l'état FT après avoir appliqué un taux de réduction par laminage à froid de 94% (CR94%-FT).

La figure 3 montre les différents profils SXRD obtenus pour les 2 états de l'alliage Ti2448 en charge et après chaque décharge.

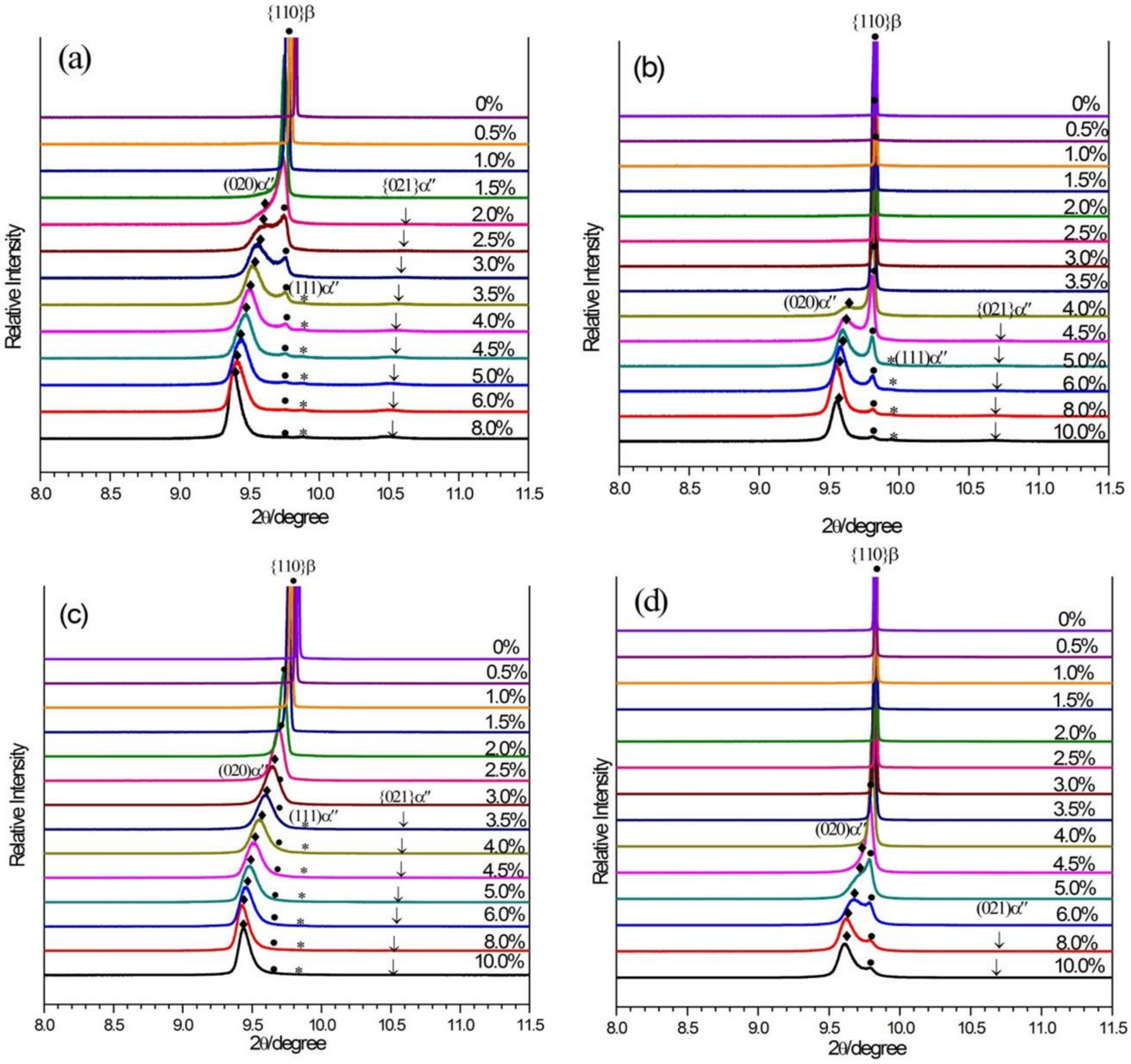

Figure 3. Profils SXRD obtenus sur l'alliage Ti2448 en charge et après chaque décharge en fonction des déformations appliquées: (a) en charge sur l'état ST, (b) après chaque décharge sur l'état ST, (c) en charge sur l'état FT et (d) après chaque décharge sur l'état FT.

Un exemple de courbes obtenus à l'aide de la DMA est présenté sur la figure 5

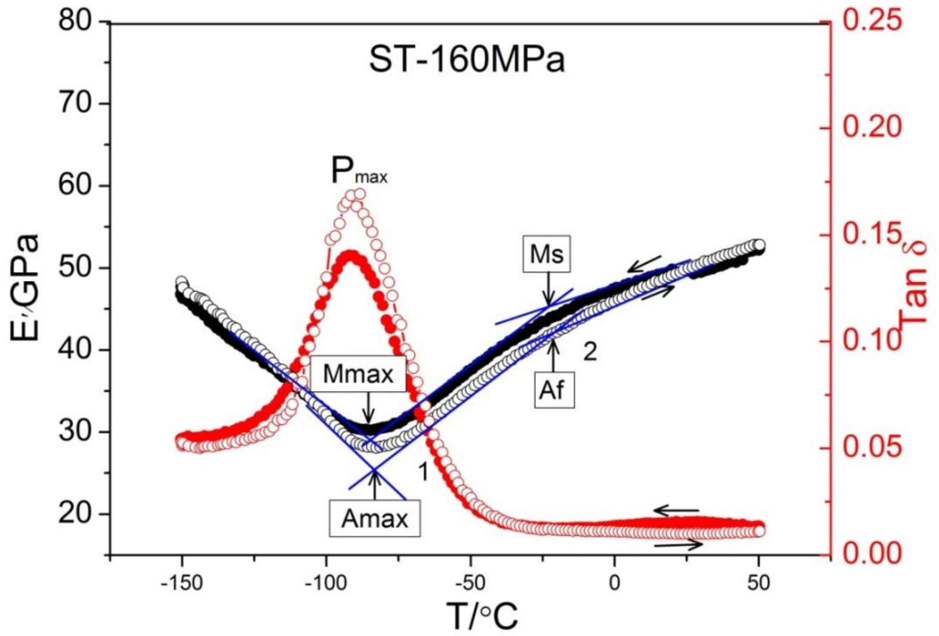

Figure 4: Evolution en fonction de la temperature du module de stockage (en noir) et du facteur d’amortissement (en rouge) sous une contrainte appliquée 160MPa au refroidissement (cercles pleins) et au chauffage (cercles ouverts) pour l’alliage Ti2448 à l’état ST.

Les résultats obtenus ont clairement indiqués une excellente concordance entre les différentes méthodes de caractérisation utilisés (SXRD, DMA, essais de traction). Les conclusions suivantes ont ainsi pu être tirées (*Yang 2015*) :

(1) Par SXRD *in situ*, les différents pics de diffraction des phases $\beta$ et $\alpha''$ à la charge et après décharge ont clairement été observés et différenciés. De ce fait, la transformation martensitique sous contrainte a clairement été mise en évidence. D’autre part, la précision des diffractogrames permis de quantifier les évolutions des différents paramètres de maille pour chaque phase lors de la transformation.

(2) A partir des analyses SXRD et des essais de traction, une séquence de déformation en 3 étapes a pu être proposée. Dans un premier temps, la phase $\beta$ se déforme élastiquement (jusqu’à une déformation d’environ 1.5-2% pour l’état ST et 2-2.5% pour l’état FT). Dans un deuxième temps, la transformation martensitique sous contrainte intervient et la phase $\alpha''$ formée se déforme élastiquement (jusqu’à 4.5% de déformation pour l’état ST et 5% pour FT). A partir de ces valeurs, la déformation des alliages n’est plus accommodée que plastiquement.

(3) A partir des expériences menées en DMA, les pics d’amortissement liés à la transformation sous contrainte ont clairement été détectés et les températures caractéristiques ($M_s$, $M_{max}$, $A_f$, and $A_{max}$) ont été évaluées en fonction de la contrainte appliquée. Les résultats se sont révélés en parfait accord avec la relation de Clausius-Clapeyron.

(4) Un très bon accord entre les valeurs de contrainte critique induisant la transformation martensitique déterminées à partir des différentes méthodes utilisées (SXRD, DMA, traction)

a été trouvé.

Concernant les aspects microstructuraux, la phase martensitique α″ de taille sub-micrométrique voire nanométrique a déjà pu être observés par microscopie électronique en transmission dans certains alliages β-métastable à base de titane après déformation (*Wang 2008, Ping 2008, Sun 2011, Ramarolahy 2012*). Il doit cependant être mentionné que cette phase n'est pas toujours observable. En effet, pour cette certaines compositions très instables, cette phase se réverse en phase β lors de la préparation de lame mince par effet de relaxation mécanique (*Lütjering 2007*) ; c'est la cas avec l'alliage Ti2448 étudié ici. Dans les alliages de titane β-métastables, la déformation plastique n'est pas seulement accomodée par le glissement des dislocations mais également par le maclage (*Besse 2011*). Dans le présent travail de thèse, la microstructure de déformation de l'alliage Ti2448 à l'état ST a été observée par EBSD au MEB et par MET. L'exemple des observations effectuées en microscopie electronique en transmission est présenté sur la figure 5.

Sur la base de ces observations le mecanisme de déformation plastique accommodé par maclage est discuté et quelques conclusions ont ainsi pu être émises :

(1) Lorsque l'alliage a été déformé à 3%, les observations MET montrent une microstructure purement β et seules quelques bandes de maclage primaire sont observées dans la microstructure. Ces macles ont toutes été identifiées comme appartenant au système {332} <113>$_\beta$.

(2) Lorsque l'alliage a été plus fortement déformé à 5 % de déformation, on observe beaucoup plus de bandes de déformation, certaines primaires et d'autres secondaires à l'intérieur des premières. Ces bandes primaires et secondaires ont également été identifiées comme appartenant au système de maclage {332} <113> $_\beta$. L'alliage ne présente toujours pas de phase α″ à cause du phénomène de relaxation mécanique qui l'a reversée en β. Par contre, il a clairement été observé la présence de phase ω à l'interface entre les macles.

(3) Comme on sait que ces macles ont, en fait, été formées dans la phase α″, les relations d'orientation cristallographique entre la phase β et la phase α″ permettent de remonter aux systèmes de maclage dans α″. Ainsi les systèmes {130} <3-10> $_{\alpha''}$ (maclage de type composé) et le système {1-72} <312> $_{\alpha''}$ (maclage de type II) ont été identifiés.

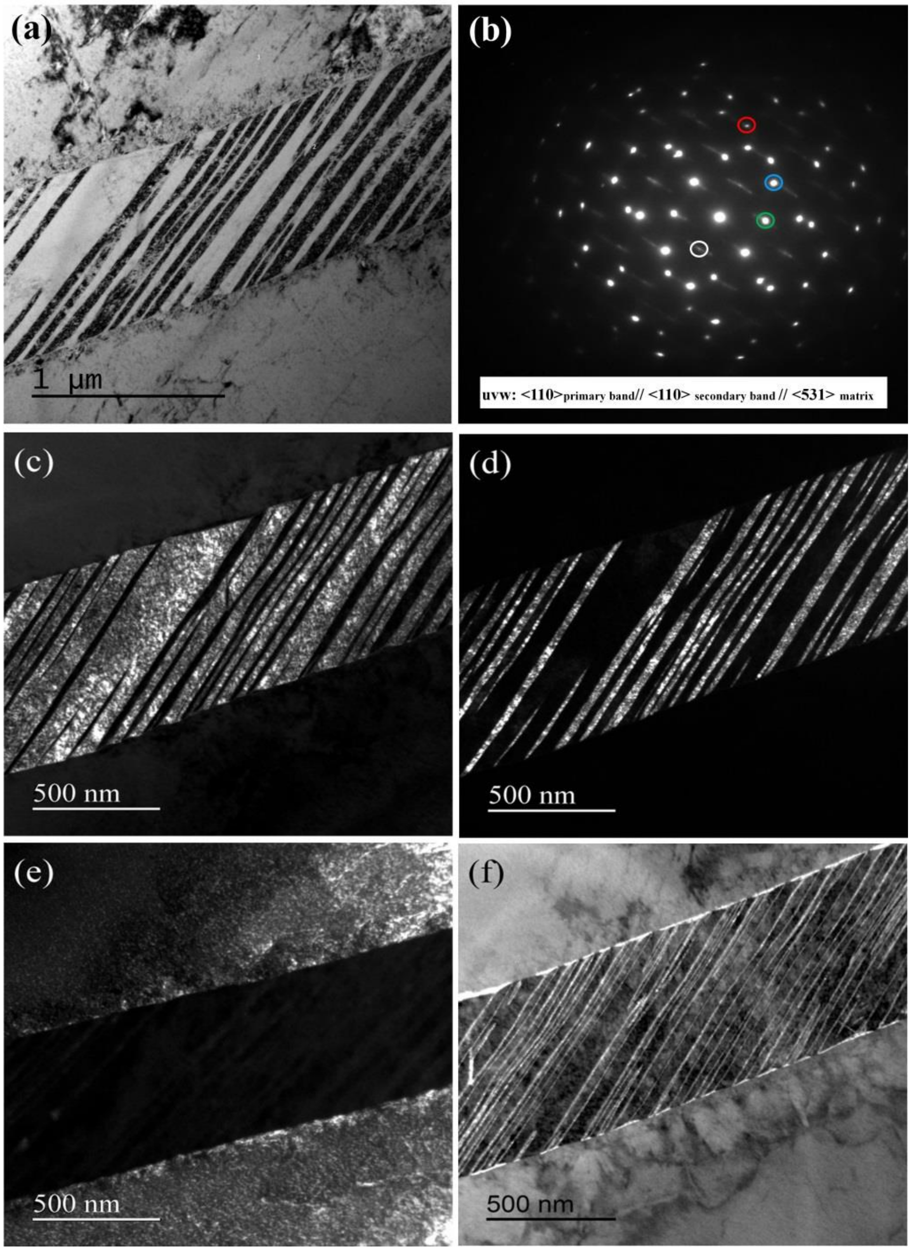
(a)
1 µm
(b)
uvw: <110>primary band// <110> secondary band // <531> matrix
(c)
500 nm
(d)
500 nm
(e)
500 nm
(f)
500 nm

Figure 5. Observations au MET de l'alliage Ti2448 : (a) image en champ clair présentant les bandes de déformation observées, (b) clichés de diffraction associé, (c) (d) (e) and (f) images en champ sombre correspondant respectivement aux tâches de diffraction encerclées de bleu, vert, rouge et blanc sur le cliché.

# References

Al-Zain Y., Kim H.Y., Koyano T., Hosoda H., Nam T.H., Miyazaki S., *Anomalous temperature dependence of the superelastic behavior of Ti–Nb–Mo alloys*. Acta Materialia, **59**, p1464, 2011.

Bertrand E., Castany P., Gloriant T., *Investigation of the martensitic transformation and the damping behavior of a superelastic Ti-Ta-Nb alloy*. Acta Materialia, **61**, p511, 2013.

Besse M., Castany P., Gloriant T., *Mechanisms of deformation in gum metal TNTZ-O and TNTZ titanium alloys: A comparative study on the oxygen influence*. Acta Materialia, **59**, p5982, 2011.

Geetha M., Singh A.K., Asokamani R., Gogia A.K., *Ti based biomaterials, the ultimate choice for orthopaedic implants-A review*. Progress in Materials Science, **54**, p397, 2009.

Hao Y.L., Li S.J., Sun B.B., Sui M.L., Yang R., *Ductile titanium alloy with low Poisson's ratio*, Physical Review Letter, **98**, p216405, 2007a.

Hao Y.L., Li S.J., Sun S.Y., Zheng C.Y., Hu Q.M., Yang R., *Super-elastic titanium alloy with unstable plastic deformation*. Applical Physics Letters, **87**, p091906, 2005.

Hao Y.L., Li S.J., Sun S.Y., Zheng C.Y., Yang R., *Elastic deformation behaviour of Ti-24Nb-4Zr-7.9Sn for biomedical applications,* Acta Biomaterial, **3**, p277, 2007b.

Hao Y.L., Zhang Z.B., Li S.J., Yang R., *Microstructure and mechanical behavior of a Ti-24Nb-4Zr-8Sn alloy processed by warm swaging and warm rolling*. Acta Materialia, **60**, p2169, 2012.

Huiskers R., Weinans H., Rietbergen B. Van., *The relationship between stress shielding and bone resorption around total hip stems and the affects of flexible materials.* Clinical Orthopaedics Related Research, **274**, p124, 1992.

Kim H.Y., Ikehara Y., Kim J.I., Hosoda H., Miyazaki S., *Martensitic transformation, shape memory effect and superelasticity of Ti-Nb binary alloys*. Acta Materialia, **54**, p2419, 2006a.

Kim H.Y., Sasaki T., Okutsu K., Kim J.I., Inamura T., Hosoda H., Miyazaki S., *Texture and Shape Memory Behavior of Ti-22Nb-6Ta Alloy*. Acta Materialia, **54**, p423, 2006b.

Kim H.Y., Satoru H., Kim J.I., Hosoda H., Miyazaki S., *Mechanical properties and shape memory behavior of Ti-Nb alloys*. Materials Transaction, **45**, p2443, 2004.

Liu Y., Van Humbeeck J., Stalmans R., Delaey L., *Some aspects of the properties of NiTi shape memory alloy*. Journal of Alloys and Compounds, **247**, p115, 1997.

Long M., Rack H.J., *Titanium alloys in total joint replacement-a materials science perspective*. Biomaterials, **19**, p1621, 1998.

Lovey F.C., Torra V., *Shape memory in Cu-based alloys: phenomenological behavior at the mesoscale level and interaction of martensitic transformation with structural defects in Cu-Zn-Al*. Progress in Materials Science, **44**, p189, 1999.

Lütjering G, Williams JC, *Titanium.* (2nd ed.)Springer-Verlag, Berlin 2007: 141

Mercier O., Melton K.N., De Préville Y., *Low-frequency internal friction peaks associated with the martensitic phase transformation of NiTi*. Acta Metallurgica, **27**, p1467, 1979.

Nag S., Banerjee R., Fraser H.L., *Microstructural evolution and strengthening mechanisms in Ti-Nb-Zr-Ta, Ti-Mo-Zr-Fe and Ti-15Mo biocompatible alloys*. Materials Science and Engineering C, **25**, p357, 2005

Niinomi M., *Fatigue performance and cyto-toxicity of low rigidity titanium alloy, Ti-29Nb-13Ta-4.6Zr*. Biomaterials, **24**, p2673, 2003a.

Niinomi M., *Recent Metallic Materials for Biomedical Applications*. Metallurgical and Materials Transactions A, **33**, p477, 2002.

Niinomi M., *Recent research and development in titanium alloys for biomedical applications and healthcare*. Science and Technology of Advanced Materials, **4**, p445, 2003b.

Otsuka K., Ren X., *Physical metallurgy of Ti–Ni-based shape memory alloys*. Progress in Materials Science, **50**, p511, 2005.

Ping D.H., Yamabe-Mitarai Y., Cui C.Y., Yin F.X., Choudhry M.A., *Stress-induced $\alpha''$ martensitic (110) twinning in $\beta$-Ti alloys*, Applied Physics Letters, **93**, p151911, 2008.

Ramarolahy A., Castany P., Prima F., Laheurte P., Peron I., Gloriant T., *Microstructure and mechanical behavior of superelastic Ti-24Nb-0.5O and Ti-24Nb-0.5N biomedical alloys*, Journal of the mechanical behavior of biomedical materials, **9**, p83, 2012.

Sander B., Raabe D., *Texture inhomogeneity in a Ti-Nb-based $\beta$-titanium alloy after warm rolling and recrystallization*. Materials Science and Engineering A, **479**, p236, 2008.

Sun F., Hao Y.L., Nowak S., Gloriant T., Laheurte P., Prima F., *A thermo-mechanical treatment to improve the superelastic performances of biomedical Ti-26Nb and Ti-20Nb-6Zr (at.%) alloys*, Journal of the mechanical behavior of biomedical materials, **4**, p1864, 2011.

Sun F., Nowak S., Gloriant T., Laheurte P., Eberhardt A., Prima F., *Influence of a short thermal treatment on the superelastic properties of a titanium-based alloy*. Scripta Materialia, **63**, p1053, 2010.

Tahara M., Kim H.Y., Hosoda H., Miyazaki S., *Cyclic deformation behavior of a Ti–26 at.% Nb alloy*. Acta Materialia, **57**, p2461, 2009.

Wang L.Q., Lu W.J., Qin J.N., Zhang F., Zhang D., *Microstructure and mechanical properties of cold-rolled TiNbTaZr biomedical $\beta$ titanium alloy*, Materials Science and Engineering A, **490**, p421, 2008.

Yang Y., Castany P., Cornen M., Thibon I., Prima F., Gloriant T., *Texture investigation of the superelastic Ti-24Nb-4Zr-8Sn alloy*. Journal of Alloys and Compounds, 85, p591, 2014.

Yang Y., Castany P., Cornen M., Prima F., Li S.J., Hao Y.L., Gloriant T., *Characterization of the martensitic transformation in the superelastic Ti-24Nb-4Zr-8Sn alloy by in situ synchrotron X-ray diffraction and dynamic mechanical analysis*, Acta Materialia, **88**, p25, 2015.

INSA de RENNES
Service des Formations

# AVIS DU JURY SUR LA REPRODUCTION DE LA THESE SOUTENUE

**Titre de la thèse:**
Etude de la transformation martensitique et des mécanismes de déformation se produisant dans l'alliage superélastique Ti-24Nb-4Zr-8Sn

**Nom Prénom de l'auteur : YANG YANG**

Membres du jury :
- Monsieur PRIMA Frédéric
- Monsieur GLORIANT Thierry
- Monsieur CASTANY Philippe
- Monsieur FAVIER Denis
- Monsieur DOUIN Joël
- Monsieur HAO Yulin

Président du jury : Joel Douin

Date de la soutenance : 24 Février 2015

Reproduction de la these soutenue

Thèse pouvant être reproduite en l'état
Th~~èse pouvant être reproduite après corrections sugg~~érées

Fait à Rennes, le 24 Février 2015

Signature du président de jury

Le Directeur,

M'hamed DRISSI

## Résumé

Les alliages de titane sont actuellement très utilisés comme implants orthopédiques de part leurs bonnes propriétés mécaniques, leur bonne résistance à la corrosion ainsi que leur excellente biocompatibilité. Cependant, l'alliage Ti-6Al-4V qui est le plus utilisé présente un module d'élasticité élevé (110GPa), ce qui peut provoquer le phénomène de « stress shielding » et finalement causer l'échec de l'implantation. De plus, l'utilisation à long terme de ce type d'alliage est remise en question à cause de la présence de certains éléments (Al et V) considérés comme cytotoxiques et/ou allergènes. Les alliages β-métastables à base de titane peuvent être des candidats de remplacement intéressants grâce à l'addition d'éléments biocompatibles tel que Nb, Zr et Sn.

L'alliage superélastique biocompatible de composition Ti-24Nb-4Zr-8Sn (% massique) a été étudié dans le cadre de cette thèse. Cet alliage montre des propriétés intéressantes telles qu'un bas module d'élasticité, une résistance mécanique élevée et une ductilité relativement importante.

Dans ce travail de thèse, différents traitements thermomécaniques ont été réalisés afin d'obtenir des textures cristallographiques différentes. Les influences de changement de texture sur les propriétés mécaniques et la superélasticité ont été ainsi préalablement étudiées. La transformation martensitique a été caractérisée par des essais *in situ* de diffraction des rayons X sous rayonnement synchrotron (SXRD) pendant une sollicitation mécanique et par analyse mécanique dynamique (DMA) sous différentes contraintes statiques. De plus, les microstructures de déformation ont été observées par EBSD et MET pour caractériser précisément les mécanismes de déformation plastique, en particulier le maclage.

## Abstract

Titanium alloys have already been extensively used as orthopedic implants due to the good mechanical properties, corrosion resistance and excellent biocompability. However, the most widely used Ti-6Al-4V alloy exhibits high elastic modulus (110GPa) which would cause the stress shield effect and eventually lead to the implantation failure. Furthermore, elements of Al and V are proved to be toxic for long-term application. Low modulus metastable β titanium alloy can be a suitable candidate through proper addition of non-toxic alloying element such as Nb, Zr and Sn.

The present investigated Ti-24Nb-4Zr-8Sn alloy is a new β-type metastable alloy potentially interesting for biomedical applications. This alloy displays high strength, low elastic modulus, high ductility, superelastic property and good biocompatibility according to previous investigations.

In this work, the as-cold rolled Ti-24Nb-4Zr-8Sn alloy was subjected to different thermo-mechanical treatments in order to introduce different crystallographic texture. Influences of texture change on mechanical properties and superelasticity have been preliminarily studied. Martensitic transformation which is responsible for the superelasticity has been characterized by both *in situ* synchrotron X-ray diffraction and dynamic mechanical analysis. Moreover, deformed microstructures have been observed by EBSD and TEM to characterize precisely the plastic deformation mechanisms, and particularly the twinning.

N° d'ordre : 15ISAR 05 / D15 - 05
INSA RENNES
Institut National des Sciences Appliquées de Rennes
20, Avenue des Buttes de Coësmes . CS 14315 . F-35043 Rennes Cedex
Tel : 02 23 23 82 00 – Fax : 02 23 23 83 96